





# Towards a Molecular Level Understanding of Active Sites for Catalysis and the Interactions with Solvents in Zirconium Based Metal–Organic Frameworks at Operating Conditions

Moleculair inzicht in de actieve sites voor katalyse en de interactie  
met solventen in zirconium gebaseerde metaal–organische roosters bij  
procescondities

Chiara Caratelli

Supervisor: prof. dr. ir. Veronique Van Speybroeck  
Dissertation submitted in fulfillment of the requirements for the degree of  
Doctor (Ph.D.) of Chemical Engineering Technology

Chair: prof. em. dr. ir. L. Taerwe  
Faculty of Engineering and Architecture  
Ghent University  
Academic year 2019–2020





## Members of the examination committee

### **Chair**

prof. em. dr. ir. Luc Taerwe (Ghent University)

### **Reading Committee**

prof. dr. ir. Toon Verstraelen (Ghent University)

prof. dr. Pascal Van Der Voort (Ghent University)

prof. dr. ir. Evert Jan Meijer (University of Amsterdam)

prof. dr. ir. Rob Ameloot (KU Leuven)

### **Supervisor**

prof. dr. ir. Veronique Van Speybroeck (Ghent University)



This research has been conducted at the **Center for Molecular Modeling**, in collaboration with:

- Instituto de Tecnología Química, Universitat Politècnica de València (Dr. F. X. Llabrés i Xamena, Dr. Francisco García Cirujano)
- Centre for Membrane Separations, Adsorption, Catalysis, and Spectroscopy for Sustainable Solutions, KU Leuven (Prof. R. Ameloot, João Marreiros)
- Van 't Hoff Institute for Molecular Sciences, Universiteit Van Amsterdam (Prof. E. J. Meijer, Dr. B. Ensing)



# Contents

<b>List of Abbreviations</b>	<b>iii</b>
<b>List of Symbols</b>	<b>v</b>
<b>Samenvatting</b>	<b>vii</b>
<b>Summary</b>	<b>xiii</b>
<b>I Towards a Molecular Level Understanding of Active Sites for Catalysis and the Interactions with Solvents in Zirconium Based Metal–Organic Frameworks at Operating Conditions</b>	<b>1</b>
<b>1 Introduction</b>	<b>3</b>
1.1 Metal Organic Frameworks . . . . .	4
1.2 Outline and goal of the thesis . . . . .	17
<b>2 Modeling metal organic frameworks</b>	<b>19</b>
2.1 Framework topology . . . . .	19
2.2 Theoretical methods . . . . .	22
2.3 Free energy . . . . .	30
2.4 Exploring the free energy surface . . . . .	33
<b>3 Major research results</b>	<b>41</b>
3.1 Activation processes in zirconium–MOFs . . . . .	42
3.2 Role of solvent: towards operating conditions . . . . .	60
<b>4 Conclusions and perspectives</b>	<b>73</b>
<b>II Published papers</b>	<b>79</b>
<b>Paper I:</b> Nature of active sites on UiO–66 and beneficial influence of water in the catalysis of Fischer esterification . . . . .	81
<b>Paper II:</b> Influence of a confined methanol solvent on the reactivity of active sites in UiO–66 . . . . .	117

<b>Paper III:</b> On the intrinsic dynamic nature of the rigid UiO–66 metal–organic framework . . . . .	137
<b>Paper IV:</b> Active Role of Methanol in Post-Synthetic Linker Exchange in the Metal–Organic Framework UiO–66 . . . . .	149
<b>Paper V:</b> Dynamic interplay between defective UiO–66 and protic solvents in activated processes . . . . .	167
<b>A Publication List</b>	<b>201</b>
Publications in international peer-reviewed journals . . . . .	201
Conference contributions . . . . .	202
<b>B Granted computational Projects</b>	<b>207</b>
Computational projects under the Vlaams Super Computing Centrum infrastructure . . . . .	207
<b>C Acknowledgement</b>	<b>209</b>
<b>Bibliography</b>	<b>211</b>

# List of Abbreviations

---

<b>AIMD</b>	<i>Ab Initio</i> Molecular Dynamics
<b>AIM</b>	Atomic layer deposition in MOF
<b>BDC</b>	Benzene-1,4-dicarboxylate
<b>BTC</b>	Benzene-1,3,5-tricarboxylic acid
<b>BO</b>	Born–Oppenheimer
<b>BOMD</b>	Born–Oppenheimer Molecular Dynamics
<b>CMM</b>	Center for Molecular Modeling
<b>CPMD</b>	Car–Parrinello Molecular Dynamics
<b>CN</b>	Coordination Number
<b>CV</b>	Collective Variable
<b>DFT</b>	Density Functional Theory
<b>FES</b>	Free Energy Surface
<b>FFA</b>	Free Fatty Acids
<b>FTIR</b>	Fourier-Transform Infrared
<b>GCMC</b>	Grand Canonical Monte Carlo
<b>GGA</b>	Generalized Gradient Approximation
<b>HF</b>	Hartree–Fock
<b>HKUST</b>	Hong Kong University of Science and Technology
<b>HPC</b>	High-Performance Computing
<b>IR</b>	Infrared
<b>IRMOF</b>	Isoreticular MOF
<b>LDA</b>	Local Density Approximation
<b>LSDA</b>	Local Spin Density Approximation
<b>M–L</b>	Metal–linker coordination
<b>MC</b>	Monte Carlo
<b>MD</b>	Molecular Dynamics
<b>MIL</b>	Matériaux de l’Institut Lavoisier
<b>MOF</b>	Metal–Organic Framework
<b>MPV</b>	Meerwein–Ponndorf–Verley
<b>MTD</b>	Metadynamics
<b>MTK</b>	Martyna–Tobias–Klein
<b>NEB</b>	Nudged elastic band
<b>NU</b>	Northwestern University
<b>PBC</b>	Periodic Boundary Conditions
<b>PCM</b>	Polarizable Continuum Model
<b>PCP</b>	Porous Coordination Polymer
<b>PHVA</b>	Partial Hessian Vibrational Analysis
<b>PES</b>	Potential Energy Surface

<b>PSE</b>	Post–Synthetic Exchange
<b>PSLE</b>	Post–Synthetic Ligand Exchange
<b>PSM</b>	Post–Synthetic Modification
<b>PXRD</b>	Powder X–Ray Diffraction
<b>QM</b>	Quantum Mechanics
<b>RE</b>	Replica Exchange
<b>RDF</b>	Radial Distribution Function
<b>RPA</b>	Random Phase Approximation
<b>SBU</b>	Secondary Building Unit
<b>SCF</b>	Self–Consistent Field
<b>SE</b>	Single Excitation
<b>SXRD</b>	Single–Crystal X–Ray Diffraction
<b>TFA</b>	Trifluoroacetic Acid
<b>TGA</b>	Thermogravimetric Analysis
<b>TPS</b>	Transition Path Sampling
<b>TS</b>	Transition State
<b>TST</b>	Transition State Theory
<b>UiO</b>	Universitetet i Oslo (University of Oslo)
<b>US</b>	Umbrella Sampling
<b>WHAM</b>	Weighted Histogram Analysis Method
<b>XRD</b>	X–Ray Diffraction
<b>ZPE</b>	Zero Point Energy

# List of Symbols

---

$\ddagger$	Transition state
$\Delta E^\ddagger$	Electronic energy barrier
$\Delta H^\ddagger$	Enthalpy barrier
$\Delta G^\ddagger$	Free energy barrier
$B_0$	Bulk modulus
$E$	Electronic energy
$E_{ZPE}$	Zero-point vibrational energy
$F$	Helmholtz free energy
$G$	Gibbs free energy
$\hat{H}$	Hamiltonian operator
$H$	Enthalpy
$h$	Planck constant
$k$	Rate coefficient unimolecular reaction
$k_B$	Boltzmann constant
$N$	Number of particles
$N_A$	Avogadro constant
$N_{dof}$	Number of degrees of freedom
$p$	Pressure
$Q$	Overall partition function
$Q_{trans}$	Translational partition function
$Q_{rot,ext}$	Rotational partition function
$Q_{vib}$	Vibrational partition function
$q_X$	Partition function of species $X$
$R$	Universal gas constant
$r_{ij}$	Distance between atoms i and j
$S$	Entropy
$T$	Temperature
$U$	Internal energy
$V$	Volume
$V_0$	Equilibrium Volume
$\epsilon_0$	Electronic energy
$\nu_i$	Vibrational frequency
$\rho$	Density

---



# Samenvatting

Nanoporeuze materialen worden intensief bestudeerd de laatste decennia omwille van hun veelzijdigheid aan toepassingen in tal van sectoren. Dit toepassingspotentieel heeft vooral te maken met hun groot intern oppervlak en porie–volume, waardoor ze uitermate geschikt zijn binnen de heterogene katalyse en adsorptie toepassingen. Een groot scala van nanoporeuze materialen zijn momenteel beschikbaar zoals zeolieten en actieve kool die op grootschalige basis worden gebruikt binnen de petrochemie, geneeskunde en milieutoepassingen.

Recentelijk werden nieuwe generaties van nanoporeuze materialen ontwikkeld waarvan het bouwconcept gebaseerd is op bouwstenen die modulair kunnen worden samengebracht. Tot deze klasse behoren onder meer metaal–organische roosters (MOFs) en covalente organische roosters (COFs). Vooral MOFs zijn op korte tijd geëvolueerd tot één van de meest onderzochte materialen en dit omwille van hun grote variabiliteit in bouwconcept, wat het mogelijk maakt materialen te ontwerpen voor specifieke toepassingen. Hoewel ze initieel vooral werden onderzocht voor adsorptietoepassingen, wordt het toepassingspalet volop uitgebreid de laatste jaren. Op dit moment zijn reeds talrijke succesvolle voorbeelden beschikbaar van MOFs binnen het domein van de heterogene katalyse.

Het uniek bouwconcept berust op het samengaan van anorganische bouwblokken met multitopische organische linkers via coördinatie bindingen. Op die manier worden 1D-, 2D- of 3D- kristallijne netten gevormd. Door het feit dat men kan uitgaan van een groot aantal anorganische bouwblokken die op hun beurt kunnen gecombineerd worden met tal van organische linkers, kunnen een bijzonder groot aantal materialen worden gesynthetiseerd. Inderdaad tot op vandaag werden er meer dan 10000 materialen experimenteel gemaakt. De grote uitdaging bestaat er echter in om de materialen zo te ontwerpen zodat ze optimaal geschikt zijn voor een bepaalde toepassing. Naast deze grote verscheidenheid gegenereerd door de grote combinatoriek van bouwblokken, kunnen de materialen ook nog verder worden gefunctionaliseerd worden door middel van post–synthetische modificaties. Het mag duidelijk zijn dat metaal organische roosters omwille van bovenstaande aspecten bijzonder veel potentieel vertonen voor ontwerp en design naar specifieke toepassingen toe.

In tegenstelling echter tot zeolieten, de welbekende familie van nanoporeuze anorganische materialen die momenteel op grote schaal worden gebruikt binnen tal van industriële toepassingen, zijn ze echter minder stabiel. Dit heeft te maken met de aanwezigheid van de metaal–ligand binding die inherent zwakker is dan de

silicium–oxide binding die aan de basis ligt van zeolieten. Echter zeolieten kunnen niet gefabriceerd worden met een even grote verscheidenheid en lenen zich in die zin minder tot molecuair ontwerp voor specifieke toepassingen.

In deze thesis worden metaal organische roosters onderzocht voor toepassingen binnen de katalyse. Zoals reeds gesteld, bieden metaal organische roosters de mogelijkheid om poreuze materialen te ontwerpen met het doel om optimale chemische conversies met gewenste productselectiviteit en opbrengst te bekomen. Naast deze specifieke eigenschappen, behoren ze uiteraard tot het domein van de heterogene katalyse, wat maakt dat ze toelaten meer duurzame processen te ontwerpen gezien inherent product separatie of toxicisch afval minder is in vergelijking met processen waarbij homogene katalysatoren worden gebruikt.

Een groot vraagstuk bestaat erin te begrijpen hoe actieve sites voor katalyse eruit zien en hoe zij kunnen worden gegenereerd en gemoduleerd. Al vrij vlug na de vlug na de initiële synthese van de eerste metaal organische roosters werd duidelijk dat deze materialen inherent een grote mate van wanorde kunnen bezitten en structurele defecten. Initieel werd dit vooral als een nadeel gepercipieerd, echter binnen de huidige wetenschappelijke context wordt de aanwezigheid van defecten en hun mogelijkheid tot modulatie geëxploiteerd voor specifieke toepassingen. Dit is met name belangrijk voor de creatie van actieve sites voor katalytische reacties. Binnen deze thesis zullen ondermeer materialen worden onderzocht die indien perfect opgebouwd enkel volledig gecoördineerde metaalsites bevatten en in die zin open metaal sites ontbreken waaraan katalytische reacties kunnen plaatsvinden. Het structureel inbouwen van defecten biedt de mogelijkheid om de materialen te activeren voor katalytische toepassingen. Verder kunnen defecten er ook voor zorgen dat de poriegrootte wordt aangepast bijvoorbeeld door structureel ontbreken van anorganische bouwbladen in het materiaalskelet. De grote uitdaging bestaat erin om de aanwezigheid van defecten te controleren en ook hun molecuair gedrag te begrijpen.

De experimentele karakterisatie van deze materialen tot op molecuair niveau is bijzonder uitdagend mede door de complexiteit van hun structuur en de aanwezigheid van structurele defecten. De aanwezigheid van wanorde maakt het niet triviaal voor experimentatoren om direct inzicht te verkrijgen in de moleculaire aard van de actieve sites en structuur–eigenschappenrelaties op te stellen. In dit opzicht zijn moleculaire modelleringstudies in nauwe samenwerking met experimentatoren van essentieel belang om het gedrag van MOFs te begrijpen en te voorspellen. Binnen het domein van de moleculaire modellering en de toepassing op nanoporeuze materialen heeft een enorme evolutie plaatsgegrepen de afgelopen tientallen jaren. Met behulp van computationele technieken is het nu mogelijk om MOFs te bestuderen op de nanoschaal. In die zin kunnen computersimulaties aangewend worden om experimentele waarnemingen te verklaren en in sommige gevallen kan gepoogd worden zelfs te voorspellen wat aangewezen materialen zijn voor bepaalde toepassingen of hoe reactieomstandigheden kunnen worden aangepast om een betere selectiviteit, activiteit te bekomen. Men moet zich echter realiseren dat dit laatste een bijzonder grote uitdaging blijft voor huidige modelleringstechnieken, gezien het zeer moeilijk is om theoretische modellen op te

stellen die met voldoende nauwkeurigheid experimentele omstandigheden kunnen nabootsen.

Een groot scala van moleculaire modelleringstechnieken zijn momenteel voorhanden om nanoporeuze materialen te bestuderen. Tal van keuzes dienen gemaakt te worden die een afweging zijn tussen enerzijds de haalbare computationele kost en anderzijds de accuraatheid waarmee het materiaal en het proces wordt beschreven. Idealiter benaderen moleculaire modellen zo goed als mogelijk de experimentele en reële condities. Afhankelijk van welke aspecten men wenst te bestuderen kunnen verschillende benaderingsmethoden worden toegepast. Indien men bijvoorbeeld geïnteresseerd is in fysische eigenschappen zoals fasetransformaties, kan het volstaan om de chemische interacties op benaderende wijze te beschrijven aan de hand van krachtvelden waardoor meer atomen kunnen worden in rekening gebracht worden. Echter voor de katalyse, is het essentieel om de chemische bindingen voldoende accuraat te beschrijven teneinde de actieve site en het reactiemechanisme correct in kaart te brengen. Dergelijke meer accurate methoden die gebaseerd zijn op een expliciete beschrijving van de elektronische structuur, vergen een hogere computationele kost waardoor de modelsystemen in grootte moeten beperkt worden. Concreet betekent dit het aantal atomen van het systeem beperkt blijft tot een paar honderdtal atomen. Een grote uitdaging bestaat erin de topologie van het materiaal correct in kaart te brengen en ook rekening te houden met procescondities zoals een realistische temperatuur, gasdruk of aanwezigheid van solventen in de poriën van het materiaal. De huidige computationele technieken zijn dermate geëvolueerd dat dergelijke beschrijving van een chemische reactie op procescondities binnen het bereik komt. Dit heeft niet alleen te maken met de opkomst van heel krachtige High Performance computers maar ook met de ontwikkeling van ingenieuze theoretische algoritmes die toelaten om grote moleculaire systemen accuraat te berekenen.

Binnen deze thesis werden zirconium materialen bestudeerd voor katalytische toepassingen. Meer in het bijzonder werd een uitgebreid onderzoek verricht van de actieve binnen het zeer stabiel UiO-66 materiaal. Er werd specifiek geopteerd om dit materiaal in detail te onderzoeken, gezien het een van de meest onderzochte materialen is voor verscheidene toepassingen en dit omwille van de zeer hoge stabiliteit binnen de familie van de metaal organische roosters. De grote stabiliteit vindt zijn oorsprong in de opbouw van het materiaal, namelijk zirconium oxide clusters worden geconnecteerd met tereftalaat linkers en dit met een heel hoge graad van connectiviteit. Elke anorganische bouwblok wordt geconnecteerd met 12 organische linkers in het defectvrije materiaal. Dit maakt dat het materiaal bijzonder robuust is in verscheidene chemische omstandigheden en thermische condities, waardoor het volop kan worden ingezet voor tal van katalytische toepassingen. Het defectvrije materiaal bevat geen open metaal sites en is in die zin niet geschikt voor katalytische toepassingen. Lange tijd was het onduidelijk hoe de actieve sites werden gecreëerd binnen dit materiaal. Door middel van geavanceerd fundamenteel wetenschappelijk experimenteel en theoretisch onderzoek, is het duidelijk geworden dat de structurele aanwezigheid van defecten aan de basis ligt van actieve sites voor katalyse. Zo kunnen ondermeer linkers ontbreken, maar aangezien het materiaal inherent een bijzonder hoge graad van connectiviteit vertoont, brengt

dit de stabiliteit niet in het gedrang. Dit materiaal met zijn veelzijdigheid van eigenschappen en mogelijkheid tot modulatie vormt een ideaal platform voor dit doctoraatsonderzoek.

Binnen dit doctoraatsonderzoek werden actieve sites voor katalyse in het UiO–66 materiaal bestudeerd met een groot scala van computationele technieken teneinde een begrip te krijgen van het reactief gedrag op procescondities. Er werd zowel gebruik gemaakt van statische technieken waarbij slechts enkele punten op het potentieel energie oppervlak werden gelokaliseerd als moleculaire dynamica technieken waarbij het gedrag in functie van de tijd op reële temperaturen en in reële omstandigheden van reactanten in aanwezigheid van solventen werd gevolgd. Het potentieel energie oppervlak werd systematisch beschreven met behulp van dichtheidsfunctionaaltheorie. Hierdoor wordt de elektronische structuur van het materiaal expliciet beschreven met een haalbare computationele kost. Initieel werd voor sommige reacties gebruik gemaakt van uitgebreide clustermodellen om een eerste inzicht te krijgen in de lokale omgeving van de katalytisch actieve site. Nadien werd systematisch overgestapt op moleculaire modellen waarbij de topologie van het materiaal met inbegrip van de periodieke randvoorwaarden correct in kaart werd gebracht. Het computationele werk werd in grote mate verricht in samenwerking met verscheidene experimentele groepen. Verder werd ook samengewerkt met internationale theoretische partners om de kennis aangaande gevanceerde moleculaire dynamica technieken te versterken.

Als startpunt van het doctoraatsonderzoek werd de Fischer esterificatie bestudeerd, welke een Lewis zuur gekatalyseerde reactie is en waarvoor een gunstig effect werd waargenomen in het experiment door de aanwezigheid van water. Initieel was het onduidelijk wat het effect was van water op de actieve site. Dankzij het toepassen van moleculaire modelleringstechnieken, werd duidelijk dat de actieve site niet alleen bestaat uit een Lewis zure site maar dat ook de aanwezigheid van Brønsted zure sites essentieel is voor optimaal functioneren van de actieve site. De aanwezigheid van waterige solventen heeft een gunstige invloed op de reactie aangezien het de mobiliteit van protonen faciliteert, waardoor een soort van dynamische aciditeit van het materiaal wordt gegenereerd.

Startende van deze specifieke case studie, werd het duidelijk dat het gebruik van statische methoden, niet altijd voldoende is voor het bestuderen van katalytische reacties in deze materialen op procescondities, gezien in de realiteit het materiaal en de actieve site een sterk dynamisch gedrag kunnen vertonen. In groot deel van de thesis werd derhalve gebruik gemaakt van meer complexere modellen waarbij het solvent dat opgesloten is in de poriën van het materiaal explicet in rekening wordt gebracht op realistische experimentele condities. Door het gebruik van dergelijke gevanceerde moleculaire modelleringstechnieken werd duidelijk dat protische solventen het gedrag van het materiaal in grote mate kunnen moduleren door continu te interacteren met de onder gecoördineerde zirconium clusters. De aanwezigheid van een dergelijke solvent laat verder toe om geladen intermediairen te stabiliseren. Een onderbouwd inzicht werd bekomen in de manier hoe defecten in deze materialen kunnen worden gevormd en gemoduleerd. Door toepassing van gevanceerd moleculaire dynamicatechnieken, werd het duidelijk

dat de organische linkers een zekere graad van mobiliteit kunnen vertonen. Zij kunnen tijdelijk loskomen van de anorganische cluster, connecteren met een andere deel van de anorganisch bouwblok en dit terwijl de structurele integriteit van het materiaal behouden blijft. Dergelijke dynamisch gedrag van linkers blijkt tevens aan de basis te liggen van de postsynthetische modificatie van het UiO–66 materiaal. In samenwerking met experimentele partners werd dit proces nader bekeken. Een uniek inzicht werd bekomen in de moleculaire processen die aan de grondslag liggen van postsynthetische modificatieroutes.

In een volgende fase werd nagegaan in hoeverre het waargenomen dynamisch gedrag van het UiO–66 materiaal met hoge connectiviteit, kon worden veralgemeend naar andere zirconium gebaseerde materialen. In dit opzicht werd het MOF-808 materiaal onderzocht, wat opgebouwd is uit gelijkaardige zirconium oxide clusters maar waarbij de connectiviteit met organische linkers lager is. Het materiaal bezit een groot porievolume waardoor het actief wordt onderzocht binnen het domein van de katalyse. Het werd duidelijk dat het waargenomen gedrag voor UiO–66 niet rechtstreeks kan worden doorgetrokken naar andere zirconium gebaseerde materialen. De lagere connectiviteit zorgt voor een aantal fundamentele verschillen met betrekking tot stabiliteit. Verdere studies in dit domein naar andere potentieel interessante zirconium materialen bieden een interessant perspectief voor toekomstige katalytische toepassingen.

Samenvattend, werden in deze thesis een groot scala van computationele technieken aangewend om de eigenschappen van actieve sites voor katalyse te begrijpen op moleculaire schaal in zirconium gebaseerde materialen. Gezien in deze hoog geconnecteerde materialen de actieve sites worden gegeneerd door de creatie van structurele defecten, is het belang van solventen in de poriën van het materiaal van uitermate belang. Dit alles echter levert een nanogestrukteerd platform voor katalyse dat bijzonder complex is maar ook een groot scala van mogelijkheid biedt voor verder exploitatie van katalytische reacties. De modelleringstechnieken die nodig zijn om dergelijk complex systeem te modelleren zijn zeer geavanceerd en inzicht kan enkel bekomen worden door complementaire technieken in te zetten. De bekomen resultaten benadrukken het belang van geavanceerde modelleringstechnieken om het katalytisch gedrag van dergelijke complexe materialen te ontrafelen op moleculaire schaal.



# Summary

In the past decades, nanoporous materials have become an intense field of study due to their numerous potential applications. This has to do mainly to their extremely high surface area and pore volume, that make them suitable in heterogeneous catalysts and adsorption applications. At present time, a wide range of nanoporous materials are available, such as zeolites and activated carbon, widely used in petrochemistry, medicine and environmental applications.

Recently, new generations nanoporous materials have been explored which rely on the concept of reticular chemistry and building blocks, such as Metal Organic Frameworks (MOFs) and Covalent Organic Frameworks (COFs). In particular, MOFs have rapidly become one of the most deeply investigated classes of materials due to their great variability in design, that allows the synthesis of materials for specific applications. Although they were initially investigated for applications as adsorbants, their range of applications has been enormously expanded in recent years. Currently, many successful examples of MOFs are available in the field of heterogeneous catalysis.

The unique construction concept of MOFs is based on the combination of inorganic building blocks with multtopic organic linkers via coordination bonds. This way, 1-, 2- or 3-D crystalline structures can be formed. A large number of inorganic building blocks can be combined with numerous organic linkers, allowing to construct a plethora of different materials. Indeed, up to today more than 10,000 MOFs have been synthesized experimentally. The big challenge lies in designing material that are optimally suited for a specific application. In addition to the large combination of building blocks, the materials can be further functionalized through post-synthetic modifications. Because of the above aspects, MOFs have a great potential to be designed to target a specific application.

However, in contrast to zeolites, the well-known family of inorganic nanoporous materials that are widely used in many industrial applications, MOFs are less stable. This is due to the presence of metal-ligand bonds that are inherently weaker than the Si-O bonds that lie at the basis of zeolites. However, zeolites cannot be manufactured with an equally large variety of structures and in this sense are less suitable for molecular design to target specific applications.

In this thesis, MOFs have been investigated for applications within catalysis. As already stated, MOFs offer the possibility to design porous materials to maximize the outcome of a given reaction, in terms of yield and selectivity for a desired prod-

uct. Moreover, as heterogeneous catalysts, they can bring numerous advantages to industry. As opposed to homogeneous catalysts, they offer the possibility to design more sustainable processes, with less toxic waste and easy product separation.

A major issue lies in the understanding of how active sites for catalysis look like and how they can be generated and modulated. Soon after the synthesis of the first MOFs, it became clear that these materials inherently possess a high degree of disorder and structural defects. If at first this was seen as a drawback, within the current scientific context it has become clear that the presence of defects and their modulation can be exploited for specific applications. This is particularly important for the creation of active sites for catalytic reactions. Some MOFs, if perfectly constructed only contain fully coordinated metal sites and in this sense are missing open metal sites where reactions can take place. The structural incorporation of defects offers the possibility to activate the materials for catalytic applications. Furthermore, defects can also increase the pore size, for instance if inorganic building blocks are missing. The big challenge lies in investigating the presence of defects and understanding their molecular behavior.

The experimental characterization of these materials at the molecular level is particularly challenging due to their structural complexity and the presence of structural defects. The presence of disorder makes it not trivial for experimentalists to have direct insight on the molecular nature of the active sites and to understand structure–property relationships. In this sense, modeling studies in close synergy with experimental research are of utmost importance to understand and predict MOF behavior.

The past decades have seen an enormous evolution within the domain of molecular modeling and its application to nanoporous materials. Using computational techniques, it is now possible to study MOFs at the nanoscale. In this sense, computer simulations can be used to explain experimental observations and in some cases even attempt to predict what are the appropriate materials for certain applications, or how reaction conditions can be adjusted to achieve better selectivity and activity. It must be realized, however, that the latter remains a major challenge for current modeling techniques, since it is very difficult to develop theoretical models that can simulate experimental conditions with sufficient accuracy.

Nowadays, a rich toolbox of molecular modeling techniques is available for the study of nanoporous materials which can be applied to MOFs. When studying such complex materials, there is always a trade-off between computational cost and the accuracy in the description of processes and material. Ideally, molecular models describe experimental conditions as closely as possible. Depending on which aspects one wants to focus on, different approaches can be used. For physical properties such as phase transformations, it may suffice to describe the chemical interactions approximately using force fields, so that more atoms can be taken into account in the model. However for catalysis it is essential to accurately describe the chemical bonds to correctly map active sites and reaction mechanisms. Such accurate methods, which are based on an explicit description of the electronic structure, are computationally more expensive, and the model systems must be

limited in size. In concrete terms, this means that the number of atoms in the system is limited to a few hundred atoms. It poses a major challenge to correctly map the topology of the material and at the same time take into account operating conditions, such as realistic pressure, temperature and presence of guest molecules. Current computational techniques have evolved to such an extent that a description of chemical reactions at operating conditions is now within reach. This is not only due to the growth in computational power of High Performance Computing facilities, but also to the development of ingenious theoretical algorithms that allow to calculate large molecular systems accurately.

Within this thesis, zirconium MOFs were examined for catalytic applications. More in particular, an extensive study was conducted on the active sites within the extremely stable UiO–66 material. UiO–66 was specifically selected as it is one of the most investigated MOFs for various applications, and because of its high structural stability within the MOF family. The exceptional stability originates from the structure of the material, in which zirconium–oxide bricks are bridged by terephthalate linkers with a high structural connectivity. In the defect-free material, each inorganic brick is connected to 12 linkers. This makes the material extremely robust and able to withstand the chemical and thermal conditions of numerous catalytic applications. The defect-free UiO–66 does not contain open metal sites and is therefore not suitable for catalytic applications. For a long time it was not understood how the active sites were created within this material. By means of advanced experimental and theoretical research, it has become clear that the presence of structural defects is responsible for the creation of active sites for catalysis. The highly connected material allows for the presence of crystal defects such as missing linkers, without compromising its stability. This material, with its versatility of properties and possibility of modulation forms an ideal platform for this doctoral research.

Within this doctoral research, the active sites in the UiO–66 material were studied with different advanced modeling techniques in order to gain an understanding of the reactive behavior at operating conditions. Static techniques were used, where only a few points on the potential energy surface are investigated, as well as molecular dynamics techniques, where the behavior was followed at realistic temperatures and operating conditions in presence of solvents. The potential energy surface was systematically described using density functional theory, which allows explicitly describe the electronic structure of the material with a feasible computational cost. For some reactions, extended cluster models were initially used to gain insight into the local environment of the active site. We then made use of periodic boundary conditions to correctly map the topology of the material. The computational work was largely carried out in collaboration with various experimental groups. Furthermore, there was also collaboration with international theoretical partners to strengthen the knowledge on advanced molecular dynamics techniques.

As a starting point for the doctoral research, the Lewis–catalyzed Fischer esterification was studied, for which a beneficial effect of the presence of water was observed experimentally. Initially, it was unclear what the effect of water was

on the active site. By use of molecular modeling techniques, it became clear that the active sites are not only composed of Lewis acid sites, but also Brønsted sites are needed for the optimal functioning of the catalyst in this reaction. The presence of aqueous solvent has a beneficial effect on the reaction, facilitating the mobility of protons and generating a sort of dynamic acidity in the material.

Starting from this specific case study, it became clear that static methods are not always sufficient to study the active sites in these materials at operating conditions, since the material can exhibit strong dynamic behavior. In the rest of this thesis, therefore, more complex models were used in which the solvent confined in the pores of the material is explicitly taken into account at realistic experimental conditions. By means of such advanced molecular modeling techniques, it became clear that protic solvents can modulate the behavior of the material to a large extent by continuously interacting with the under coordinated zirconium clusters. The presence of such a solvent also makes it possible to stabilize charged reaction intermediates. A substantial insight was obtained into how defects in these materials can be formed and modulated. By applying advanced molecular dynamics techniques, it became clear that the organic linkers can show a certain degree of mobility. They can temporarily decoordinate from the inorganic cluster and connect with another part of the inorganic building block, while maintaining the structural integrity of the material. Such dynamic behavior of linkers seems to lie at the basis of the post-synthetic modification of the UiO-66 material. This process was further examined in collaboration with experimental partners. A unique insight was obtained into the molecular processes that form the basis of post-synthetic modification routes.

In a subsequent phase, it was investigated to what extent the observed dynamic behavior of the UiO-66 material, with high connectivity, could be generalized to other zirconium-based materials. In this respect, the MOF-808 material was investigated, composed by similar zirconium–oxide clusters, but with lower structural connectivity. The material has a large pore volume and for this reason it is actively investigated in catalysis. It became clear that the behavior observed for UiO-66 cannot be directly extended to other zirconium- based materials. The lower connectivity provides fundamental differences with regard to stability. Further studies in this domain into other potentially interesting zirconium materials offer an interesting perspective for future catalytic applications.

In summary, a rich computational toolbox was used in this thesis to gain molecular understanding on the properties of active sites for catalysis in zirconium based material. As the active sites in these highly connected materials are generated by creation of structural defects, the role of solvent confined in the pores is extremely important. This provides a platform for catalysis that is particularly complex, but also offers many possibilities for further exploitation of catalytic reactions. The modeling techniques required to model such a complex system are very advanced and insight can only be obtained by using complementary techniques. The results obtained emphasize the importance of advanced modeling techniques to unravel the catalytic behavior of such complex materials at the molecular scale.

# List of Figures

1.1	Schematic representation of the building block design in Metal-Organic Frameworks (MOFs). Left panel: some examples of inorganic bricks; middle panel: some examples of organic linkers; right panel: some MOFs with different topologies, pore size and shape . . . . .	5
1.2	Schematic representation of some of the numerous MOF applications. . . . .	6
1.3	Number of publications on MOFs and catalysis in MOFs in years 1985–2018, showing the importance of catalysis in MOFs as indicated by Web of Science . . . . .	8
1.4	Structure of UiO–66 (top) and MOF–808 (bottom), the two Zr-MOFs investigated in this work of thesis. . . . .	10
1.5	Representation of the UiO–66 material with missing linkers and clusters displayed in red. In this dissertation, we mainly focus on missing linkers. . . . .	11
1.6	Lewis and Brønsted sites that are created when a linker is removed from the UiO–66 zirconium brick, with different number of coordinated water molecules. . . . .	13
1.7	Schematic representation of as synthesized and upon activation MOF–808 structures . . . . .	16
2.1	Left: extended cluster model cut from the periodic structure of UiO–66. The cluster contains the active site, the brick and the linkers in the closest proximity to the active site. Right: representation of the unit cells containing the defect. In blue, the conventional 4–brick unit cell, in orange, the 2–brick unit cell used for the calculations. The two different bricks are highlighted in orange. The 10–fold coordinated brick has two terephthalate linkers missing. Adapted from ref. [86] with permission of the American Chemical Society. . . . .	21
2.2	Representation of the different ways to remove up to three linkers from a 4–brick UiO–66 unit cell. Adapted from Ref. [89] with permission of the American Chemical Society. . . . .	22
2.3	The two lowest PES in the BO approximation for a diatomic molecule. In blue, the electronic PES for the ground state and first electronic excited state (UV–Vis transitions). In orange, the vibrational energy levels (IR transitions), in grey the rotational levels (microwave transitions). . . . .	24

2.4	Representation of some of the molecular modes taken into account in a generic force field model. . . . .	24
2.5	Schematic representation of the potential energy surface and the stationary points. . . . .	27
2.6	Representation of the atoms taken into account in the Partial Hessian Vibrational Analysis (PHVA) approach. Top: a schematic representation of a reactive process in nanoporous material, bottom: a snapshot from the static calculations where the atoms of the active site and the adsorbates are highlighted . . . . .	29
2.7	1D free energy profiles for a given reaction with and without catalyst, indicating the adsorbed initial, final states and the localized transition state, schematically illustrated in below. The adsorption free energy, intrinsic and apparent barriers are obtained by static calculations and indicated by $\Delta G_{ads}$ , $\Delta G_{‡}$ , and $\Delta G_{app}$ , respectively; . . . . .	32
2.8	a) 1D free energy profiles for a given reaction on two different active sites in UiO-66 (insets), indicating the adsorbed initial and final states and the localized transition state for this reaction; (b) possible 2D representation of the given reaction on the two active sites as obtained using advanced dynamic techniques, indicating the three critical points on the potential energy surface. Adapted from ref. [26] with permission of the Royal Society of Chemistry. . . . .	34
2.9	Schematic of the various computational methods applied to heterogeneous catalysis, which lie between an idealized ultra-high vacuum/0 K model and a realistic, <i>operando</i> model. The traffic light key depicts the quality of each method with respect to catalyst model complexity (Cat), reaction coordinate accuracy (RCN) and reaction network complexity (RxN). Adapted from ref. [125] with permission of the Royal Society of Chemistry. . . . .	36
2.10	Schematic representation of different MD techniques that can be used to explore the PES. Adapted from Ref. [129] with permission of the American Chemical Society . . . . .	38
3.1	Schematic representation of the UiO-66 structure with possible configurations of the bricks that give rise to coordinatively unsaturated zirconium atoms. The colors indicate the coordination of the zirconium atoms. Adapted from ref. [159] with permission of the Royal Society of Chemistry. . . . .	42

- 3.2 Coordination free energies at reaction temperature of 351 K of one, two and three water molecules at coordinatively unsaturated zirconium bricks in defective UiO-66 with respect to a water coordination free site (site R). The structure of the opposite site B corresponds with configuration 2' with two water molecules and consistently used in all periodic calculations considered in the figure. Free energies (in black) are given in kJ/mol, and their decomposition into enthalpic  $\Delta H$  (blue) and entropic  $-T\Delta S$  (grey) contributions. Energies are resulting from periodic calculations with PBE-D3 level of theory. In each configuration Lewis acid and Brønsted sites are indicated. Adapted from ref. [86] with permission of Elsevier. . . . . 44
- 3.3 Top: Fischer esterification reaction; bottom: three different types of UiO-66 active sites. . . . . 46
- 3.4 Mechanism and free energy profile for the esterification of propionic acid with methanol on a hydrated and defective UiO-66 material (blue), a hydrated defective UiO-66 material with amino functionalization of the BDC linkers (red), and on a dehydrated defective UiO-66 (black). Periodic calculations at B3LYP-D3//PBE-D3 level of theory, T=351 K. R corresponds with an empty frame with one linker defect and a pool with all reactants to guarantee mass balance. In P the defective Zr-brick is coordinated with two water molecules (configuration 2'). P' corresponds to the empty frame with the ester as final product and remaining water molecules in gas phase. Adapted from ref. [86] with permission of Elsevier. . . . . 47
- 3.5 Transition states belonging to three cases where no suitable mechanism for Fischer esterification was found, suggesting that the reaction needs a concerted participation of Lewis and Brønsted sites 48
- 3.6 Energy diagrams for defective UiO-66 unit cells. Each dot represents a possible distribution of missing-linker defects (1 or 3 in total) within the unit cell; the connecting dotted line represents a weighted average. Values are normalized by the number of missing linkers in the unit cell. (a) Enthalpy difference between defect sites capped in different ways versus the non-defective material at T = 298, 313, 373, 473 K. (b) Temperature-dependence of the free energy difference of the defective structures indicated above (capped with  $\text{H}_2\text{O}/\text{OH}^-$ ,  $\text{H}_2\text{O}/\text{MeO}^-$  and  $\text{MeOH}/\text{MeO}^-$ ) versus the non-defective structure. A representation of the clusters with different missing linker connectivities is also provided. Adapted from ref. [89] with permission of the American Chemical Society. . . . . 50

3.7 Umbrella sampling in two windows of CV = 1.45 and 1.51, showing two distinct motions of the linkers. On the left column, a translation of the linker L1 generates a chelated structure and a subsequent shift in the carboxylic oxygen connected to Zr2 (configuration 4t). On the right column, a rotation of the linker L1 and a partial decoordination of linker L2 forming a hydrogen bond with an $\mu_3$ -OH hydroxyl group is shown (configuration 4r). A proton transfer between the carboxylic oxygen O3 and the bridging $\mu_3$ -O is also observed and is an indication of the occurrence of an intrinsic dynamic acidity. Colors indicate the coordination number of zirconium atoms. Adapted from ref. [159] with permission of the Royal Society of Chemistry. . . . .	53
3.8 Schematic representation of as synthesized and upon activation MOF-808 structures . . . . .	54
3.9 Radial distribution functions (full lines) and cumulative radial distribution functions (dotted lines) obtained from the three MD simulations with zirconium coordination ranging from 8 to 6, for a: oxygen and hydrogen; b: zirconium and oxygen; c: zirconium and zirconium; d: zirconium and carbon. . . . .	55
3.10 Change of volume in time of the three investigated structures with different zirconium coordination . . . . .	56
3.11 Porosity evolution during PSE of UiO-66 Top: MeO <sup>-</sup> content in the MOF material during PSE (dashed brown) as determined by NMR and TGA. The total number of ligands per cluster is shown in dashed green. The evolution of BET areas measured for samples collected at selected instances is shown in gray. Bottom: Representation of an energy-optimized UiO-66 structure with both dangling linkers and MeO <sup>-</sup> /MeOH pairs. Adapted from ref. [89] with permission of the American Chemical Society. . . . .	57
3.12 Proposed PSE mechanism in non-defective and defective UiO-66. MeOH facilitates ligand exchange through the creation and stabilization of defects. Enthalpy differences are given in kJ/mol at 313 K (PSE temperature). Adapted from ref. [89] with permission of the American Chemical Society. . . . .	58
3.13 Network of hydrogen bonds between acid, methanol, hydroxyl group and amino groups. a) reactive complex 8, b) an additional water molecule present in solution. Key O-H and N-H distances are indicated in Å. Adapted from ref. [86] with permission of Elsevier.	60
3.14 Schematic representation of solvent being inserted in the UiO-66 unit cell. Adapted from ref. [164] with permission of Wiley. . . . .	61
3.15 Top: schematic representation of the empty pore, pore with the solvent, and confined solvent without the material. Bottom: vibrational density of states obtained from the velocity autocorrelation function power spectra of selected atoms of the simulation. Bottom left: solvated material compared to the empty material. Bottom right: water in the pores compared to bulk water. . . . .	62



3.22 Top: evolution of the collective variable $CN_W$ and free energy profile for the first MTD simulation along the CV representing the coordination between the zirconium atom Zr1, highlighted in yellow, and all water molecules (green curve). $CN_L$ between Zr1 and the neighbouring defect-bridging linker oxygen (red curve) is also monitored; bottom: snapshots on the linker decoordination triggered by overcoordination . . . . .	70
3.23 Top: free energy profile for the first MTD simulation along the CV representing the coordination between two zirconium atoms and a linker, middle: evolution of the collective variable, bottom: snapshots of the linker decoordination . . . . .	71
4.1 Different stages of the close relationship between modeling and experiments. . . . .	78

## **Part I**

**Towards a Molecular Level  
Understanding of Active Sites  
for Catalysis and the  
Interactions with Solvents in  
Zirconium Based  
Metal–Organic Frameworks  
at Operating Conditions**



# 1

## Introduction

Catalysis, from Ancient Greek *κατά* (katá = “down”) and *λύω* (lúō = “loosen”), is at the heart of almost every industrially relevant chemical process. A catalyst intervenes in the reaction, allowing chemical species to come in contact and react with a specific mechanism, without being consumed. Outstanding catalysts do not only increase the rate of a given reaction, enabling processes that would not happen spontaneously, but can even be selective towards specific end products. Catalysts can be divided in homogeneous and heterogeneous, according to the phase where they are located with respect to the reactants. Homogeneous catalysts share the same phase with the reactants, and can be for instance molecules dissolved in a solvent, such as with organometallic compounds. These type of catalysts are used in many industrial processes, but have the drawback of being difficult to separate from the products, and in many cases separation is the most costly step in the catalytic cycle. For instance, in the case of biodiesel production, the recovery and purification of the products accounts for 60-80% of the whole cost [1].

Heterogeneous catalysts, on the other hand, are located in a different phase with respect to the reactants, and for this reason they have the advantage of being easily separable from the reaction products. Especially green chemistry can widely benefit from heterogeneous catalysts, lowering the production costs and providing a viable alternative to petroleum [2]. Even if the name heterogeneous does not refer to a specific phase, industrially relevant heterogeneous catalysts are often in the solid phase. In order to exert their function, these materials must possess specific

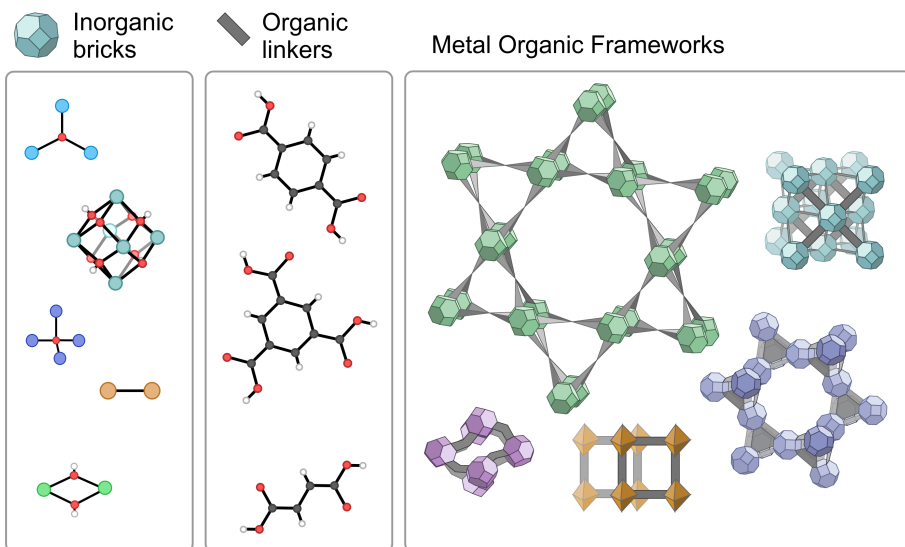
active sites that are easy to reach for the reactants, where these can adsorb, react, desorb, and ultimately diffuse back in the bulk to leave space for a new cycle. For these processes to occur, the number of active sites and the area of contact between the two phases (or surface area) must be sufficiently high, and reactants and products must be able to easily diffuse in the material.

All the above mentioned properties can be found in nanoporous materials, which possess pores with a diameter of < 100 nm, and are extensively used in the field of heterogeneous catalysis. According to the classification by the International Union of Pure and Applied Chemistry (IUPAC) [3], nanoporous materials can be differentiated on the basis of their pore size into microporous (pore size < 2 nm), mesoporous (pore size between 2 and 50 nm) and macroporous (pore size > 50 nm). Their pore structure provides them with an exceptionally high surface area, that for some materials can reach values larger than  $7000\text{ m}^2/\text{g}$  [4, 5]. This facilitates diffusion of reactants inside the material, and allows shape selectivity to give specific products. Well-known classes of nanoporous materials include zeolites and metal organic frameworks (MOFs) [6]. Zeolites were one of first heterogeneous catalysts to be industrially exploited, and are the workhorses of petrochemistry, among other applications. They are extremely robust due to their inorganic nature and can withstand harsh reaction conditions. In contrast, MOFs are novel hybrid materials that are less robust, but extremely versatile. They possess even higher porosity, diverse composition, high metal content and tunable organic functions, and for these reasons they have a high catalytic potential.

In general, the study of solid heterogeneous catalysts is not trivial, as the exact concentration and nature of the active sites is often unknown. It is not always clear, in fact, where exactly the active sites may be located in the material, and how they interact with molecules. Moreover, these materials are far from perfect, and are often the defects which are tremendously important to induce the catalytic properties. In this sense, molecular modeling offers a complementary platform, not only to understand the catalytic function, but also to determine structure–activity relationships and to design structures to target specific applications [7].

## 1.1 Metal Organic Frameworks

MOFs are one of the most intriguing class of materials of current science. These materials, first called 'porous coordination polymers' (PCPs) were discovered in the late 50's, but only at the end of the past century with the works of Robson [8, 9], Kitagawa [10, 11], Yaghi [12] and Férey [13], the scientific community started to understand their full potential. At first the main focus of MOF research was in the discovery of new structures. However, in the last few decades, the field has seen an incredible explosion in scientific and industrial interest, with new applications being continuously explored [14]. MOFs are hybrid nanoporous materials that are composed by metal or metal–oxo clusters connected by multtopic organic

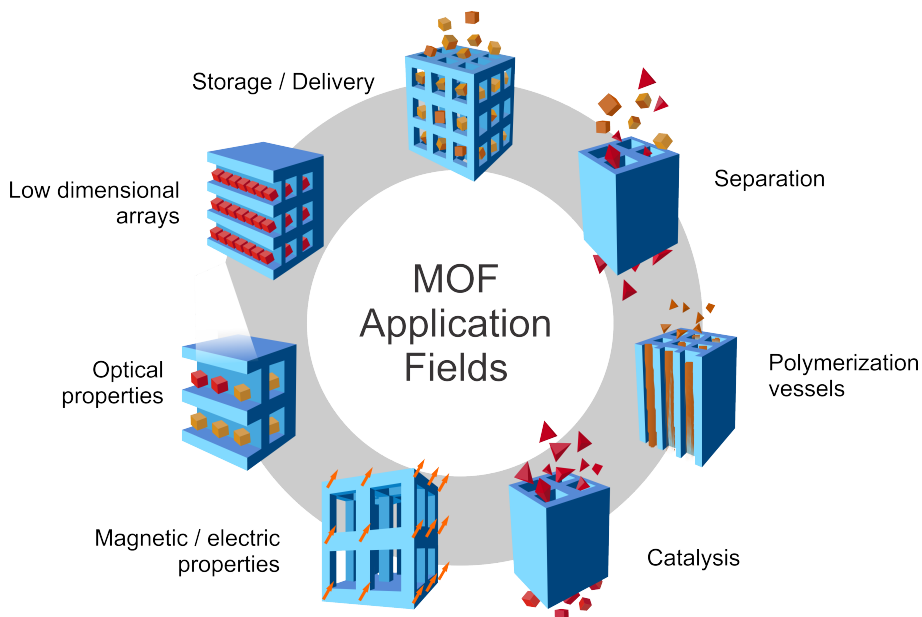


**Figure 1.1:** Schematic representation of the building block design in Metal-Organic Frameworks (MOFs). Left panel: some examples of inorganic bricks; middle panel: some examples of organic linkers; right panel: some MOFs with different topologies, pore size and shape

linkers, to form multidimensional porous structures. Compared to the already well-known zeolites, MOFs can be constructed without templating agents, with a far greater number of metals and with an exceptional structural diversity. In fact, their particular building block design (Figure 1.1), that makes use of secondary building units (SBUs), allows the creation of an almost infinite number of crystalline structures with different topology and chemical composition.

The coordination bonds which lie at the basis of MOF structures are weaker than in other heterogeneous catalyst such as zeolites. This on the one hand makes them less robust, but on the other allows facile structural modifications which are impossible to do on zeolites. In principle, the nature of the SBUs and their association can be finetuned [15], allowing control of properties such as pore shape and size, functionalization, or surface area. The response to chemical and physical stimuli can this way be easily modulated [16, 17]. One of the most intriguing concepts is the isoreticular synthesis, by which inorganic or organic SBUs can be replaced by topologically identical (or similar) building blocks. This way, starting from a given MOF precursor, whole families of MOF materials can be synthesized spanning a range of pore size and functionality. For instance, the pore size can be significantly increased up to the mesoporous range by using longer isoreticular linkers, such as in the IRMOF series, based on the MOF-5 precursor [18].

The tunability of MOF structures, along with their high crystallinity, metal content and porosity, are very appealing for application in different industrially relevant fields, such as catalysis, gas storage and separation, drug delivery or sensing, as displayed in Figure 1.2. More specific applications are being further explored, such as warfare agents decomposition, magnetic applications, or membrane separation [14]. At present moment, the main limitation for large scale application lies in the structural stability.



**Figure 1.2:** Schematic representation of some of the numerous MOF applications.

The study of MOFs has seen a continuous evolution in the past decades. Following the nomenclature proposed by Kitagawa, we can differentiate between three generations of MOFs [19]. First generation MOFs are defined as having a guest–molecules supported pore system that collapses when these are evacuated. For this reason, this first generation of MOFs found very limited use for practical applications. Those of second generation are more robust and have permanent porosity, that is retained even in absence of guest molecules. These materials show high potential for catalysis and other applications and are the main object of this dissertation. Finally, third generation MOFs are characterized by flexible pores that can reversibly change shape with the presence of guest molecules, or upon certain stimuli, such as temperature or pressure. Matsuka *et al.* [20] identified five types of response mechanisms in MOFs, denoted as shrinking, expanding, reshaping, swelling and gate opening or closing. A perspective on the types of stimuli that can induce responsive in MOFs has been reported in the work of Coudert [21].

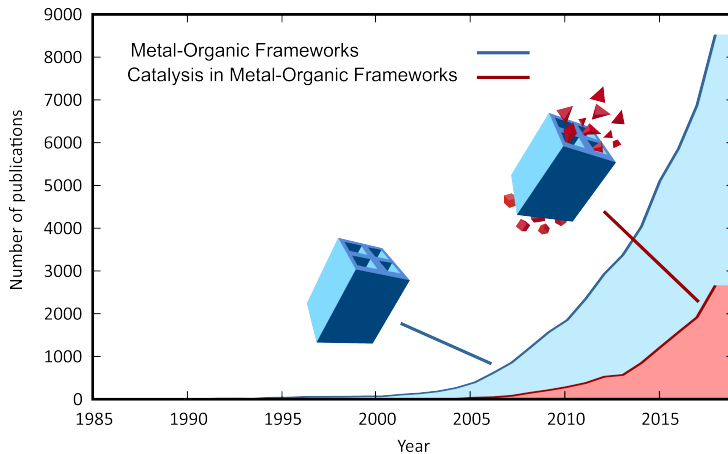
## Defects and active sites

MOFs are crystalline materials that possess structural disorder, such as vacancies. If at first this was seen as a drawback, limiting stability, it has been accepted that they can play a key role in the performance of the material. Defect-containing MOFs and defect engineering have become an active field in MOF research, representing an additional way to finetune and enhance the material properties. Following the classification proposed by Sholl *et al.* [22], defective sites in MOFs can be either point vacancies (such as missing linkers or clusters) or extended ones. Fang *et al.* [23] further divided extended defects into dislocations, planar defects, and micro- and mesoscale volume defects.

At low defect concentration, a random distribution of isolated point defects can be found, whereas at higher concentrations, clustering could occur [24] if the presence of a vacancy is influenced by other vacancies in proximity. The complexity arising from structural disorder makes the study of defects a current challenge in MOF research. In order to control their effect on certain properties, it is important to have precise information on their location, type and dispersion. Common experimental strategies for the characterization of defects in MOFs involve electron and fluorescence microscopy, Raman, infrared and X-ray spectroscopy, powder and single-crystal X-ray diffraction [23]. Complementary to experiment, molecular modeling provides an important tool to obtain atomic scale resolution on the defect sites and understand how they impact specific properties.

Particularly for catalysis and adsorption, vacancies in the material lead to two main effects: 1) an increase in porosity and mass transport, and 2) the presence of undercoordinated metal atoms, introducing highly desired Lewis acid sites. In this sense, provided the structures are stable at reaction conditions (i.e. no leaking is observed), MOFs are true single-site heterogeneous catalysts, that contain well-defined active sites which are inherent part of the framework [25]. We particularly refer to the importance of catalysis in MOF research, shown by the number of publications on the topic (Figure 1.3). According to the classification proposed by Rogge *et al.* [26], we can distinguish between three types of single-site catalysts in nanoporous materials, in which active sites for catalysis can arise from coordinatively unsaturated metals (type I), metal atoms embedded in porphyrin-based ligands (type II) or reactive functional groups (type III).

Coordinatively unsaturated metals are Lewis acid sites that can be present in the framework such as in HKUST-1 [27], or can be introduced by intentional creation of defects, such as in the stable UiO-66 MOF [28]. Another procedure that can lead to open metal sites without generating vacancies is the dehydration upon thermal treatment. To date, a plethora of MOFs have been synthesized containing open metal sites that possess different Lewis acidity. Moreover, their acidic properties can further be tuned by functionalization of linkers and bricks.



**Figure 1.3:** Number of publications on MOFs and catalysis in MOFs in years 1985–2018, showing the importance of catalysis in MOFs as indicated by Web of Science

This way, it is in principle possible to engineer a material for a target catalytic application.

## Post-synthetic modification

When it is not possible to introduce functionalities with direct synthesis, post-synthetic modification (PSM) [29, 30] has become a well established procedure that allows the preparation of MOF materials with specific chemical composition. Via this technique, it is possible to modify the crystal after the synthesis, allowing to finetune the properties of the material. Moreover, multi-functional sites can be integrated at the same time in the crystals [31]. PSM strategies include encapsulation of guest molecules or nanoparticles in the pores, modifications of the linkers without breaking the metal–ligand bond, or post synthetic exchange (PSE) of linkers and metals, where building blocks are dynamically exchanged. PSE can also involve terminal ligands, or modulators, that do not contribute in connecting different bricks. This way, building blocks can be exchanged in a dynamic way. Moreover, they can also be eliminated from the framework to create vacancies, provided the material retains its crystallinity. For this reason, PSM has been used as an efficient strategy to introduce defective sites in MOFs. As one may expect, sufficient structural stability under the PSM conditions is a necessary prerequisite in order to apply PSM techniques [32].

## Stability

In general, to function at operating conditions and to withstand modifications, materials need to retain their mechanical, thermal and chemical stability at those conditions [33]. For instance, mechanical stability is needed when compressing

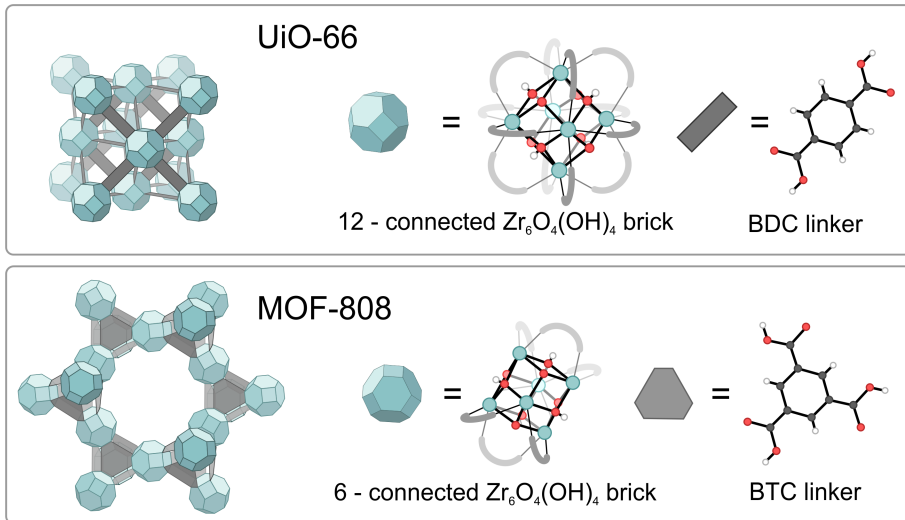
MOF in pellets or other shapes for industrial processes [34]. Catalysis often also requires thermal stability, as the materials must be able to resist harsher conditions for certain processes such as in petrochemistry. Finally, chemical stability is crucial for many applications, such as drug delivery, molecular separation, or catalysis [35].

Unfortunately, the M–L coordination bond that makes MOFs so tunable is also regarded as one of their main drawbacks [36–38], as it is responsible for the lower structural stability when compared to already established nanoporous catalysts such as zeolites. For example, the first synthesized MOFs such as  $\text{Cu}_2^+$  trimesate HKUST-1, or MOF-5, composed by  $\text{Zn}_2^+$  clusters and BDC linkers were degraded by water even at mild conditions [39–42]. Moreover, mechanical, thermal and chemical stabilities can further decrease in the presence of defects. Very few MOFs show stability towards water and at different pH conditions [43], in particular the family of Zr-based MOFs.

## Zr-based MOFs

Recently, a class of outstandingly robust MOFs have been synthesized [44]. Zr-based MOFs [45] which exploit the robustness of the Zr–O bond, show an unprecedented stability and are at present time one of the most studied classes of MOFs (Figure 1.4). Moreover, zirconium is an ubiquitous metal that is present in biological systems and has low toxicity, as well as limited cost. This makes Zr-based MOFs particularly promising for applications in catalysis, gas sorption, and drug delivery. An overview of the plethora of possible structures that can be synthesized with different inorganic SBUs can be found in a recent review by Bai *et al.* [45].

The vast majority of these materials is characterized by Zr(IV) atoms in a high coordination state (Figure 1.4), which interact strongly with the oxygens of carboxylate linkers of various topology. These MOFs are characterized by a  $\text{Zr}_6\text{O}_4(\text{OH})_4$  cluster in which each of the 6 zirconium atoms is connected to 4 oxygen atoms (two  $\mu_3\text{--OH}$  and two  $\mu_3\text{--O}$ ), each of which is in turn connected to three zirconium atoms, forming a polyhedron. Each zirconium atom can form 4 other bonds with ligands, accommodating up to 24 metal–ligand bonds per cluster. Every zirconium atom can therefore form a total of 8 coordination bonds oriented in a square–antiprismatic geometry, yielding a rich range of possible structures that can be synthesized with connectivity ranging from 12, as in UiO-66 [46], to 6 which is found in MOF-808 [44] (see Figure 1.4). The dual Lewis acid/base nature of the Zr–carboxylate bonds, along with the high metal oxidation state, gives rise to strong interactions between the SBUs, thus allowing processes such as PSM without compromising the stability of the structures. The high degree of connectivity between inorganic and organic SBUs lies at the origin of the high structural stability found in Zr-based MOFs [43, 45]. Open metal sites in these materials can be present if the brick connectivity is lower than 12. This can be an



**Figure 1.4:** Structure of **UiO-66** (top) and **MOF-808** (bottom), the two Zr-MOFs investigated in this work of thesis.

inherent property of the structure, such as in the 8-fold connected NU-1000 [47], or can be induced by introduction of structural defects. Zirconium atoms that remain undercoordinated are Lewis acid sites where reactants can adsorb and that can function as catalytic centers.

## UiO-66

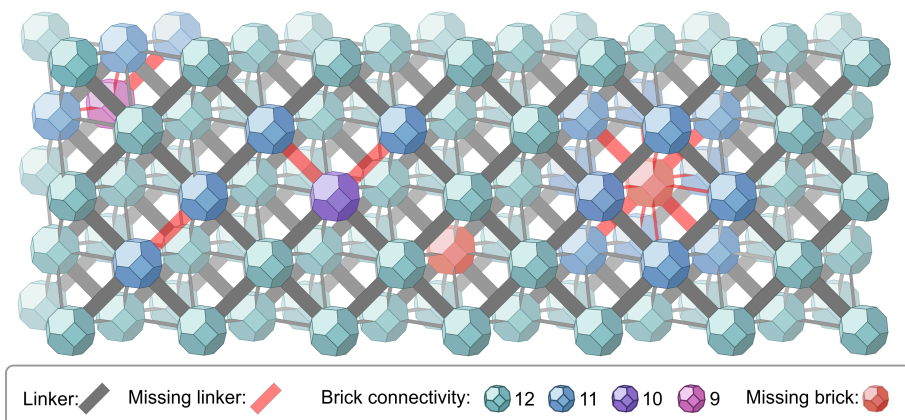
The first material belonging to this class of Zr-based MOFs is the Zr-therephthalate based **UiO-66**, and was first synthesized at the Universiteit i Oslo (UiO) by Lillerud and coworkers [46]. The **UiO-66** material, shown in Figure 1.4 (top), is one of the most studied MOFs thus far and was an inspiration of other MOFs within this family. **UiO-66** is characterized by an extremely high connectivity that gives rise to an exceptional structural stability. In this material, each  $\text{Zr}_6$  SBU is connected to 12 therephthalate (or benzenedicarboxylate (BDC)) linkers forming a cubic close packed structure with a space group  $\text{F}\bar{m}3\text{m}$ , No. 225. In this structure there are two different cavities of octahedral and tetrahedral shape, with window sizes of 10 Å and 25 Å, respectively. Each octahedral cage shares triangular windows with eight tetrahedral cages. This results in an extremely robust material which is stable up to 648 K and in a broad range of protic and aprotic solvents and pH conditions. Moreover, the  $\text{Zr}_6\text{O}_4(\text{OH})_4$  bricks can be reversibly dehydrated upon thermal treatment at temperatures between 523 and 573 K. Up to two water molecules can be formed this way, yielding a  $\text{Zr}_6\text{O}_6$  brick, where the zirconium atoms have a coordination of 7 [48]. Lowering of zirconium coordination by dehydration can be a strategy to create open metal sites, along with the creation

of defects.

A whole family of isoreticular MOFs can be derived from UiO–66 by using linkers of different size, spanning from fumaric acid [49] up to terphenyldicarboxylic acid [50], allowing to significantly tune pore size and surface area. Interpenetrated MOFs with UiO–66 topology have been also reported if longer linkers are used [51], however with a decrease in surface area. Moreover, different functional groups can be appended to the phenyl rings, such as bromo, amino, nitro, or naphthalene. Garibay and Cohen showed that UiO–66–NH<sub>2</sub> can be further modified to yield new functionalized frameworks [32]. Also the inorganic SBUs can be modified, for instance introducing titanium or hafnium [52]. Moreover, PSM can lead to creation of defects and open metal sites, as will be shown in **PAPER IV**. The exceptional thermal and chemical stability of UiO–66, along with its high connectivity, allows all these modifications of the structure, and for this reason, this material is often considered as a perfect MOF archetype, where new techniques can be tested.

### Defects on UiO-66

The high connectivity of the UiO–66 material allows the presence of structural vacancies. It has been generally accepted that the material can contain defects in the form of missing linkers or clusters (Figure 1.5). These defects naturally originate during synthesis, as shown by experimental results, such as symmetry-forbidden reflections in the PXRD pattern, metal–linker ratio obtained by thermogravimetric analysis (TGA), higher than expected surface area, appearance of O–H stretching bands in the FTIR spectrum etc. [48,53]. Moreover, it was later discovered that the number of defective sites can easily be tuned by adapting the synthesis conditions, such as temperature and type of modulator [54, 55].



**Figure 1.5:** Representation of the UiO–66 material with missing linkers and clusters displayed in red. In this dissertation, we mainly focus on missing linkers.

Defects can influence the material properties to a large extent. The beneficial role of defects in UiO–66 has been explored in many applications such as gas storage and separation [54,56], sensing [57], drug delivery [58] and catalysis [26,59]. The physical properties of defective UiO–66 differ according to the number of defects and their location, as has been extensively studied both theoretically and experimentally [24, 60–62]. A decrease in the connectivity in the structure will naturally lead to a decrease in stability of the material. However, the extremely high connectivity of UiO–66 allows the presence of both missing linkers and clusters without loss of crystallinity. In this context, Rogge *et al.* investigated the influence of all possible configurations of one to two linker vacancies on the stability of UiO–66. The equilibrium volume is not affected by such vacancies, however properties such as bulk modulus and loss-of-crystallinity pressure, which in turn influence the stability, are affected by the number and configuration of missing linkers [60]. De Vos *et al.* [61] investigated the electronic properties for all possible configuration of defective UiO–66 with up to three missing linkers, showing that some configurations are energetically more stable than others, and that the number and position of missing linkers affect the band gap of the material. From these studies performed on small unit cells, it is already clear that the number of possible defective configurations can be extremely high, and it is still unclear to what extent such point defects are disordered in the material. A regular distribution of point defects that involve missing clusters can lead to different phases in the material, from *fcu* (non-defective), to *bcu* (missing linkers with open channels), *reo* (missing clusters) to *scu* (missing linkers and missing clusters). Missing clusters could in principle increase the catalytic activity of the material more than missing linkers due to the larger pore size. Recently, Cliffe *et al.* [24] showed in a combined theoretical-experimental work that missing clusters on UiO–66(Hf) were correlated and formed nanodomains in the material, characterized by a *reo* phase. The presence of missing clusters or missing linkers can be affected by the choice of modulator [63]. These reports shed light into the complex nature of defects in nanoporous materials.

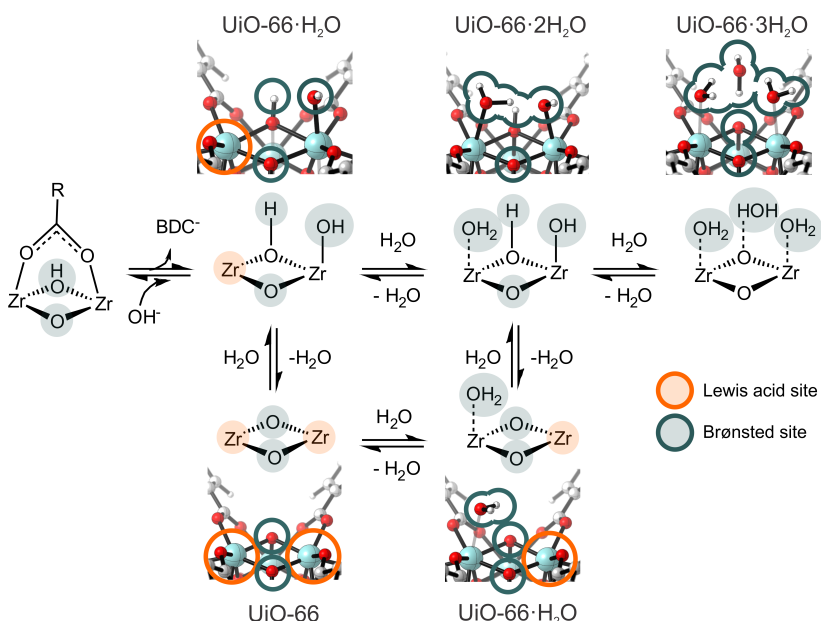
### Active sites for catalysis in UiO–66

One of the breakthroughs of MOF research was the discovery that UiO–66 could contain a high number of open metal sites. As reported earlier, active sites for catalysis in UiO–66 and other Zr–MOFs are present when the zirconium connectivity is decreased from its equilibrium value of 8.

A first way to obtain coordinatively unsaturated zirconium sites is by creation of defects, in the form of missing linkers or clusters. The inherent vacancies in UiO–66 bring unsaturated zirconium Lewis acid sites [28,53,54,59,64] and at the same time enhance the accessibility of the reactants to the active sites as the pore volume increases. The synthesis of defective UiO–66 can be tuned via modulators such as formic acid or trifluoroacetic acid (TFA), that are competing with BDC linkers in binding to the inorganic SBU. Vermoortele *et al.* first showed in a dual

computational–experimental study that the Lewis catalyzed cyclization of citronellal requires missing linkers [65]. For Meerwein reduction, another Lewis catalyzed reaction, the catalytic activity of UiO–66 could be significantly increased by making use of TFA, that introduced a large number of linker vacancies. Additionally, the non-modulated material that contained only a small number of defects showed nearly no catalytic activity [59]. Such relationship between catalytic activity and amount of defects has been reported for different Lewis catalyzed reactions giving clear evidence that the catalytic centers are located on the defective sites [59, 65].

The molecular characterization of the defective sites on UiO–66 has been an ongoing research interest in MOF literature. Particular focus has been given on the species adsorbed on the defective site and on the coordination environment of zirconium (Figure 1.6). Early experimental work by Lillerud and coworkers [66] reported that when linker vacancies were present, XRD characterization of the material showed two types of Zr–bonded oxygen atoms. The first type was BDC oxygen, and the other was associated to water species coordinated to the zirconium on the defect site. Later from SXRD measurements, the group of Yaghi [67] proposed that the two Zr–bonded oxygens belonged to physisorbed water molecules and that the charge compensating species was a hydroxyl group. However, following reports did not confirm such configuration.



**Figure 1.6:** Lewis and Brønsted sites that are created when a linker is removed from the UiO–66 zirconium brick, with different number of coordinated water molecules.

Molecular simulations were essential to shed light into the detailed molecular structure of the defective brick. Ling and Slater [68] performed MD simulations starting from the configuration proposed by Yaghi and showed a progressive stabilization towards another structure where the two adjacent zirconium atoms were coordinated to a physisorbed water molecule and a hydroxyl group, as shown in Figure 1.6. These sites have been confirmed by a comprehensive computational study of different adsorption possibilities of up to three water molecules on defective UiO–66 performed by Vandichel *et al.* [69] and by simulations performed in this thesis. Such water and hydroxy species are strongly interacting with the zirconium atoms and are sources of Brønsted sites, as indicated in Figure 1.6. It was remarkable to discover that some catalytic processes are not catalyzed by undercoordinated Lewis acid sites, but need also Brønsted sites arising from defect–coordinating species, as will be shown in **PAPER I**. Apart from the interactions of water with the active sites, they may also have a strong influence on the proton conductivity of the material. Serre and coworkers reported that a hydrogen bonded network that spans the octahedral and tetrahedral cages is responsible for the high proton conductivity showed by UiO-66 at high temperatures [62]. Kitagawa *et al.* showed the positive role of defects in proton conductivity in the UiO-66 material, as defective sites provide both larger pores and zirconium undercoordinated sites where water species are adsorbed and can function as proton donors [70]. Farha and coworkers identified three types of acidic protons in the material by means of potentiometric titration:  $\mu_3\text{--OH}$  belonging to the inorganic SBU, and two arising from subsequent deprotonation of the physisorbed water and hydroxyl group on the defective site. They made use of the acidic protons belonging to physisorbed water for a quantification of defects in the material as alternative to TGA [71]. The mechanism associated to the change in topology of the hydroxyl groups on the inorganic SBU has been investigated by Yang *et al.* [72]. The interaction between defect–coordinating water molecules and zirconium atoms is strong, and UiO–66 can be partially hydrolized [73] while retaining its stability, as will be further discussed in this dissertation.

The defect–coordinating species can be removed by thermal activation at  $T > 423\text{ K}$  (more information on this process is given in **PAPER I**). The more loosely bonded physisorbed water is the first to leave the defective site, followed by the chemisorbed water. The dehydrated active site obtained this way is missing a  $\mu_3\text{--OH}$  proton and has two 7-fold coordinated zirconium open metal sites as shown in Figure 1.6 (bottom left).

The second activation process by which open metal sites can be created on UiO–66 is the reversible dehydration of the  $\text{Zr}_6\text{O}_4(\text{OH})_4$  cornerstone to obtain  $\text{Zr}_6\text{O}_6$  by removal of up to two water molecules performed at a temperature range between 523 and 573 K [48]. In this case also 7-fold coordinated zirconium atoms are created and may take the role as Lewis active sites, however the increase in pore size due to linker vacancies does not occur, and the active sites are less accessible

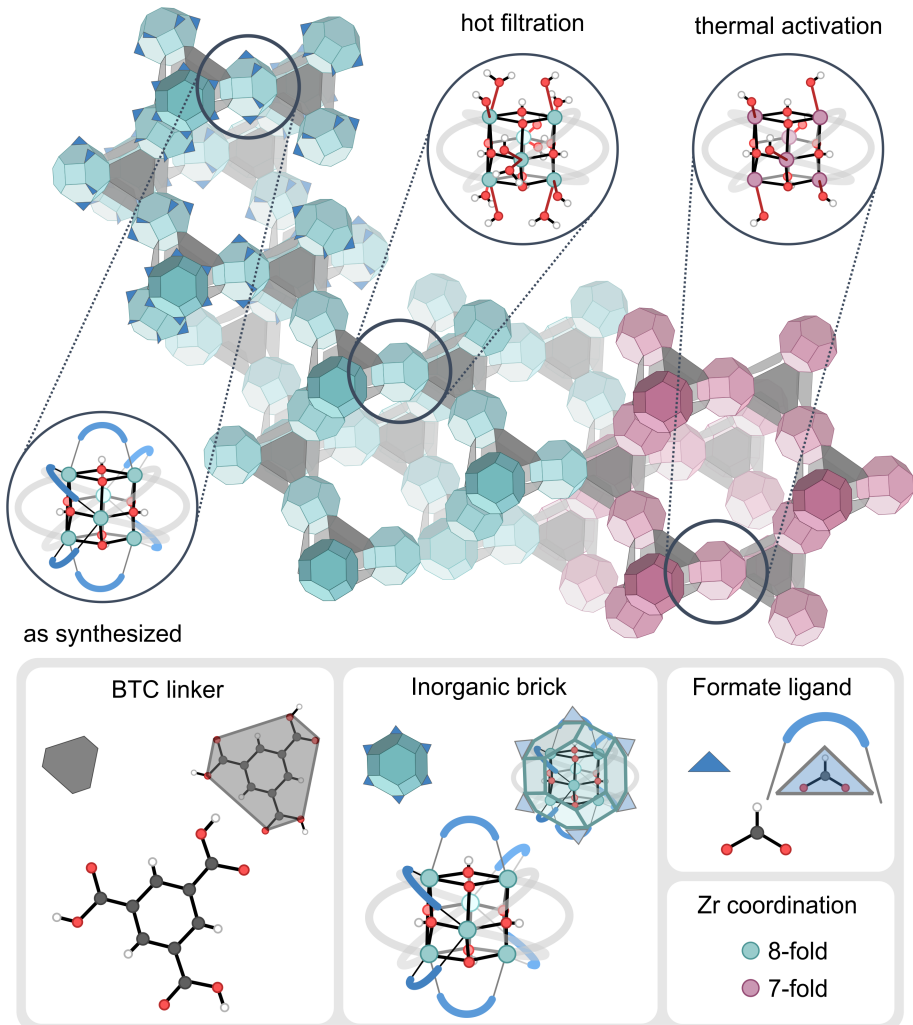
than in the defective material. For instance for the citronellal cyclization [65], in absence of defects, linkers should still be partially decoordinated to make space for the reactants to adsorb on the zirconium atoms, therefore the process is less likely to occur.

### Functionalization of UiO–66

Reactions on UiO–66 can proceed exploiting purely the Lewis acidity of under-coordinated zirconium atoms, or can also make use of Brønsted sites located on the defect sites. The acidic and basic properties of such groups can be further influenced by linker functionalization [74–76]. Functionalization, which can be done via PSM, represents a strategy to further finetune the properties of the material. For instance, the presence of electron–donating substituents showed an increase in catalytic activity for jasminaldehyde condensation [77]. A positive effect of electron–withdrawing groups was found by the same authors for Lewis catalyzed citronellal cyclization [65]. The beneficial role of amino groups was reported as well by Timofeeva *et al.* [78] for acetylation of benzaldehyde, as well as by Cirujano *et al.* [79, 80] for esterification. The electron donating effect of amino groups would in principle lead to a decrease in the Lewis acidity of the defective zirconium atoms, lowering the reaction rate. Therefore, a change in mechanism in the presence of BDC–NH<sub>2</sub> was hypothesized. However, Hajek *et al.* further studied aldol condensation in a computational work [81], and reported a beneficial, but passive role of amino groups, which is further confirmed in **PAPER I** for Fischer esterification.

### Active sites on MOF–808

So far it was shown how active sites can be introduced on UiO–66 by linker or brick removal and dehydration. In the Zr–based MOF family, other less connected materials such as NU–1000 and MOF–808 contain inherent vacancies due to their topology. Although less robust than UiO–66, they possess a higher number of active sites and larger pores and for this reason they are regarded as promising heterogeneous catalysts. Moreover, their large pore size allows for interesting modifications such as atomic layer deposition in MOFs (AIM) [47]. MOF–808, formed by the inorganic Zr<sub>6</sub>O<sub>4</sub>(OH)<sub>4</sub> cornerstone and trimesate (BTC) linkers, represent the least connected MOF in the Zr–MOF family [44], and its brick can be regarded as an extreme case of the defective UiO–66 (Figure 1.7). MOF–808 is a promising catalyst that is still less studied than UiO–66, but has a lot of potential for possible applications. For instance, it shows a higher catalytic activity for certain Lewis catalyzed reactions, such as Meerwein–Ponndorf–Verley (MPV) reduction [82, 83]. Moreover, MOF–808 represents the first evidence of a superacid in MOFs, showing superacidity after post–synthetic treatment with sulfuric acid [84].



**Figure 1.7:** Schematic representation of as synthesized and upon activation MOF-808 structures

The rigid BTC tritopic linkers stabilize the structure and yield exceptionally wide channels which are required for the diffusion of substrates. The octahedral crystals contain 6 BTC linkers per inorganic node and are characterized by a *spn* topology. In the material, each zirconium atom is bonded to four oxygens from the inorganic brick and two oxygens from the BTC linkers. The other two bonds that are needed to reach the total coordination of 8 are provided by species present in solution that do not contribute to the framework connectivity.

In the as-synthesized material (Figure 1.7), the zirconium atoms are capped with the relative mobile formate modulator. The material at this stage does not contain catalytically active sites and must be activated by post-synthetic treatment. By hot filtration, the formate groups can be eliminated and replaced by solvent water and hydroxyl groups [82, 83]. In the catalytically active material, each brick is connected to six BTC linkers, six water molecules and six hydroxyl groups, and possesses a high number of potential Brønsted sites. Klet *et al.* reported the presence of four different types of protons in the material [71], each yielding a different acidity. The acidity of these protons can influence reactions, and its characterization represent a current challenge. From this structure, Lewis acid sites can be created by thermal activation, similarly as in UiO-66. In this case, hydroxyl groups remain connected to the zirconium atoms and the material possesses both Lewis and Brønsted sites that can be used for reactions. Moreover, the hydroxyl groups could further be used as anchors to incorporate new features in the material.

## 1.2 Outline and goal of the thesis

In this PhD dissertation, state of the art molecular modeling techniques were used to unravel at the nanoscale the molecular nature of defects and active sites in two zirconium MOFs: UiO-66 and MOF-808. From a purely experimental basis it is very hard to follow processes such as activation, reactions or formation of defects at the molecular level. The comprehensive insight obtained from molecular modeling can offer precious understanding in these processes at the nanoscale level. Furthermore it is the ambition to model the described processes at operating conditions, thus at realistic conditions of temperature, pressure and guest loadings in the pores of the material. This can ultimately allow to fine-tune the active sites to target specific applications. Processes taking place in MOFs usually occur at mild conditions in the presence of solvent confined in the pores therefore, multilevel modeling techniques are required to accurately describe both, the material and reaction environment. Moreover, the processes happening at the molecular level are very dynamic and can involve rare molecular events. All these complex dynamics need to be mapped appropriately. It is shown that enhanced sampling methods used in this thesis are crucial to reveal the strong interactions of protic solvent with the active sites modulating their nature and actively participating in chemical

transformations. The insight obtained in this PhD into the solvent assisted ligand exchange mechanism shed light on the role of solvent in modulating the properties of the active sites at operating conditions, which influence structural stability and create active sites for catalysis. The research was performed in close collaboration with experimental and theoretical partners. The results obtained in this thesis rationalize the experimental findings and shed light on the molecular processes that occur around the active site, which are crucial to engineer MOFs for future applications. This PhD thesis is organized as follows:

- In Chapter 2, a condensed theoretical overview of current molecular modeling techniques within MOF research is given. Particular attention is drawn on how these techniques can be applied to obtain insight into structural and catalytic properties at operating conditions.
- In Chapter 3, the main results of this PhD thesis are summarized. The links between theory and experiment are highlighted throughout the chapter. All results are the result of fruitful experimental and theoretical collaborations and have been published in international peer-reviewed journals.
- In Chapter 4, the main conclusions of this thesis work, as well as perspectives on future research are given.

# 2

## Modeling metal organic frameworks

The understanding of catalytic processes in MOFs is a very challenging task. MOFs are materials of complex nature, and reactive processes in these materials are elusive and difficult to track on a purely experimental basis. Molecular simulations offer an alternative approach that starts from the construction of models that can explain, complement, and predict experiments. With growing computational power, computational models can aim at giving a more and more accurate description of materials at operating conditions, narrowing the gap between theory and experiment. Often, the structural properties and chemical transformations that take place on the active sites need to be investigated using a combination of multiple computational techniques, and the problems need to be tackled from different angles. In this chapter, an overview of the different computational methods that can be used to study reactive processes in MOFs will be given.

### 2.1 Framework topology

A crucial decision when performing simulations lies in the choice of the model system, and what should be included in it. When choosing a model to represent the system under study, there is always a fine balance between accuracy and computational cost. On the one hand, it is crucial to use a computational model that captures all the relevant properties of the material and mimics the experimental structure as closely as possible. On the other hand, it is often convenient to use

approximations in order to obtain a description of the processes at a larger scale. The focus in this work are the active sites that can be used for catalysis, therefore an accurate electronic description of this region of the material is imperative. Nevertheless, the activity of these sites for chemical reactions can also be influenced by other factors, such as the pore size or functionalization. Therefore, to describe active sites in MOFs and other nanoporous materials, which can have rather large unit cells and non-periodic structural defects, the first question that needs to be asked is how to account for periodicity or molecular environment. Two conceptually different approaches can be used as shown below.

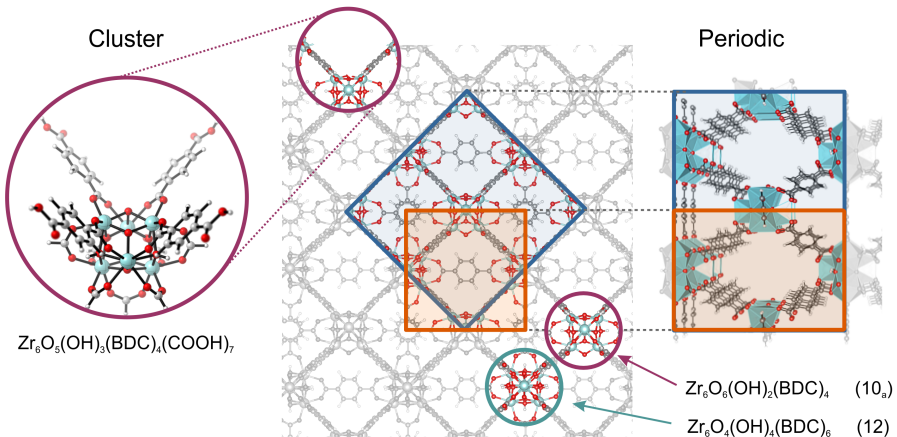
### Extended cluster model

A very computationally efficient approach consists in neglecting periodicity and extracting a finite cluster of atoms from the periodic structure. This cluster model, displayed in Figure 2.1, contains the active sites and their surroundings but consists in a limited number of atoms, allowing to substantially decrease the computational cost. This allows both a more accurate treatment of the electronic structure, and a screening of different possible geometrical configurations of adsorbates, which is useful in the search for transition states (TS). Moreover, very efficient TS searching algorithms have been developed for such systems in Gaussian [85], the most widely used code for cluster calculations and that we used in the framework of this thesis. When extracting a cluster, particular attention has to be drawn to the termination of bonds and the charge compensation, that have to be done in the most realistic way. The rest of the crystal structure does not surround the external cluster atoms. Some of these atoms need to be fixed in order to mimic the periodic environment and prevent nonphysical deformations that would affect an estimation of the entropy [87].

Cluster calculations are an excellent way to benchmark and perform a first qualitative screening of reactions and possible configurations and have been for long the standard computational tool when studying reaction in nanoporous materials. However, confinement effects and possible structural rearrangements are neglected in this model, and for certain reactive processes they could play an important role. The influence of solvent in the pores can also be crucial for the outcome of a reaction and cannot be explicitly studied by cluster models. Periodic calculations resolve this shortcoming, and as computational power grows, the heterogeneous catalysis community is shifting towards these more expensive, however more accurate models.

### Periodic model

Periodic models, that fully take into account the periodicity of the crystal, enable to describe the whole topology of the framework. These calculations make use of periodic boundary conditions (PBC), which allow to simulate bulk phases with a

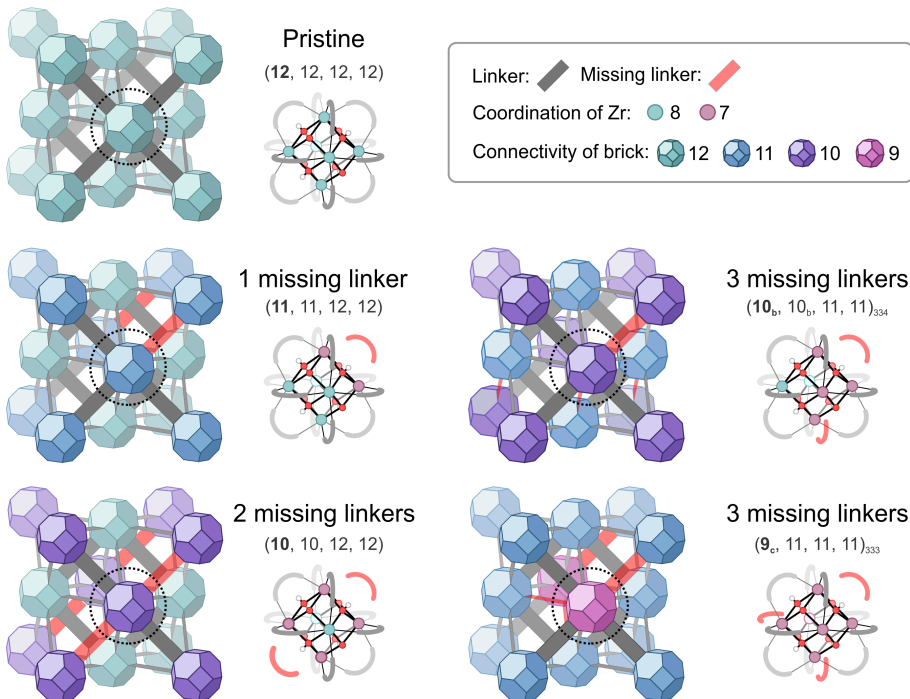


**Figure 2.1:** Left: extended cluster model cut from the periodic structure of UiO-66. The cluster contains the active site, the brick and the linkers in the closest proximity to the active site. Right: representation of the unit cells containing the defect. In blue, the conventional 4-brick unit cell, in orange, the 2-brick unit cell used for the calculations. The two different bricks are highlighted in orange. The 10-fold coordinated brick has two terephthalate linkers missing. Adapted from ref. [86] with permission of the American Chemical Society.

limited number of atoms. In this model, the unit cell is replicated infinite times in each direction. When one atom disappears from one side of the unit cell it will reappear on the opposite side and each atom interacts with its neighbors in the same unit cell but also in the adjacent ones. Spurious interactions between the atoms can be avoided by applying a *minimum image convention*, for which each atom interacts with its nearest neighbor or periodic image. In the case of long range interactions, such as the electrostatic ones, other techniques need to be used, such as Ewald summation [88], where the potential is divided into a short range contribution, calculated in real space, and a long range contribution, calculated in reciprocal space using a Fourier transform.

In the case of UiO-66, the conventional unit cell [46] contains 4 zirconium bricks (Figure 2.2, blue). In the calculations of this thesis, BDC linkers have been removed from the unit cell to introduce defects which are active sites in catalysis. Different amounts of missing linkers with different topologies have been considered 2.2. An interesting topology is the one denoted as type 6 in the work of Rogge et al. [26] that is characterized by a channel which offers good perspectives for the diffusion of guest molecules. This unit cell (displayed in blue in Figure 2.2) can be reduced by symmetry to a 2-brick unit cell (in orange, Figure 2.1) which offers the best compromise between accuracy and computational cost. This reduced unit cell is used in most of the calculations performed in this thesis. In **PAPER I** we

show that for catalytic purposes, the free energy differences calculated for the same chemical processes on the two unit cells is negligible, therefore the 2–brick unit cell represents a good model system. When modeling disorder, however, periodicity decreases and bigger unit cells have to be taken into account. For this reason, in **PAPER IV**, we studied defective 4–bricks unit cell with missing linkers ranging from zero to three. Moreover, in some cases it may be necessary to use supercells to avoid spurious interactions between adjacent cells.



**Figure 2.2:** Representation of the different ways to remove up to three linkers from a 4–brick UiO-66 unit cell. Adapted from Ref. [89] with permission of the American Chemical Society.

## 2.2 Theoretical methods

### Electronic energy methods

A key concept involved in the study of any chemical or physical transformation is the knowledge of the potential energy surface (PES), which is a function of the coordinates of all the atoms of the system. The PES is always the reference quantity in our simulations and every atomic configuration can be represented as a point in this hypersurface, with a given value of potential energy (Figure 2.3).

Ideally, by calculating the value of the PES for each atomic configuration we can obtain all information on the system and on the transformations that can occur. However, the complexity of this surface escalates quickly with the number of atoms, and the sampling of its relevant regions represents the main challenge of molecular simulations. The information gained by exploring the PES is tightly connected to the experimental observables. Statistical physics acts like a bridge between the microscopic insight that is gained through molecular simulations and the macroscopic properties which are measured experimentally. In principle, all macroscopic properties of a system can be derived from its wavefunction. To calculate it, the stationary Schrödinger equation is solved:

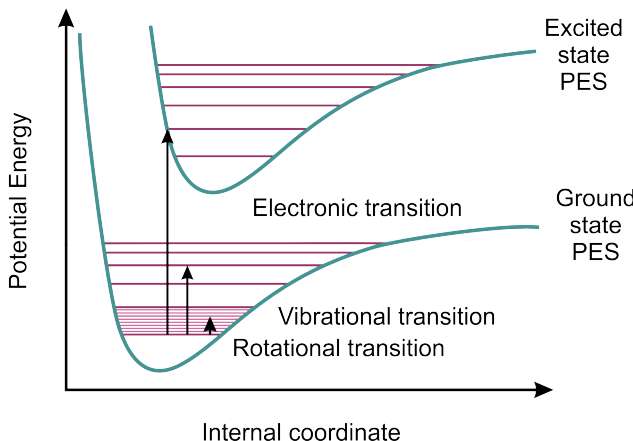
$$\hat{H} |\psi\rangle = E |\psi\rangle$$

where  $\psi$  is the wavefunction,  $\hat{H}$  is the Hamiltonian of the system, and  $E$  is the total energy. The resolution of this equation is at the heart of computational chemistry and will in principle provide the exact description of matter, but it is nevertheless extremely difficult to solve for most of the electron systems. The presence of electron–electron interactions makes it a many-body problem which is very hard to solve. Therefore, a series of approximations need to be made to solve this problem for systems with a high degree of complexity.

## Born–Oppenheimer approximation

For all calculations performed in this work, we rely on the so-called Born–Oppenheimer (BO) approximation [90]. In this treatment, nuclei are considered as classical points which move in the potential energy surface generated by the electrons (Figure 2.3). This way, to each nuclear configuration a corresponding electronic energy can be assigned, and nuclear coordinates enter in the Schrödinger equation only as parameters, allowing to construct a BO surface, or PES. This approximation holds since nuclei are much slower than electrons, therefore the motion of electrons is instantaneous from the nuclei point of view.

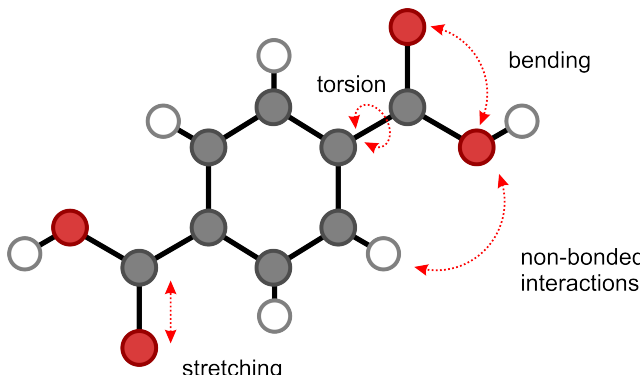
This approximation does not always hold, especially when dealing with light nuclei such as hydrogen. In these cases, nuclear quantum effects can have an impact on the measured properties [91]. In most cases, the electronic ground state is also not interacting with the higher electronic states because of the high energy difference. In the BO approximation, the electronic energy levels are also considered fully separated and do not interact with each other. For this reason, the approximation is also called adiabatic approximation. Additional interactions have to be considered when two surfaces lie close to each other, for instance in the neighborhood of conical intersections.



**Figure 2.3:** The two lowest PES in the BO approximation for a diatomic molecule. In blue, the electronic PES for the ground state and first electronic excited state (UV–Vis transitions). In orange, the vibrational energy levels (IR transitions), in grey the rotational levels (microwave transitions).

## Force Fields

The simplest way to describe interactions between atoms which determine the PES is the so-called “balls and springs” model. In this treatment, all interactions are represented by interatomic classical potentials which are parametrized to reproduce the results of more accurate quantum mechanical calculations (Figure 2.4). In this work, generic force field calculations have been used in some cases to give preliminary input structures for more costly *ab initio* calculations, through which the description of chemical transformations is possible.



**Figure 2.4:** Representation of some of the molecular modes taken into account in a generic force field model.

Force fields are often constituted by harmonic potentials, and the relative parameters are generated from reference experimental or *ab initio* data, with packages such as QuickFF [92]. Force fields can be successfully applied to describe physical transformations but cannot be employed in case of chemical reactions where bonds may be formed and broken. Reactive force fields, such as ReaxFF [93] are currently being developed, but their application in complex heterogeneous reactions is still an ongoing chemical challenge and is out of the scope of this work. For this reason, the description of reactive processes needs a more advanced treatment, where electronic distributions are explicitly taken into account.

## Density Functional Theory

Density functional theory (DFT) has become the method of choice for the study of chemical systems, due to its good trade-off between computational cost and accuracy of the obtained results. DFT began in the 1920's with the work of Thomas and Fermi [94, 95], but it was only in the '60s that it became a complete and accurate theory, shown in the work of Kohn, Hohenberg and Sham [96]. The fundamental property that DFT describes is electron density as opposed to many body electron wavefunctions, which allows to reduce enormously the number of variables in the case of complex systems. Two fundamental theorems by Hohenberg and Kohn state that there is a unique relation between electronic density and total wavefunction, therefore the ground state density allows us to determine all properties of the system. Moreover, the ground state density can be obtained from a minimization of the total energy functional with a variational method by solving the so-called Kohn-Sham equations. The global minimum value of the functional determines the exact ground state of the system. This way it is possible to obtain the total energy of the system and the forces which act on the atoms, two quantities which are needed in all the simulations performed in this work.

To minimize the energy, Kohn and Sham [97] introduced a method which replaces the many-body problem with an auxiliary system of non-interacting particles, allowing a fast solution of the eigenvalue problem. What needs to be added in this treatment is an additional functional which describes exchange and correlation. Nowadays one of the greatest challenges in DFT consists in the search for an accurate expression for the exchange-correlation functional. The simplest method is known as Local Density Approximation (LDA) initially proposed by Kohn and Sham [97] and can also be adapted to include spin in the Local Spin Density Approximation (LSDA) [98]. A more refined method is the Generalized Gradient Approximation (GGA) which involves the calculation of the gradient of electron density and includes functionals such as B88 [99], LYP [100] and PBE [101, 102], used in this thesis. More recent functionals are the so-called hybrid functionals, which include the Hartree-Fock (HF) exchange, such as B3LYP [99, 100, 103], which is a combination of B88, LYP and LDA with HF, and PBE0 [104], which mixes PBE with HF. These functionals can give a more accurate electronic descrip-

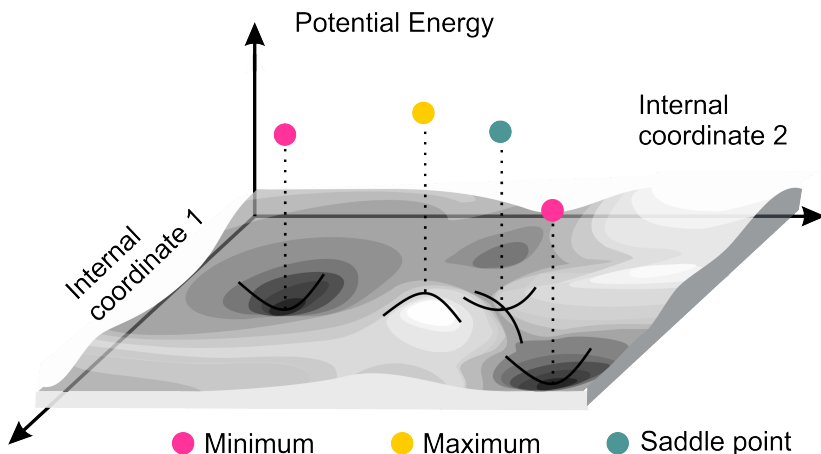
tion of the system but are computationally very expensive. As compromise between accuracy and computational cost is a geometry optimization with PBE, and a single point calculation to refine the energies with B3LYP, as performed in **PAPER I**. This approach, denoted as B3LYP//PBE, allows to avoid the high computational cost associated to B3LYP geometry optimizations, especially in periodic calculations. A comparison of different combinations of functionals has been reported by Hajek *et al.* [81] for aldol condensation in cluster models. This work shows that PBE geometry optimizations are sufficiently accurate, and provide energy barriers that are comparable to B3LYP for this kind of systems.

### Dispersion interactions

In this thesis we often encounter noncovalent interactions which need to be treated with high accuracy, such as the adsorption of guest molecules on the zirconium Lewis acid sites or interaction between solvent molecules. One of the challenges of DFT methods is the description of long range dispersive interactions such as London forces, which are commonly referred to as van der Waals interactions. These interactions are due to many particle electron correlation effects which are present also in absence of charges and can have a significant impact on the noncovalent interaction energy. To tackle this problem, various dispersion schemes have been proposed. One of the most used is currently the Grimme–D3 method [105], where a damped  $-C_6R^{-6}$  function is added to the DFT functional. Recently, more advanced dispersion schemes have been developed, such as the many body dispersion scheme [106], or the one of Tkatchenko and collaborators [107], although for the systems we are studying not many benchmarks of these new methods have been performed so far. Wieme *et al.* [108] recently compared different dispersion methods with respect to RPA + SE (random phase approximation with single-excitation effects calculations) in reproducing the breathing behavior of the flexible MIL–53(Al) MOF. The influence of difference functionals and dispersion schemes was also tested by Hajek *et al.* for the adsorption of pentene on the H–ZSM–5 zeolite [109].

### Geometry optimization

In order to obtain molecular structures that have physical significance and their relative energies, the arrangement of the atoms needs to be optimized. There are generally two types of molecular structures that we need to find in our simulations, the equilibrium geometries, which correspond to *minima* of the PES, and the transition state geometries, which correspond to first order saddle points, as displayed in Figure 2.5. These points are characterized by null first derivatives of the energy (the total forces acting on each atom are sufficiently close to zero), all positive second derivatives for local *minima* and one negative second derivative for first order saddle points, which correspond to transition states.



**Figure 2.5:** Schematic representation of the potential energy surface and the stationary points.

The geometrical optimization of reactants and products consists in a minimization of the energy along the nuclear coordinates. Often the starting point is the experimental structure which can be obtained from diffraction data. In the most used codes several minimization methods are implemented, each characterized by a different computational cost and robustness, such as steepest descent, conjugated gradient or simulated annealing. The algorithms will find local *minima*, and do not guarantee that the system will be in a global *minimum*, therefore the minimizations must start from a sufficiently good guess.

The search for transition states is far from trivial and often requires an iterative procedure involving different methods and requiring a good knowledge about the system and chemical process under study. In the calculations performed in this thesis, we often start from an equilibrium structure and as a first guess, we adapt the bond lengths and angles to be close to the transition state with a molecular editor such as Zeobuilder [110]. These bond lengths are then fixed, and the rest of the structure is reoptimized. The Hessian of this partly optimized structure needs to be then computed, and the vibrational modes analyzed, to check which (if any) negative frequency corresponds to the transition state. The system can be optimized again without the constraint using an improved dimer method along a selected eigenvector [111] which is followed by the optimization with a quasi-Newton method [112]. In some difficult cases, the TS search can be initiated on simpler cluster models and optimized in a code in which methods are usually implemented to directly find the TS structure. This way, a first guess of the TS geometry might be obtained and further transferred to the periodic model. In both transition states and *minima*, if there are superfluous negative frequencies, these need to be removed. Often, it is sufficient to minimize the energy along that vibrational mode. Single point energy calculations can be performed for different

values of the displacement along that mode, and the lowest point in energy can be used as starting point for a subsequent minimization of all the coordinates.

### Cell optimization

In the case of periodic systems, not only the structure, but also the unit cell needs to be optimized. This is not trivial, as when using a finite plane wave basis set the number of plane waves depends on the volume of the unit cell. If the volume changes during the optimization, artificial forces which go under the name of Pulay stress can arise. This would require many iterations to optimize the volume. In this thesis, another approach was used [113] which relies on an equation of state fit. For a given volume, for instance taken from experimental data, the unit cell is optimized. Then a set of equally spaced different volumes is defined and for each of these points the geometry and unit cell parameters are optimized. This way it is possible to construct an energy–volume curve, which for a rigid system can be fitted with a Birch–Murnaghan equation of state [114, 115], allowing to extract the volume  $V_0$  which corresponds to the *minimum* electronic energy  $E_0$ .

$$E(V) = E_0 + \frac{9V_0B_0}{16} \left\{ \left[ \left( \frac{V_0}{V} \right)^{\frac{2}{3}} - 1 \right]^3 B'_0 + \left[ \left( \frac{V_0}{V} \right)^{\frac{2}{3}} - 1 \right]^2 \left[ 6 - 4 \left( \frac{V_0}{V} \right)^{\frac{2}{3}} \right] \right\}$$

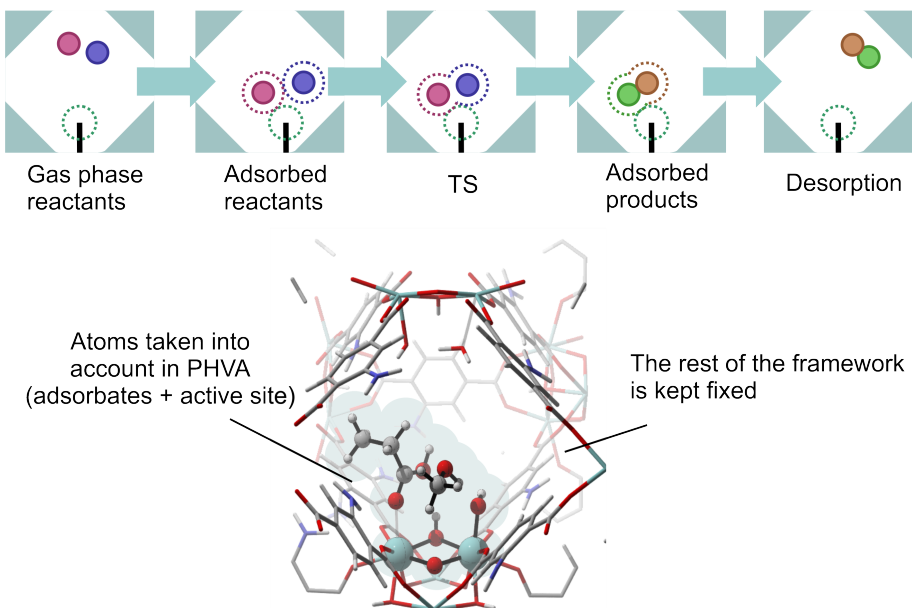
Where  $B_0$  and  $B'_0$  are the bulk modulus and its derivative. A new structure is then generated at this given volume and coordinates and unit cell parameters are optimized again.

### Molecular vibrations

As seen in the previous paragraph, for many purposes in this thesis we need to calculate the second order derivatives (Hessian matrix) of the PES, which are associated to molecular vibrations. First of all, the Hessian gives us information about the curvature of the surface and the nature of the stationary points encountered during the minimization. The second order derivatives are obtained by displacing the atoms in the three directions and calculating the energies, then the Hessian is diagonalized to determine the eigenvectors that correspond to the vibrational motions. From the Hessian we can calculate the vibrational frequencies, which open the door to a lot more information on the system than a single point calculation. As a matter of fact, single point calculations are performed at 0 K, but even at this temperature nuclei vibrate around their equilibrium positions, and this movements are responsible for vibrational entropy. We can approximate these motions with those of harmonic oscillators, by using the vibrational frequencies constructed from the Hessian.

These frequencies can then be used to estimate the value of the vibrational entropy at finite temperatures, as will be explained later. In the calculations

performed in this thesis, due to computational limits, a partial Hessian approach (PHVA) was used when dealing with reactions, as implemented in the TAMkin toolkit [116]. The quantity that needs to be derived from these calculations is the change in free energy, which mainly depends on the parts of the system that change during the reaction, in the case of a heterogeneous catalyst the active site and the adsorbed reactants. Therefore, restricting the entropy calculations only to this part of the system is a good approximation that allows to decrease enormously the computational cost [117]. This approach has been used in the calculation of the free energy barriers for the Fischer esterification on UiO-66 (**PAPER I**), where the atoms taken into account were the adsorbed reactants and four atoms of the active sites in their immediate proximity, as displayed in Figure 2.6.



**Figure 2.6:** Representation of the atoms taken into account in the Partial Hessian Vibrational Analysis (PHVA) approach. Top: a schematic representation of a reactive process in nanoporous material, bottom: a snapshot from the static calculations where the atoms of the active site and the adsorbates are highlighted

In many cases, negative or low frequencies can be present, especially when involving large systems such as species adsorbed in MOFs [87]. Negative frequencies with large absolute value ( $\nu < -50 \text{ cm}^{-1}$ ) can arise if the system is not fully optimized, meaning that the energy can be further minimized along this coordinate. In this case, a series of geometries can be extracted along the coordinate corresponding to the negative eigenvalue. For each of these structures, the electronic energy can be obtained with a single point calculation. The geometry corresponding

to the lowest energy along the vibrational mode can be then further optimized to find a lower energy minimum. This procedure can be iteratively performed for each of the negative frequencies. In case of frequencies approaching zero, the harmonic oscillator model would break down. Therefore, low frequency modes, or so-called soft modes ( $|\nu| < 50 \text{ cm}^{-1}$ ) are artificially replaced by a frequency of  $50 \text{ cm}^{-1}$  [87]. In this sense, PHVA approach allows to avoid considering all spurious low-frequency modes arising from lattice vibrations of the framework and only limit to those arising from the reactants.

## 2.3 Free energy

The central thermodynamic quantity that determines the outcome of a reaction is the free energy change associated to the process. In general, a chemical system will undergo changes in a direction that minimizes its free energy, until an equilibrium is reached. Knowing the difference in free energy between reactants and products allows us to know the equilibrium constant for a given reaction. The Gibbs Free energy can be decomposed in an enthalpic and an entropic contribution, that can be evaluated from the simulations knowing the molecular partition functions. Initially, the total internal energy  $U$  has to be obtained from the electronic energy  $\varepsilon_0$ , the zero-point vibrational energy  $E_{ZPE}$  and the molecular partition function  $Q$  at constant number of particles  $n$  and volume  $V$ :

$$U = U_0 + RT^2 \left( \frac{\partial \ln Q}{\partial T} \right)_{n,V}$$

$$U_0 = \varepsilon_0 + E_{ZPE}$$

Where  $R$  is the gas constant, equal to the product  $N_A \cdot k_B$  between Avogadro's number and Boltzmann constant. The molecular partition function  $Q$  can be split in its translational, rotational, and vibrational components:

$$Q = Q_{trans} Q_{rot,ext} Q_{vib}$$

The enthalpy  $H$  corresponds to the total energy plus the work associated to the change in volume.

$$H = U + p_0 V$$

The entropy  $S$  can be directly obtained from the partition function:

$$S = R \ln Q + RT \left( \frac{\partial \ln Q}{\partial T} \right)_{n,V}$$

Finally, the Gibbs free energy  $G$  will be:

$$G = H - TS = U_0 + p_0 V - RT \ln Q$$

Where in the case of non-interacting particles  $p_0 V = RT$  following the ideal gas law. We can therefore define a free energy surface (FES) that is function of coordinates of the system, and can be derived from the PES.

## Equilibrium

As explained above, there is a tight connection between free energy and equilibrium concentrations in chemical reactions. As an example, an equilibrium which is of utmost importance in chemistry is the acidic dissociation of species in aqueous solution:



The acidic dissociation constant ( $K_a$ ) is an important equilibrium constant in chemistry and is equal to the ratio between the concentration of products and reactants when the reaction reaches the equilibrium. It is often reported with its negative decimal logarithm as  $pK_a$ .

$$K_a = \frac{[\text{A}^-][\text{H}^+]}{[\text{HA}]}$$

The equilibrium constant is equal to the Gibbs free energy change from reactants to products.

$$\Delta G = RT \ln K_a$$

$$pK_a = \frac{\ln 10}{RT} \Delta G$$

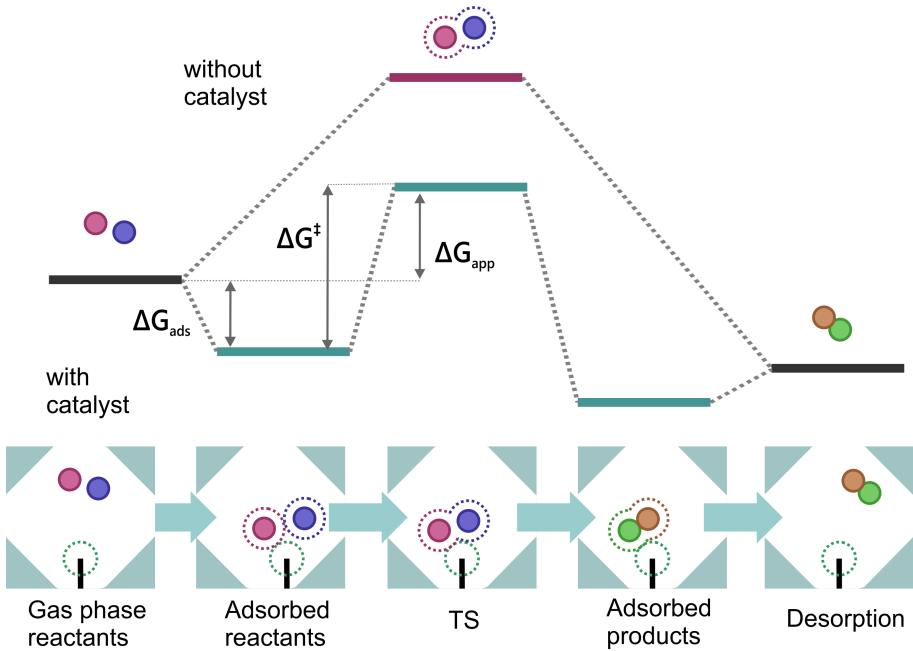
Therefore, knowing the Gibbs free energy difference between reactants and products, we can have important information about the equilibrium composition of a chemical system. However, kinetic factors can sometimes play a major role, and equilibrium cannot always be easily reached.

## Transition state theory

A chemical reaction is a process that through rearrangement of the atoms transforms one stable state into another. Every elementary reaction can be represented as a minimum energy path connecting two *minima* along the FES. Furthermore, along this reaction path the existence of a saddle can be postulated, which is the highest point in energy that needs to be crossed to go to the product state. The states are schematically indicated in Figure 2.7.

The saddle point is typically called transition state or activated complex and it is the basis for the transition state theory (TST) developed by Eyring in the 1930's, one of the most successful chemical theories which allows to explain reaction rates of elementary chemical reactions. The assumption of the theory is that there is a *quasi-equilibrium* between reactants and activated complex, and the rate constant can be obtained by the size of the energy barrier and by the frequency at which the system can cross the barrier. This is possible because the barrier acts as a bottleneck in the reaction, its crossing is a rare event and all the kinetics depends only on it. For a unimolecular reaction, the rate constant can be derived from the partition functions of reactants, TS and their energy difference:

$$k(T) = \frac{k_B T}{h} \frac{q_{TS,\ddagger}}{q_R} e^{-\frac{\Delta E^\ddagger}{k_B T}}$$



**Figure 2.7:** 1D free energy profiles for a given reaction with and without catalyst, indicating the adsorbed initial, final states and the localized transition state, schematically illustrated in below. The adsorption free energy, intrinsic and apparent barriers are obtained by static calculations and indicated by  $\Delta G_{ads}$ ,  $\Delta G^\ddagger$ , and  $\Delta G_{app}$ , respectively;

Where  $k_B$  is the Boltzmann constant,  $h$  is the Planck constant,  $q_R$  and  $q_{TS,\ddagger}$  are the molecular partition functions of reactants and activated complex for all co-ordinates except the reaction coordinate, evaluated from the zero-point vibrational level.

$$q_{vib,i} = \prod_{i=1}^{N_{dof}} \frac{1}{1 - e^{-\frac{h\nu_i}{k_B T}}}$$

Where  $N_{dof}$  is the number of vibrational degrees of freedom of the system. The energy difference  $\Delta E^\ddagger$  includes electronic energy and zero-point vibrational energy difference at 0 K:

$$\begin{aligned} \Delta E^\ddagger &= E_0^{TS} - E_0^R + \Delta E_{0,vib} \\ \Delta E_{0,vib} &= \sum_{i=0}^{N_{dof}-1} \frac{h\nu_i^{TS,\ddagger}}{2} - \sum_{i=0}^{N_{dof}} \frac{h\nu_i^R}{2} \end{aligned}$$

A distinction has to be made between intrinsic ( $\Delta G^\ddagger$ ) and apparent ( $\Delta G_{app}$ ) energy barrier, indicated in Figure 2.7.  $\Delta G^\ddagger$ , or intrinsic barrier, corresponds to

the reference state in which all reactants are adsorbed on the material, and to a unimolecular rate equation. These are the barriers commonly reported in theoretical works.  $\Delta G_{app}$  is the apparent activation energy measured in experiments, and corresponds to a reference state in which reactants are not yet adsorbed. In this case, a multimolecular rate equation has to be used. To properly compare the two activation energies, a good estimate of the adsorption energy of reactants is needed [118].

TST has some limitations, and may fail in the case of labile intermediates, when nuclei deviate from a classical behavior, or at high temperatures. For a given reaction, in fact, there will be many paths characterized by different barriers, and at low temperature only the lowest one will be likely to be crossed. When the kinetic energy is high enough, many other paths will be activated. The transition state will occupy a larger region of the PES, and it will not be possible to derive entropy from the vibrational partition functions.

## 2.4 Exploring the free energy surface

Static calculations, where molecular vibrations are approximated using harmonic oscillators, can fail to give an accurate representation of the entropy when there is a high configurational freedom. When the FES is flat with respect to  $k_B T$ , the system at equilibrium can evolve in a larger region of the PES and move along more than one *minimum*. In this case, vibrational frequencies are anharmonic and it is not possible to represent the system by approximating around one single *minimum* (Figure 2.8). Therefore, static calculations are not always sufficient in describing the system at operating conditions. In this view, molecular dynamics (MD) techniques, which follow the time evolution of the system, can resolve this shortcoming.

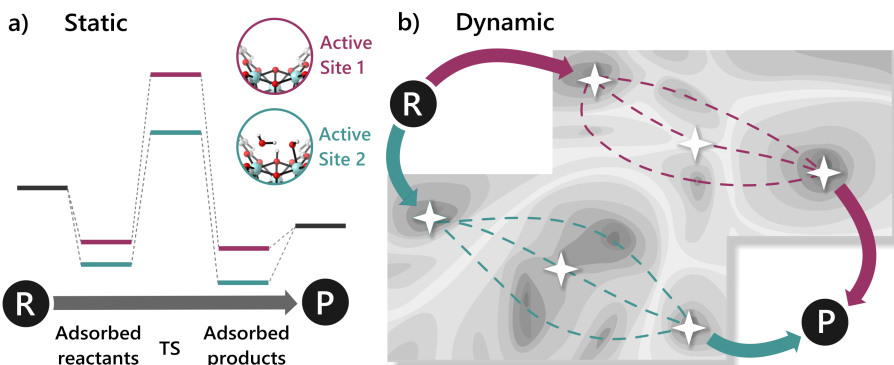
### Ab initio Molecular Dynamics

From MD simulations, thermodynamic properties such as free energy can be obtained taking into account a whole region of the PES instead of a single point. This is based on the ergodic theorem, that in one of its formulations states that the time average of equilibrium properties is equal to the ensemble average, in the limit of a sufficient long simulation.

MD simulations are based on solving Newton's equations of motion:

$$M_i \ddot{\mathbf{R}}_i = \mathbf{F}_i = -\nabla_i V$$

where  $M_i$  and  $\mathbf{R}_i$  are the mass of a given nucleus and its coordinates,  $\mathbf{F}_i$  the forces that act on it, which correspond to the gradient  $\nabla_i V$  of the PES. There are many ways to calculate these quantities and to integrate the equations of motion,



**Figure 2.8:** a) 1D free energy profiles for a given reaction on two different active sites in UiO-66 (insets), indicating the adsorbed initial and final states and the localized transition state for this reaction; (b) possible 2D representation of the given reaction on the two active sites as obtained using advanced dynamic techniques, indicating the three critical points on the potential energy surface. Adapted from ref. [26] with permission of the Royal Society of Chemistry.

and at present time, chemists and physicists can choose between a plethora of MD techniques which span a whole range of complexity, accuracy and computational cost. In the calculations performed in this thesis, potential energy and forces on the PES are calculated from first principles by means of DFT to account for the full dynamic behavior of the material by ab initio molecular dynamics (AIMD). The calculation of electronic properties which define the PES is decoupled from the propagation of nuclear motions, in a method called Born–Oppenheimer Molecular Dynamics (BOMD). Other famous AIMD methods, which differ by how the calculations of electronic potential and the equation of motion are combined, are the Car–Parrinello MD (CPMD) [119], where a fictitious electronic kinetic energy is added to the lagrangian, or the Ehrenfest MD, based on the namesake theorem [120, 121].

The first MD calculations were performed in the microcanonical (NVE) ensemble, where total energy, number of particles and volume are fixed. However, in experiments it is often the temperature that is fixed, not the energy. In general, the choice of the ensemble depends on the thermodynamic quantities that need to be determined. Nowadays there are many thermodynamic ensembles in which the simulation can be performed, an overview of which has been given by Rogge *et al.* [122]. The most convenient for a comparison with experiments are the canonical (NVT), with fixed number of molecules, volume and temperature, or the isothermal–isobaric (NpT), with fixed number of molecules and temperature, but where the volume can fluctuate. In order to have a fixed average temperature, some control of the kinetic energy of the atoms is needed. Various thermostats,

which differ in terms of speed and robustness, are implemented in every MD code. In this thesis, Nose'–Hoover thermostat was used, where the system is connected to a heat bath. The pressure is also controlled in simulations by means of a barostat. The most commonly used is the one developed by Martyna, Tobias, and Klein (MTK) [123].

### Radial distribution functions

From MD trajectories, different macroscopic properties can be derived. An important structural property is the radial distribution function (RDF) or pair correlation function  $g(r)$ , that describes the probability density between specific atoms as a function of the distance, normalized with respect to a probability distribution of a homogeneous gas with the same density. The RDF can be calculated from the following expression:

$$g_{ij}(r) = \frac{dn_{ij}(r)}{4\pi r^2 dr \rho_i}$$

where  $dn_{ij}/dr$  represent the number of atoms of type  $j$  within a certain distance of the atoms of type  $i$ , and  $\rho_i = V/N_i$  represent the density of the homogeneous distribution. The integral of the RDF can also give valuable insight into the number of atom pairs at a given distance, such as what is the average coordination of a certain chemical species.

### Vibrational density of states

Information on the time evolution of certain quantities in the system can be obtained by calculating time autocorrelation functions. The correlation of a certain variable with itself is equal to:

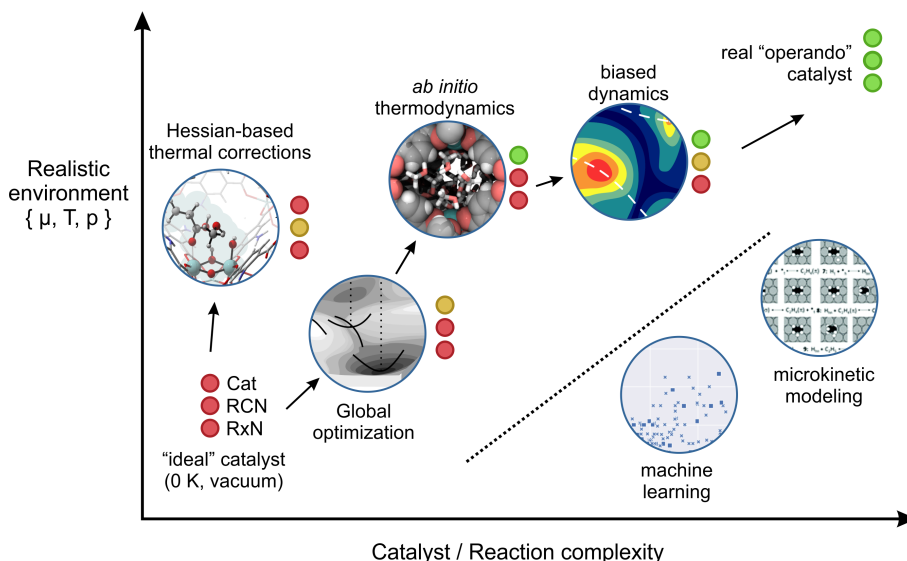
$$\langle X(0) : X(t) \rangle = \lim_{N \rightarrow \infty} \frac{1}{T} \int_0^T X(t) X(t + \tau) d\tau$$

Autocorrelation functions offer a measure of the response of the system to a given stimulus, which is function of the density of states. The response of a system to a perturbation is equal to the power spectrum of the autocorrelation function of the fluctuations of the involved observable [124]. For instance, by calculating the power spectrum of the atomic velocities autocorrelation function, we can obtain the vibrational density of states, as done in **PAPER IV**. These spectra contain all the dynamic and anharmonic information that is neglected in the static frequency calculations.

### Towards modeling at operating conditions

With the growth in computational time, the new challenge is constituted by modeling the system at operating conditions. To describe the active sites at reaction conditions, the computational model should reflect the realistic conditions during

the reaction, and its complex reaction environment. Within the challenge of *operando* modeling, Grajciar *et al.* [125] gave a recent review on the various computational methods applied to heterogeneous catalysis, as shown in Figure 2.9.



**Figure 2.9:** Schematic of the various computational methods applied to heterogeneous catalysis, which lie between an idealized ultra-high vacuum/0 K model and a realistic, *operando* model. The traffic light key depicts the quality of each method with respect to catalyst model complexity (Cat), reaction coordinate accuracy (RCN) and reaction network complexity (RxN). Adapted from ref. [125] with permission of the Royal Society of Chemistry.

Many chemical reactions in MOFs are performed at mild conditions involving the presence of a solvent. In order to move closer to modeling the system at operating conditions, the solvent in the pores can also be taken into account. This adds a lot of degrees of freedom to the system, and for this reason often an implicit description of the solvent is done, such as in the Polarizable Continuum Model (PCM) [126]. In the case of the work in this thesis, however, it is necessary to fully model the solvent molecules, as they are actively involved in proton transfers. To do so, the number of solvent molecules that can fit in the unit cell needs to be estimated. Monte Carlo method (MC) is an alternative approach to MD to explore the PES for complex systems. It was initially developed for the calculation of multidimensional integrals and is nowadays largely used in chemistry, especially when dealing with adsorption. In the framework of this thesis, it has been applied in the Grand Canonical ensemble ( $\mu VT$ , fixed chemical potential, volume and temperature) to determine the number of solvent molecules that could fill the

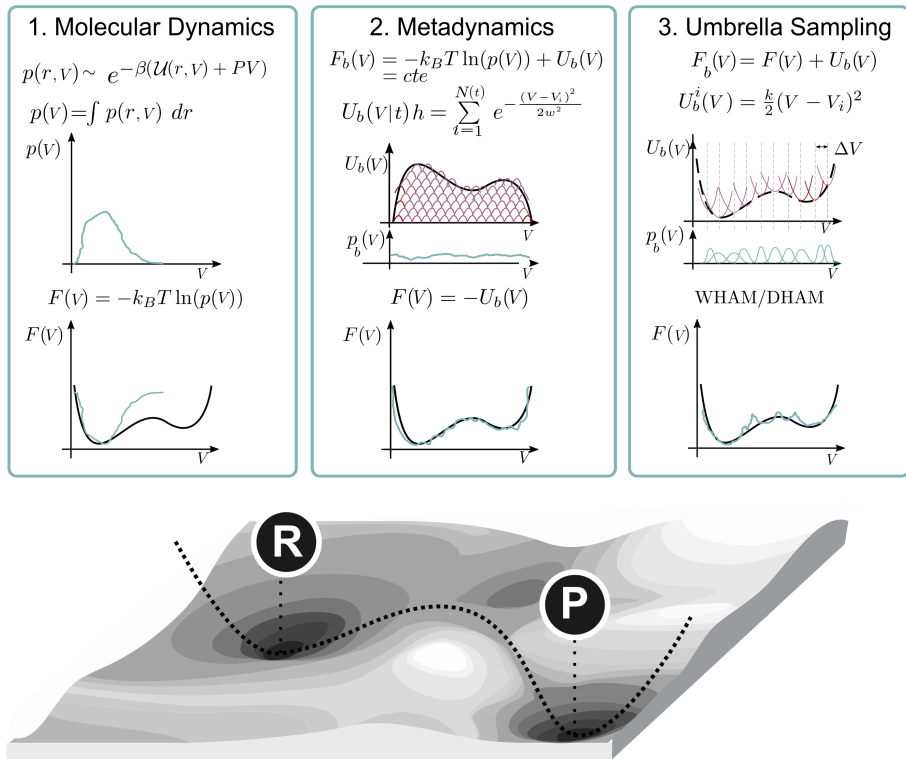
pores of the material at realistic conditions [127]. The estimation of this number is not trivial, and depends on many factors such as the defect topology, or the choice of force field model used, as reported by Vandenbrande *et al.* [128].

## Enhanced sampling MD methods to describe activated processes

MD simulations can offer valuable insights into the behavior of a chemical system at equilibrium conditions. From these simulations, many properties can be extracted, such as free energy differences, equilibrium geometries, vibrational spectra, diffusion coefficients, structural parameters etc. Configurations associated to higher (or lower) values of potential energy will be sampled for shorter (or longer) times, and in principle, if a certain process is sufficiently sampled, based on the ergodic theorem we can know its equilibrium constant, and in turn the free energy barrier associated to it. In general, to have reliable free energy for a given process, three components are needed: (i) an appropriate description of the potential energy, (ii) a sampling protocol that allows to generate an ensemble of configurations that is representative for the process, and (iii) the right method to estimate the relevant free energy differences [129]. Point (i) was already tackled in previous sections, and herein we focus on the last two points.

Chemical reactions, where bonds are broken and formed, are generally rare events that will not be sampled with a regular exploration of the PES. If the free energy barrier is high compared to  $k_B T$ , the probability that such event would spontaneously occur during the simulation time is practically none. This is especially true for complex molecular systems, in which processes occur in different time scales and that can only be simulated for a limited amount of time. For this reason, different enhanced sampling techniques have been developed to enhance the sampling of low probability regions of the free energy landscape [130–137]. Recently, enhanced sampling techniques have been successfully applied in heterogeneous catalysis to study processes at operating conditions [118, 138–143].

There are two main classes of methods that can be used to explore rare events on the free energy surface. The first class is characterized by methods that encompass all degrees of freedom and do not need any prior information on the free energy landscape between two points. Examples of these methods are Transition Path Sampling (TPS) [144] and Replica exchange (RE) [145]. The other class of techniques encompasses methods in which the sampling is enhanced along certain coordinates of the system, such as Umbrella Sampling (US) [146, 147] and Metadynamics (MTD) [131], shown in Figure 2.10.



**Figure 2.10:** Schematic representation of different MD techniques that can be used to explore the PES. Adapted from Ref. [129] with permission of the American Chemical Society

### Choice of collective variable

The PES is a highly dimensional surface, defined by the positions of all atoms in the system. However, often a reactive process can be described by few important coordinates called “collective variables” (CVs), which are projections of the high dimensional space. In fact, what can be considered a chemical configuration is an ensemble of microstates that are different in terms of absolute coordinates of each atom, but all contribute to the same macrostate. In some cases, a simple CV can represent the reaction coordinate for the process, but often the choice is not trivial [148]. In general, choosing the right collective variable is crucial to describe the correct process. Often geometric parameters are used, such as distances, angles, dihedrals, or combinations of the latter. When studying certain processes, a switch function such as a coordination number (CN) derived from distance information is often the preferred choice. CNs represent a smart choice compared to distances, because for each pair of atoms, the coordination is zero for distances higher than a certain threshold.

$$\text{CN} = \sum_{i,j} \frac{1 - (r_{ij}/r_0)^{nn}}{1 - (r_{ij}/r_0)^{nd}}$$

Where CN is defined between two sets of atoms  $i$  and  $j$ ,  $r_{ij}$  corresponds to the distance between atoms  $i$  and  $j$ , and  $r_0$  is a threshold distance. The exponential parameters  $nn$  and  $nd$  define how sharply the function behaves around the value  $r_0$ . In processes such as in the ones of **PAPER V**, we considered the coordination between a zirconium atom and the oxygen atoms of the solvent water. Such collective variable allows to consider the possibility that different water molecules could decoordinate and recoordinate, defining the same macrostate for a given value of the CN. We show that such processes cannot be studied by employing distances as CVs.

### Metadynamics

Metadynamics (MTD) is a popular enhanced sampling method, used to overcome barriers in the free energy landscape, which was first proposed by Laio and Parrinello [131, 149]. During MTD, a history dependent bias potential is added in the form of gaussian hills to the PES along a certain CV. This way, potential energy is added to already visited states, allowing to escape local *minima* and explore different regions of the PES. When all states are sampled with equal probability, the free energy profile along the biased CV can be obtained from the added bias potential. As the bias is added, the system is able to evolve along all the other degrees of freedom. For this reason, this method can also provide insight into the mechanisms that occur during the exploration of the different regions of the CV, as has been done in **PAPER V**.

### **Umbrella sampling**

In the umbrella sampling method, a series of biased MD simulations are performed along the chosen CV. In each simulation, a bias potential is added to constrain the system to adopt a specific value of the CV, while it can evolve along all the other degrees of freedom. This way, the whole range of the CV can be explored. As each simulation is independent, this method is highly parallelizable. The free energy profile can then be estimated by using different methods to combine the information obtained from the set of simulations, such as the weighted histogram analysis (WHAM) or the multistate Bennett acceptance ratio [146, 150]. Even if the CV is constrained in each simulation, this method can also offer valuable insight into the evolution of the system at different values of the CV, as has been done in **PAPER III**.

### **Computational details**

In this thesis, cluster calculations were performed with Gaussian '09 [85]. Static periodic calculations were done with the Vienna Ab Initio Simulation Package (VASP) [151–155]. Molecular dynamics simulations were performed with CP2K [156]. GCMC calculations were performed with the RASPA code [157]. Enhanced sampling was applied by means of the PLUMED code [158] along with CP2K. For what concerns calculation time, an extended cluster calculation takes less than 1 node day. A static periodic optimization with frequency calculations on the 2-brick UiO-66 unit cell takes approximately 20–25 node days. A 50 ps CP2K calculation on the same unit cell including solvent takes about 150 node days. The simulations were run on the TIER1 Flemish supercomputer centrum, with access granted on a project basis, for a total of about 20000 node days used for the calculations in this thesis (Appendix B). The computational time indicated refers to nodes consisting of 2x14-core Intel Xeon processors, with 128 GiB RAM.

In summary, this chapter gives an overview of the many methods that have been employed to understand the properties of MOFs. Reactive processes can be studied by using a plethora of different computational techniques that differ in cost and accuracy. Cluster calculations were used for a first estimate of the energies, whereas periodic models were used for all the remaining part of this thesis. The increase in computational time allowed to include more complexity in the model, and to explicitly take into account the role of solvent and structural modifications in the material. During the time frame of this thesis, we moved from a static description of the chemical events towards modeling at operating conditions that allows to better describe and predict real processes.

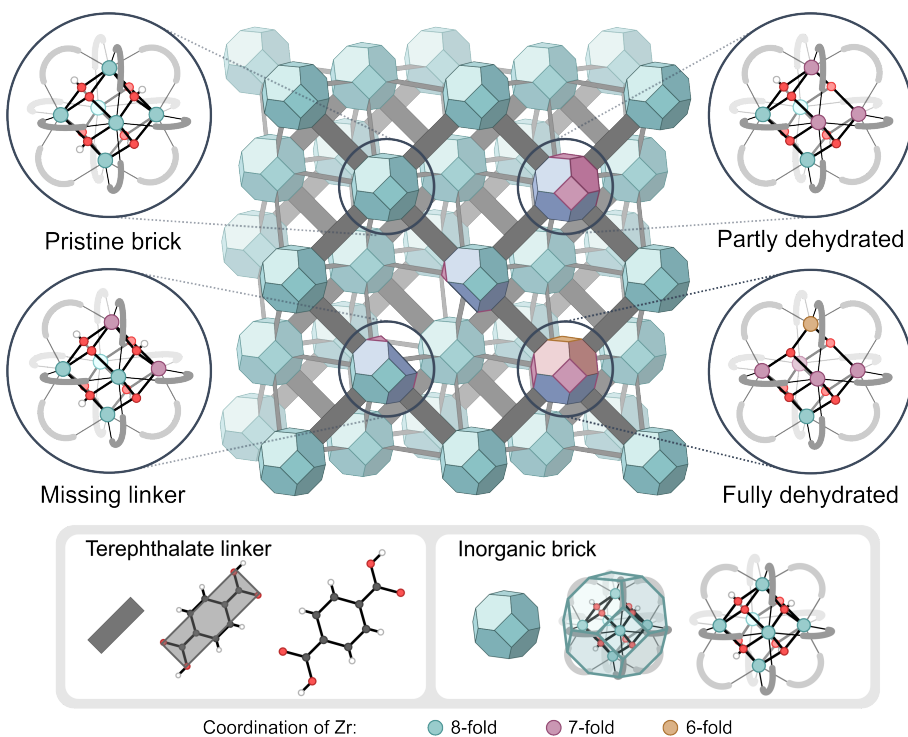
# 3

## Major research results

This Chapter illustrates the main research results obtained in the framework of this thesis. The main goal of this work was the study of the nature of active sites on UiO-66 and MOF-808 upon activation processes, and how the solvent and the functionalization influenced their behavior. The role of active sites on defective UiO-66 was studied for Fischer esterification of free fatty acids (FFA), where it became clear that solvent played an unexpected active and beneficial role in the reaction mechanism. This study was inspired by experimental work performed by Cirujano *et al.* [79, 80]. Starting from this initial experimentally inspired problem, the level of complexity was increased in our modeling approach to obtain a fundamental understanding on the nature and creation of active sites as operating conditions. Different molecular modeling techniques based on static and dynamic methods have been applied to gain insight into the interaction between active sites and reactants in the material, as has been introduced in Chapter 2. Contrary to reactions in zeolites, processes in MOFs are often performed ad mild conditions in the presence of a solvent, which adds complexity to the model. So far, solvent in MOFs had been studied only with force-field approaches, but with the increase in computational power it became possible to include a full *ab initio* treatment of water and methanol solvent in the UiO-66 pores and to go towards an *operando* description of activation processes in MOFs, where realistic experimental conditions are taken into account. The most important scientific results will be highlighted in this Chapter. More details are to be found in the original articles, enclosed in Part II.

### 3.1 Activation processes in zirconium–MOFs

One of the main challenges in MOF research is the understanding of how active sites are created and how they impact the properties of the material. For this purpose, molecular modeling offers a platform that allows to study such activation processes and nature of active sites at the molecular level. In this sense, UiO–66, characterized by an exceptional stability, represents a perfect case study where different activation and PSM processes can take place without disrupting the stability of the structure. Initially, it was not clear how active sites were created in UiO–66, as the non-defective material contains only fully saturated sites. It was later understood from experimental and computational evidence [65] that defects, such as missing linkers, are necessary for the generation of active sites for catalysis (Figure 3.1).



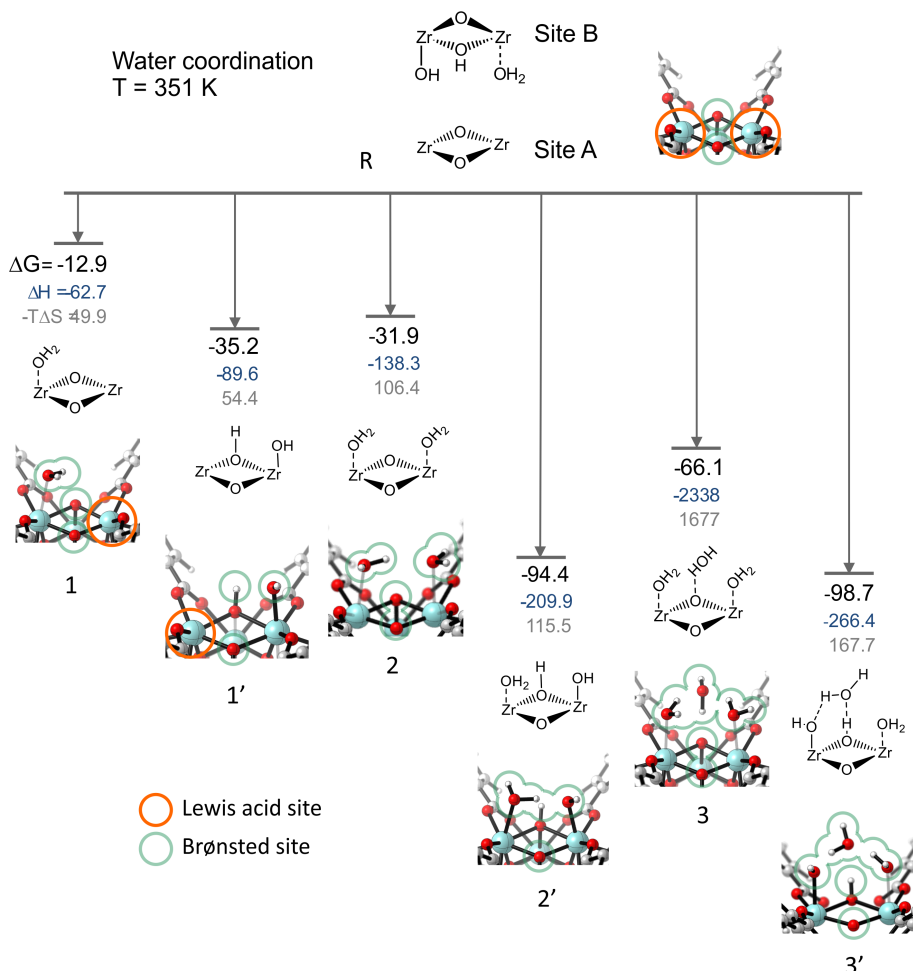
**Figure 3.1:** Schematic representation of the UiO-66 structure with possible configurations of the bricks that give rise to coordinatively unsaturated zirconium atoms. The colors indicate the coordination of the zirconium atoms. Adapted from ref. [159] with permission of the Royal Society of Chemistry.

## Molecular structure of SBUs with missing linkers

In **PAPER I** we investigated the local defect topology upon removal of a linker on UiO-66 as starting point to investigate the catalytic role of defect coordinating species in the mechanism of Fischer esterification. This research was done in collaboration with the group of Dr. Francesc X. Llabrés i Xamena (Instituto de Tecnología Química, Universitat Politècnica de València), where they experimentally observed that the thermal treatment of the material had a strong effect on its catalytic behavior for Fischer esterification, but the reason was not well understood. When studying the catalytic behaviour of UiO-66, it is essential to understand the reactivity of the inorganic SBU and its molecular structure upon removal of a linker. On these sites, defect coordinating species can be adsorbed and have an impact on the catalytic properties of the MOF by introducing additional sites. Upon removal of one of the twelve negatively charged BDC linkers from the inorganic  $Zr_6O_4(OH)_4$  SBU, a positive charge remains on the brick. Charge neutralization can be accomplished by either coordinating a negative ion such as hydroxyl group to one of the zirconium atoms, or by removing a proton from the brick. This latter case is characterized by two zirconium open metal sites, and is the type of active site that is obtained upon thermal treatment of the brick at  $T > 423$  K. Initial studies on the catalytic properties of UiO-66 mainly pointed towards the Lewis sites as active sites for catalysis. However more recently it has been shown how Brønsted sites in the neighborhood of the Lewis sites may play also an active role for particular reactions [37, 64, 66, 68, 69, 71, 160, 161]. The presence of multiple sites makes it difficult to establish a simple structure–activity relation. In particular, it is important to understand from a mechanistic point of view how the presence of defect coordinating species may affect the catalytic activity on Zr-MOFs. The capping of these defect sites with various labile species was studied within the framework of **PAPER I** and the main results are shown in Figure 3.2.

The coordination of water species near the active sites can occur with different configuration, as schematically shown in Figure 3.2. In all structures the presence of possible Lewis and Brønsted sites which may play a role in reactions is highlighted. The simplest case taken as reference configuration is the unsaturated site obtained upon thermal activation, containing two  $\mu_3$ -oxygens bridging the zirconium atoms which may act as Brønsted sites. From this structure, the coordination of one physisorbed water molecule to one of the zirconium atoms is energetically favorable. A decrease in energy is observed when the molecule is deprotonated to the oxo atom as in configuration 1'. The chemisorption of this water molecule shields the Lewis character of the zirconium atom, but introduces an additional Brønsted site in proximity to the open metal site.

The most stable configurations are observed in presence of 2 or 3 adsorbed water molecules on the adjacent zirconium atoms. Two physisorbed water molecules of configuration 2' can be adsorbed to the two zirconium atoms, followed by an immediate dissociation of one of the two molecules into a hydroxyl group and a



**Figure 3.2:** Coordination free energies at reaction temperature of 351 K of one, two and three water molecules at coordinatively unsaturated zirconium bricks in defective UiO-66 with respect to a water coordination free site (site R). The structure of the opposite site B corresponds with configuration 2' with two water molecules and consistently used in all periodic calculations considered in the figure. Free energies (in black) are given in kJ/mol, and their decomposition into enthalpic  $\Delta H$  (blue) and entropic  $-T\Delta S$  (grey) contributions. Energies are resulting from periodic calculations with PBE-D3 level of theory. In each configuration Lewis acid and Brønsted sites are indicated. Adapted from ref. [86] with permission of Elsevier.

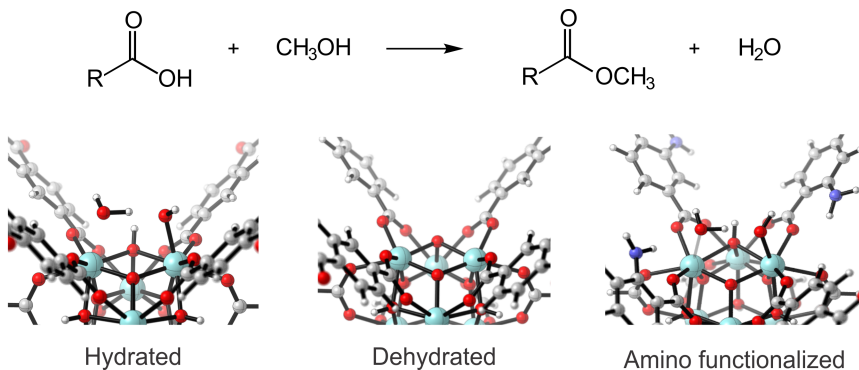
proton on the adjacent  $\mu_3$ -oxygen. This configuration is characterized by a free energy difference of -94.4 kJ/mol at reaction temperature of 351 K compared to the dehydrated defective site. This is in agreement with previous SXRD results by Lillerud *et al.* [66], which show that in the defective material zirconium atoms are fully coordinated by oxygen. When starting from the thermally activated material that contains open Lewis sites, at standard condition, water present in the atmosphere will immediately coordinate to restore the 8-fold coordination of the zirconium atoms to give structure 2. This structure is consistent with the one proposed by the group of Farha [71] who identified three types of protons from potentiometric titration:  $\mu_3$ -OH, Zr-OH and Zr-OH<sub>2</sub>.

A third bridging hydroxyl species as charge neutralizing species was proposed by Yaghi [67] from XRD data. They propose two physisorbed water molecules bridged by an OH<sup>-</sup> counterion that is stabilized by a hydrogen-bond interaction with the neighboring  $\mu_3$ -OH of the brick. However, a recent study Ling and Slater [68] did not succeed in finding a corresponding minimum on the PES. In this work, we observe that the  $\mu_3$ -OH atom immediately deprotonates in proximity of such OH<sup>-</sup> anion (configuration 3). Similarly as in the previous case, this structure can further stabilized by a deprotonation of one of the two physisorbed water molecules, to yield configuration 3' of Figure 3.2, in agreement with a previous report by Vandichel *et al.* [69]. Adsorption of reactants involved on the Fischer esterification reaction was also taken into account. Similar considerations on the deprotonation processes can be drawn when considering methanol instead of water as reported more in detail in **PAPER I** and **PAPER II**. The energies obtained clearly demonstrate that water molecules preferentially adsorb on the zirconium atoms and that a subtle balance between enthalpic stabilization and entropic penalty will determine the number of water molecules adsorbed on the inorganic brick. We here find that the inorganic brick will tend to stabilize itself with capping molecules to obtain the optimal coordination number of 8. However it must be emphasized that some of these capping species will have to be removed at the onset of the reaction to make place for the active reagents.

## Nature of active sites for Fischer esterification explored by static simulation methods

Among the reactions that can be catalyzed by UiO-66, Fischer esterification, shown in Figure 3.3 is an important process in the production of biodiesel, a biofuel that is obtained from renewable sources, such as oils and animal fats [1, 2]. UiO-66 has been shown to be a stable and reusable Lewis catalyst with high conversion rate for the reaction [79, 80]. Experimental findings performed on both hydrated and dehydrated UiO-66 show that water has a beneficial role in the process, but a theoretical rationalization of the underlying causes was missing. Moreover, amino functionalization was shown to increase the reaction rate. To address these questions, the role of active sites on UiO-66 during the Fischer

esterification reaction was studied in **PAPER I**. Two possible lowest activated reaction pathways were identified for the hydrated and dehydrated active site.

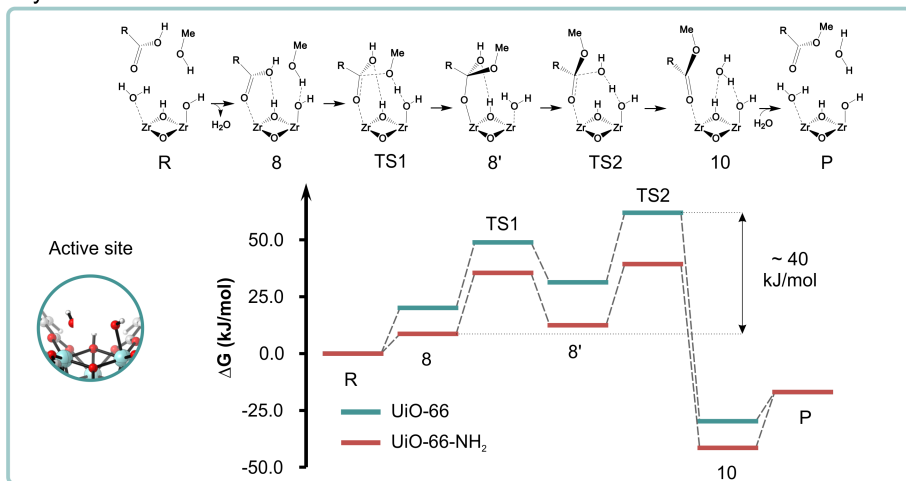


**Figure 3.3:** Top: Fischer esterification reaction; bottom: three different types of UiO-66 active sites.

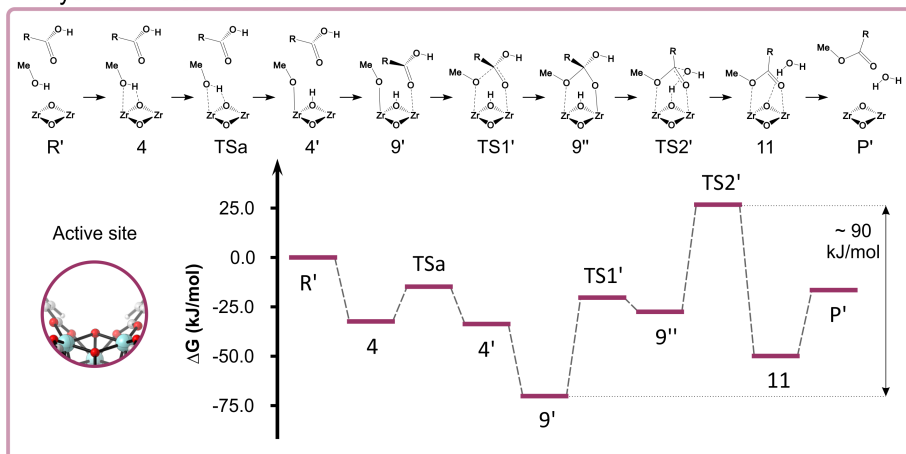
The proposed reaction mechanism is shown in Figure 3.4 (top). From the reactant configuration, the physisorbed water molecule is displaced by the carboxylic acid that coordinates on the zirconium atom. The resulting configuration was identified after a series of static calculations probing possible geometries. In this configuration, the acid carbonyl group is bonded to the zirconium, and at the same time methanol is hydrogen bonded to the hydroxyl group coordinated to zirconium. The adsorption of the acid on the Lewis acid site gives to the carboxylic carbon a more electrophilic character, making it more prone to interact with the alcohol. The oxygen of methanol is at the same time made more nucleophilic due to the hydrogen–bonding interaction with the Brønsted basic site situated in close proximity. This favors the condensation between activated carboxylic carbon of the acid and methanol. Two TS are involved in the process, in which first a tetrahedral intermediate is formed, and then water is removed. In both, the hydroxyl group plays a role, first as proton acceptor, then as proton donor, while the acid maintains the bond with the carbonyl oxygen. The low energy barriers associated to the two TS are 28.9 and 30.6 kJ/mol at 351 K. The reaction can proceed both ways, until an equilibrium is reached. This mechanism is characterized by a dual participation of Brønsted and Lewis sites, and overlays with the experimental findings.

Upon thermal treatment at 423 K, UiO-66 loses the adsorbed solvent molecules without compromising the structure of the inorganic SBU, contrary to the dehydroxylation with release of two water molecule that takes part at  $T > 523$  K [162]. In principle, these open metal sites should be more catalytically active, but a decrease in catalytic activity is experimentally observed. In the proposed mechanism, shown in Figure 3.4 (bottom), two Lewis acid sites, the zirconium atoms, and one Brønsted basic site, the  $\mu_3$ -oxygen, play an active role in the reaction. This mechanism is

## Hydrated material



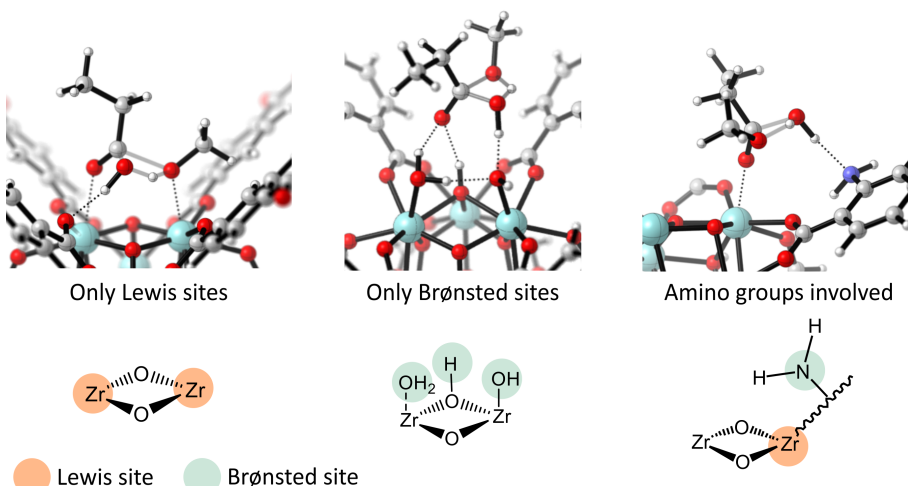
## Dehydrated material



**Figure 3.4:** Mechanism and free energy profile for the esterification of propionic acid with methanol on a hydrated and defective UiO-66 material (blue), a hydrated defective UiO-66 material with amino functionalization of the BDC linkers (red), and on a dehydrated defective UiO-66 (black). Periodic calculations at B3LYP-D3//PBE-D3 level of theory, T=351 K. R corresponds with an empty frame with one linker defect and a pool with all reactants to guarantee mass balance. In P the defective Zr-brick is coordinated with two water molecules (configuration 2'). P' corresponds to the empty frame with the ester as final product and remaining water molecules in gas phase. Adapted from ref. [86] with permission of Elsevier.

characterized by three TS, in which: 1) methanol is deprotonated to the oxo atom, 2) an adduct is formed between the electrophilic carbon and the oxygen of methanol 3) the  $\mu_3\text{-OH}$  group deprotonates to form water. This reaction is characterized by higher activation barriers (a total barrier of 90 kJ/mol at 351 K), which explain the lower catalytic activity of the dehydrated material.

Other mechanisms that do not make use of either Lewis or Brønsted sites were investigated without success (Figure 3.5), as the energy barriers were too high to be likely to occur. Both proposed mechanisms are characterized by a dual participation of Lewis and Brønsted sites that work complementary to each other. The presence of acid and basic centers within molecular distances has been shown to be essential in the performance of the catalyst during Fischer esterification, as they cooperate in a concerted way during the chemical transformation. Most of the previous mechanistic studies on the UiO-66 material merely focused on the Lewis acidity of the undercoordinated sites, but it has become more and more clear that the bifunctional nature of the UiO-66 catalyst will play an important role in its future applications.



**Figure 3.5:** Transition states belonging to three cases where no suitable mechanism for Fischer esterification was found, suggesting that the reaction needs a concerted participation of Lewis and Brønsted sites

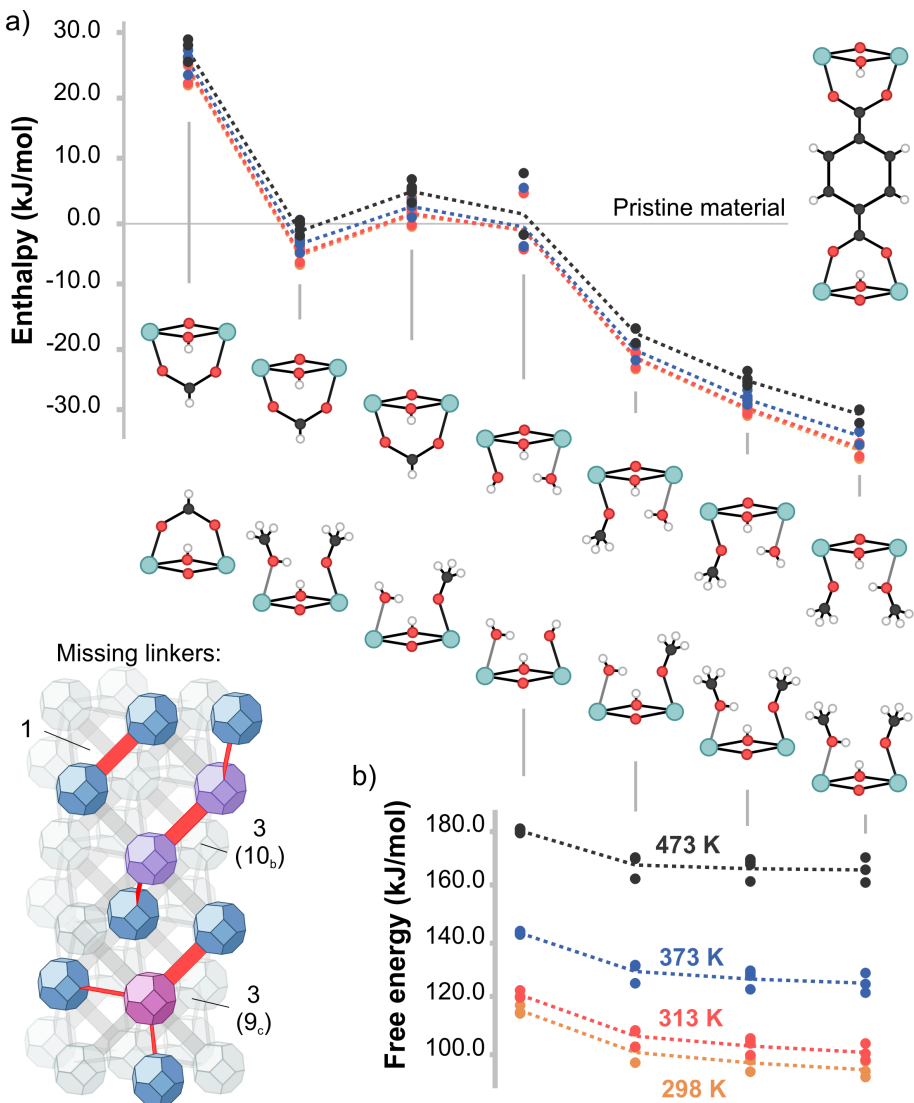
The proposed mechanisms overlay with experimental findings showing that the reaction rate decreases when the material undergoes thermal treatment, and that defective sites are the source of the catalytic activity. The effect of functionalization on the reaction barriers for this reaction will be further explored later in the thesis.

## Active sites in larger defective unit cells

Understanding the nature of active sites on UiO–66 is not only important for reactions, but also for processes such as PSLE, where ligands are dynamically exchanged. For this reason, the adsorption of species present in the reaction environment of PSLE process was studied in the framework of **PAPER IV**. This work was done in collaboration with the group of Prof. Rob Ameloot (Centre for Membrane Separations, Adsorption, Catalysis, and Spectroscopy for Sustainable Solutions, KU Leuven), where experimental evidence was given of the active role of methanol in modulating the exchange of linkers and the number of missing linker defects during the process.

To rationalize the experimental findings, the first step was to see how different species present in solution would interact with the UiO–66 material at different defect concentration. To obtain this information, we made use of a larger unit cell, to be able to represent different amount of missing linker defects [60, 61, 63]. This increase in complexity of the model entails a higher computational cost. The defective structures taken into account in the modeling are obtained by removal of linkers from the conventional unit cell containing four inorganic  $Zr_6(O)_4(OH)_4$  bricks [46]. Different numbers of missing linkers were modeled, to represent the different amount of defects in the experimental samples. A case with a low amount of defects is modeled by a unit cell with one missing linker. In this structure, two bricks are 12-fold coordinated, and two bricks are 11-fold coordinated, with an average of 11.5 linkers per brick. A second type of unit cell was taken with three missing linkers, corresponding to a higher amount of defects, with an average of 10.5 linkers per brick. De Vos et al. and Rogge et al. [60, 61] shown in their comprehensive studies that there are multiple topologically diverse possibilities to remove linkers from a 4-brick unit cell. In this work, we chose two possible, discrete cases to represent different coordination of the inorganic brick with this amount of defects. In a first unit cell with three missing linkers, two bricks are 10-fold coordinated and two are 11-fold coordinated. The other represents a more extreme case, with one 9-fold coordinated brick and three 11-fold coordinated bricks. The structures taken into account are denoted as  $(10_b, 10_b, 11, 11)_{334}$  and  $(9_c, 11, 11, 11)_{333}$  in the work of De Vos et al [61] and are reported in Figure 2.2.

The zirconium atoms on the defect sites have been capped by a variety of species which can be present in the framework during the activation process. In this sense, various combinations were possible by capping with water, hydroxo species, methanol, methoxide and formate. In our models, all zirconium atoms have been capped and are fully (8-fold) coordinated, being the most stable state at experimental conditions. On each defect site there is always a negatively charged species, to compensate for the removal of a carboxylate. When multiple species are adsorbed, configurations with different symmetries can arise, according to how the molecules are positioned on the defective sites. When possible, multiple possibilities for the positioning of these species were taken into account and modeled. The



**Figure 3.6:** Energy diagrams for defective UiO-66 unit cells. Each dot represents a possible distribution of missing-linker defects (1 or 3 in total) within the unit cell; the connecting dotted line represents a weighted average. Values are normalized by the number of missing linkers in the unit cell. (a) Enthalpy difference between defect sites capped in different ways versus the non-defective material at T = 298, 313, 373, 473 K. (b) Temperature-dependence of the free energy difference of the defective structures indicated above (capped with H<sub>2</sub>O/OH<sup>-</sup>, H<sub>2</sub>O/MeO<sup>-</sup> and MeOH/MeO<sup>-</sup>) versus the non-defective structure. A representation of the clusters with different missing linker connectivities is also provided. Adapted from ref. [89] with permission of the American Chemical Society.

removal of a negative charge can be also compensated by removal of a proton, as obtained in the dehydrated material, with subsequent physisorption of two neutral species, but these configurations are higher in energy, as seen in **PAPER I**. The adsorption enthalpies for the different configurations are reported in Figure 3.6. Our results show a clear enthalpic preference for the methanol/methoxide pair in detriment of formate and water. The defective material synthesized with formate modulator is promptly attacked by methanol species present in solution. The obtained results are in line with a previous report [72] and highlight the preference of zirconium active sites for  $\text{MeOH}/\text{MeO}^-$  substitution as opposed to  $\text{H}_2\text{O}/\text{OH}^-$ , alternatively assumed as preferential charge balancing element for missing linker defects [67, 68]. No substantial difference in enthalpy is observed between the unit cells with different amount of defects (energy in each defective structure represented by a dot in Figure 3.6). This is an indication that the thermodynamics that governs the process does not depend on the starting number of missing linkers. Such theoretical finding is in agreement with the experimental observations of **PAPER IV**, where it is shown that an equilibrium defect concentration is reached that does not depend on the initial defectivity.

The effect of temperature on the free energy was also investigated on the relative stability of defective configurations with respect to the pristine unit cell, where the linker is not missing. The first observation is that configurations involving water and methanol are more stable at lower temperature, thus the formation of missing linker defect through ligand exchange is enthalpically driven and favored by lower temperatures. Secondly, at 473 K the energy of the non-defective framework is much lower than the defective cases, which explains why the synthesis of the non-defective UiO–66 is favorable at such high temperature [53].

The findings support the evolution of the ligand coordination on the UiO–66 material during the PSE process in methanol, which can successfully proceed at low temperatures. The PSE mechanism will be illustrated more in detail later in the chapter.

## Activation by dehydration

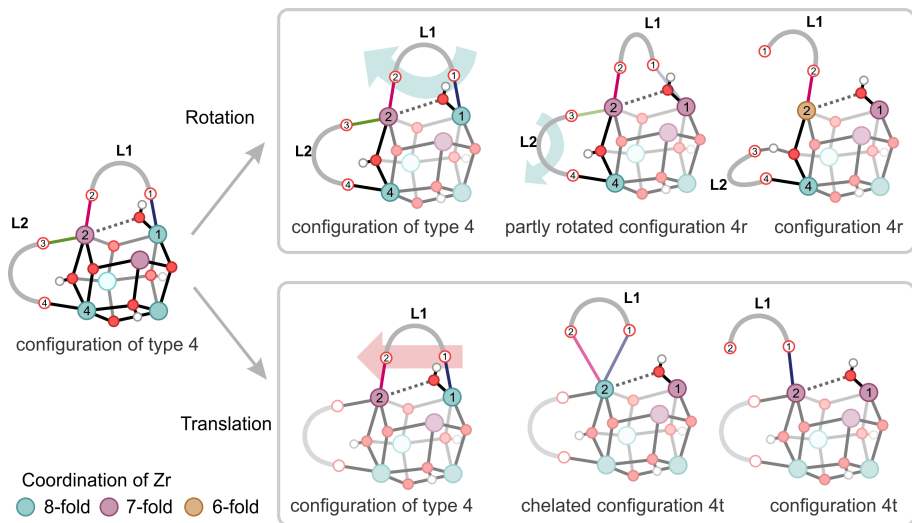
The other process that can lead to activation of the UiO–66 material is the reversible dehydration of the brick performed at  $T > 523$  K. The dehydration mechanism may have a decisive effect on certain catalytic reactions, where next to the Lewis acid site also the neighboring Brønsted base or acid site may take a cooperative role in the reaction mechanism. It is still unclear whether this lowering in the zirconium coordination without lowering of the brick connectivity is enough to induce catalytic activity. As shown for citronellal cyclization, missing linkers are required for the reaction to be catalyzed [65].

At elevated temperatures and low pressures, the zirconium core gets dehydrated and rearranged, and two water molecules are subsequently removed from the

brick, as displayed in Figure 3.1. The fully dehydrated  $\text{Zr}_6\text{O}_6$  brick contains undercoordinated sites [28, 48, 73, 162], with coordination of the zirconium atoms ranging from 8 to 6. The structure of UiO–66 is however preserved and the brick can easily be hydrated again with a reversible mechanism, giving evidence that the inorganic SBU can undergo dynamic processes. During these structural rearrangements, the presence of a infrared band related to hydroxy groups was observed by Nishida *et al.* [163] and by Shearer *et al.* [162] pointing towards structural rearrangements of the inorganic bricks. The mechanism of dehydration was first studied by Vandichel *et al.* by means of nudge elastic band calculations [69], showing the presence of loose hydroxyl groups, in agreement with former experimental reports, as well as partially decoordinated linkers. These findings point towards an intrinsic mobility of the framework structure, that can accommodate rearrangements without disrupting its stability. However, the static study of this process poses serious limitations.

To go beyond the static approach and follow the dehydration process *operando* and *in-situ*, in **PAPER III**, we follow on the fly the fast dynamic of the UiO–66 material at dehydration temperature of 573 K by means of umbrella sampling simulations. The results show an intrinsic dynamic behavior of the material, with open metal sites being created by continuous changes in the network connectivity due to labile M–L bonds. We identify two types of motions of the linkers, namely translation along the axis connecting the two adjacent zirconium atoms, and rotation along the linker axis connecting the two inorganic SBUs, as shown in Figure 3.7. At the same time, these motions are accompanied by a high mobility of hydroxy groups created by decoordination of the  $\mu_3\text{--OH}$  groups. These results show that linkers are more mobile than originally anticipated. The high connectivity between the two SBUs of UiO–66 allows all these reversible rearrangements with activation barriers that can be easily accessible at experimental conditions.

These findings on the dynamic nature of UiO–66 were an eye-opener, as the structure of UiO–66 is regarded as one of the most stable and rigid among the whole MOF family. Herein, we discovered that the UiO–66 material possesses an intrinsic dynamic behavior, where the zirconium atoms have a degree of flexibility in changing their coordination number. This is connected to its high versatility in undergoing other processes where the coordination environment of the brick can change, such as in PSLE.



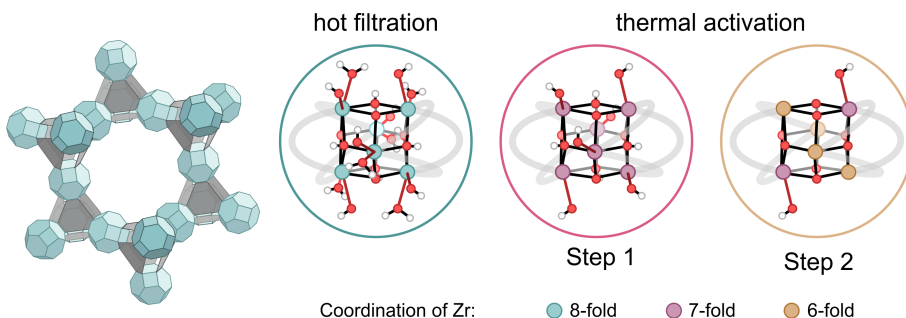
**Figure 3.7:** Umbrella sampling in two windows of  $\text{CV} = 1.45$  and  $1.51$ , showing two distinct motions of the linkers. On the left column, a translation of the linker L1 generates a chelated structure and a subsequent shift in the carboxylic oxygen connected to Zr2 (configuration 4t). On the right column, a rotation of the linker L1 and a partial decoordination of linker L2 forming a hydrogen bond with an  $\mu_3\text{-OH}$  hydroxyl group is shown (configuration 4r). A proton transfer between the carboxylic oxygen O3 and the bridging  $\mu_3\text{-O}$  is also observed and is an indication of the occurrence of an intrinsic dynamic acidity. Colors indicate the coordination number of zirconium atoms. Adapted from ref. [159] with permission of the Royal Society of Chemistry.

## Thermal activation of MOF-808

The active sites and coordination changes upon thermal activation have been studied in the case of MOF-808. MOF-808 shares the  $\text{Zr}_6\text{O}_4\text{OH}_4$  brick with UiO-66, but the brick is connected to only six tritopic BTC linkers, making it the least connected MOF in the Zr-MOF family. The material possesses a high catalytic potential due to the intrinsic presence of defective sites of complex nature, and large pores [44]. For instance, it shows a higher catalytic activity than UiO-66 for MPV reduction [82, 83].

In this work, we wanted to see in how far the material can be activated by thermal treatment to obtain such Lewis acid sites, and whether the conclusions obtained for UiO-66 could be applied also to other MOFs possessing the same inorganic SBU. In particular, we were interested in the stability of the material upon these activation processes.

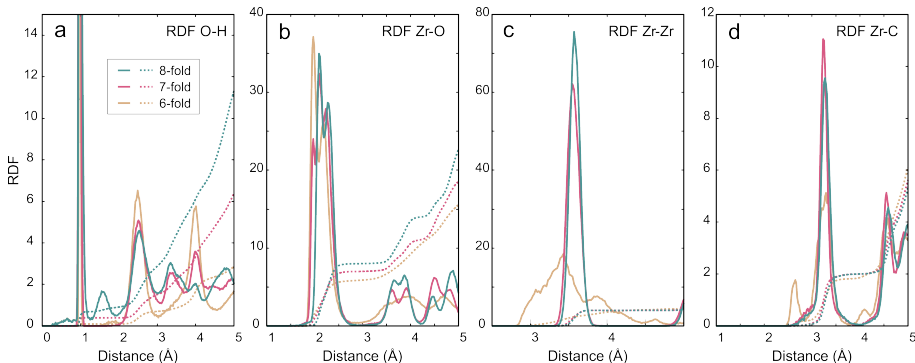
In the as synthesized material (Figure 3.8), the zirconium atoms that are not connected to BTC linkers are capped by formate groups. The material is activated by hot filtration, whereby each formate is replaced by water and hydroxyl group, for a total of six water molecules and six hydroxyl groups per inorganic SBU [82, 83]. Each pair of adjacent zirconium atoms has a similar configuration as the stable configuration 2 of Figure 3.2, but the presence of multiple Brønsted sites in close proximity gives rise to a more complex nature of the active sites. Experimentally, four different types of protons can be identified in this material [71], each yielding a different acidity.



**Figure 3.8:** Schematic representation of as synthesized and upon activation MOF-808 structures

By thermal activation, similarly to UiO-66, water can be removed from the active sites to open Lewis acid sites for catalysis. From each brick, six physisorbed water molecules can be decoordination. In a second stage, up to four of the hydroxyl groups could in principle be further decoordination by extracting a  $\mu_3\text{-OH}$  proton from the brick to form water, giving rise to mixed-coordination bricks with 6 and 7-fold coordinated zirconium atoms.

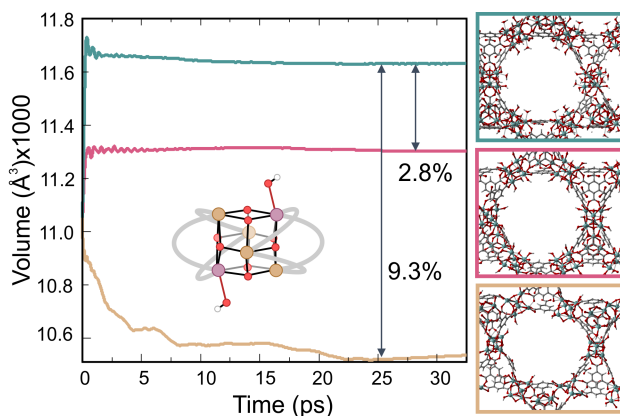
The behavior and stability of the material upon activation processes was investigated by means of a series of independent MD simulations at 300 K at variable unit cell parameters. We show that the dehydration of the inorganic brick, shown in Figure 3.8, substantially affects the stability of the structure. In the hydrated form, the material possesses a high number of Brønsted sites that show dynamic acidity in the form of proton transfer between water and hydroxyl groups that are located in close proximity. This can be seen in the O–H RDF of Figure 3.9a, and may be important for proton conductivity.



**Figure 3.9:** Radial distribution functions (full lines) and cumulative radial distribution functions (dotted lines) obtained from the three MD simulations with zirconium coordination ranging from 8 to 6, for a: oxygen and hydrogen; b: zirconium and oxygen; c: zirconium and zirconium; d: zirconium and carbon.

Upon thermal treatment, first the physisorbed water is removed leading to a homogeneous distribution of 7-fold coordinated zirconium atoms in the brick. Upon this dehydration, only a slight decrease in the unit cell volume is observed (Figure 3.10, pink curve), and the structure remains stable, even though it possesses a high amount of undercoordinated sites. The Zr–O distances decrease (Figure 3.9b), and the hydroxyl groups are oriented towards neighboring bricks which slightly distorts the pore shapes, as shown in the 3D representation of Figure 3.10. Moreover, these Lewis sites are located in proximity to Brønsted sites arising from hydroxyl groups, making dehydrated MOF-808 a dual heterogeneous catalyst.

Further removal of the hydroxyl groups together with the  $\mu_3$ -OH protons causes a collapse of the structure. The structural deformations occur mainly on the inorganic bricks as can be seen by the Zr–Zr RDF (Figure 3.9c). However, the length of the Zr–O bond is not heavily affected pointing towards the possible decomposition to  $ZrO_2$ . In this case we observe that some linkers connectivity is also affected by the bricks deformation. The BTC linkers translate along the two adjacent zirconium atoms forming a chelated structure on one out of the three connecting sides. This behavior is shown by the first peak in the Zr–C RDF (Figure



**Figure 3.10:** Change of volume in time of the three investigated structures with different zirconium coordination

3.9d) and is only observed for the fully dehydrated structure. Due to the overall low structure connectivity the adsorbed hydroxyl groups have to be considered as inherent part of the framework composition and their removal results in the collapse of the material (Figure 3.10, yellow curve).

In contrast to UiO–66, that can undergo reversible dehydration processes where the coordination of the zirconium atoms can be lowered to 6 without disrupting the structure, MOF–808 cannot sustain such decrease in coordination. The physical and chemical properties of UiO–66 cannot be easily extended to MOF–808, even though they share the same inorganic SBU. The lowest possible zirconium coordination is 7. These observations are especially significant in the context of potential applications in heterogeneous acid-base catalyzed reactions.

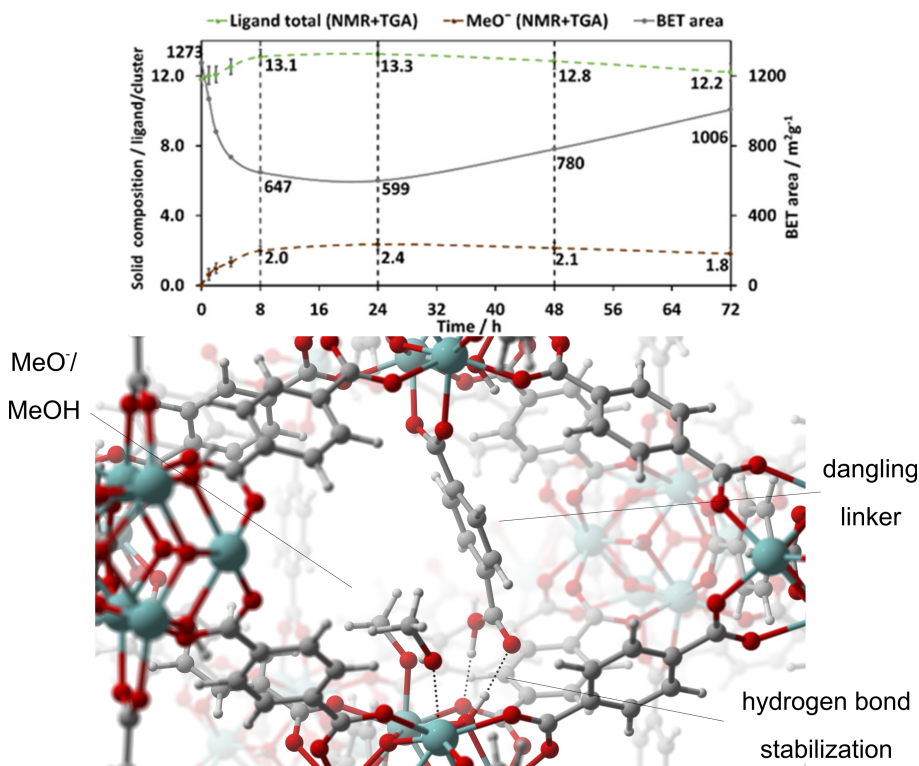
## Linker functionalization on UiO–66

Linker functionalization can play an important role in MOF catalyzed reactions and in modulating the nature of the active sites. For instance, the acidic and basic properties of the active sites can be altered by the presence of electron-donating or electron-withdrawing groups and have an effect on the energy barriers on reactions, such as in Fischer esterification. MOFs can be functionalized by PSLE procedures. On UiO–66, functionalization is particularly easy due to its intrinsic dynamic nature and its structural stability. The following results concern linker functionalization on UiO–66 and its effects on the catalytic activity of the material.

### Post synthetic linker exchange

As reported in Chapter 1, functionalization in UiO–66 can be induced by PSLE, exploiting the robustness of the framework, which can easily undergo coordination

changes. In **PAPER IV**, the mechanism of PSLE was investigated in a dual experimental–computational study performed in collaboration with the group of Prof. Rob Ameloot. The PSLE in UiO–66 that leads to functionalization of the BDC linkers with amino groups was performed in methanol at mild conditions (313 K). Results show that the initial amount of missing linkers did not have an effect on the final composition of the material, pointing towards low energy barriers for the exchange. Moreover, the process was accompanied by an initial lowering of the BET surface area, shown in Figure 3.11, that could be explained with a hindering of the pores by additional adsorbed species.

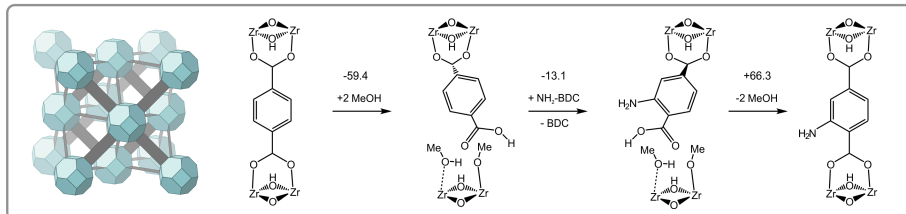


**Figure 3.11:** Porosity evolution during PSE of UiO–66 Top:  $\text{MeO}^-$  content in the MOF material during PSE (dashed brown) as determined by NMR and TGA. The total number of ligands per cluster is shown in dashed green. The evolution of BET areas measured for samples collected at selected instances is shown in gray. Bottom: Representation of an energy-optimized UiO–66 structure with both dangling linkers and  $\text{MeO}^-/\text{MeOH}$  pairs. Adapted from ref. [89] with permission of the American Chemical Society.

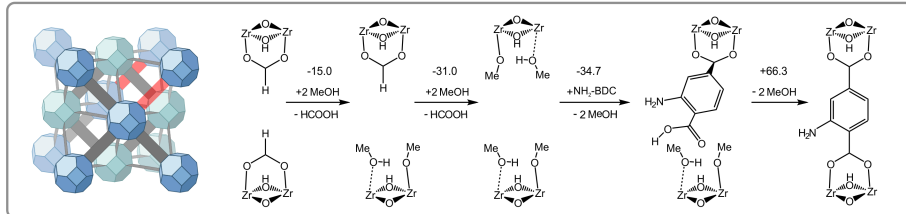
In light of these experimental observations and the computational findings reported in Figure 3.6, a hypothetical exchange mechanism was modeled starting from both pristine and defective material (Figure 3.12). In the proposed mech-

anism, linker exchange is initiated by coordination of methanol on the zirconium sites, causing a partial hydrolysis of one of the BDC linkers. This metastable state is characterized by a dangling linker which is stabilized by hydrogen bonds with other carboxylic oxygen atoms and the  $\mu_3\text{-OH}$  hydrogen from the brick, in a similar fashion as what observed in **PAPER III**. This structure causes a hindrance of the pore in agreement with the reduction in BET surface area, shown in Figure 3.11. From this configuration, exchange of mono-coordinated BDC linkers with  $\text{NH}_2\text{-BDC}$  quickly ensues, with partial coordination of the new linker. In a following step, methanol is desorbed from the active site. We postulate that after this step the linker can connect to the zirconium atoms, reestablishing the binding between the two bricks. This preferential adsorption of  $\text{BDC-NH}_2$  is explained by the lowering of the enthalpy of about 7 kJ/mol per linker.

#### Non-defective material:



#### Defective material:



**Figure 3.12:** Proposed PSE mechanism in non-defective and defective  $\text{UiO}-66$ . MeOH facilitates ligand exchange through the creation and stabilization of defects. Enthalpy differences are given in kJ/mol at 313 K (PSE temperature). Adapted from ref. [89] with permission of the American Chemical Society.

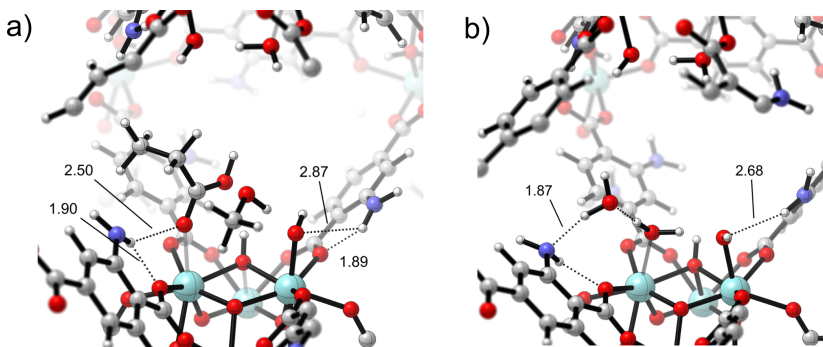
When starting from a defective material (Figure 3.12), a similar mechanism can be proposed. In this second scenario, the synthesized material contains formate on both defective sides. Formate will be substituted by methanol present in solution, and the defect healing can proceed in a similar way as in the previous case. All these rearrangements proceed rather fast, as the final experimental composition of the material does not depend on the initial percentage of functionalized or missing linkers. During the process, the zirconium atoms rapidly change their coordination number, however, giving preference to 8-fold coordinated active sites that enhance the stability of the structure.

In conclusion, we showed how molecular modeling can support experimental findings to give insight into the PSE process on UiO-66. The active role of MeOH solvent was revealed, in the creation and stabilization of dangling linker configurations. A fast exchange of these dangling linkers was also observed. We showed that the initial number of defects in the material does not have an effect on the final composition. This points towards low activation energies for the rearrangements of linkers in the material and to a dynamic behavior of UiO-66. These static results were the onset for further work on the coordination changes of the zirconium atoms, which will be further explored later in this thesis.

### Effect of linker functionalization on Fischer esterification in UiO-66

In order to understand the effect of the functionalization of the BDC linkers on the catalytic activity of defective UiO-66, the esterification reaction (Figure 3.4) was investigated also on the amino functionalized UiO-66-NH<sub>2</sub>, as it showed higher catalytic activity. Amino functionalization on UiO-66 brings an electron donating group that would in principle lower the strength of the Lewis acid site. However, experimental insights into the Fischer esterification reaction showed that the amino functionalized UiO-66 was more catalytically active than its non-functionalized counterpart. For this reason, it was speculated that amino groups located in proximity to the defect sites would play an active role during the reaction. Our computational results showed that pathways that actively involve the amino groups are highly activated. We therefore studied the reaction following the same pathway that we propose for the hydrated brick (Figure 3.4) in the non-functionalized material.

The decrease in Lewis acidity upon amino functionalization is indeed confirmed by the increase of the Zr–O distances of the adsorbates [65]. However, for UiO-66-NH<sub>2</sub>, stronger stabilization of the adsorbates is observed, as well as a slight decrease in the overall energy barrier of about 11 kJ/mol, which confirms the experimental findings [79, 80]. The amino groups, although not playing an active role in the reaction mechanism, indirectly modulate the properties of the Lewis and Brønsted sites. A stronger adsorption of the reactants is caused by the formation of a network of hydrogen bonds with the amino groups that cannot be observed in the pristine material. Amino groups provide additional sites where solvent can form hydrogen bonds, as displayed in Figure 3.13. This indirect positive effect of amino groups on the catalytic properties was also observed by Hajek et al. for aldol condensation [28]. The effect of other functional groups was further analyzed (see Supplementary Material of **PAPER I**). Electron-withdrawing substituents such as –NO<sub>2</sub> did not decrease the energy barriers, although increasing the Lewis acidity of the metal. Once again, this confirms the dual Lewis/Brønsted character of the UiO-66 catalyst, that can be enhanced by the presence of additional sites within molecular distance.



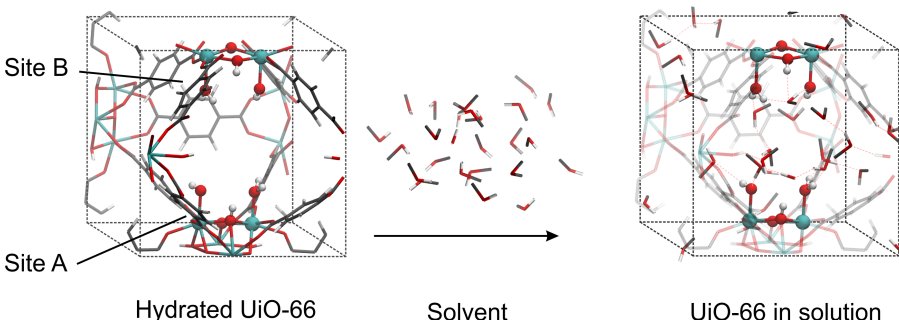
**Figure 3.13:** Network of hydrogen bonds between acid, methanol, hydroxyl group and amino groups. a) reactive complex 8, b) an additional water molecule present in solution. Key O–H and N–H distances are indicated in Å. Adapted from ref. [86] with permission of Elsevier.

### 3.2 Role of solvent: towards operating conditions

So far, a simple model to represent the active sites was used, where only the species immediately coordinated to the zirconium atoms were considered. Moreover most conclusions taken so far, were based on static calculations, relying on a discrete number of points on the PES, as shown in Chapter 2. When considering a more realistic reaction environment, solvent may be present in the pores of the material, which has an intrinsic dynamic nature and structure. In robust heterogeneous catalysts such as zeolites, processes take place at high temperatures and reactants are often in gas phase. However, in MOFs reaction conditions are usually milder, and liquid solvent is present. Moreover, coordination bonds are more labile and can be broken by interactions with the solvent, so it is important to consider all these possible interactions. A first level of complexity could be to take into account the solvent using microsolvation, adding a small amount of solvent molecules. However, the findings of the previous section point towards a complex nature of the active sites in the material, where solvent may play an active role in reactive processes and structural modifications. For instance, water was shown to have a beneficial effect on the catalytic performance of Fischer esterification by providing additional Brønsted sites as well as stabilization of intermediates through hydrogen bonding. Moreover, methanol solvent played an active role in solvent assisted PSLE, by allowing to exchange linkers and introduce or repair defective sites in the material in a dynamic way. Moreover, UiO–66 can be partially hydrolyzed [73] while retaining its stability.

Based on this knowledge, in **PAPER II** and **PAPER V** we went beyond the static approach and simple microsolvation approach by including an explicit treatment of the solvent in the pores of the UiO–66 material, as schematically indicated in Figure 3.14. This increase in complexity of the model allows to

take into account the processes that can occur at operating conditions, and to represent the full solvent environment within the pores at realistic temperatures and pressures. The following results are work performed in a theoretical collaboration with the group of Evert Jan Meijer (Van 't Hoff Institute for Molecular Sciences, Universiteit Van Amsterdam).



**Figure 3.14:** Schematic representation of solvent being inserted in the UiO-66 unit cell.  
Adapted from ref. [164] with permission of Wiley.

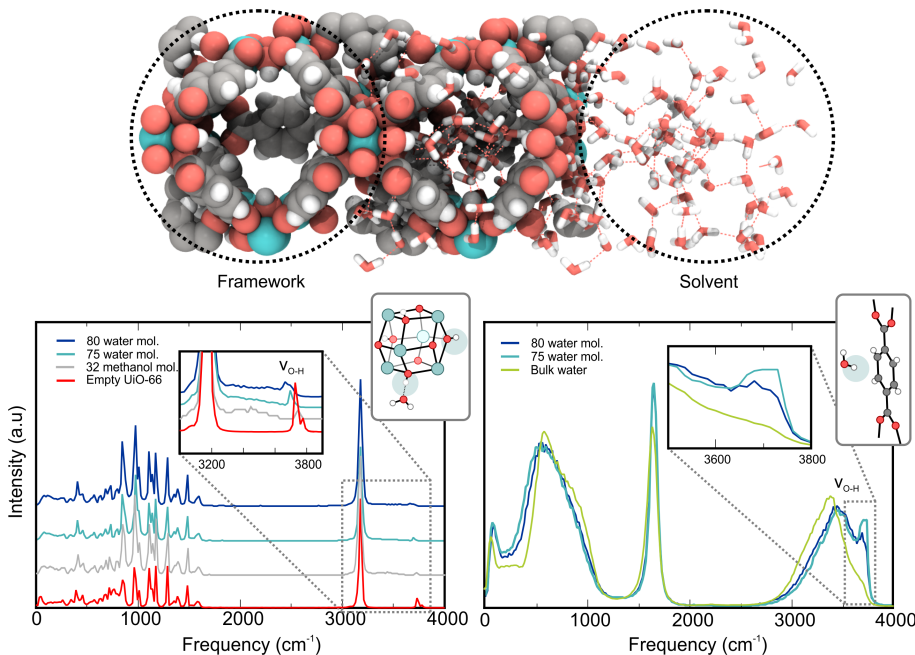
### Interaction between UiO-66 and confined solvent

The behavior of a liquid in a confined space, such as in the pores of the UiO-66 material, is substantially different from the bulk. Moreover, UiO-66 possesses both hydrophobic and hydrophilic regions, linkers and bricks, that can interact with a protic solvent in different ways. Molecular simulations allow to investigate how the material responds at the molecular level to the presence of solvent and how the solvent behaves when it is confined in the pores.

To understand how a protic solvent such as water and methanol interacts within the UiO-66 material, in **PAPER II** and **PAPER V**, solvent was inserted in the pores. GCMC simulations were used (see Chapter 2) to estimate the maximum uptake of solvent molecules in the defective hydrated UiO-66 unit cell and the starting molecular configurations. On the defective UiO-66 unit cell, a series of independent *ab initio* MD simulations were performed in which a full loading of methanol and two different loadings of water are included in the pores. In order to have a comparison, the empty material and the bulk solvent were also simulated.

Molecular simulations can offer precious structural insight into the interactions between solvent and material. In particular, vibrational density of states and radial distribution functions can provide information on the hydrogen bond structure and on the structural stability of the material (see Chapter 2). Moreover, unlike in experiments, such analysis from theoretical data can be performed for only part of the system under study, allowing to isolate specific interactions. In this case,

for the sake of the analysis of these properties, the system can be divided in two components: material and solvent. We were interested in comparing the properties of the solvated material with the empty one, and the properties of the confined solvent with the bulk solvent. Figure 3.15 displays the vibrational density of states obtained from the power spectrum of the velocity autocorrelation function for the atoms of material and solvent.

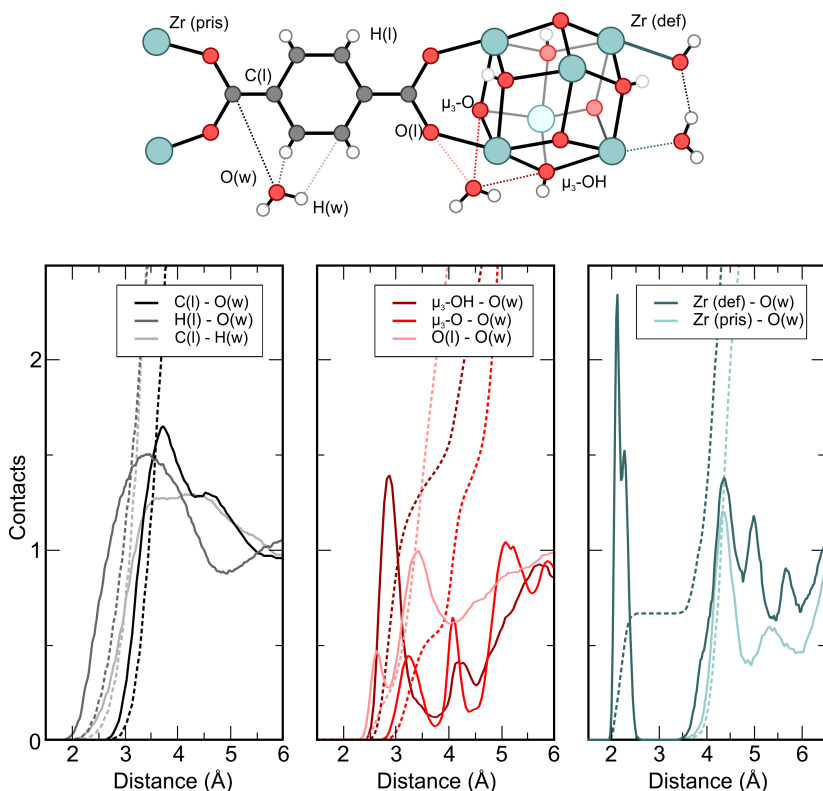


**Figure 3.15:** Top: schematic representation of the empty pore, pore with the solvent, and confined solvent without the material. Bottom: vibrational density of states obtained from the velocity autocorrelation function power spectra of selected atoms of the simulation. Bottom left: solvated material compared to the empty material. Bottom right: water in the pores compared to bulk water.

The spectrum of the UIO-66 atoms under  $3000 \text{ cm}^{-1}$  shows no shifts in the peaks between empty and solvated pores, giving insight on the stability of the framework in protic solvents. For the OH stretching at  $3750 \text{ cm}^{-1}$ , however, there is a broadening when solvent is included. This is due to the strong interactions between  $\mu_3$ -OH hydrogens of the bricks and oxygens of solvent, that form hydrogen bonds. To further investigate this, we analysed the vibrational density of states for the solvent and compared it to the bulk solvent simulated in the same unit cell and at the same conditions. We can notice the appearance of a peak at  $\nu > 3700 \text{ cm}^{-1}$  in the confined solvent, which is due to O-H bonds that do not form

hydrogen bonds. This peak is due to the water molecules whose hydrogen atoms are pointed towards the linkers and do not interact with them, in line with previous reports on hydrophobic confinement [165–167].

These results point towards a dual hydrophobic–hydrophilic interaction between solvent and material, where on the one hand, the solvent experiences a hydrophobic confinement due to the interaction with the linkers, on the other it binds strongly to the  $\mu_3$ -OH hydrogens of the bricks. To further gain insight into this behavior, we analyzed the RDFs for specific pairs of atoms of material and solvent. The results in case of water are displayed in Figure 3.16.



**Figure 3.16:** Radial distribution functions or pair correlation functions  $g(r)$  between oxygen and hydrogen of water ( $O(w)$ ,  $H(w)$ ), and different atoms of the material obtained from the simulation with 80 water molecules in the unit cell. Full lines indicate the  $g(r)$ , dashed lines indicate its integral. Left panel: RDFs between water and linker carbons and hydrogens ( $C(I)$ ,  $H(I)$ ); middle panel: RDFs between water and oxygen atoms of the linkers and bricks ( $O(I)$ ,  $\mu_3$ -OH,  $\mu_3$ -O); right panel: RDFs between water and zirconium atoms of defective and pristine bricks ( $Zr(def)$ ,  $Zr(pris)$ ).

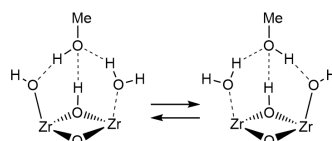
The RDF between carbon atoms of the linkers and water clearly shows a hydrophobic confinement behavior, being nearly zero at distances below 3 Å. On the other hand, a strong interaction is observed between water and oxygen atoms belonging to bricks and linkers, showing formation of a network of hydrogen bonds. The coordination between zirconium atoms and water is also analyzed. In the defective brick, the first peak is due to the coordination between water and zirconium on the defect site.

From this data, we can conclude that solvent does not leave the active site during the simulation time, as the interaction is rather strong, in agreement with the previous static calculations and dynamic results on small models. These simulations give indication of the changes in behavior of the solvent upon confinement and the strong interactions around the bricks and in particular on the active site. The dynamic behavior of the solvent around the active sites will be examined from a mechanistic point of view in the next two sections.

### Local structure of the solvent on the defective sites

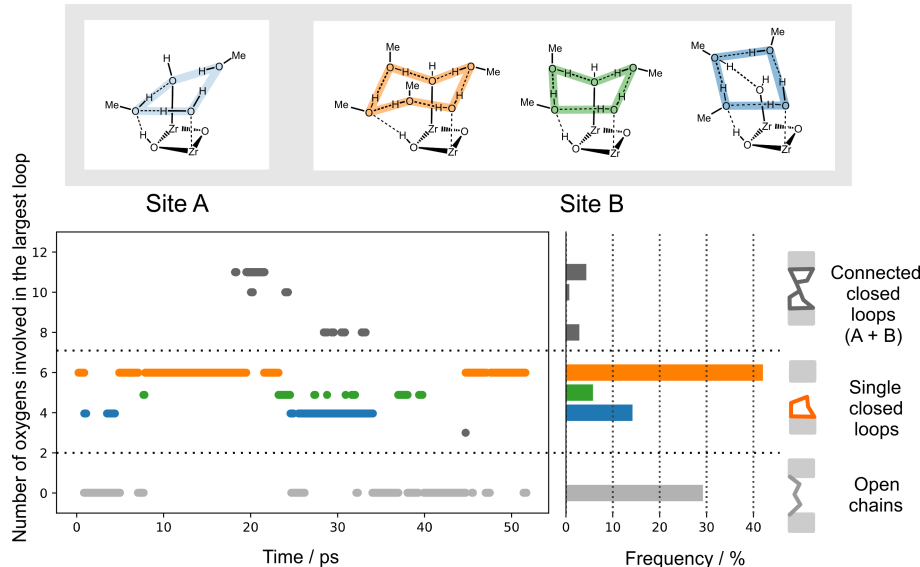
The local interactions between solvent and defect sites play an important role in reactive processes. It is particularly important to assess the topology of such interactions and what type of phenomena can occur around the active sites at operating conditions. For instance, it is known that protons in defective UiO–66 show a dynamic acidity [68], that is reflected on the high proton conductivity measured experimentally measured in the defective material [70].

In PAPER II, we used a multilevel modeling approach to analyze the local behaviour of methanol solvent around the active sites from a mechanistic point of view. We observe a breakage of the symmetry for the two active sites generated by linker removal. In an arbitrary way, we indicated the two different sites as site A and site B. The site denoted as Site A shows a trigonal network, similar to what reported in static calculations where three molecules were taken into account. This configuration is not broken during the simulation, giving evidence of its stability. Moreover, proton transfers in a similar fashion to what was reported by Ling and Slater [68] are observed between hydroxyl group and physisorbed water, with the bridging methanol molecule shuttling the proton from one site to the other (Figure 3.17).



**Figure 3.17:** Dynamic Brønsted acidity in one of the structures established on the active site in defective UiO–66 and liquid methanol in the pores.

No proton transfers are observed from the  $\mu_3\text{-OH}$  proton to the hydrogen-bonded methanol molecule, as this configuration is higher activated. Site B, however, shows a more complex evolution, with chains of hydrogen bonds connecting up to 5–6 methanol molecules and forming closed loops. This evolution is reported in Figure 3.18, where the number of molecules involved in these loops is followed during the simulation time. The system alternates between 4 to 6-membered rings that are anchored on the defect-coordinating water species and the  $\mu_3\text{-OH}$  group.

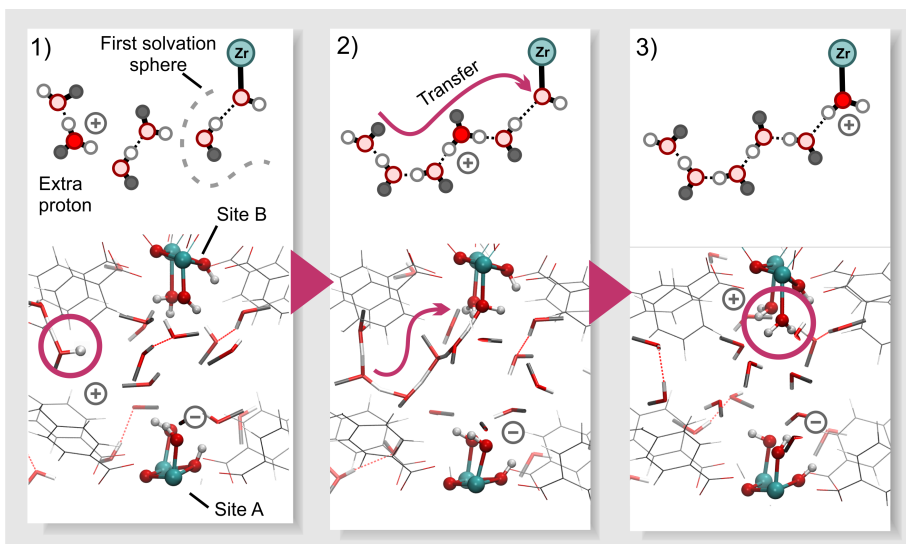


**Figure 3.18:** Top: Ring configurations observed at site A and site B originating from the interaction between the Zr-bonded hydroxo and water and the solvent molecules. Bottom: Appearance of the various structures during the simulation. The frequency of occurrence of the different structures is also reported. A threshold of  $2.2 \text{ \AA}$  for the donor-acceptor distance was chosen to determine a hydrogen bond and observations were smoothed over 0.5 ps. Adapted from ref. [164] with permission of Wiley.

The behaviour is similar to what observed for bulk methanol [168–170], in which a mixture of chain and ring structures formed by six to eight methanol molecules was observed. In this case, the chains are shorter because of confinement, nevertheless, the pore size of defective UiO-66 allows these structures to form. Moreover, open chains of methanol molecules are observed that for part of the simulation connect the two active sites and can in principle provide a way to transfer protons from one site to the other. However, during the simulation time this event is not observed due to the barrier associated to the charge separation.

Processes involving proton transfers may also be important for reactions. Ex-

perimental reports show that the network of hydrogen bonds is responsible for a high proton conductivity observed at high temperatures [62]. Moreover, defective sites increase pore size and provide sites where water species are adsorbed and can function as proton donors [70]. To understand how proton transfers occur from a mechanistic point of view, proton mobility in the pores of the material was further analyzed. A charge displacement was induced by artificially removing a proton from the active site and inserting it in different positions in the pore of the material (Figure 3.19) and the system response was followed. In the methanol solvent, the proton can be either stabilized by solvent molecules and maintain its position in the unit cell, or a Grotthuss charge transfer mechanism can occur in which the charge defect travels through a chain of hydrogen bonds, similarly as what observed by Morrone et al. [170]. In one of the simulations, the proton is transported towards the other active site (Figure 3.19).



**Figure 3.19:** Three snapshots of the molecular dynamics simulation which starts from a deprotonated site A and a protonated methanol molecule, with corresponding schematic representation of the process (above). 1) starting structure with protonated solvent 2) a snake-like chain of hydrogen bonds is formed which leads a proton to site B 3) site B is protonated, while site A is missing a proton. Adapted from ref. [164] with permission of Wiley.

A configuration is obtained where the original site remains deprotonated and the other is protonated. This configuration is retained for the whole remaining simulation time and is stabilized by the presence of solvent molecules. The zirconium–oxygen distance in the protonated case increases, and the two water molecules physisorbed on the site are more mobile and prone to leave the active site, and a proton transfer could be the initiator to reactant exchanges on the active site.

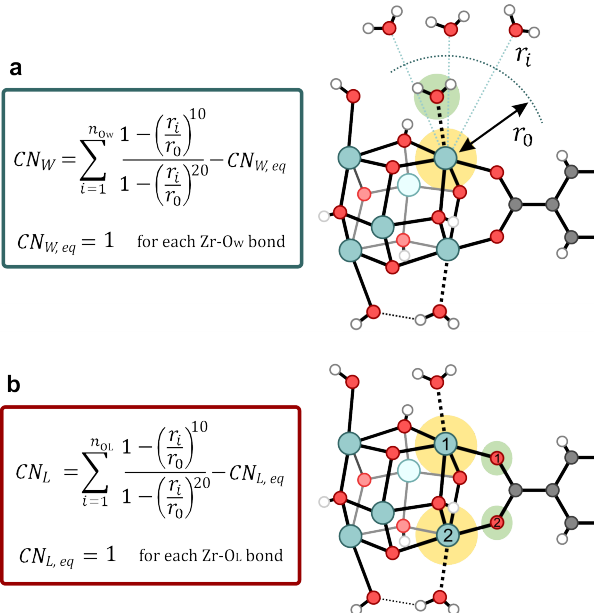
Static periodic calculations were performed to investigate the energy difference related to this charge separation which report a value of 89.4 kJ/mol difference in free energy. Such difference between static and dynamic picture gives indication of the positive role of a protic solvent in stabilizing charged configurations that can be reflected in the stabilization of charged intermediates during catalytic processes. These simulations shed light on the role of Brønsted sites in the material. The  $\mu_3\text{--OH}$  group is heavily involved in the stabilization of supramolecular structures around the active site, but does not deprotonate to the solvent, contrary to water and hydroxyl groups that show dynamic acidic behavior. These findings show the importance of a solvent beyond being a substrate in the reaction, as it can exchange protons, affect reaction mechanisms, and stabilize intermediates through its remarkable interactions with the active sites. In the next section we will see how solvent can be exchanged on the active sites and induce structural rearrangements in the material.

### Activated processes related to dynamic changes in the zirconium coordination number

The interaction between solvent and zirconium atoms on the defective sites investigated in the previous sections is strong, and during regular MD simulations, the coordination is never broken. Previous simulations do not show any change in the zirconium coordination, as such processes are rare events characterized by an activation barrier that does not allow their sampling at normal conditions. However, Zr–O bond breaking is a fundamental event in many processes, such as in the exchange of solvent around the active sites, dehydration, defect formation or PSLE. For this reason, in **PAPER V**, we further focused on the dynamic changes in coordination of the zirconium atoms on the defective sites. We made use of enhanced sampling by means of a series of independent MTD simulations to investigate the coordination changes around the defective zirconium atoms in water solvent.

We particularly focus on the changes in coordination of zirconium with the adsorbed water molecules and with the linkers. Undercoordinated and overcoordinated zirconium states can be observed when a solvent is present. Undercoordination is crucial for catalysis, as the Lewis acid site needs to be open for the reactants to adsorb. Overcoordination, on the other hand, can be the trigger for a decoordination of the linker which is a key step in PSE.

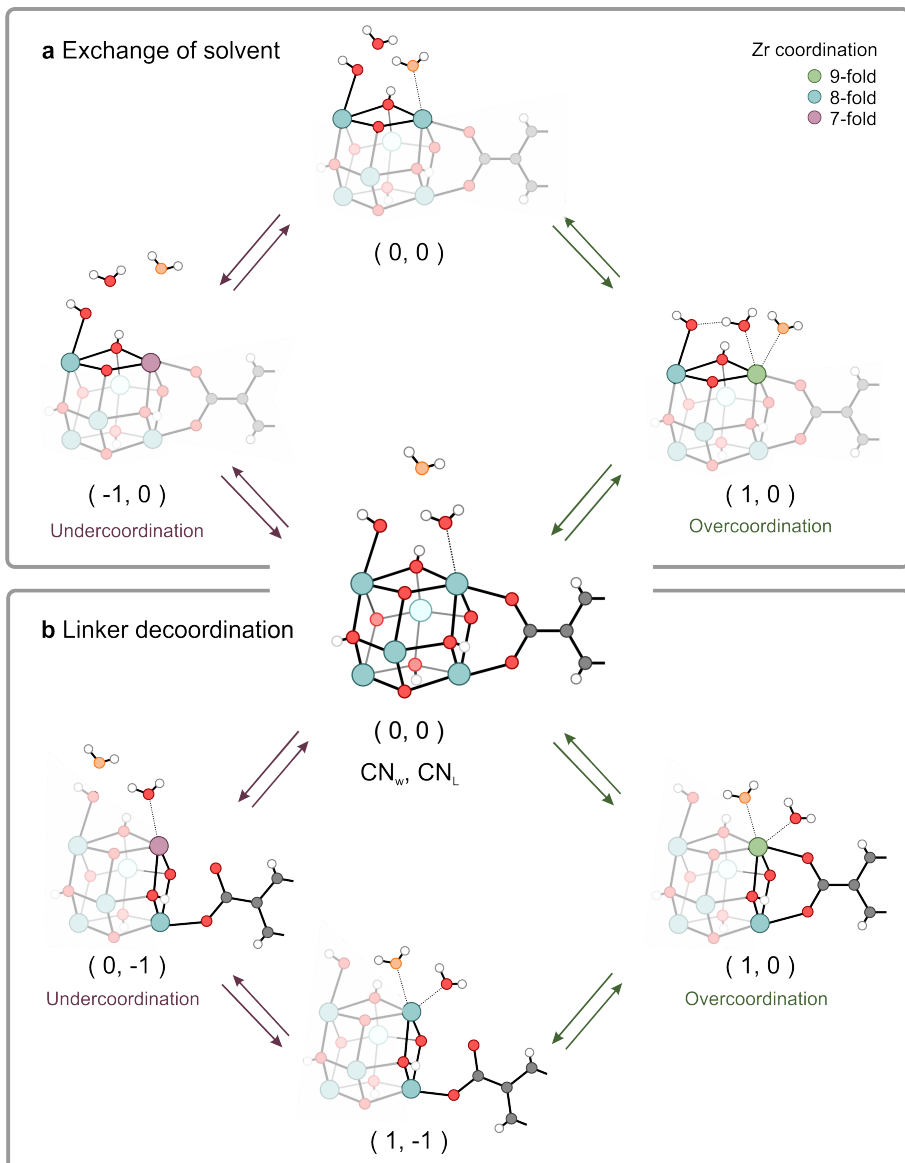
To describe these two possible phenomena, two CVs were chosen, as displayed in Figure 3.20: a first one, denoted as  $\text{CN}_W$ , representing the coordination between zirconium and oxygen atoms of water, and a second one, denoted as  $\text{CN}_L$ , describing the coordination between zirconium and oxygen atoms of a defect–bridging linker.



**Figure 3.20:** Coordination numbers used in the simulation a: coordination number  $CN_W$  between zirconium and all water oxygens. Also the linker that shows dynamic movement which induces changes in the zirconium coordination number is visualized. b: coordination number  $CN_L$  between each zirconium atom and linker oxygen atoms.  $n_{OW}$  and  $n_{OL}$  are the number of oxygen atoms considered in the two cases,  $r_i$  is the zirconium-oxygen distance,  $r_0$  a cutoff distance of 2.9 Å. In yellow, the zirconium atoms considered in the CN. In green, the oxygen atoms that have a weight close to one and substantially different from zero in the summation.

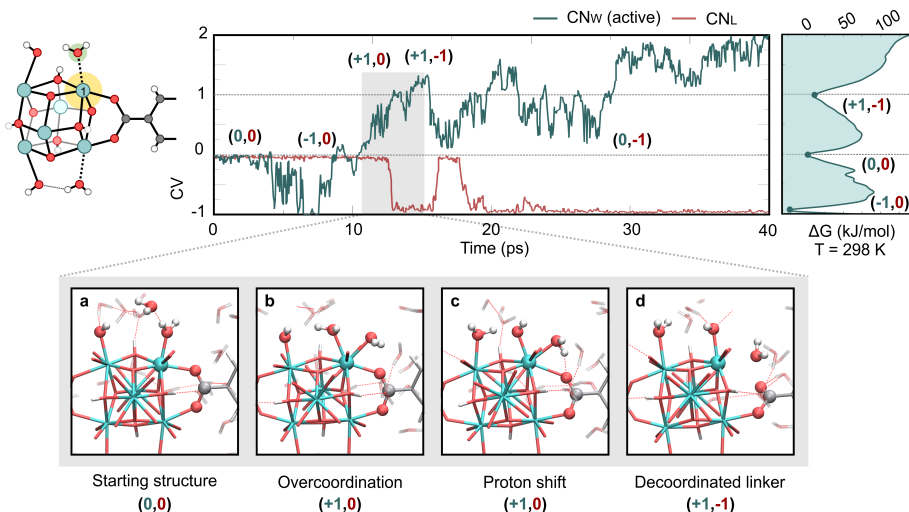
Both CVs refer to the difference between the coordination state and its equilibrium state. Therefore, starting from an equilibrium value of zero, when a bond is broken, the coordination will decrease by one, describing the undercoordinated case, or increase by one if an additional bond is formed, describing overcoordination. Using these two coordination numbers, it is possible to describe many events taking place around the brick, which are schematically reported in Figure 3.21.

In the equilibrated structure, the state defined by the two CNs is (0,0), where the numbers refer to the values of  $CN_W$  and  $CN_L$ , respectively. Undercoordination and creation of open Lewis acid sites can occur by desorption of water or by breakage of Zr-linker bond to give a zirconium coordination number of 7. Overcoordination is observed when an additional water molecules coordinates to the zirconium atom increasing its coordination number to a value of 9.



**Figure 3.21:** Coordination and value of the CV during (a) the exchange of solvent and (b) linker decoordination in the MTD simulations. top paths: stepwise pathway which goes through undercoordinated zirconium; bottom paths: concerted pathways which go through overcoordinated zirconium.

In a first case study, the coordination  $CN_W$  between one of the defective zirconium atom and the water oxygens was biased. At the same time the  $CN_L$  between the same zirconium atom and the oxygen belonging to the defect bridging linker is monitored, as displayed in Figure 3.22.

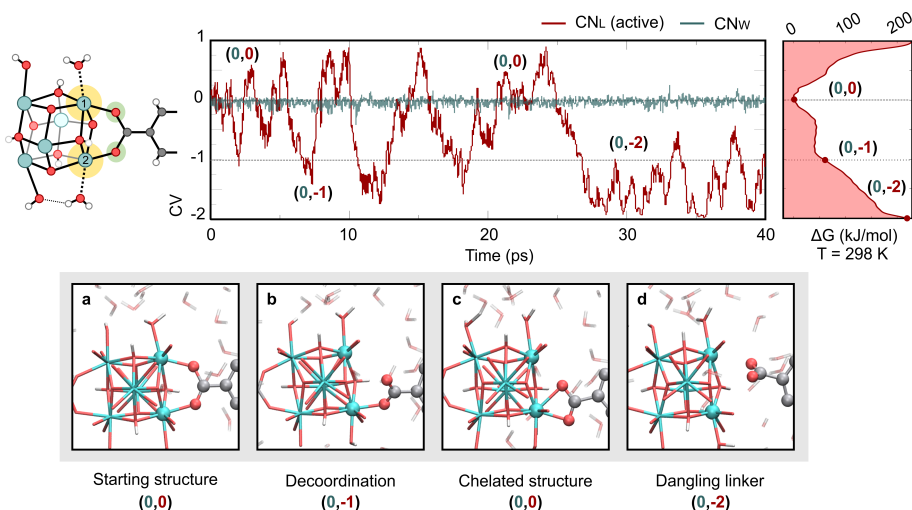


**Figure 3.22:** Top: evolution of the collective variable  $CN_W$  and free energy profile for the first MTD simulation along the CV representing the coordination between the zirconium atom Zr1, highlighted in yellow, and all water molecules (green curve).  $CN_L$  between Zr1 and the neighbouring defect-bridging linker oxygen (red curve) is also monitored; bottom: snapshots on the linker decoordination triggered by overcoordination

In this simulation, fluctuations of the coordination towards negative values are observed, where the open Lewis acid site is created. Via this undercoordinated pathway, solvent molecules can be exchanged on the active site in a stepwise fashion. After this process has been sampled, the system evolves towards an overcoordination of the zirconium atom, to which an additional water molecule is coordinated. From this metastable configuration, the system evolves with structural rearrangements which are reported in the bottom of Figure 3.22. After the second water molecule has entered the coordination sphere of zirconium, it transfers a proton to the neighboring hydroxyl group and pushes the parent water molecule closer to the linker. The water molecule forms a hydrogen bond interaction with the linker which is in turn decoordinated from the zirconium atom, restoring the equilibrium coordination of 8 in the zirconium atom. After these events, the linker recoordinates to the zirconium, to decoordinate again few ps later. In the simulation, we observe a plethora of events such as undercoordination and overcoordination of zirconium, proton transfers, exchange of solvent molecules, and reversible linker decoordination. These fluctuations show how the role of

solvent is crucial in inducing such coordination changes and in stabilizing partially decoordinated linkers that can lead to structural rearrangements, while maintaining the stability of the material.

In a second case study, we biased the coordination  $CN_L$  between one linker and two defective zirconium atoms, and at the same time monitored the coordination  $CN_W$  between the latter atoms and solvent water. In this case, we are directly biasing the coordination between zirconium and the linker. The evolution of the collective variable is displayed in Figure 3.23, as well as snapshots that offer mechanistic insights on the different processes.



**Figure 3.23:** Top: free energy profile for the first MTD simulation along the CV representing the coordination between two zirconium atoms and a linker, middle: evolution of the collective variable, bottom: snapshots of the linker decoordination

During the simulation, different states are explored, in which the linker is partially deordinated, can translate to give chelated structures, similarly to what observed in **PAPER III**, or be in a dangling state where both Zr–O bonds are broken, giving an indication of what was postulated in **PAPER IV**. In this case, the linker is deordinated without intermediate role of solvent, and represents an alternate mechanism by which PSLE, defect creation, or even hydrolysis of the material could occur. This dangling linker scenario is stabilized by hydrogen bonding interactions with the solvent. The process would be completed if two water molecules would diffuse to the zirconium atom and restore the 8-fold coordination, while at the same time one of the two deprotonates to the linker. However this is not observed during the simulation time, as water does not have the time to diffuse, while hindered by the motions of the linker.

By means of this series of simulations, we conclude that both solvent exchange around the active sites and structural rearrangements can either occur via a step-wise mechanism where zirconium atoms are undercoordinated or a concerted one, mediated by an overcoordination. The mobility of the linkers observed in **PAPER III** is herein observed without rearrangements of the bricks that are induced at dehydration conditions. In the presence of a solvent, such processes can undergo at much milder conditions, without disrupting the stability of the material. The role of solvent in allowing these processes is crucial, as it provides hydrogen bonds that can stabilize charged configurations, and can itself strongly interact with the zirconium atoms.

# 4

## Conclusions and Perspectives

In this thesis, we shed light on the molecular characterization of the active sites in MOFs by means of different computational techniques. We focused in particular on zirconium based MOFs as they have been used extensively for catalysis. Molecular modeling can offer a rich toolbox to understand the properties of materials and how these properties can be tuned to target specific applications. This is especially true in MOF catalysis, where the active sites are often complex and arise from disorder in the material that cannot be easily tracked experimentally. We especially focus on the UiO–66 material, which is an example of an extremely stable MOF that due to its exceptional connectivity can be easily tuned and undergo modifications without losing its crystallinity. In close collaboration with experimental partners, we gained insights into the nature of active sites and the interaction of solvents with the inorganic brick, and on the role of complex events that can be observed when modeling processes at operating conditions. To unravel these processes, it was shown that a complementary modeling approach is mandatory. Within this approach, initial understanding of the local structure of the active sites is obtained from static calculations, and subsequently more advanced techniques are employed to investigate realistic reaction environments. First principles MD simulations in presence of a realistic loading of solvent have been used, as well as enhanced sampling techniques that allow to study events that take place at activated conditions.

The high thermal, mechanical and chemical stability of UiO–66 allows the

material to undergo different activation processes. In this thesis, we focused on the decrease in the zirconium coordination caused by missing linker defects and dehydration. Changes in the zirconium coordination number are necessary to induce catalytic activity of the material.

At the start of this doctoral research work, we investigated the Fischer esterification in close synergy with the experimental group of Francesc Llabrés i Xamena of ITQ (**PAPER I**). This Lewis catalyzed reaction was modeled on UiO–66, initially focusing on the role of the hydration state of the defective sites of the material. We used a series of static calculations, first on small cluster models, then taking into account the periodic MOF structure, with thermal corrections. We show that in the most stable configuration, water is coordinated to the defective zirconium atoms, in line with previous reports. In the proposed reaction mechanism, the chemisorbed water acts as a Brønsted base site that actively takes part in the reaction, along with the zirconium Lewis acid site. It was an eye opener to discover that the catalytic centers are not restricted to Lewis sites in this material. An alternative mechanism was investigated on the dehydrated material, where the reaction proceeds without the assistance of water. We show that in this case, the inorganic brick is actively involved in the reaction, in which zirconium plays a role as Lewis acid site, while  $\mu_3\text{-O}$  acts as Brønsted base. However, the beneficial role of water is missing, and the catalytic activity is remarkably decreased due to higher energy barriers, in agreement with the experimental findings. In both proposed mechanisms, UiO–66 acts as dual Lewis/Brønsted catalyst where reactions proceed with a remarkable interplay between the two catalytic centers. The acidic/basic character of protons and oxygens on the brick seems to have a major role, and could be further investigated by pKa calculations. Experimentally by potentiometric titration it was shown that in the defective material three types of protons are present, each possessing different acidity. Proton transfers are a fundamental step in many reactions, and the acidity of Brønsted sites can alter both reaction mechanism and yield. Further theoretical studies could allow to understand the dependency of acidity of various protons of zirconium materials on different conditions and their reactivity.

A remarkable property of UiO–66 is that it can be reversibly dehydrated upon thermal treatment. Dehydration also lowers the coordination number of zirconium up to 6, therefore introducing Lewis functionalities. In **PAPER III**, we followed on the fly the behavior of the material during the activation process of dehydration. We discovered that UiO–66 possesses an intrinsic dynamic nature by means of an exceptional linker mobility. We showed that linkers can decoordinate and recoordinate to the brick without disrupting the stability of the material.

Apart from UiO–66, a series of other zirconium based materials have been synthesized with larger pore sizes and a varying degree of zirconium coordination number. These materials are fully tested and exploited for applications, however

it remains an open question in how far concepts found in the stable UiO–66 are generic for other materials. To this end, some of the information obtained on UiO–66 can in principle be extended to other zirconium–MOFs possessing the same inorganic SBU. However, the behavior of UiO–66 cannot be easily generalized, as the exceptionally high connectivity and the local environment can play a major role in the stability and activity of the material. We further investigated how MOF–808 responds to similar activation processes such as the UiO–66 dehydration. We show that the MOF–808 material possesses an exceptional amount of Brønsted sites that can be created upon hot filtration. By thermal activation, Lewis sites can be created in proximity of the Brønsted sites without disrupting the stability of the structure, offering great potential for future catalytic applications. However, we also observe that further dehydration generates a collapse of the framework and loss of crystallinity. In MOF–808 the coordination of zirconium cannot be decreased below 7 without causing a collapse of the structure.

Another process that can influence the catalytic activity of the material is the introduction of linker functionalization, that can be done by PSE procedures. In **PAPER IV**, we studied the PSE mechanism by means of static periodic calculations at various defect composition and concentration. The work was performed in strong collaboration with the group of Rob Ameloot from KU Leuven. Experimental findings showed the active role of methanol during the process, which can be performed at mild conditions. From the computational and experimental insight, we postulate the presence of dangling linkers as intermediate states during the exchange, that are induced and stabilized by interaction with methanol. These structural rearrangements in the material lead to the replacement of BDC with BDC–NH<sub>2</sub>. Moreover, the modified material is characterized by a specific concentration of defects that does not depend on the initial number of missing linkers or nodes. This gives insight on the low energy barriers associated to the process and on the role of methanol in facilitating the exchange.

Experimentally, the presence of amino functionalized linkers that can be introduced by PSE was shown to have a beneficial role in the catalytic performance of the material for different Lewis catalyzed reactions. However, the cause of this improvement was not well understood. For this reason, in **PAPER I** we further focused on the role of BDC–NH<sub>2</sub> functionalization on the catalysis of Fischer esterification. The electron-donating amino groups are shown to decrease the Lewis acidity of the metal centers, therefore should in principle lower the activity. However, we found that amino groups play a positive role in the reaction although not actively taking part in the mechanism. Stronger adsorptions of reactants and lower energy barriers are observed for the functionalized UiO–66 compared to the pristine material. Investigation of the reactants geometries and experimental results pointed towards an increase on water adsorption around the active site due to a stronger network of hydrogen bonds supported by the amino groups. This stabilization could play a positive role in facilitating specific reactant geometries

and supporting metastable intermediate configurations. Theoretical modeling of Fischer esterification performed in **PAPER I** shed light on the crucial role of water in the reaction and on the complex nature of the active sites and their interaction with protic solvents. These results already hint towards the impact of solvent species in the pores of the material on the reaction outcome.

Reactions in MOFs are often performed at mild conditions where reactants are in the liquid phase, which adds further complexity to the model. For this reason, the understanding of the role of solvent close to the active site cannot be neglected. Solvent can have an impact on the creation of active sites, be a substrate, determine the formation of particular isomers, influence the rate and selectivity, affect the reaction mechanism, or even activate/deactivate a specific reaction. Moreover, the M–L bonds in MOFs are more labile than in other heterogenous catalysts composed of covalent bonds. This makes MOFs more prone to structural rearrangements and modifications mediated by protic solvents. In order to move towards an operating description of the processes, it is crucial to understand the behavior of the solvent when confined in the pores of the material.

The role of solvent was investigated in **PAPER II** and **PAPER V**, in which a multilevel modeling approach was employed to study the behavior of defective UiO–66 in presence of a full loading of methanol and water. By means of GCMC simulations the pores of the material were filled with methanol or water solvent, to reproduce the temperature and pressure conditions during a reactive process. The confined solvent behaves differently from the bulk when confined into the pores of the material. Besides pores, UiO–66 possesses both hydrophobic and hydrophilic regions. By performing a series of MD simulations, in **PAPER V** we show that on the one hand, the linkers provide hydrophobic confinement, and on the other, solvent strongly interacts with the inorganic SBUs and in particular with the zirconium atoms on the defective sites.

We further investigated the possible interactions between solvent and active sites in the case of methanol from a mechanistic point of view (**PAPER II**). We observed a remarkable dynamic behavior of the solvent. Supramolecular structures stabilized by hydrogen bonds are formed around the active sites and evolve dynamically during the simulations. Within these active sites, a dynamic behavior of the protons is observed, as anticipated in **PAPER I**. Such proton transfers may play a substantial role in catalytic processes like Fischer esterification, or in structural rearrangements which occur during PSE. Moreover, we show how solvent can transfer protons within the pores and stabilize charged configurations in proximity of the active site. These findings point towards a positive role of protic solvents in reactions involving charged intermediates, that goes beyond simple solvation. These simulations shed light on how the active sites may be modulated via these dynamic interactions. However, regular MD simulations do not allow to track activated processes.

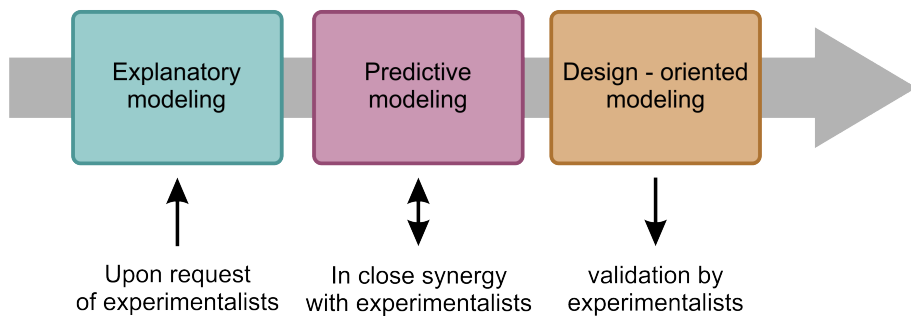
During regular MD simulations, the coordination number of zirconium atoms does not change. Nevertheless, activated processes often involve coordination changes of zirconium metal centers. In order to understand the dynamic interactions between solvent and material on these sites and explore the rare events that can take place, we relied on enhanced sampling simulations. We performed a series of independent MTD simulations where we explore the changes in the coordination of the zirconium at operating conditions. These simulations show that the total coordination number of zirconium can either decrease from 8 to 7 or increase from 8 to 9. Undercoordination is crucial for the creation of Lewis acid sites while overcoordination can trigger linker decoordination. In these two events we observe dynamic exchange of solvent around the active sites, as well as structural rearrangements which are characteristic of PSE processes. The strong interaction between solvent molecules and defective sites can lead to a dynamic behavior of the linker, similarly as what observed in **PAPER III**, but this time at milder conditions, by solvent mediation and without altering the brick. These findings shed light on the dynamic interplay between a protic solvent and the UiO–66 material at operating conditions during PSE. Moreover, one can postulate that these active sites may be dynamically opened for catalysis by temporary linker decoordination, giving a variable Lewis acidity to the metals and more opportunities for Lewis catalyzed reactions. The highly connected UiO–66 material allows all these structural rearrangements where a plethora of active sites that can work in synergy can be generated.

The findings reported in this thesis gave valuable insight into the complexity of the Zr–MOF catalysts, with UiO–66 as main case study. We investigated how the presence of disorder and the interactions with solvent lead to the creation of active sites of different nature that can work in a cooperative fashion during Lewis catalyzed reactions. There is an intriguing interplay between solvent and material, and much work is still to be done in this area of research which is in full exploration. The exceptional chemical versatility of MOFs can be exploited only if we gain enough understanding at the molecular level of their properties at operating conditions. The analysis of the relation between intrinsic properties and desired application have become an important research factor. The use of well-studied model systems such as UiO–66 is therefore crucial to connect theoretical and experimental findings and to understand the sources of errors in the models. The methods used in this thesis reveal molecular level insight into the activation of one of the most stable Metal-Organic Frameworks. They open perspectives to study and benchmark new materials, and further explore the role of active sites and disorder at operating conditions.

In the past years, computational research in MOFs has evolved from providing simple representations of model systems to more complex models that can represent the events that can occur at operating conditions. The growth in computational power will allow to access larger time and length scales, and to make models that

can represent processes at realistic conditions more accurately, especially in complex fields such as heterogeneous catalysis (Figure 4.1). As the modeling field matured, we went from a stage in which it was limited to the rationalization of experimental data to being able to work in synergy with experiments and make new predictions. The further step is the understanding of how computational modeling can help to design active sites and the screening of structural databases to target a specific property, that can then be validated by experiments. The multiple theoretical and experimental tools that have been developed so far complement each other on the investigation of complex phenomena. For this reason, the use of databases in which different computational and experimental results can be stored and accessed will be more and more important in the future of MOF research. Therefore, the publication of data cannot be limited to successful experiments, but has to be extended to failures, which also carry precious information. This way, with more data available, it will ultimately be possible to use statistical models to predict structures that match specific properties. The new theoretical predictions will be able to guide new experiments, that can in turn provide new data, and ultimately lead to materials and conditions that can target specific applications.

Molecular modeling has evolved substantially thanks to ingenious theoretical models and stronger computational power



**Figure 4.1:** Different stages of the close relationship between modeling and experiments.

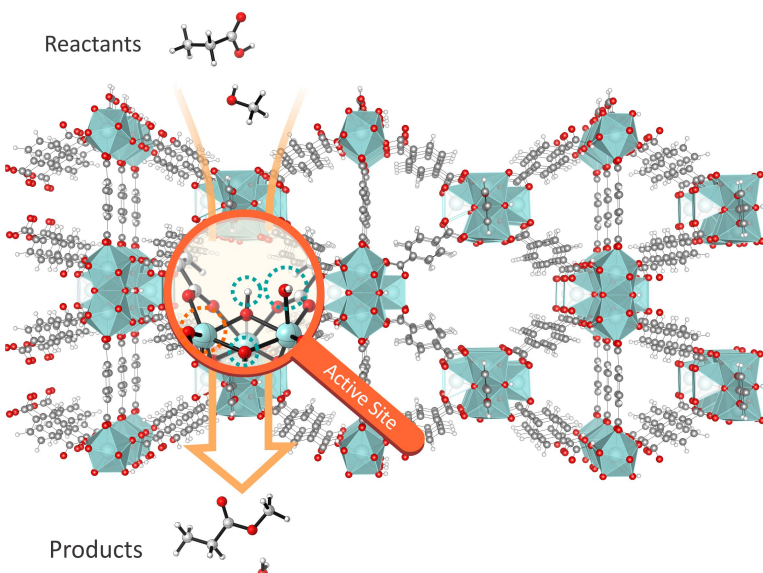
## **Part II**

# **Published papers**



## Paper I

### Nature of active sites on UiO–66 and beneficial influence of water in the catalysis of Fischer esterification



C. Caratelli, J. Hajek, F. G. Cirujano, M. Waroquier, F. X. Llabrés i Xamena, V. Van Speybroeck, *Journal of Catalysis*, **352**, 401–414 (2017)

C. Caratelli performed all the calculations and prepared the manuscript.

©2017 Elsevier Inc.

Reprinted with permission from Elsevier.





Contents lists available at ScienceDirect

# Journal of Catalysis

journal homepage: [www.elsevier.com/locate/jcat](http://www.elsevier.com/locate/jcat)



## Nature of active sites on UiO-66 and beneficial influence of water in the catalysis of Fischer esterification



Chiara Caratelli<sup>a</sup>, Julianna Hajek<sup>a</sup>, Francisco G. Cirujano<sup>b</sup>, Michel Waroquier<sup>a</sup>,  
Francesc X. Llabrés i Xamena<sup>b</sup>, Veronique Van Speybroeck<sup>a,\*</sup>

<sup>a</sup>Center for Molecular Modeling (CMM), Ghent University, Technologiepark 903, B-9052 Zwijnaarde, Belgium

<sup>b</sup>Instituto de Tecnología Química, Universidad Politécnica de Valencia, Consejo Superior de Investigaciones Científicas, Avda. de los Naranjos, s/n, 46022 Valencia, Spain

### ARTICLE INFO

#### Article history:

Received 13 February 2017  
Revised 8 June 2017  
Accepted 11 June 2017  
Available online 29 June 2017

#### Keywords:

UiO-66  
UiO-66-NH<sub>2</sub>  
Heterogeneous catalysis  
Fischer esterification  
First-principle kinetics  
DFT

### ABSTRACT

Zirconium terephthalate UiO-66 type metal organic frameworks (MOFs) are known to be highly active, stable and reusable catalysts for the esterification of carboxylic acids with alcohols. Moreover, when defects are present in the structure of these MOFs, coordinatively unsaturated Zr ions with Lewis acid properties are created, which increase the catalytic activity of the resulting defective solids. In the present work, molecular modeling techniques combined with new experimental data on various defective hydrated and dehydrated materials allow to unravel the nature and role of defective active sites in the Fischer esterification and the role of coordinated water molecules to provide additional Brønsted sites. Periodic models of UiO-66 and UiO-66-NH<sub>2</sub> catalysts have been used to unravel the reaction mechanism on hydrated and dehydrated materials. Various adsorption modes of water and methanol are investigated. The proposed mechanisms are in line with experimental observations that amino groups yield a reduction in the reaction barriers, although they have a passive role in modulating the electronic structure of the material. Water has a beneficial role on the reaction cycle by providing extra Brønsted sites and by providing stabilization for various intermediates through hydrogen bonds.

© 2017 The Authors. Published by Elsevier Inc. This is an open access article under the CC BY-NC-ND license (<http://creativecommons.org/licenses/by-nc-nd/4.0/>).

### 1. Introduction

The need of developing alternative energy sources is one of the world's highest priorities, as fossil sources are limited and their refinement and combustion contribute substantially to global warming. In this context, biofuels represent a possible solution to overcome the need of fossil fuels in sectors such as transportation [1]. Biodiesel is a kind of biofuel that is obtained from organic feedstocks rich in lipids, such as vegetable oils and animal fats. It is similar in properties to petroleum diesel and represents a good renewable candidate that can already replace it in part. Its industrial production is currently performed via transesterification of triglycerides with low molecular weight alcohols, using strong Brønsted bases as homogeneous catalysts in anhydrous conditions [1,2]. In this process, triglycerides, the main components of the feed, are converted into esters and glycerol is formed as a byproduct. This process, however, is very sensitive to the presence of Free Fatty Acids (FFA), which instead give water as a byproduct, leading to saponification and formation of emulsions in a basic environment.

To avoid this problem, the feed must be purified from these components with quite expensive treatments contributing substantially to the production cost. An alternative approach consists in performing the esterification using strong inorganic acids as catalysts. A benefit of this process is that both the transesterification of triglycerides and the esterification of free fatty acids can be catalyzed without unwanted side effects, allowing the production of biodiesel from low-cost feedstocks rich in FFA. However, these acids are highly corrosive and harmful to the environment. A way to overcome this issue consists in replacing mineral acids by solid heterogeneous acid catalysts as they could simultaneously convert both free fatty acids and triacylglycerols [3] while avoiding corrosion issues or dilution effects due to the generation of water. In addition, solid acid catalysts can be reused or applied in continuous processes, thus reducing the production cost. Besides biodiesel production, esterification is an important reaction also in the production of other derivatives of acids obtained by renewable sources, such as alkyl levulinates [1]. Therefore, the study of the esterification reaction mechanism and the development of good catalysts are of interest for a broad range of applications. So far, several suitable solid acid catalysts have been proposed, including zeolites, ion-exchange resins, and mixed metal oxides [4–6].

\* Corresponding author.

E-mail address: [veronique.vanspeybroeck@ugent.be](mailto:veronique.vanspeybroeck@ugent.be) (V. Van Speybroeck).

Few theoretical DFT studies on acid-catalyzed esterification of carboxylic compounds are available in the literature. They all describe the reaction in gas phase or with small cluster models considering different pathways. Evidence was found that the reaction proceeds through a concerted mechanism [7,8] although the literature is not always consistent in the description of the reaction mechanism [9]. The esterification of a generic carboxylic acid by methanol is schematically shown in Scheme 1.

Recently, metal organic frameworks (MOFs) have attracted a lot of interest for their catalytic properties [10–14], among the wide range of other possible applications, such as drug delivery, gas and liquid sorption. MOFs are highly tunable materials, where metal or metal-oxo clusters are connected via organic linkers to form three dimensional crystalline porous networks. Their porosity, high metal content and tunability make MOFs outstanding candidates as catalysts. In particular, a Zr-terephthalate based MOF named UiO-66 [15] shows an exceptional stability [16–18] which allows its use in a wide range of thermal and chemical conditions. The key to its stability lies in the high topological connectivity of the  $[Zr_6O_4(OH)_4]^{12+}$  secondary building unit (SBU), which is connected with strong Zr-O bonds to 12 terephthalate (BDC) linkers. It is known that defects are present in the structure when linkers, metal ions or nodes are missing from the crystalline network [18]. Their amount can be tuned [19–22] without compromising the high stability of the material [23,24]. However, the presence of defects in these materials can have a large impact on their catalytic properties.

Recently, defect engineering in UiO-66 has drawn a lot of attention from both a theoretical and experimental point of view [20,23–28]. These defects can arise from one or more missing linkers and other building units, and their nature and spatial distribution are difficult to characterize experimentally. Nevertheless, their understanding is crucial and has been the subject of several studies on UiO-66 [23,24,26–32]. Defects increase the pore size, create room at metal centers for possible reactant adsorbates, and give rise to additional sites where molecules can be adsorbed. Therefore their presence is important for applications such as gas and liquid adsorption [33,34]. In particular, it has been accepted that defects are responsible for the catalytic activity of this MOF [22,24,25], since missing linkers introduce coordinatively unsaturated Zr atoms in the solid, resulting in open Lewis acid sites. In particular, we refer to the extraordinary property of UiO-66 and variants to catalytically hydrolyze nerve agent simulants and thus to destruct chemical warfare agents [35,36]. Furthermore, linkers can also be functionalized [37,38], allowing a fine-tuning of the catalytic behavior of the material [39]. UiO-66 has been shown to be a successful acid catalyst for the Fischer esterification [40,41], with activities that are comparable and in some cases even superior to other homogeneous acid catalysts. In addition, the advantage of using a solid acid catalyst such as UiO-66 is that the material is stable under reaction conditions and that it can easily be reused without significant loss of activity. In particular, it has been shown that the activity of UiO-66 in the esterification of levulinic acid (LA) and lauric acid increases with amino functionalization, but the role of these  $NH_2$ -substituents was not yet clear [40,41]. However, recent experiments suggest an enhancing effect of the reaction due to the close position of the  $NH_2$ -group to the metal center, allowing a simultaneous activation of both LA and the alcohol. UiO-66-NH<sub>2</sub> behaves as a bifunctional acid-base catalyst as already proposed for cross-aldo condensation [42]. This feature has also been studied theoretically demonstrating the stabilizing effect of the amino-group in the condensation reaction without playing effectively an active role in the reaction [43].

The essential step to unravel the mechanism of the esterification reaction lies in understanding the nature of the active sites on defective UiO-66. It has been previously accepted that the key

to the catalytic activity of UiO-66 lies in the presence and accessibility of Lewis acid sites, but recent studies point toward a more complex scheme involving additional Brønsted sites formed by water and hydroxyl groups coordinated to the Zr atoms [24,25,28,31,33,44,45]. Generally, because the structure possesses different potential catalytic centers, namely Lewis and Brønsted, a simple relation between the structure and the activity cannot easily be established.

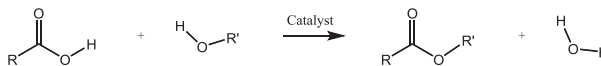
In this work we go beyond the current state of the art in the theoretical exploration of (defective) UiO-66 materials as solid acid catalysts for the esterification reaction of propionic acid; being a representative model for a generic carboxylic acid, including the more interesting biomass derived FFAs and levulinic acid. We particularly want to understand how the presence of water may affect the catalytic activity on Zr-MOFs from a mechanistic point of view. First, the water coordination around the metal and its immediate impact on the nature of the active site center will be investigated theoretically. Second, the catalytic effect on the esterification reaction resulting from a dehydration of the MOF will be described. New experimental data performed on different catalyst samples containing a varying number of linker vacancies showed the beneficial effect of water in line with the theoretical results. We show that the lowest activated mechanism takes place in a water environment creating Brønsted sites in the network of coordinated water molecules next to Lewis sites on the coordinatively unsaturated Zr atoms, arisen from the removal of linkers. Our results support the mechanism of a concerted bifunctional pathway providing a specific example of acid-base catalysis and this is in full agreement with experimental observations.

## 2. Methodology

### 2.1. Computational methods

All reactions studied in this work are investigated by means of static approaches using periodic models. The same methodology and levels of theory are used as employed in the study of aldol condensation reactions in a previous work of part of the authors [43]. Extended cluster calculations were used as a first guess to explore the different possibilities for adsorption of reactants and reaction pathways. However, in this work preference is given to periodic calculations as extended cluster calculations have the disadvantage that they are inadequate to correctly describe the environment surrounding the active site. Periodic calculations fully resolve this shortcoming. We made use of the periodic VASP (Vienna Ab Initio Simulation Package) code [46–50], applying the projector augmented wave approximation (PAW) [51] and the  $\Gamma$ -point approximation for the sampling of the Brillouin zone. The influence of  $k$ -points was tested on this system in a previous work, and a minimal effect on the electronic energy ( $\sim 0.2$  kJ/mol) was observed by increasing the sampling to a  $2 \times 2 \times 2$  Monkhorst-Pack mesh [43]. The structures were optimized within DFT-D3 with PBE as exchange-correlation functional [52,53] and including Grimme D3 dispersion corrections [54,55]. Energy cutoff for the plane waves was set to 700 eV, while the convergence threshold for the electronic self-consistent field (SCF) calculations was fixed to  $10^{-5}$  eV. A Gaussian smearing of 0.025 eV was also included to improve convergence. The energies were then only refined for the reaction mechanisms with single point calculations at B3LYP-D3 level of theory [56–58].

The periodic unit cell of UiO-66 consists of four hexameric Zr-bricks following the crystallographic structure provided by Cava et al. [15]. To make some metal sites accessible to guest molecules acting as reactants for potential reactions, at least two linkers should be removed from the entire unit cell. A rationalization on



Scheme 1. Esterification of a generic carboxylic acid to an acid ester by alcohol.

the different structures that can be generated by removing two linkers has been done in recent work of some of the present authors [23,59]. There exist seven distinct classes of structures containing two linker vacancies. In the present study we select the configuration (type 6 in Fig. 2 of Ref. [23]) which offers the best perspectives for guest intrusion through the channels to the coordinatively unsaturated Zr-surface. This particular defect structure is visualized in Fig. 1 where the two missing linkers in the 4-brick unit cell (blue) are clearly observed. The symmetry of this linker deficiency permits in reducing the dimension of the unit cell to two bricks (orange) with different coordination number 10 and 12. They are displayed in the right panel of Fig. 1. This reduced cell represents a good compromise between computational cost and accuracy, as the reactants adsorbed on the active site are always separated from their periodic images by a Zr brick and have a minimal interaction with each other. The defective brick has two active sites A and B (see Fig. 1). Reactions will be simulated on site A while site B will not actively participate in the reaction. We refer to the ESI for further computational details.

While in an earlier paper of some of the authors [41] the esterification of free fatty acids has been experimentally simulated by lauric acid (with an alkyl chain of 12 C-atoms ( $n = 12$ )), in the computational calculations the carboxylic acid is replaced by propionic acid with three carbon atoms. This is a seriously simplified model compound of a free fatty acid but it is large enough to investigate the reaction mechanism of the esterification reaction. A longer alkylic chain would add an excessive amount of degrees of freedom to the system, making the free energy surface of the adsorbate adduct much more complex and consequently would complicate the search for the most stable configuration. However, lauric acid or free fatty acids with longer chain lengths will not easily penetrate the pores of the UiO-66 material and reaction will take place at the surface and at the pore mouth. But as the active Zr-sites at the pore mouth are not structurally different from those in the interior (we refer the interested reader to the SM where an active surface site is constructed following the lines reported by Chizallet et al. [60,61]), it is plausible to assume that the employed model in this work to describe the esterification reaction mechanism is realistic. In the same context the alkyl chain of the acid can be regarded as passive and thus not affecting the reaction mechanism.

In order to account for the finite temperature, thermal corrections were performed from the frequency calculations. Using the in-house developed processing toolkit TAMkin [62] we calculated enthalpic and entropic contributions to the free energy barriers associated with each state at reaction conditions: temperature of 351 K and atmospheric pressure. Coordination free energies of water are calculated according to the standard procedure as outlined in the *Supplementary Material*. The partial pressure of the gas phase water molecule(s) is systematically taken as 1 atmosphere. A partial Hessian vibrational analysis approach was used [62], as it has been demonstrated [63] that this approximation does not affect substantially the entropy and enthalpy differences. The nature of stationary points was also verified by normal mode analysis using the partial Hessian frequency calculations. Only positive eigenvalues were found for reactants and products (minima on the potential energy surface), while for transition states the presence of one negative eigenvalue associated with the normal mode along the reaction coordinate ensured that the system was in a first order saddle point. The atoms that were included in this

partial Hessian frequency calculations are the reactants, the two Zr atoms, the two bridging  $\mu_3$ -oxygen atoms of the active site, and the water molecules that are adsorbed. More details on various theoretical procedures to estimate the kinetics of heterogeneous catalyzed reactions may be found in Refs. [64,65].

### 3. Experimental methods

#### 3.1. Synthesis of the MOFs

Several batches of UiO-66 and UiO-66-NH<sub>2</sub> solids were prepared using the procedure reported by Kandiah et al. [38]. 750 mg of ZrCl<sub>4</sub> and 740 mg of terephthalic acid (for UiO-66) or 800 mg of 2-amino terephthalic acid (for UiO-66-NH<sub>2</sub>) were dissolved in 90 mL of DMF (Zr:ligand:DMF molar ratio of 1:1:220) and kept in a flask at 80 °C without stirring for 12 h, and at 100 °C for other 24 h in an oil bath. The resulting material was recovered by filtration, and then washed with fresh DMF. The solids were then washed three times by soaking in dichloromethane for 3 h. Finally, the solids were filtered and dried under vacuum. The high crystallinity and the structure of the materials were confirmed by X-ray diffraction (Phillips XPert, Cu K $\alpha$  radiation). MOFs were further characterized by thermogravimetric analysis (Mettler Toledo TGA/SDTA851e) and transmission electron microscopy (JEOL JEM-1010 operated at 100 kV) in order to determine linker deficiency and particle size, respectively. For further details on the synthesis of UiO-66, we refer to Cirujano et al. [40,41].

#### 3.2. General procedure for the esterifications

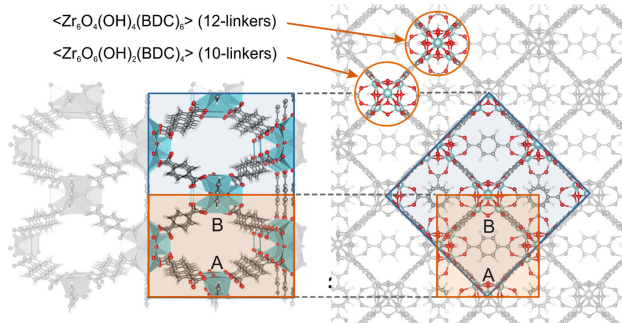
Esterification reactions of levulinic acid with ethanol were performed in a batch reactor at 78 °C, where 1 mmol of acid and ethanol (0.6 mL, 15 mmol) was contacted with the MOF (0.018 mmol Zr). The reaction products were analyzed with GC-MS (Varian 3900) with a BP20(WAX) capillary column (15 m long, i.d. 0.32 mm), with dodecane as internal standard and comparing retention times with those of commercial standards.

### 4. Results and discussion

#### 4.1. Molecular level characterization of defects - Water, methanol and acid coordination on the defective metal sites

In order to understand the reaction mechanism, it is crucial to have knowledge about the structure of the different active sites present on the material. Defects are generated during the synthesis, and the creation of a missing linker defect in the material can be imagined as a removal of one of the twelve negatively charged BDC<sup>2-</sup> linkers from the [Zr<sub>6</sub>O<sub>4</sub>(OH)<sub>4</sub>]<sup>12+</sup> brick. This produces a positive charge on the brick, which can be compensated either by removing a positively charged proton of the  $\mu_3$ -OH groups of the oxoclusters (see Scheme 2), or - in the presence of water - by coordinating a negative species such as a hydroxyl group to one of the Zr atoms.

Experimental determination of the nature of such defects on the molecular level is a very difficult task to accomplish. Single-crystal X-ray diffraction (SXRD) is a suitable tool to experimentally observe the presence of terminating hydroxyl groups and/or coor-



**Fig. 1.** Representation of the unit cells containing the defect. In blue, the conventional 4-brick unit cell, in orange, the 2-brick unit cell used for the calculations. The two different bricks are highlighted in orange. The 10-fold coordinated brick has two terephthalate linkers missing, one at site A and one at the opposite site B.

dinating water molecules [26,31]. In the work of Yaghi et al. [26] an extra hydroxide anion per defect site has been observed bringing the total of water molecules that can coordinate with a defective Zr–O–Zr site to three. In addition, it has been postulated that the charge compensating OH<sup>−</sup> counterion upon removal of one linker is stabilized by a hydrogen bond with a neighboring μ<sub>3</sub>-OH of the brick, while the two adjacent Zr atoms are capped with physisorbed water molecules. However, recent ab initio molecular dynamics simulations with water molecules moving in the pores of the UiO-66 material have shown that this state proposed by Yaghi does not correspond to a minimum on the potential energy surface [28,45]. In the present work we did not succeed in reproducing it as an intermediate stationary state either. On the contrary configuration 3 of Fig. 2 with three water molecules coordinated to the defective Zr–O–Zr site goes over to a more stable configuration with the hydroxide ion coordinated to one of the Zr-atoms (complex 3').

Potentiometric acid-base titrations have been very recently applied as an alternative experimental technique to measure the number of defect sites in a MOF [25]. This technique is also useful to measure the Brønsted acidity or to trace the proton topology [66]. It helps to understand the role of the Brønsted acidity of the protons present on the inorganic nodes. Tuning of the chemistry of reactive groups such as hydroxyl groups on MOF nodes has become possible for the first time [67], whereby the formation of methoxy or ethoxy groups on node vacancy sites as intermediate states has been shown to be crucial for conversion between different structures of hydrogen bonded OH/OH<sub>2</sub> groups on the Zr<sub>6</sub>-nodes. The various types of hydroxyl groups on the Zr<sub>6</sub>-nodes have markedly different properties. The chemistry associated with these various face topology changes on the Zr<sub>6</sub> nodes has been investigated in Ref. [67], and will be part of the discussion in this work.

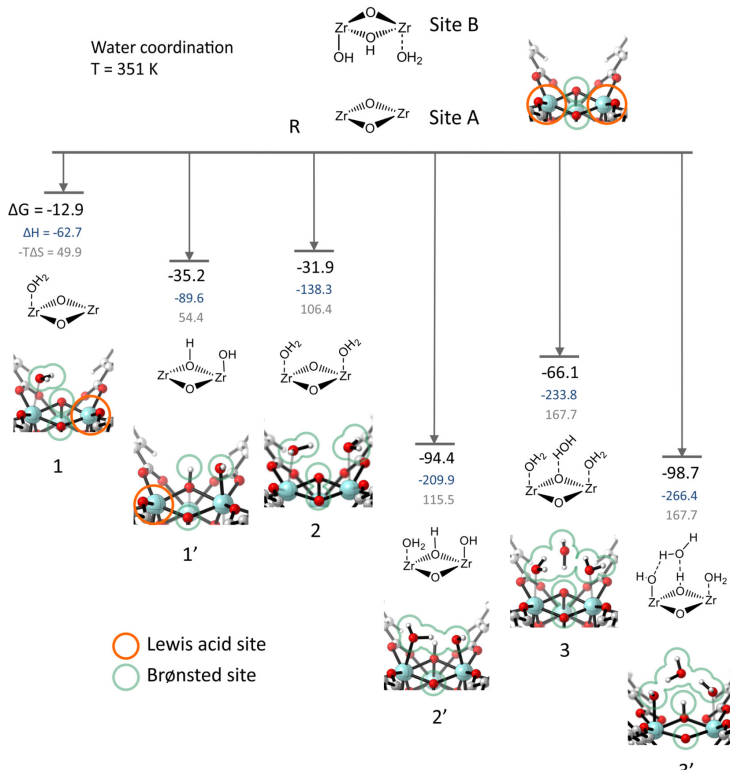
Water coordination near the defective site can occur in several configurations which are all displayed in Fig. 2. The active sites in the complex are not limited to Lewis acid sites. The unsaturated site formed after removal of a BDC linker (Scheme 2) is taken as the reference configuration R. The active site A contains two μ<sub>3</sub>-oxygens bridging the Zr-atoms figuring as two Brønsted basic sites (reference configuration R in Fig. 2).

The simplest state is chosen as reference and is displayed in the bottom of Scheme 2. The stability of all face topologies displayed in Fig. 2, has been investigated with respect to this reference configuration R. In all calculations a hydrated node surface structure (site

B, located at the opposite brick) has been consistently taken into consideration, allowing a comparative discussion on the coordination energies.

The coordination of one water molecule to one Zr-atom of the inorganic brick shields the Lewis acid character of the Zr-atom but the coordinated water molecule can act as an additional Brønsted acid site (configuration 1). In all other structures different possible Lewis and Brønsted sites appear which may play a role in a catalytic reaction. The various sites are encircled in all structures displayed in Fig. 2. The most stable configurations at the reaction temperature of 351 K are complexes with two or three water molecules. Configuration 2' originates from a complex with two physisorbed water molecules on two adjacent Zr atoms (complex 2). One water molecule immediately dissociates into a hydroxyl group adsorbed on one of the Zr-atoms and a proton adsorbed on the adjacent μ<sub>3</sub>-oxygen, while the second water molecule is physisorbed on the other Zr atom. Structure 2 forms a strongly stable configuration with a free energy difference of −94.4 kJ/mol compared to reference configuration R representing the unsaturated Zr site without water coordination. Adding a third water molecule yields a complex (configuration 3) which is more stabilized than the complex with two coordinated water molecules (configuration 2). Similarly as in the previous case, one water molecule dissociates with the OH<sup>−</sup> counterion directly attached to one of the Zr-atoms, and the proton forming a μ<sub>3</sub>-hydroxyl group, and a second water molecule is coordinated to the adjacent Zr-atom, while the remaining water molecule is coordinated to the μ<sub>3</sub>-hydroxyl group and the Zr–OH group. This configuration 3' is slightly more stable than structure 2' with two water molecules, but the difference is small (~4 kJ/mol), which can be ascribed to the seriously increasing entropy effects dominating the gain in enthalpy by the extra coordination. The position, orientation of the water molecules and the coordination energies of configuration 3 are in agreement with what was observed by Vandichel et al. and Ling et al. [28,45].

When reactant molecules (i.e., methanol and propionic acid) come into play, they can be hindered by the coordinating water molecules to access the active metal site, or the water can be displaced to make room for the incoming reactants, or the water molecules can form a complex with the reactants by means of hydrogen bonds. These complexes with reactants are considered in Figs. 3 and 4. These states are consistently modeled on a unit cell where the two Zr atoms on the opposite active site generated by removal of a linker (site B in Fig. 1) are hydrated (configuration



**Fig. 2.** Coordination free energies at reaction temperature of 351 K of one, two and three water molecules at coordinatively unsaturated Zr-bricks in defective UiO-66 with respect to a water coordination free site (site R). The structure of the opposite site B corresponds with configuration 2' with two water molecules and consistently used in all periodic calculations considered in the figure. Free energies (in black) are given in kJ/mol, and their decomposition into enthalpic  $\Delta H$  (blue) and entropic  $-T\Delta S$  (gray) contributions. Energies are resulting from periodic calculations with PBE-D3 level of theory. In each configuration Lewis acid and Brønsted sites are indicated.

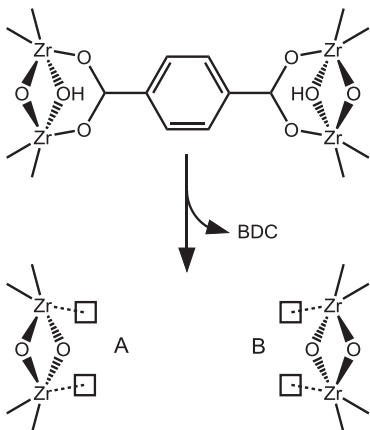
2'). Analogous structures with the dehydrated site B are reported in the ESI (Figs. S3 and S4). Configuration 4 in Fig. 3 corresponds to the physisorbed complex with methanol on the Zr Lewis center (i.e., MeOH + configuration R). This configuration is found to be less stable than its chemisorbed structure with formation of a methoxide (configuration 4'). With the presence of one water molecule, more stabilized methanol complexes are formed (configurations 5 and 5', coming from MeOH coordinated to configurations 1 and 1'). We did not study the dynamics of the methanol substitution process, as done in Ref. [67], but thermodynamically we found that structure 5' is the most favorable with the substitution of one water molecule by one methanol molecule in 2' and abstraction of the coordinated methanol proton to the terminating hydroxide.

Water in configuration 5' can be removed and replaced by the acid as second reactant to form a stable reactive complex 9', displayed in Fig. 4. In a hydrous environment methanol can even indirectly coordinate with the Zr-center through a hydrogen bond with

a terminal OH group. This complex 8 is even more stabilized ( $-60.9$  kJ/mol).

In all complexes displayed in Fig. 4, the acid is coordinated to the Zr-atom via its carbonyl oxygen. All the configurations considered are energetically favored (structures 6 to 9'), but the presence of water in the environment is beneficial in the formation of stable complexes of the two reactants (acid + methanol) with the catalyst. The extra stabilization results from the formation of a hydrogen bonded adduct, e.g. in configuration 7, with the  $\mu_3$ -hydroxyl group present in UiO-66-H<sub>2</sub>O (configuration 1').

Taken into account the results discussed so far, we propose structure 8 as reactive complex to study the esterification reaction of the acid by methanol in a hydrous environment, as it is the most stable adduct containing both reactant molecules, plus one water molecule that provides further stabilization through hydrogen bonding. The complex contains additional Brønsted acid and basic sites which may affect the esterification reaction of the acid with



**Scheme 2.** Unsaturated sites upon removal of a terephthalate linker.

methanol, and forms a highly consistent structure of an adsorbed complex with all reactants in a hydrated UiO-66 material. It is taken as starting structure to test the reaction mechanism. On a dehydrated catalyst the situation is slightly different, water molecules are not present in the cavities of the material and a network of hydrogen bonded water molecules does not occur. Obviously, the most suitable configuration to start the reaction under anhydrous conditions is thus structure **9'**, formed upon propionic acid physisorption and dissociative chemisorption of methanol on the fully dehydrated defect site (configuration **R**). In following sections, the esterification reaction in both, hydrated and anhydrous conditions will be considered.

#### 4.2. Reaction mechanism on hydrated brick

The coordination free energy diagrams in Figs. 2–4 clearly demonstrate that water molecules preferentially adsorb on the coordinatively unsaturated Zr-bricks in defective UiO-66, creating additional Brønsted sites which may assist in the esterification reaction. According to the proposed reaction mechanism and the catalytic effect of the defective UiO-66 material [40,41], the adsorption of the carboxylic acid onto the Lewis Zr acid sites increases the electrophilic character of the carboxylic carbon atom. At the same time the presence of weak Brønsted basic sites in the close vicinity of the alcohol (formation of hydrogen bonded adducts) will increase the nucleophilic character of the oxygen of the alcohol, thus favoring the condensation with the activated carboxylic carbon of the acid. So far, the eventual beneficial influence of the presence of a water environment on the catalytic activity has not been tested theoretically. In a hydrated brick the most favorable complex for esterification is configuration **8** with the methanol hydrogen bonded with the water coordinated on the open metal site. The corresponding energy profile obtained starting from configuration **8** is shown in Fig. 5, while the enthalpic and entropic contributions to the free energies of the states at different stages of the reaction are reported in Table 1.

The first transition state (**TS1**) is a concerted one, which corresponds to a deprotonation of methanol to the hydroxyl group that acts as a Brønsted base, and to a simultaneous formation of a C–O bond between the oxygen of methanol and the carboxylic carbon.

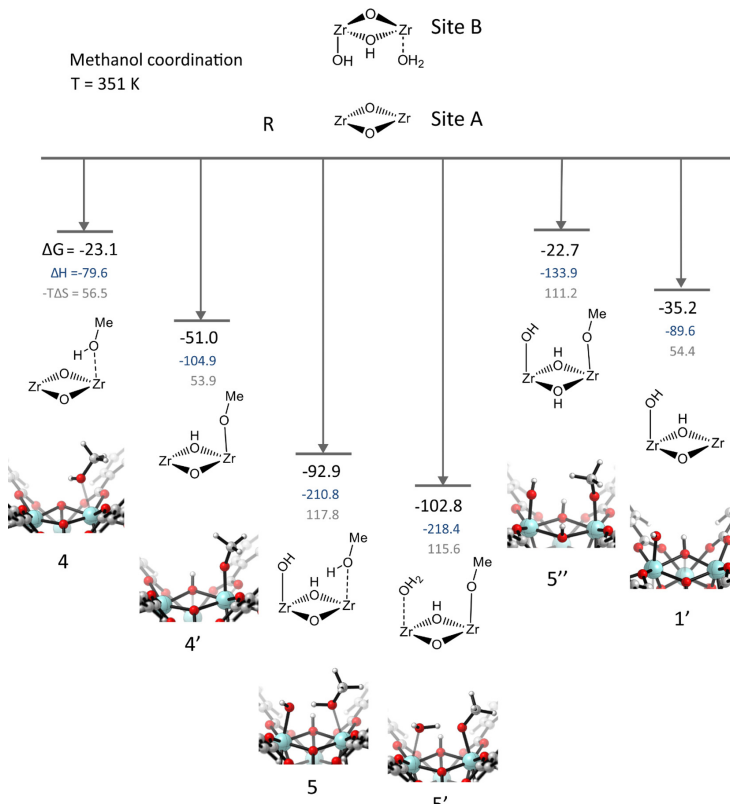
The free energy barrier for this first transition state is 28.9 kJ/mol with an almost equal enthalpic and entropic contribution. The post-transition state (configuration **8'**) is characterized by a tetrahedral intermediate coordinated to a Zr atom and a water molecule physisorbed on the adjacent Zr site. This intermediate has an almost similar free energy as the first reactive complex (configuration **8**) due to the extra-stabilization of a hydrogen bond with the  $\mu_3$ -hydroxyl group. The second transition state (**TS2**) is characterized by an approaching of a hydroxyl group from the tetrahedral intermediate to the water molecule adsorbed on the other Zr atom. Simultaneously, a proton shifts from the water molecule to the hydroxyl group, so that water is formed as a byproduct. The energy barrier for this transition state is 30.6 kJ/mol, which is similar to the first energy barrier and makes it difficult to attribute a rate determining step for the final product formation. The reaction products (configuration **P**) are ester and water, but in a water environment the catalyst will remain in the strongly stabilized configuration **2'** and solely the ester will desorb from the catalyst whereas the water remains coordinated to the brick. The energy barrier for the reverse reaction is 91.7 kJ/mol, which allows part of the products to be converted again into the reactants, until a chemical equilibrium is attained. Indeed, it is also observed experimentally that this reaction is under thermodynamic control. The suggested mechanism characterized by relatively low free energy barriers overlays with experimental findings regarding the high activity of esterification on UiO-66 and shows a dual participation of conjugated Lewis acid and Brønsted sites, as suggested earlier [40,41].

#### 4.3. Reaction mechanism in anhydrous conditions

Dehydration takes place after thermal activation of the catalyst. In an earlier paper of some of the authors [45] the mechanistic pathway for the dehydroxylation processes that takes place at activation conditions ( $T > 300^\circ\text{C}$ ) [18] of the various Zr-bricks present in defective UiO-66 material has been unraveled. Herein, experimental data that will be discussed later in this paper, have been obtained after heat treatment of the material at a temperature of around  $150^\circ\text{C}$ . At this temperature the solvent water molecules are all removed, but the  $[\text{Zr}_6\text{O}_6(\text{OH})_2]^{10+}$  brick (structure **B0** of Ref. [45]) on which the reaction takes place remains still intact; i.e., no dehydroxylation of the brick takes places. The experimental results predict a drop of the catalytic activity after this heat treatment at  $150^\circ\text{C}$  (vide infra), and we will now demonstrate that, indeed, the esterification reaction on a dehydrated brick (reference configuration **R'** in Fig. 5) in a water-free environment requires larger activation energies.

In the dehydrated brick the active sites are the uncoordinated Zr atoms, which are Lewis acid sites, and the  $\mu_3$ -oxygen atom which is a Brønsted base. Methanol, present in large excess in the reactant mixture, is first physisorbed on one of the two unsaturated Zr centers (configuration **4**) with an adsorption energy of  $-32.3$  kJ/mol at B3LYP-D3/PBE-D3 level of theory.<sup>1</sup> In this complex the  $\mu_3$ -oxygen atom represents a Brønsted basic site that facilitates the deprotonation of the methanol forming a methoxide, while the abstracted methanol proton forms a terminating  $\mu_3$ -hydroxide (configuration **4'**). The methoxide complex is slightly thermodynamically favored with respect to its physisorbed configuration **4** and its formation requires a transition state **TSa** with a low free energy barrier of about 17 kJ/mol. Finally, the acid adsorbs on the adjacent free Zr-site, and a reactive complex (configuration **9'**) is formed ready to start the esterification. The reaction proceeds with the formation of the C–O

<sup>1</sup> Please note that for the reaction free energy profile the level of theory has been increased from PBE-D3/PBE-D3 to B3LYP-D3/PBE-D3. It explains the difference in adsorption energy of complex 4 from  $-23.1$  kJ/mol in Fig. 3 to  $-32.3$  kJ/mol in Fig. 5.



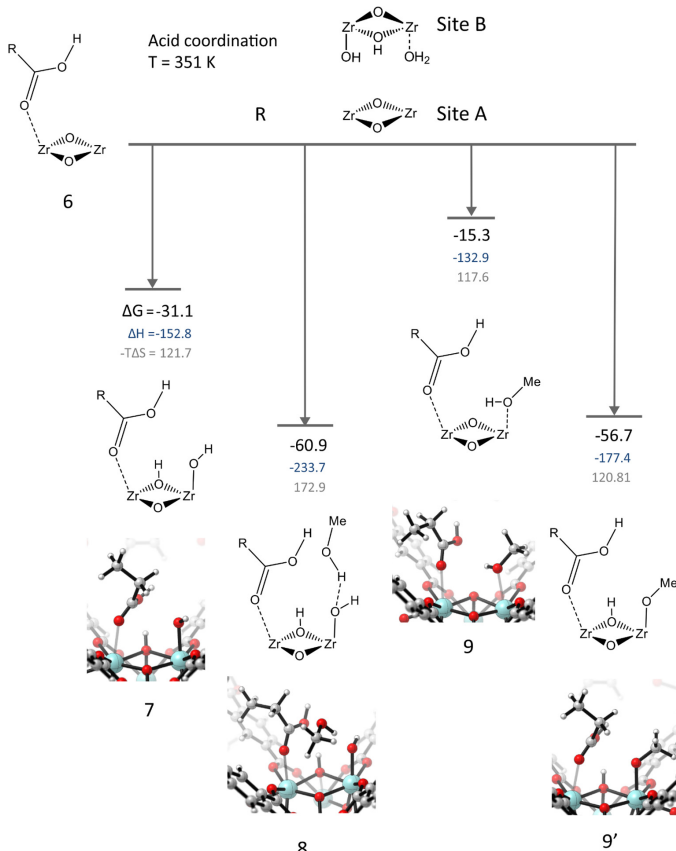
**Fig. 3.** Coordination free energies at reaction temperature of 351 K of methanol at coordinatively unsaturated Zr-bricks in defective UiO-66 with respect to a water coordination free frame. The structure of the opposite site B corresponds with configuration **2'** with two water molecules and consistently used in all periodic calculations taken up in the figure. Free energies (in black) are given in kJ/mol, and their decomposition into enthalpic  $\Delta H$  (blue) and entropic  $-\Delta S$  (gray) contributions. Energies are resulting from periodic calculations with PBE-D3 level of theory.

bond between the carbonyl carbon of the acid and the oxygen of the deprotonated methanol. In this step the free energy barrier (**TS1'**) is 49.8 kJ/mol and is attributed to an enthalpic contribution of 19.0 kJ/mol and an entropic contribution of 19.0 kJ/mol. This barrier is significantly higher in these water-free conditions than in the previous case where water molecules are involved in hydrogen bonded adducts, creating weak Brønsted basic sites assisting in increasing the nucleophilic character of the oxygen of the deprotonated alcohol. In accordance with the proposed mechanism on the hydrated brick, we investigated whether a similar concerted mechanism of the deprotonation and O–C bond formation (**TS1** in the “hydrated” reaction path) is also valid on the dehydrated complexes, but this search failed. On the contrary, we found the following intermediate (configuration **9''**) which is very close in energy and geometry to the transition state (**TS1'**), with a slightly shorter bond distance between oxygen and carbon. Subsequently the intermediate complex **9''** loses a hydroxyl group that binds to the hydrogen adsorbed

on the  $\mu_3$ -oxygen atom (see reaction scheme in the bottom of Fig. 5) to form a water molecule. This activated process also needs a high energy (barrier of transition state **TS2'** amounts to  $\Delta G^\ddagger = 54.3$  kJ/mol). This implies that starting from the reactive complex **9'** a total barrier of around 96.8 kJ/mol should be overcome, which is more than two times higher than what is observed when water actively participates in the reaction.

The esterification reaction on a dehydrated Zr-brick gives always water as a byproduct that can be removed leaving the catalyst as a dehydrated Zr-brick (product **P'**). If this water molecule is not removed it disturbs the equilibrium of the reaction and will play a role in the further esterification as it will coordinate with the open metal sites and the subsequent reactions will come in competition with the reaction on a hydrated brick.

This dual behavior of the  $\mu_3$ -oxygen atom was also observed in recent work by Hajek et al. on aldol condensation [43] and Oppenauer oxidation [68], where a deprotonation occurs on this site.

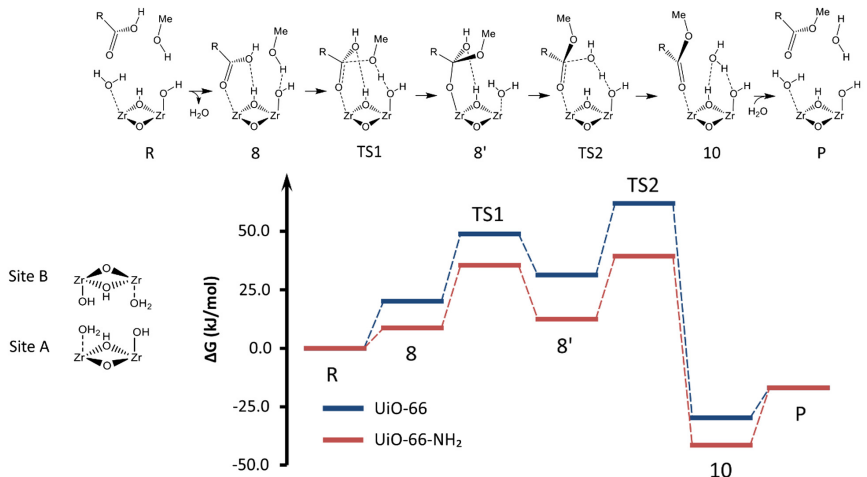
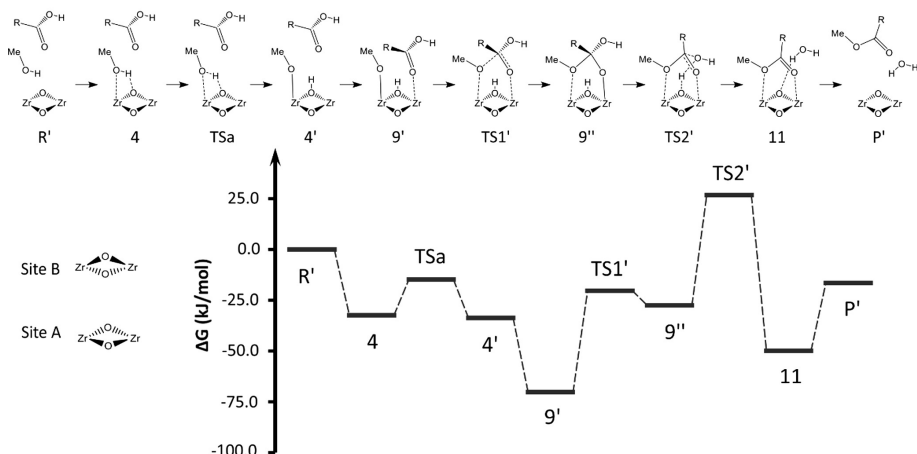


**Fig. 4.** Coordination free energies at reaction temperature of 351 K of the propionic acid and coadsorption of methanol and water at coordinatively unsaturated Zr-bricks in defective UiO-66 with respect to a water coordination free frame. The structure of the opposite site B corresponds with configuration 2' with two water molecules and consistently used in all periodic calculations taken up in the figure. Free energies (in black) are given in kJ/mol, and their decomposition into enthalpic  $\Delta H$  (blue) and entropic  $-T\Delta S$  (gray) contributions. Energies are resulting from periodic calculations with PBE-D3 level of theory.

The same site donates the proton back to form water in the last transition state. Therefore, also in this case we have a Brønsted site that acts as a base in a first step and as an acid in the next step. Note that in this pathway both Zr Lewis sites adsorb the reactants. We do not find a plausible pathway for the reaction that only makes use of the Lewis sites, therefore we conclude that the full catalytic effect is accomplished when the Brønsted sites are also taken into account.

The different kinetics of the esterification reaction in a water and a water-free environment require a more fundamental insight regarding the role of both Lewis and Brønsted sites present in the catalyst. It has been proposed that UiO-66 acted as a pure Lewis acid catalyst, given the Lewis acidity of the non-fully coordinated Zr atoms on the defect site. However, it is known that in other

MOFs Brønsted groups such as hydroxyl, water, alcohol and acids can be coordinated to the metal sites on the bricks [69]. This acidity is difficult to characterize, as the acid sites are not homogeneous, and often lack an acid-base equilibrium. Moreover, because the structure possesses different potential catalytic centers - Lewis and Brønsted sites - a simple relation between the structure and the activity cannot easily be established. A compatible experimental technique to measure the Brønsted acidity or to trace the proton topology of MOFs in an aqueous environment is potentiometric acid-base titration. Using this technique three types of protons have been detected in UiO-66 material, attributed to:  $\mu_3\text{-OH}$ ,  $\text{Zr-OH}_2$  and  $\text{Zr-OH}$  [66]. This picture is totally consistent with what we have proposed when removing a linker and replacing it by  $-\text{OH}_2$  and  $-\text{OH}$  groups. A similar model has been proposed

Hydrated materialDehydrated material

**Fig. 5.** Mechanism and free energy profile for the esterification of propionic acid with methanol on a hydrated and defective UIO-66 material (blue), a hydrated defective UIO-66 material with amino functionalization of the BDC linkers (red), and on a dehydrated defective UIO-66 (black). Periodic calculations at B3LYP-D3/PBE-D3 level of theory,  $T = 351$  K. R corresponds to an empty frame with one linker defect and a pool with all reactants to guarantee mass balance. In P the defective Zr-brick is coordinated with two water molecules (configuration 2'). P' corresponds to the empty frame with the ester as final product and remaining water molecules in gas phase.

in recent computational studies of Ling and Slater [28] and Vandichel et al. [45] demonstrating that a proton is exchanged between the Zr-OH<sub>2</sub> and Zr-OH groups. This is in line with the proposed mechanism on the hydrated brick, as in the two transition states (TS1 and TS2) there is a proton exchange between reactants and

the Zr-OH group, which in the first part of the reaction acts as a Brønsted base and in the second as a Brønsted acid. The reaction can be classified as some prototype of a dual acid-base catalytic reaction, where during the reaction Brønsted sites may alternatively switch of character. Their action works complementary to

**Table 1**

Free energy, enthalpic and entropic contributions in kJ/mol for the esterification of propionic acid with methanol on the hydrated, hydrated with NH<sub>2</sub>-functionalization and dehydrated UiO-66 material. Periodic calculations at B3LYP-D3//PBE-D3 level of theory, T = 351 K.

	Hydrated UiO-66				Hydrated UiO-66-NH <sub>2</sub>			
	ΔG	ΔG <sup>‡</sup>	ΔH	-TΔS	ΔG	ΔG <sup>‡</sup>	ΔH	-TΔS
8	20.1		-32.3	52.4	8.7		-46.5	55.2
TS1	48.9	28.9	-17.9	66.8	35.5	26.8	-33.4	68.9
8'	31.3		-31.3	62.6	12.5		-55.0	67.5
TS2	62.0	30.6	-11.7	73.7	39.3	26.9	-31.9	71.2
10	-29.7		-87.0	57.3	-41.5		-98.3	56.8
P	-16.9		-20.1	3.2	-16.9		-20.1	3.2
Dehydrated UiO-66								
	ΔG	ΔG <sup>‡</sup>	ΔH	-TΔS		ΔH	-TΔS	
4	-	-32.3			-	-88.9		56.5
TSa	-	-14.8		17.5	-	-75.6		60.7
4'	-	-33.7			-	-88.2		54.5
9'	-	-70.1			-	-191.8		121.7
TS1'	-	-20.3		49.8	-	-161.0		140.7
9''	-	-27.5			-	-164.6		137.1
TS2'	-	-26.7		54.3	-	-113.3		140.0
11	-	-49.8			-	-169.6		119.7
P'	-	-16.5			-	-19.8		3.2

the Zr Lewis acid site whose role remains crucial in the esterification reaction. An actual theoretical study of the difference in acidity of the various protons would be very interesting but beyond the scope of the present paper.

#### 4.4. Reaction mechanism with amino functionalization

One of the great advantages of MOFs is the easiness to functionalize the linkers and herewith to change the catalytic properties of the material. In order to understand the effect of the functional group substitution at the ligand benzene ring on the catalytic activity of the defective UiO-66 material, the esterification reaction was also investigated on the amino functionalized material, UiO-66-NH<sub>2</sub>. It was originally speculated that amino groups would play an active role in the reaction. We investigated different pathways in which the amino group was actively involved, but no plausible mechanism was found. This brings us to the conclusion that the reaction needs Brønsted sites to be catalyzed, and that amino groups are not basic enough to deprotonate the reactants, which react preferentially with other basic sites, such as the Zr-OH group in the hydrated brick and the  $\mu_3$ -oxygen atom in the dehydrated one. These results are in line with the recent study of Hajek et al. on the aldol condensation reaction on the UiO-66 materials [43]. Therefore, the pathway that we have proposed previously for the hydrated brick of UiO-66, is still prevalent here with the amino functionalized material UiO-66-NH<sub>2</sub>. However, even if the amino groups do not play a direct role in the reaction mechanism they could indirectly modulate the electronic structure of the framework and influence the reaction free energies. With an electron-donating substituent we may expect that the Lewis acid character of the coordinatively unsaturated neighboring Zr center decreases [39] and would lead to a decrease in the reaction rate. The lower Lewis acidity is reflected in longer distances between the carboxyl oxygen of the adsorbate and Zr in configuration **8** (Zr-O distance increases from 2.30 Å to 2.34 Å for UiO-66 and UiO-66-NH<sub>2</sub>, respectively). However, the presence of a hydrogen bond network makes the electron modulation much more complex in this case, due to the interplay between the Lewis acid and the several Brønsted basic sites present in the hydrated complex, and leads overall to a slight increase in the reaction rate with amino functionalization. This is indeed what is observed here as different stabilization energies and barriers are obtained, compared with the amino-free material (see Fig. 5 and Table 1). The role of the amino

group is passive and not visible in the reaction scheme. Nevertheless, a stronger adsorption of the reactants on the amino functionalized hydrated solid is noticed (configuration **8**) and systematically lower energy barriers, although not really spectacular. The stronger adsorption of the reactants on the UiO-66-NH<sub>2</sub> material is due to the formation of a network of hydrogen bonds which are not present in the pristine material (Fig. 6a), and to additional electronic effects. This extra stabilization affects all the states (intermediate, transition states and products), but the most striking effect is observed in the magnitude of the barrier (TS2) in the second reaction with the bond breaking between the carbonyl carbon and the oxygen of the leaving group. It lowers from 30.6 kJ/mol to 26.9 kJ/mol. The global effect of the amino functionalization is best expressed in the rate determining step which decreases by 11 kJ/mol, while the reaction is highly exothermic and under thermodynamic control. These results give rise to a higher catalytic effect that is indeed observed experimentally [40,41]. Furthermore, amino groups provide additional sites where water can be adsorbed and form additional hydrogen bonds, as displayed in Fig. 6b. To summarize, in the proposed reaction mechanism, amino groups don't play an active role, but their presence induces a positive effect on the catalytic activity of the material, which completely agrees with the experimental observations. This effect was also observed in a recent theoretical work on aldol condensation [43]. The choice of an electron-withdrawing substituent such as -NO<sub>2</sub> will not enhance the esterification, despite the stronger Lewis acidity at the Zr-atom (see *Supplementary Material*). This is in line with our conclusion on the dual Lewis/Brønsted character of the active site in the Fischer esterification.

## 5. Experimental results

The relevant role of water in the formation in UiO-66 materials of the active sites for esterification can be inferred experimentally by analyzing the thermograms of various samples containing different amounts of linker deficiencies. Indeed, TGA curves provide a means for evaluating the amount of missing linker defects of a solid, which can be calculated following the method proposed by Valenzano et al. [18]. In our previous paper on levulinic acid esterification over UiO-66-type materials [40], we showed that the use of a non-modulated synthesis procedure to prepare these materials (i.e., without the aid of auxiliary molecules, such as acetic acid), usually leads to materials with an amount of defects that can lar-

gely vary from one sample to another in a random way. In this way, we were able to prepare several samples with linker deficiencies ranging from 2.5 to 13.2% for UiO-66, and between 2.1 and 8% for UiO-66-NH<sub>2</sub>. We made use of this large variability of defect content from sample to sample to establish a direct correlation between catalytic activity for esterification and the number of defects of the solid, in such a way that the catalytic activity was found to increase with the number of linker defects [40]. An almost 9-fold increment of the reaction rate constant ( $k$ ) was observed on comparing the most defective (2.5% linker defects,  $k = 0.07 \text{ h}^{-1}$ ) to the less defective (13.2%,  $k = 0.61 \text{ h}^{-1}$ ) UiO-66 materials. Interestingly, by comparing the TGA curves of these UiO-66 samples, we have also noticed that a clear trend exists between the amount of linker vacancies and the total amount of physisorbed water of the solid (i.e., the weight lost between room temperature and 150 °C in the corresponding TGA curve (see Fig. 7, left). Moreover, as the amount of linker defects in UiO-66 increases, water molecules are more strongly bound (i.e., desorbed at a higher temperature), as shown in Fig. 7, right. This trend is clearly visible in the corresponding derivative of the TGA curves (red curves in Fig. S10 in ESI), in which the minima correspond to the inflection point of the first weight loss in the corresponding TGA curves. In contrast, in UiO-66-NH<sub>2</sub> water molecules are desorbed in general at higher temperatures than in UiO-66 with a similar concentration of defects; i.e., water molecules are more strongly bound. However, in UiO-66-NH<sub>2</sub> the desorption temperature does not seem to depend on the amount of missing linkers. Taken together, these results indicate that: (i) The defects associated with linker vacancies increase the hydrophilic character of UiO-66, as already anticipated by Snurr and coworkers [33]; and (ii) the presence of amino groups in the terephthalate linkers favors water adsorption, also in line with previous results by Walton and coworkers [70]. Therefore, these experimental findings give strong support to the hypothesis of a direct participation of water molecules in the active (defective) sites for esterification, as suggested by our theoretical models. Moreover, they also offer a plausible explanation to understand the higher catalytic activity of UiO-66-NH<sub>2</sub> with respect to UiO-66. Even though our models do not predict a direct participation of the -NH<sub>2</sub> groups in any of the steps of the catalytic process, their presence clearly increases the amount of water adsorbed inside the pores and strengthens the interaction with the material, which is beneficial for the final catalytic activity.

An item that stirs a lot of experimentalists are the linker exchanges in MOFs. A recent perspective is given by Seth Cohen [71] and it is not excluded a priori that the carboxylic acid used in the esterification reaction exchanges with a terephthalate linker of the UiO-66 material. Linker exchange of terephthalate linkers by the carboxylate reaction substrates is in principle a feasible process

that can take place during the reaction, leading to the creation of further defect sites that could contribute to the catalytic process. Although we cannot completely rule out the occurrence of this phenomenon in the general case of any carboxylic acid, in the particular case of levulinic acid (LA) esterification we were not able to detect by <sup>1</sup>H NMR and FTIR spectroscopy the presence of LA in the solid recovered after the catalytic experiment. Therefore, the amount of linker exchange (if any) should be certainly below the detection limits of these techniques. Indeed, if linker exchange of the pristine ditopic terephthalate linker by LA would take place to a significant extent, it would eventually lead to a severe reduction in the stability and crystallinity of the material. We have checked that the crystallinity of the material recovered after the reaction is virtually unchanged with respect to the fresh material (see Fig. S11 in the Supporting Information). Therefore, although ligand exchange cannot be totally ruled out for other carboxylic substrates, this should not be a significant process taking place during the reaction of LA with ethanol.

Finally, it is also possible to see experimentally a clear decrease of the catalytic activity of UiO-66 materials upon removal of physisorbed water molecules. To demonstrate this point, Fig. 8 shows the time-conversion plots obtained for the esterification of levulinic acid (LA) with ethanol catalyzed by two UiO-66 samples containing 7% (left part) or 2% (right part) missing linkers defects. The corresponding pseudo-first order reaction rate constants are  $k = 0.21 \text{ h}^{-1}$  and  $0.07 \text{ h}^{-1}$  for samples with 7% and 2% missing linkers, respectively; following the trend observed in our previous work [40]. It is also observed in Fig. 8 that dehydration of the samples by thermal treatment at 150 °C (open symbols in both left and right parts) brings about a definite decrease of the catalytic activity of both UiO-66 samples; passing from  $0.21 \text{ h}^{-1}$  to  $0.12 \text{ h}^{-1}$ , and from  $0.07 \text{ h}^{-1}$  to  $0.02 \text{ h}^{-1}$ , for the samples containing 7% and 2% of defects, respectively. These results clearly reveal the relevant role of water in the catalytic activity of UiO-66 materials, which is a further support to our theoretical models and in complete agreement with the present findings.

The presence of defects in MOFs (both missing linkers and missing nodes) can eventually lead to an increase in the specific surface area and pore volume of the material, as compared to a pristine defect free material [72]. However, even if this type of defects would facilitate the diffusion of reactants throughout the pore system of the MOF, this would not translate into an improvement of the catalytic performance of the material for this particular reaction of the LA esterification with ethanol. However, we don't discard that other carboxylate substrates might eventually benefit for an increase in the material's porosity associated with missing nodes. We refer to the [Supplementary Material](#) for more details on this issue.

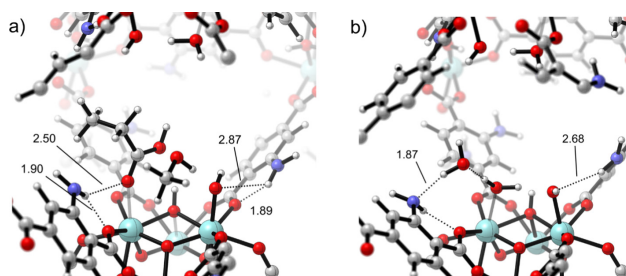
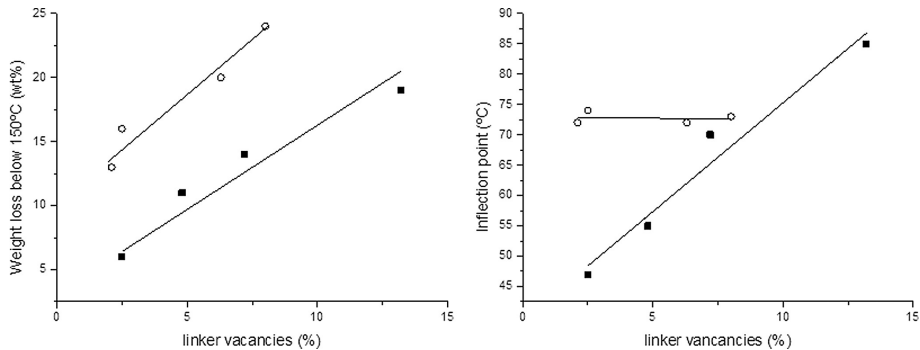
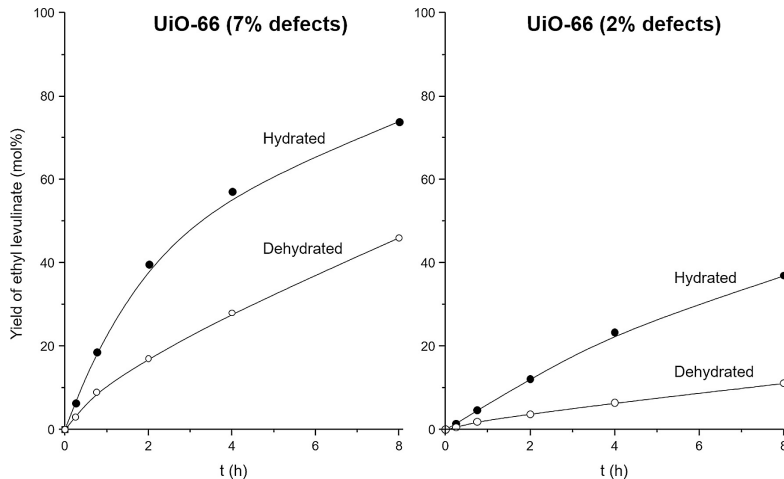


Fig. 6. Network of hydrogen bonds between adsorbates and amino groups. (a) Reactive complex 8, (b) an additional water molecule present in solution.



**Fig. 7.** (Left) Weight lost between room temperature and 150 °C by UiO-66 (black squares) and UiO-66-NH<sub>2</sub> (white dots) as a function of the different amount of missing linker defects. (Right) Desorption temperature of physisorbed water (determined from the corresponding TGA derivative curves) as a function of missing linker defects for UiO-66 (black squares) and UiO-66-NH<sub>2</sub> (white dots). Both TGA and derivative TGA curves are shown in Fig. S10 in ESI.



**Fig. 8.** Time-conversion plots for esterification of levulinic acid (LA) with ethanol on UiO-66 with 7% defects (left) and 2% defects (right) when water is coordinated to the brick (black dots) and when the material is dehydrated (white dots).

## 6. Conclusions

In this work we have investigated the mechanism of Fischer esterification of an organic carboxylic acid with methanol on UiO-66 and UiO-66-NH<sub>2</sub> with a linker deficiency. Particular attention has been drawn to the hydration state of the active sites on the materials. Theoretical modeling shows that in the most stable brick two water molecules are adsorbed on the defect site: one is chemisorbed as a Zr-OH group and a hydrogen on the  $\text{t}_{1g}$ -oxygen, while the other is physisorbed on the adjacent Zr. In the proposed mechanism, the carboxylic acid can displace the physisorbed water to coordinate with a Zr atom and react with methanol previously che-

misorbed on the neighbor Zr site to form a methoxide. An alternative mechanism on the dehydrated brick and without the assistance of water was investigated, but the energy barriers were substantially higher than in the previous case. This is in line with the experimental results reported herein that show a lowering in the catalytic activity upon dehydration of the material. Theoretical modeling confirms that the role of water molecules is crucial in the reaction, as water plays an active role as both Brønsted base and acid. As the role of the Zr Lewis acid centers is indispensable the proposed reaction mechanism is based upon a dual Lewis/Brønsted catalytic function. A positive effect of amino functionalization of the linkers was also observed, even though they don't participate

actively in the reaction mechanism. An indirect participation of the amino groups in increasing and strengthening water adsorption on the solid can be inferred from the analysis of the corresponding thermogravimetric curves, which would result beneficial for the formation and stabilization of the proposed active sites.

The model reaction studied in the present work between propionic acid and methanol can be taken as representative for other more relevant esterifications, in particular for the production of biodiesel from free fatty acids. Furthermore, water molecules could play an active role also in other reactions catalyzed by UiO-66 and other Zr based MOFs, such as MOF-808 and Nu-1000.

Finally, once more we want to emphasize the high potential of UiO-66 and its variants as catalyst due to its dual acid/base character by the appearance of Lewis and Brønsted sites working complementary to each other. Defective UiO-66 material is a prototype of how a MOF can be designed and composed such to fulfill all ingredients needed to construct such a combined Lewis/Brønsted network. The facile way to change the composition, topology of a MOF opens a lot of perspectives to use MOFs in catalytic applications.

## Acknowledgments

This work is supported by the Fund for Scientific Research Flanders (FWO) (project number 3G048612), the Research Board of Ghent University (BOF) and BELSPO in the frame of IAP/7/05. This project has received funding from the European Union's Horizon 2020 research and innovation programme under the Marie Skłodowska-Curie grant agreement No. 641887 (project acronym: DEFNET). Funding was also received from the European Union's Horizon 2020 research and innovation programme [consolidator ERC grant agreement no. 647755-DYNPOR (2015–2020)]. Computational resources (Stevin Supercomputer Infrastructure) and services were provided by Ghent University. Financial support from the Generalitat Valenciana (project AICO/2015/065), the Spanish Ministry of Economy and Competitiveness (program Severo Ochoa SEV20120267), and the Spanish Ministry of Science and Innovation (project MAT2014-52085-C2-1-P) is gratefully acknowledged.

## Appendix A. Supplementary material

Supplementary data associated with this article can be found, in the online version, at <http://dx.doi.org/10.1016/j.jcat.2017.06.014>.

## References

- [1] A. Corma, S. Iborra, A. Velty, Chemical routes for the transformation of biomass into chemicals, *Chem. Rev.* 107 (2007) 2411–2502.
- [2] G.W. Huber, S. Iborra, A. Corma, Synthesis of transportation fuels from biomass: chemistry, *Catal. Eng., Chem. Rev.* 106 (2006) 4044–4098.
- [3] N. Lerkkaseemarn, N. Abdouloumouine, L. Achenie, F. Agblevor, Mechanistic modeling of palmitic acid esterification via heterogeneous catalysis, *Indust. Eng. Chem. Res.* 50 (2011) 1177–1186.
- [4] A.A. Kiss, A.C. Dimian, G. Rothenberg, Solid acid catalysts for biodiesel production – towards sustainable energy, *Adv. Synth. Catal.* 348 (2006) 75–81.
- [5] E. Lotero, Y. Liu, D.E. Lopez, K. Suwannakarn, D.A. Bruce, J.G. Goodwin, Synthesis of biodiesel via acid catalysis, *Indust. Eng. Chem. Res.* 44 (2005) 5353–5363.
- [6] F. Ma, M.A. Hanna, Biodiesel production: a review, *Bioresour. Technol.* 70 (1999) 1–15.
- [7] M. Vafeaezadeh, A. Fattah, DFT investigations for “Fischer” esterification mechanism over silica-propyl-SO3H catalyst: is the reaction reversible?, *Comput. Theor. Chem.* 101 (2017) 27–32.
- [8] L. Zaramella, C.A. Ruhnen, E.L. Dal’Oglio, P.T. de Sousa Jr., DFT study of gas phase acid-catalyzed ethanolation of butyric acid triglyceride, *Fuel* 94 (2012) 473–479.
- [9] T. Yu, H.-B. Chang, W.-P. Lai, X.-F. Chen, Computational study of esterification between succinic acid and ethylene glycol in the absence of foreign catalyst and solvent, *Polym. Chem.* 2 (2011) 892–896.
- [10] A. Corma, H. García, F.X. Llabrés i Xamena, Engineering metal organic frameworks for heterogeneous catalysis, *Chem. Rev.* 110 (2010) 4606–4655.
- [11] A. Dhakshinamoorthy, M. Alvaro, H. García, Commercial metal-organic frameworks as heterogeneous catalysts, *Chem. Commun.* 48 (2012) 11275–11288.
- [12] D. Farrusseng, S. Aguado, C. Pinel, Metal-organic frameworks: opportunities for catalysis, *Angew. Chem. Int. Ed.* 48 (2009) 7502–7513.
- [13] J. Lee, O.K. Farha, J. Roberts, K.A. Scheidt, S.T. Nguyen, J.T. Hupp, Metal-organic framework materials as catalysts, *Chem. Soc. Rev.* 38 (2009) 1450–1459.
- [14] P. Valvekens, F. Vermoortele, D. De Vos, Metal-organic frameworks as catalysts: the role of metal active sites, *Catal. Sci. Technol.* 3 (2013) 1435–1445.
- [15] J.H. Cavka, S. Jakobsen, U. Olsbye, N. Guillot, C. Lamberti, S. Bordiga, K.P. Lillerud, A new zirconium inorganic building brick forming metal organic frameworks with exceptional stability, *J. Am. Chem. Soc.* 130 (2008) 13850–13851.
- [16] Y. Bai, Y. Dou, L.-H. Xie, W. Rutledge, J.-R. Li, H.-C. Zhou, Zr-based metal-organic frameworks: design, synthesis, structure, and applications, *Chem. Soc. Rev.* 45 (2016) 2327–2367.
- [17] K. Leus, T. Bogaert, J. De Decker, H. Depauw, K. Hendrickx, H. Vrielink, V. Van Speybroeck, P. Van Der Voort, Systematic study of the chemical and hydrothermal stability of selected “stable” metal organic frameworks, *Micropor. Mesopor. Mater.* 226 (2016) 110–116.
- [18] L. Valenzano, B. Civalieri, S. Chavan, S. Bordiga, M.H. Nilse, S. Jakobsen, K.P. Lillerud, C. Lamberti, Disclosing the complex structure of UiO-66 metal organic framework: a synergic combination of experiment and theory, *Chem. Mater.* 23 (2011) 1700–1718.
- [19] O.V. Gutov, M.G. Hevia, E.C. Escudero-Adán, A. Shafir, Metal-Organic Framework (MOF) defects under control: insights into the missing linker sites and their implication in the reactivity of zirconium-based frameworks, *Inorg. Chem.* 54 (2015) 8396–8400.
- [20] G.C. Shearer, S. Chavan, S. Bordiga, S. Svelle, U. Olsbye, K.P. Lillerud, Defect engineering: tuning the porosity and composition of the metal-organic framework UiO-66 via modulated synthesis, *Chem. Mater.* 28 (2016) 3749–3761.
- [21] G.C. Shearer, S. Chavan, J. Ethiraj, J.G. Vitillo, S. Svelle, U. Olsbye, C. Lamberti, S. Bordiga, K.P. Lillerud, Tuned to perfection: ironing out the defects in metal-organic framework UiO-66, *Chem. Mater.* 26 (2014) 4068–4071.
- [22] F. Vermoortele, B. Bueken, G.L. Le Bars, B. Van de Voorde, M. Vandichel, K. Houthoofd, A. Vimont, M. Daturi, M. Waroquier, V. Van Speybroeck, Synthesis modulation as a tool to increase the catalytic activity of metal-organic frameworks: the unique case of UiO-66 (Zr), *J. Am. Chem. Soc.* 135 (2013) 11465–11468.
- [23] S.M.J. Rogge, J. Wieme, L. Vanduyfhuys, S. Vandenbrande, G. Maurin, T. Verstraeten, M. Waroquier, V. Van Speybroeck, Thermodynamic insight in the high-pressure behavior of UiO-66: effect of linker defects and linker expansion, *Chem. Mater.* 28 (2016) 5721–5732.
- [24] J. Canivet, M. Vandichel, D. Farrusseng, Origin of highly active metal-organic framework catalysts: defects? Defects!, *Dalton Trans* 45 (2016) 4090–4099.
- [25] Y. Liu, R.C. Kett, J.T. Hupp, O. Parra, Probing the correlations between the defects in metal-organic frameworks and their catalytic activity by an epoxide ring-opening reaction, *Chem. Commun.* 52 (2016) 7806–7809.
- [26] C.A. Trickett, K.J. Gagnon, S. Lee, F. Gandara, H.-B. Buergi, O.M. Yaghi, Definitive molecular level characterization of defects in UiO-66 crystals, *Angew. Chem. Int. Ed.* 54 (2015) 11162–11161.
- [27] M. Vandichel, J. Hajek, F. Vermoortele, M. Waroquier, D.E. De Vos, V. Van Speybroeck, Active site engineering in UiO-66 type metal-organic frameworks by intentional creation of defects: a theoretical rationalization, *CrystEngComm* 17 (2015) 395–406.
- [28] S.L. Ling, B. Slater, Dynamic acidity in defective UiO-66, *Chem. Sci.* 7 (2016) 4706–4712.
- [29] J.K. Bristow, K.L. Svane, D. Tiana, J.M. Skelton, J.D. Gale, A. Walsh, Free energy of ligand removal in the metal-organic framework UiO-66, *J. Phys. Chem. C* 120 (2016) 9276–9281.
- [30] M.J. Cliffe, W. Wan, X. Zou, P.A. Chater, A.K. Kleppe, M.G. Tucker, H. Wilhelm, N. P. Funnell, F.-X. Couder, A.L. Goodwin, Correlated defect nanoregions in a metal-organic framework, *Nat. Commun.* 5 (2014) 4176.
- [31] S. Olsen, D. Wragg, H. Reinsch, S. Svelle, S. Bordiga, C. Lamberti, K.P. Lillerud, Detailed structure analysis of atomic positions and defects in zirconium metal-organic frameworks, *Crystal Growth Des.* 14 (2014) 5370–5372.
- [32] D.S. Sholl, R.P. Lively, Defects in metal-organic frameworks: challenge or opportunity?, *J. Phys. Chem. Lett.* 6 (2015) 3437–3444.
- [33] P. Ghosh, Y.J. Colon, R.Q. Snurr, Water adsorption in UiO-66: the importance of defects, *Chem. Commun.* 50 (2014) 11329–11331.
- [34] H. Wu, Y.S. Chua, V. Krungleviciute, M. Tyagi, P. Chen, T. Yildirim, W. Zhou, Unusual and highly tunable missing-linker defects in zirconium metal-organic framework UiO-66 and their important effects on gas adsorption, *J. Am. Chem. Soc.* 135 (2013) 10525–10532.
- [35] J.E. Mondloch, M.J. Katz, W.C. Isley III, P. Ghosh, P. Liao, W. Bury, G.W. Wagner, M.G. Hall, J.B. DeCoste, G.W. Peterson, R.Q. Snurr, C.J. Cramer, J.T. Hupp, O.K. Farha, Destruction of chemical warfare agents using metal-organic frameworks, *Nat. Mater.* 14 (2015) 512–516.
- [36] A.M. Plonka, Q. Wang, W.O. Gordon, A. Balboa, D. Troya, W. Guo, C.H. Sharp, S. D. Senayake, J.R. Morris, C.L. Hill, A.I. Frenkel, In situ probes of capture and decomposition of chemical warfare agent simulants by Zr-based metal organic frameworks, *J. Am. Chem. Soc.* 139 (2017) 599–602.
- [37] S.J. Garibay, S.M. Cohen, Isoreticular synthesis and modification of frameworks with the UiO-66 topology, *Chem. Commun.* 46 (2010) 7700–7702.

- [38] M. Kandiah, M.H. Nilsen, S. Usseglio, S. Jakobsen, U. Olsbye, M. Tilset, C. Larabi, E.A. Quadrelli, F. Bonino, K.P. Lillerud, Synthesis and stability of tagged  $\text{UiO-66}$  Zr-MOFs, *Chem. Mater.* 22 (2010) 6632–6640.
- [39] F. Vermoortele, M. Vandichel, B. Van de Voorde, R. Ameloot, M. Waroquier, V. Van Speybroeck, D.E. De Vos, Electronic effects of linker substitution on Lewis acid catalysis with metal-organic frameworks, *Angew. Chem. Int. Ed.* 51 (2012) 4887–4890.
- [40] F. Cirujano, A. Corma, F.L. i Xamena, Conversion of levulinic acid into chemicals: synthesis of biomass derived levulinate esters over Zr-containing MOFs, *Chem. Eng. Sci.* 124 (2015) 52–60.
- [41] F.G. Cirujano, A. Corma, F.X. Llabrés i Xamena, Zirconium-containing metal organic frameworks as solid acid catalysts for the esterification of free fatty acids: synthesis of biodiesel and other compounds of interest, *Catal. Today* 257 (Part 2) (2015) 213–220.
- [42] F. Vermoortele, R. Ameloot, A. Vimont, C. Serre, D. De Vos, An amino-modified Zr-terephthalate metal-organic framework as an acid-base catalyst for cross-aldol condensation, *Chem. Commun.* 47 (2011) 1521–1523.
- [43] J. Hajek, M. Vandichel, B. Van de Voorde, B. Bueken, D. De Vos, M. Waroquier, V. Van Speybroeck, Mechanistic studies of aldol condensations in  $\text{UiO-66}$  and  $\text{UiO-66-NH}_2$  metal organic frameworks, *J. Catal.* 331 (2015) 1–12.
- [44] J. Canivet, A. Fateeva, Y.M. Guo, B. Coasne, D. Farrusseng, Water adsorption in MOFs: fundamentals and applications, *Chem. Soc. Rev.* 43 (2014) 5594–5617.
- [45] M. Vandichel, J. Hajek, A. Ghysels, A. De Vos, M. Waroquier, V. Van Speybroeck, Water coordination and dehydration process in defective  $\text{UiO-66}$  type metal-organic frameworks, *CrystEngComm* 18 (2016) 7056–7069.
- [46] G. Kresse, J. Furthmuller, Efficient iterative schemes for ab initio total-energy calculations using a plane-wave basis set, *Phys. Rev. B* 54 (1996) 11169–11186.
- [47] G. Kresse, J. Furthmuller, Efficiency of ab-initio total energy calculations for metals and semiconductors using a plane-wave basis set, *Comput. Mater. Sci.* 6 (1996) 15–50.
- [48] G. Kresse, J. Hafner, Ab initio molecular dynamics for liquid metals, *Phys. Rev. B* 47 (1993) 558.
- [49] G. Kresse, J. Hafner, Ab initio molecular-dynamics simulation of the liquid-metal-amorphous-semiconductor transition in germanium, *Phys. Rev. B* 49 (1994) 14251.
- [50] G. Kresse, D. Joubert, From ultrasoft pseudopotentials to the projector augmented-wave method, *Phys. Rev. B* 59 (1999) 1758–1775.
- [51] P.-E. Blochl, Projector augmented-wave method, *Phys. Rev. B* 50 (1994) 17953–17979.
- [52] J.P. Perdew, K. Burke, M. Ernzerhof, Generalized gradient approximation made simple, *Phys. Rev. Lett.* 77 (1996) 3865.
- [53] J.P. Perdew, K. Burke, M. Ernzerhof, Generalized gradient approximation made simple [Phys. Rev. Lett. 77, 3865 (1996)], *Phys. Rev. Lett.* 78 (1997) 1396.
- [54] S. Grimme, Accurate description of van der Waals complexes by density functional theory including empirical corrections, *J. Comput. Chem.* 25 (2004) 1463–1473.
- [55] S. Grimme, J. Antony, S. Ehrlich, H. Krieg, A consistent and accurate ab initio parametrization of density functional dispersion correction (DFT-D) for the 94 elements H–Pu, *J. Chem. Phys.* 132 (2010).
- [56] A.D. Becke, Density-functional exchange-energy approximation with correct asymptotic behavior, *Phys. Rev. A* 38 (1988) 3098–3100.
- [57] A.D. Becke, Density functional thermochemistry. 3. The role of exact exchange, *J. Chem. Phys.* 98 (1993) 5648–5652.
- [58] C.T. Lee, W.T. Yang, R.G. Parr, Development of the Colle-Salvetti correlation-energy formula into a functional of the electron-density, *Phys. Rev. B* 37 (1988) 785–789.
- [59] A. De Vos, K. Hendrickx, P. Van Der Voort, V. Van Speybroeck, K. Lejaeghere, Missing linkers: an alternative pathway to  $\text{UiO-66}$  electronic structure engineering, *Chem. Mater.* (2017).
- [60] C. Chizallet, S. Lazare, D. Bazer-Bachi, F. Bonnier, V. Lecocq, E. Soyer, A.-A. Quineaud, N. Bats, Catalysis of transesterification by a nonfunctionalized metal-organic framework: acid-baseity at the external surface of ZIF-8 probed by FTIR and ab initio calculations, *J. Am. Chem. Soc.* 132 (2010) 12365–12377.
- [61] C. Chizallet, N. Bats, External surface of zeolite imidazolate frameworks viewed ab initio: multifunctionality at the organic–inorganic interface, *J. Phys. Chem. Lett.* 1 (2010) 349–353.
- [62] A. Ghysels, T. Verstraeten, K. Hemelsoet, M. Waroquier, V. Van Speybroeck, TAMkin: a versatile package for vibrational analysis and chemical kinetics, *J. Chem. Inform. Model.* 50 (2010) 1736–1750.
- [63] A. Ghysels, D. Van Neck, M. Waroquier, Cartesian formulation of the mobile block Hessian approach to vibrational analysis in partially optimized systems, *J. Chem. Phys.* 127 (2007) 164108.
- [64] V. Van Speybroeck, K. De Wispelaere, J. Van der Mynsbrugge, M. Vandichel, K. Hemelsoet, M. Waroquier, First principle chemical kinetics in zeolites: the methanol-to-olefins process as a case study, *Chem. Soc. Rev.* 43 (2014) 7326–7357.
- [65] M. Waroquier, K. De Wispelaere, J. Hajek, S.M.J. Rogge, J. Van der Mynsbrugge, V. Van Speybroeck, Theoretical tool box for a better catalytic understanding, in: Nanotechnology in Catalysis: Applications in the Chemical Industry, Energy Development, and Environment Protection, 3 Volumes, Wiley-VCH, 2017.
- [66] R.C. Klet, Y.Y. Liu, T.C. Wang, J.T. Hupp, O.K. Farha, Evaluation of bronsted acidity and proton topology in Zr- and Hf-based metal-organic frameworks using potentiometric acid-base titration, *J. Mater. Chem. A* 4 (2016) 1479–1485.
- [67] D. Yang, V. Bernales, T. Islamoglu, O.K. Farha, J.T. Hupp, C.J. Cramer, L. Gagliardi, B.C. Gates, Tuning the surface chemistry of metal organic framework nodes: proton topology of the metal-oxide-like  $\text{Zr}_6$  nodes of  $\text{UiO-66}$  and  $\text{NU}-1000$ , *J. Am. Chem. Soc.* 138 (2016) 15189–15196.
- [68] J. Hajek, B. Bueken, M. Waroquier, D. De Vos, V. Van Speybroeck, The remarkable amphoteric nature of defective  $\text{UiO-66}$  in catalytic reactions, *ChemCatChem* 9 (2017) 2203–2210. <http://dx.doi.org/10.1002/cctc.201601689>.
- [69] J. Jiang, O.M. Yaghi, Bronsted acidity in metal-organic frameworks, *Chem. Rev.* 115 (2015) 6966–6997.
- [70] P.M. Schoenecker, C.G. Carson, H. Jasuja, C.J.J. Flemming, K.S. Walton, Effect of water adsorption on retention of structure and surface area of metal-organic frameworks, *Indust. Eng. Chem. Res.* 51 (2012) 6513–6519.
- [71] S.M. Cohen, The postsynthetic renaissance in porous solids, *J. Am. Chem. Soc.* 139 (2017) 2855–2863.
- [72] M.R. DeStefano, T. Islamoglu, S.J. Garibay, J.T. Hupp, O.K. Farha, Room-temperature synthesis of  $\text{UiO-66}$  and thermal modulation of densities of defect sites, *Chem. Mater.* 29 (2017) 1357–1361.

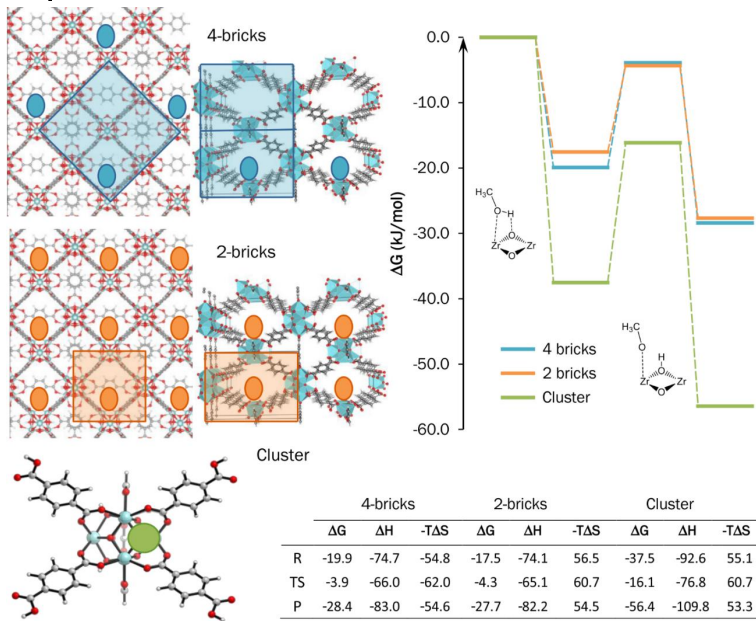
## Nature of active sites on UiO-66 and UiO-66-NH<sub>2</sub> in the catalysis of Fischer esterification

Chiara Caratelli, Julianna Hajek, Francisco G. Cirujano, Michel Waroquier, Francesc X. Llabrés i Xamena and Veronique Van Speybroeck

### Supplementary Material

The same defect model for UiO-66 used in this work has been used in previous works to describe chemical reactions at the coordinatively unsaturated Zr-surface. This reduced unit cell model has been benchmarked with respect to a description in the full 4-brick unit cell. Differences are negligible for this particular defect structure.

#### Comparison between 2 bricks and 4 bricks unit cell



**Figure S1** In graph, free energy profile at T = 351 K for the deprotonation of methanol on UiO-66 on the 4 brick unit cell, 2 brick unit cell and cluster model. Level of theory for the cluster: B3LYP/6-311++G(d,p)-D3//B3LYP/6-31G(d). Level of theory on the periodic unit cell: PBE-D3. In table, free energy, enthalpic and entropic contributions.

### **Cluster calculations :**

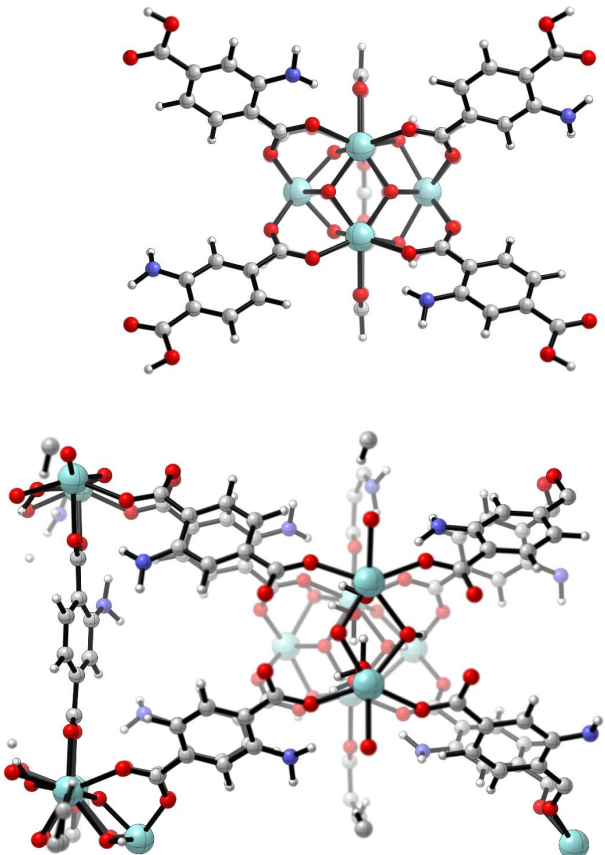
The reaction mechanism of the esterification reaction has in first instance also been investigated in extended cluster calculations. Their results are not taken up and discussed in the main manuscript. As they are available, they could serve as additional material to compare with results from periodic calculations.

#### **Methodology of the extended cluster calculations:**

The extended UiO-66 cluster is cut from a supercell that contains four inorganic bricks with unit cell formula  $[Zr_6O_9(OH)_3(RCOO)_{11}]_2[Zr_6O_4(OH)_4(RCOO)_{12}]_2$  in which we incorporate one linker defect. The in-house developed toolkit Zeobuilder [1] is used to construct the cluster, which comprises one brick with eleven BDC linkers, of which seven were replaced by formic groups while the four remaining linkers surround the active site. The terminal oxygens of the terephthalate linkers and the hydrogens of formate were assigned an infinite mass in the geometry optimization in order to mimic the periodic environment. All cluster calculations were performed with Gaussian '09. [2] Geometry optimizations were performed at the B3LYP/6-31G(d) level of theory, while the energies were refined using a triple zeta Pople basis set, at B3LYP/6-311G(d,p) level of theory. [3-5] As basis set for the metal Zr, we chose LanL2DZ and pseudopotential for the geometry optimization and LanL2TZ for the energy refinements. [6-8] Grimme D3 corrections were added to the energies [9] to account for dispersion effects. Summarized, the level of theory used for all the cluster calculations can be represented by the shorthand notation B3LYP/6-311++g(d,p)-D3//B3LYP/6-31G(d)\*, following the conventional form LOT-E//LOT-G, where LOT-E is the level of theory for the energy refinement and LOT-G the level of theory for the geometry optimization.

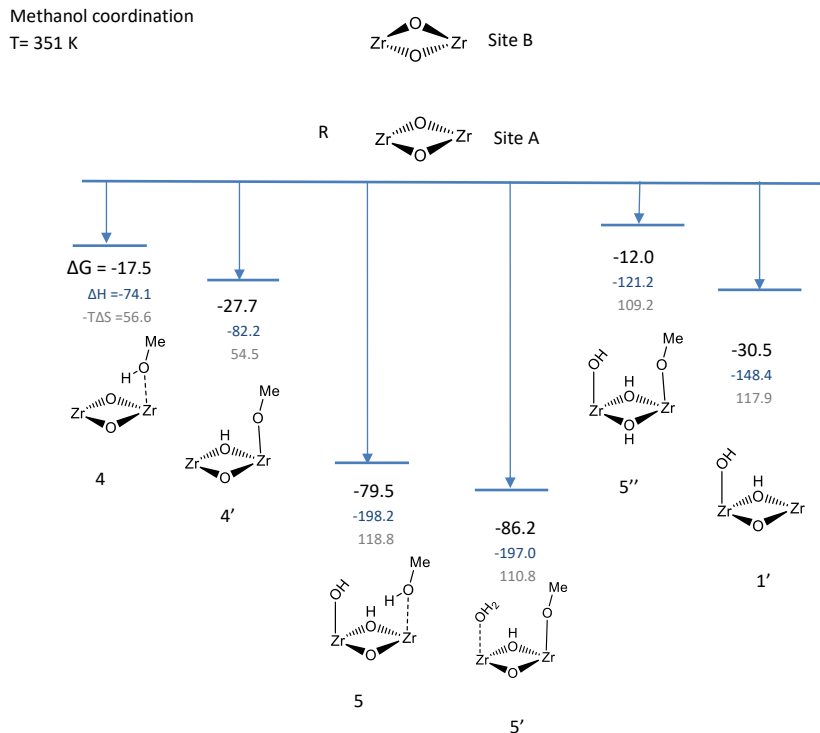
### Position of amino groups

One amino group was randomly distributed for each linker (by replacing the other equivalent positions on the linker by hydrogen atoms). The position of the groups in both periodic and cluster model was chosen in such a way to allow close proximity to the adsorbates during the reaction.

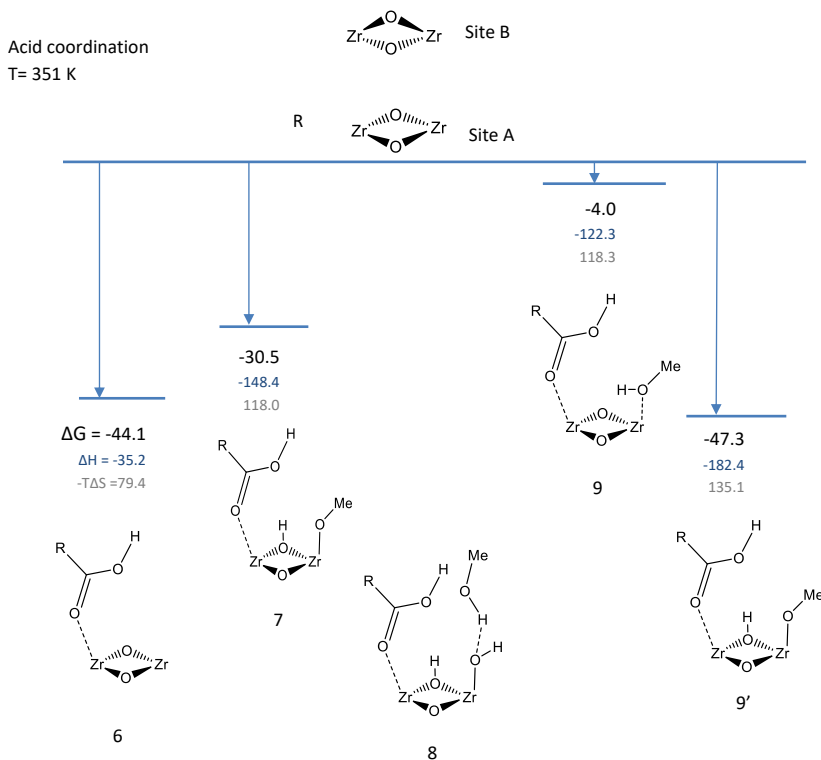


**Figure S2** Position of amino groups in the cluster and periodic model. (Level of theory for geometry optimization: B3LYP/6-31G(d) for cluster, PB3-D3 and PBE-D3 for periodic).

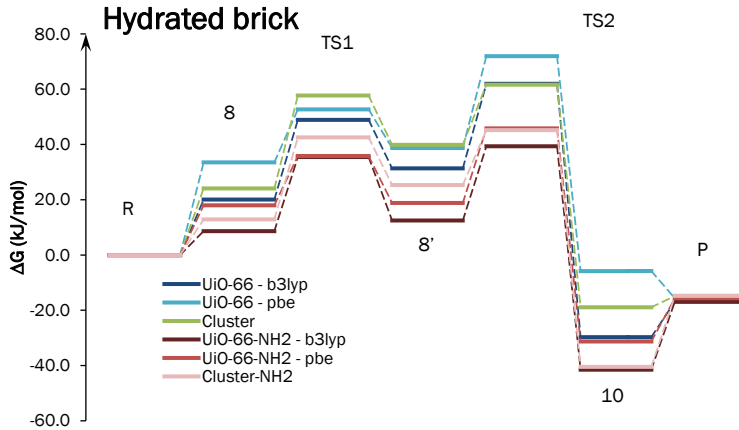
### Adsorption of reactants on the dehydrated unit cell



**Figure S3** Coordination free energies at reaction temperature of 351 K of methanol at coordinatively unsaturated Zr-bricks in defective UiO-66 with respect to a water coordination free frame. Free energies (in black) are given in kJ/mol, and their decomposition into enthalpic  $\Delta H$  (blue) and entropic  $-\Delta S$  (grey) contributions. Energies resulting from periodic calculations with LOT PBE-D3. This scheme differs from Figure 3 of the main manuscript by the structure of site B. In the dehydrated material we considered a water free site B.



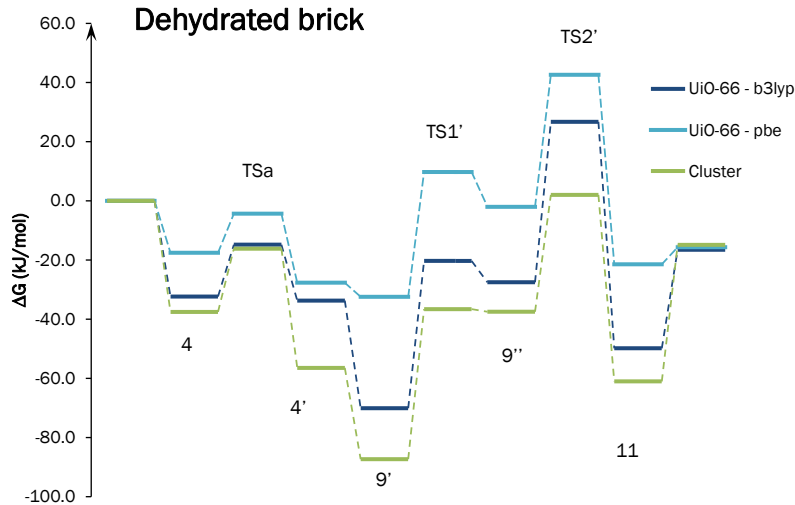
**Figure S4** Coordination free energies at reaction temperature of 351 K of propionic acid and coadsorption of methanol and water at coordinatively unsaturated Zr-bricks in defective UiO-66 with respect to a water coordination free frame. Free energies (in black) are given in kJ/mol, and their decomposition into enthalpic  $\Delta H$  (blue) and entropic  $-T\Delta S$  (grey) contributions. Energies resulting from periodic calculations with LOT PBE-D3. This scheme differs from Figure 3 of the main manuscript by the structure of site B. In the dehydrated material we considered a water free site B.



**Figure S5** Free energy profile at  $T = 351\text{ K}$  for the reaction on hydrated  $\text{UiO-66}$  and  $\text{UiO-66-NH}_2$ , on the periodic model and on the cluster model (Level of theory: B3LYP/6-311++G(d,p)-D3//B3LYP/6-31G(d) for cluster, PB3-D3 and PBE-D3//B3LYP for periodic).

**Table S1** Free energy, enthalpic and entropic contributions in  $\text{kJ/mol}$  at  $T = 351\text{ K}$  for the reaction on hydrated  $\text{UiO-66}$  and  $\text{UiO-66-NH}_2$  in the periodic and cluster model (Level of theory: B3LYP/6-311++G(d,p)-D3//B3LYP/6-31G(d) for cluster, PB3-D3 and PBE-D3//B3LYP for periodic).

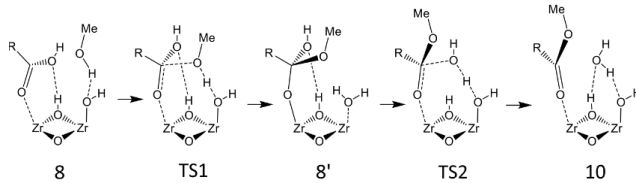
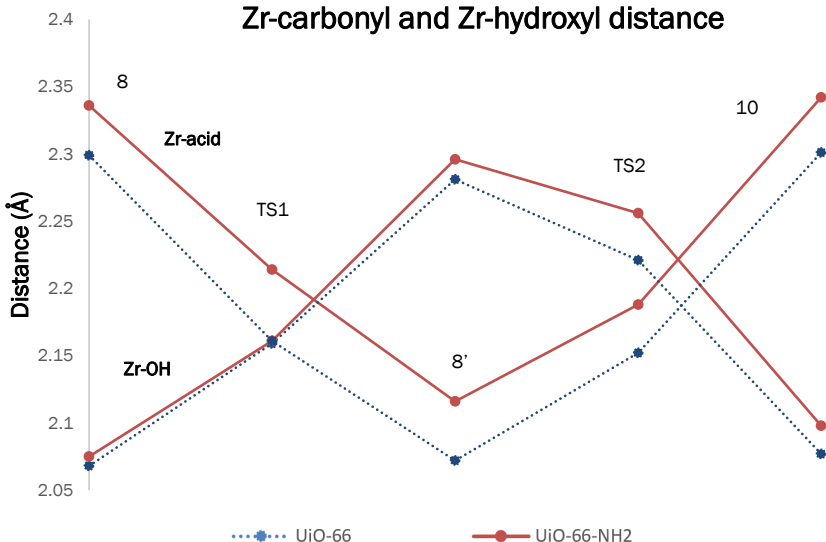
UiO-66-Periodic-b3lyp				UiO-66-NH <sub>2</sub> -periodic-b3lyp					
	$\Delta G$	barrier	$\Delta H$	$-\Delta S$	$\Delta G$	barrier	$\Delta H$	$-\Delta S$	
8	20.1		-32.3	52.4	8.7		-46.5	55.2	
TS1	48.9	<b>28.9</b>	-17.9	66.8	35.5	<b>26.8</b>	-33.4	68.9	
8'	31.3		-31.3	62.6	12.5		-55.0	67.5	
TS2	62.0	<b>30.6</b>	-11.7	73.7	39.3	<b>26.9</b>	-31.9	71.2	
10	-29.7		-87.0	57.3	-41.5		-98.3	56.8	
UiO-66-Periodic-pbe				UiO-66-NH <sub>2</sub> -periodic-pbe					
	$\Delta G$	barrier	$\Delta H$	$-\Delta S$	$\Delta G$	barrier	$\Delta H$	$-\Delta S$	
8	33.5		-23.8	57.4	18.0		-42.5	60.5	
TS1	52.7	<b>19.1</b>	-21.3	73.9	35.8	<b>17.8</b>	-40.4	76.2	
8'	38.7		-30.3	69.1	18.8		-55.6	74.4	
TS2	71.9	<b>33.2</b>	-9.7	81.6	45.8	<b>27.0</b>	-33.1	78.9	
10	-5.8		-68.5	62.8	-31.3		-93.6	62.3	
UiO-66-cluster-b3lyp				UiO-66-NH <sub>2</sub> -cluster-b3lyp					
	$\Delta G$	barrier	$\Delta H$	$-\Delta S$	$\Delta G$	barrier	$\Delta H$	$-\Delta S$	
8	24.1		-30.7	54.8	12.9		-52.4	65.3	
TS1	57.7	<b>33.6</b>	-19.2	76.9	42.6	<b>29.7</b>	-41.7	84.2	
8'	39.8		-35.0	74.8	25.3		-57.9	83.3	
TS2	61.6	<b>21.8</b>	-16.8	78.4	45.2	<b>19.8</b>	-38.6	83.8	
10	-18.9		-79.1	60.2	-40.5		-102.8	62.3	



**Figure S6** Free energy profile at T = 351 K for the reaction on a dehydrated UiO-66 – brick in a periodic model and in a cluster model (B3LYP/6-311++G(d,p)-D3//B3LYP/6-31G(d) level of theory).

**Table S2** Free energy, enthalpic and entropic contributions in kJ/mol at T = 351 K for reaction on Uio-66 and Uio-66-NH<sub>2</sub> in the periodic and cluster model (B3LYP/6-311++G(d,p)-D3//B3LYP/6-31G(d) level of theory).

	Uio-66-Periodic-b3lyp			Uio-66-Periodic-pbe			Uio-66-Cluster-b3lyp		
	$\Delta G$	$\Delta H$	$-\Delta S$	$\Delta G$	$\Delta H$	$-\Delta S$	$\Delta G$	$\Delta H$	$-\Delta S$
4	-32.3	-88.9	56.5	-17.5	-74.1	56.5	-37.5	-92.6	55.1
TSa	-14.8	-75.6	60.7	-4.3	-65.1	60.7	-16.1	-76.8	60.7
4'	-33.7	-88.2	54.5	-27.7	-82.2	54.5	-56.4	-109.8	53.3
9'	-70.1	-191.8	121.7	-32.4	-154.2	121.8	-87.3	-206.2	118.9
TS1'	-20.3	-161.0	140.7	9.8	-130.9	140.7	-36.6	-174.7	138.1
9''	-27.5	-164.6	137.1	-2.0	-139.1	137.1	-37.5	-174.5	137.0
TS2'	26.7	-113.3	140.0	42.6	-97.4	140.0	2.0	-136.5	138.5
11	-49.8	-169.6	119.7	-21.4	-141.1	119.7	-61.0	-178.4	117.3

**Bond distances****Zr-carbonyl and Zr-hydroxyl distance**

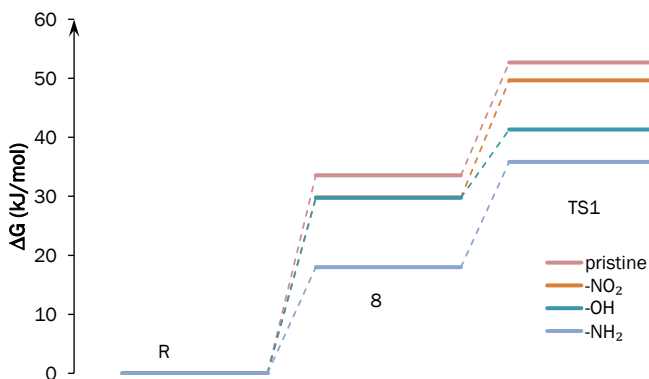
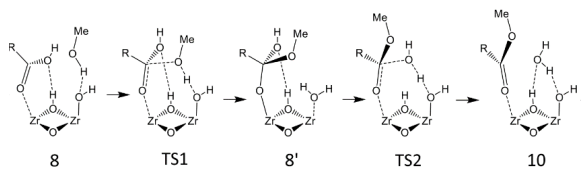
**Figure S7** Bond distances between Zr and carbonyl group of acid and Zr and hydroxyl group at T = 351 K for the reaction on hydrated Uio-66 and Uio-66-NH<sub>2</sub> on the periodic model (B3LYP/6-311++G(d,p)-D3//B3LYP/6-31G(d) level of theory).

**Table S3** Bond distances between Zr and carbonyl group of acid and Zr and hydroxyl group at T = 351 K for the reaction on hydrated Uio-66 and Uio-66-NH<sub>2</sub> on the periodic model (B3LYP/6-311++G(d,p)-D3//B3LYP/6-31G(d) level of theory).

	Zr-acid distance			Zr-OH distance		
	UiO-66	UiO-66-NH <sub>2</sub>	Δr	UiO-66	UiO-66-NH <sub>2</sub>	Δr
8	2.299	2.336	0.007	2.068	2.075	0.037
TS1	2.161	2.214	0.002	2.159	2.161	0.053
8'	2.072	2.116	0.015	2.281	2.296	0.044
TS2	2.152	2.188	0.035	2.221	2.256	0.036
10	2.301	2.342	0.021	2.077	2.098	0.041

## Effect of linker functionalization

Effect of linker functionalization was checked performing the reaction with different electron withdrawing groups. Contrary to what we expect for a purely Lewis catalyzed reaction as in the work of D. De Vos [10], we find a higher barrier for the transition  $8 \Rightarrow 8'$  in case of NO<sub>2</sub> functionalization. And this is in line with our conclusion on the dual Lewis/ Brønsted character of the active site in the Fischer esterification.



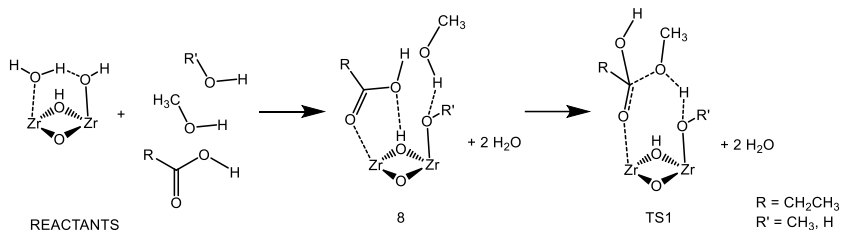
**Figure S8** Free energy for the first three states of the reaction on the hydrated material with different functionalization of the linkers. PBE-D3 level of theory, T=351 K

**Table S4** Free energy, enthalpic and entropic contributions in kJ/mol at T = 351 K for the first three states of the reaction on hydrated material with different functionalization of the linkers. PB3-D3 level of theory

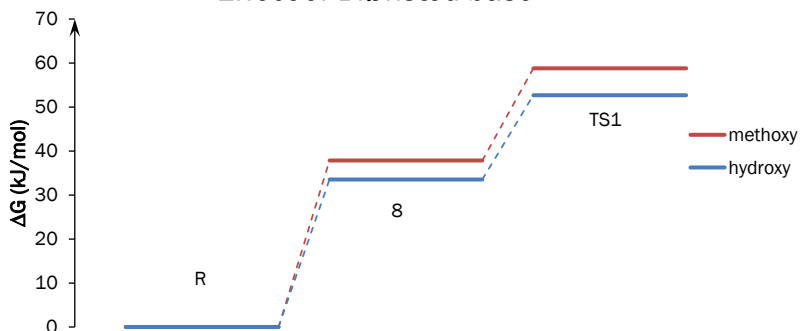
UiO-66				UiO-66-NH <sub>2</sub>				
	$\Delta G$	barrier	$\Delta H$	$-\Delta S$	$\Delta G$	barrier	$\Delta H$	$-\Delta S$
8	33.5		-23.8	57.4	18.0		-42.5	60.5
TS1	52.7	<b>19.1</b>	-21.3	73.9	35.8	<b>17.8</b>	-40.4	76.2
UiO-66-NO <sub>2</sub>				UiO-66-OH				
	$\Delta G$	barrier	$\Delta H$	$-\Delta S$	$\Delta G$	barrier	$\Delta H$	$-\Delta S$
8	29.8		-30.7	60.4	29.7		-34.3	64.0
TS1	49.6	<b>19.9</b>	-31.1	80.7	41.3	<b>11.6</b>	-32.0	73.3

### Effect of methoxide as Brønsted base

In Figure S9 we report the results obtained for the first step of the reaction at PBE-D3 level of theory. We observe an energy barrier that is comparable to the one obtained with hydroxyl group as a Brønsted base, but slightly higher. This is in agreement with the similar Brønsted acidity of methanol ( $pK_a = 15.5$  at 298 K) and water ( $pK_a = 15.7$  at 298 K).



### Effect of Brønsted base



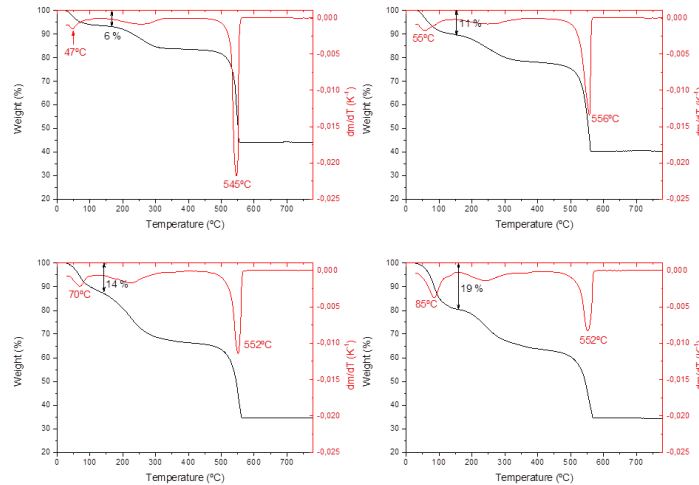
**Figure S9** Free energies for the first three states of the reaction, with hydroxyl group (blue) or methoxy (orange) as Brønsted base. PBE-D3 level of theory, T=351 K

**Table S5** Free energy, Enthalpic and Entropic contributions in kJ/mol at T=351 K for the first three states of the reaction, with hydroxyl group (blue) or methoxy (orange) as Brønsted base. PBE-D3 level of theory.

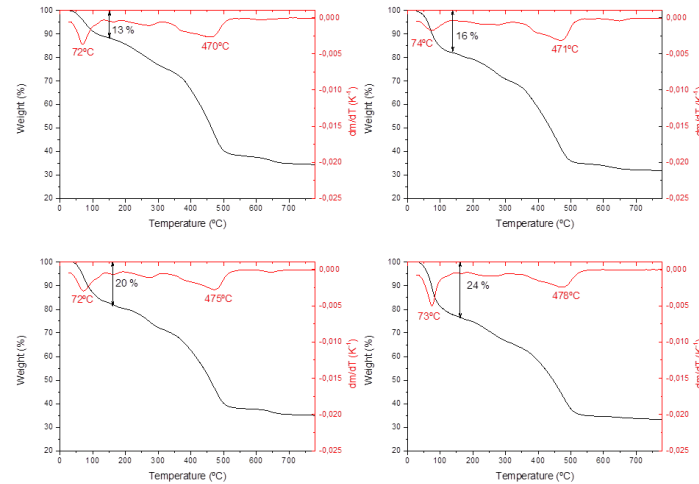
	UiO-66 + hydroxy				UiO-66 + methoxy			
	$\Delta G$	barrier	$\Delta H$	$-\Delta S$	$\Delta G$	barrier	$\Delta H$	$-\Delta S$
8	33.5		-23.8	57.4	37.9		-27.3	65.2
TS1	52.7	<b>19.1</b>	-21.3	73.9	58.8	<b>22.8</b>	-20.7	79.5

## Thermogravimetric Analysis

### UIO-66

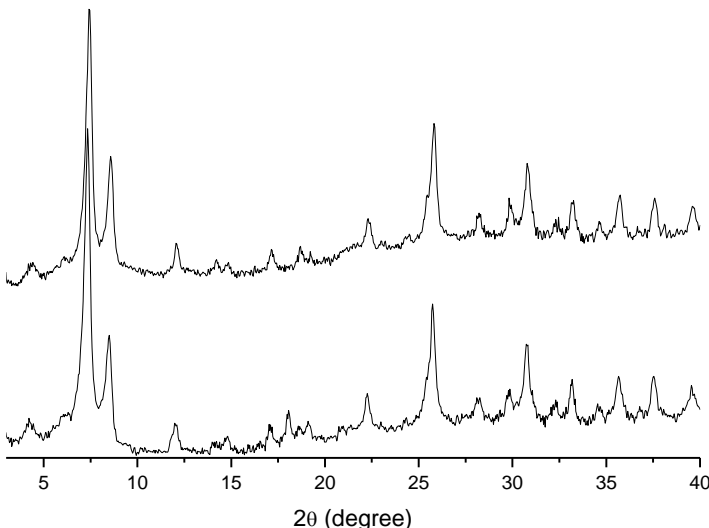


### UIO-66-NH<sub>2</sub>



**Figure S10** Thermograms for UIO-66 and UIO-66-NH<sub>2</sub> with different amount of missing linkers: 2.5%, 4.8%, 7.2%, and 13.2% for UIO-66; and 2.1%, 2.5%, 6.3%, and 8.0% for UIO-66-NH<sub>2</sub>.

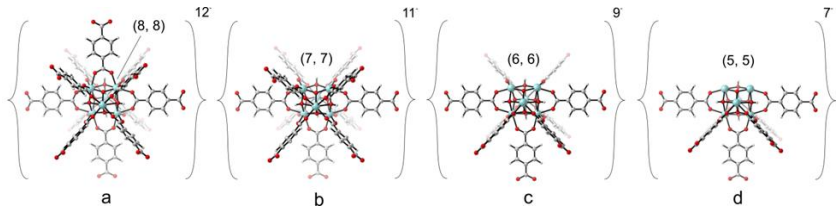
### X-Ray power diffraction patterns



**Figure S11:** XRD patterns of UiO-66 before (top) and after reaction (down).

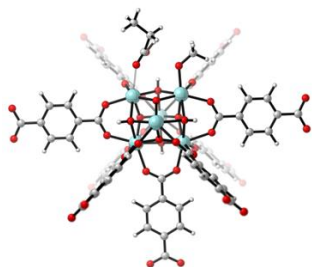
### Active Zr-sites at the surface

To get an idea about the structural difference between active Zr-sites at the surface and pore mouth from those in the interior, we construct the external surface sites of UiO-66 following the procedure as proposed by Chizallet et al. [11, 12]. The method is based on a cluster approach which takes into account the local environment of the active surface site. An inorganic Zr-brick is cut from the pristine UiO-66 material keeping the twelve BDC ligands:  $[Zr_6O_4(OH)_4(BDC)_{12}]^{12-}$  (displayed in Figure S12a). We imagine the upper hemisphere to lie in the vacuum, and the lower hemisphere to be oriented toward the interior of the material. From the parent cluster the ligand which is positioned more or less perpendicular to the surface and oriented toward the empty space, is cleaved. By this cleavage an active surface site is created; its structure is displayed in Figure S12b. Coordination number of the two Zr-atoms decreases to 7. This one-linker defect creates already a surface site which is accessible for small reactant adsorbates. We can further remove ligands which are pointing toward the open hemisphere of the surface. We present two cleaved structures : (b) with cleavage of two additional ligands (Figure S12c) with removal of four additional ligands (Figure S12d).



**Figure S12 :** cluster model of one inorganic Zr-brick. The pristine structure with 12 BDC linkers is displayed in (a). Further cleavage of ligands leads to the other structures which may act as active surface sites. Coordination numbers of the two Zr-atoms of the active Zr-O-Zr (or Zr-OH-Zr) sites are also given.

In Figure S13 we add the two adsorbates (the acid and the alcohol) at the active surface site with one missing ligand (see Figure S13). Some similar cluster of adsorbed complex is obtained with three missing ligands. This complex (Fig. S13) resembles a lot with structure 9' of the manuscript, which stands for a defective active site in the interior of the material. An adsorbed complex on the structure of Fig. S12c will also lead to the same reaction mechanism of the esterification. Solely, the coordination number is decreased to 6. Active surface sites of type Fig. S12d are open for long reactant molecules. This is not investigated, but is also completely out of the scope of this work.



**Figure S13 :** Adsorption complex of the acid and the alcohol at the active surface site with one missing ligand.

There is a large similarity with the adsorbed complex at an active site in the interior of the material.

## Computation of water coordination energy in a periodic unit cell

In Figure 2 of the main manuscript the coordination free energies at reaction temperature of 351 K of one, two and three water molecules at coordinatively unsaturated Zr-bricks in defective UiO-66 are given, respectively represented by configurations 1, 2 and 3. They have been computed with respect to a water coordination free site (site R). The reference state R contains a pool of water molecules in gas phase at atmospheric pressure  $p_0$ . We assume that they obey the ideal gas law :  $p_0V=RT$ .

The coordination free energy is given by :

$$\Delta G_{coord}(nH_2O; T, p_0) = G_{complex}(nH_2O; T) - (G_{empty}(T) + n \mu_{H_2O}^{(g)}(T, p_0))$$

$G_{complex}(nH_2O; T)$  stands for the free energy of the complex formed by the host with n water molecules coordinated to the active site A , as represented by configurations 1, 2 and 3.

$G_{empty}(T)$  is the free energy of the empty host.

$\mu_{H_2O}^{(g)}(T, p_0)$  is the chemical potential of water in gas phase. In order to be compatible with the periodic calculations (with VASP) performed on the material, also a single gas-phase water molecule should be described within the same methodology, as explained in the Methodology section of the main manuscript. A water molecule is placed in a periodic cubic box of 20.0 Å x 20.0 Å x 20.0 Å.

We apply some established thermodynamic expressions for the calculation of  $\mu_{H_2O}^{(g)}(T, p_0)$ .

- (i) The total internal energy is given by :  $U = U_0 + U_{therm}$  with  $U_0 = E_0 = \varepsilon_0 + E_{ZPE}$  including the electronic ground-state energy  $\varepsilon_0$  and the zero-point energy  $E_{ZPE} = \sum_{k=1}^{3N-6} \frac{1}{2} h\nu_k$  , and the internal thermal energy  $U_{therm} = U_{trans} + U_{rot,ext} + U_{vib}$  with

$$U_{trans} = \frac{3}{2} RT$$

$$U_{rot,ext} = \frac{3}{2} RT \quad (\text{for a non-linear molecule}) ; U_{rot,ext} = RT \quad (\text{for a linear molecule})$$

$$U_{vib} = R \sum_{k=1}^{3N-6} \frac{h\nu_k}{k_B} \cdot \frac{1}{e^{\frac{h\nu_k}{k_B T}} - 1}$$

calculated from the thermodynamical expression  $U_{therm} = RT^2 \left( \frac{\partial \ln Q}{\partial T} \right)_{N,V}$  with the total

partition function  $Q = Q_{trans}Q_{rot,ext}Q_{vib}$  taking into account the modified vibrational

$$\text{partition function } Q_{vibr} = \prod_{i=1}^{3N-6} \frac{1}{1 - e^{-\frac{h\nu_i}{k_B T}}}.$$

- (ii) Enthalpy :  $H = U + p_0V$

The work  $p_0V$  is here replaced by  $RT$  following the ideal gas law and respecting constant pressure of the water molecule ( $p_0 = 1 \text{ atm}$ )

(iii) Entropy :  $S = R \ln Q + RT \left( \frac{\partial \ln Q}{\partial T} \right)_{N,V}$

- (iv) Gibbs free energy :

$$G = H - TS$$

$$= U_0 + p_0V - RT \ln Q$$

Second term of the entropic contribution is canceled by the  $U_{therm}$  in the enthalpy.

- (v) Summarizing : within the NpT ensemble we get :

$$\mu_{H_2O}^{(g)}(T, p_0) = U_0 + RT - RT(\ln Q_{trans}(T, p_0) + \ln Q_{rot,ext}(T) + \ln Q_{vibr}(T))$$

with

$$Q_{trans}(T, p_0) = \frac{(2\pi m k_B T)^{3/2}}{h^3} V = \frac{(2\pi m k_B T)^{3/2}}{h^3} \frac{RT}{p_0}$$

$$Q_{rot,ext}(T) = \frac{\sqrt{\pi}}{\sigma} \left( \frac{8\pi^2 k_B T}{h^2} \right)^{3/2} (I_x I_y I_z)^{1/2} \text{ with moments of inertia } I_x, I_y, I_z \text{ and symmetry number } \sigma (=2 \text{ for water molecule})$$

$$Q_{vibr}(T) = \prod_{i=1}^{3N-6} \frac{1}{1 - e^{-\frac{\hbar \nu_i}{k_B T}}}$$

- (vi) For water in the gas phase on temperature T and pressure p the chemical potential is

$$\text{given as } \mu_{H_2O}^{(g)}(T, p) = \mu_{H_2O}^{(g)}(T, p_0) + RT \ln \left( \frac{p}{p_0} \right)$$

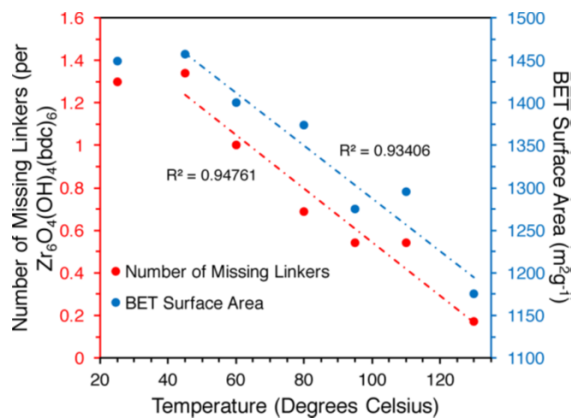
which agrees with the expression given in the SI of ref. [13].

In the paper we systematically considered a pressure of 1 atmosphere for the water in gas phase. The free energy calculation of the complex and the empty frame - both are in condensed phase - is performed along the same lines as explained above. The  $pV$  term in the expression of the (Gibbs) free energy is not kept, but this is not of any relevance as this term disappears in the difference of  $G_{complex}(nH_2O; T)$  and  $G_{empty}(T)$ . Calculation of translational and rotational contributions are also not of physical significance for the periodic complex and empty frame. In addition, even if some contributions would be calculated, they cancel each other when taking the difference between the two materials.

All steps are incorporated in the in-house developed processing toolkit TAMkin . The procedure to compute coordination free energies is completely automated. [14]

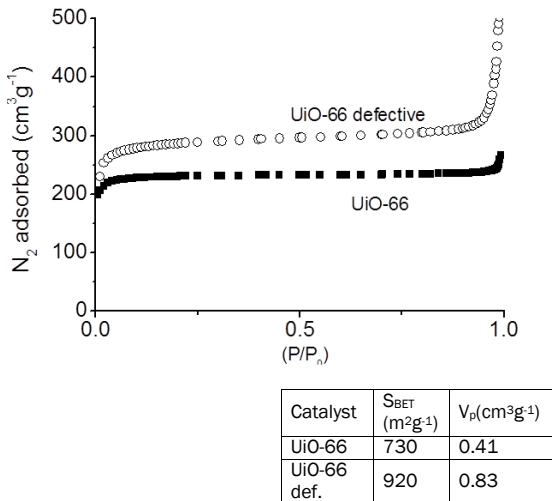
### Diffusion of reactants due to the presence of defects

The presence of defects in MOFs (both missing linkers and missing nodes) can lead to an increase of the specific surface area and pore volume of the material, as compared to a pristine, defect free material. Indeed, very recently [15] have reported that a direct correlation exists between the density of defects and the BET surface area and the total pore volume. According to these authors, the presence of defect sites, whether arising from missing linkers or clusters, results in more accessible space in the framework. A direct consequence of an increased number of defects is the formation of larger micropores, giving rise to larger pore volumes and more accessible space and thus larger surface areas. This is clearly shown in Figure S14 of their paper, which is reproduced below:



**Figure S14 :** correlation between BET surface area and number of missing linkers.

In our hands, we have also observed an increment of both, BET surface and pore volume on increasing the amount of defects, as shown in Figure S15 :



**Figure S15 :** BET surface and pore volume on increasing the amount of defects

It is evident that an increase of both specific surface area and pore volume will facilitate the diffusion of molecules throughout the pore system of a MOF. Therefore, it is reasonable to hypothesize that diffusion will be faster on a defective UiO-66 as compared with a defect free sample, due to the higher porosity of the former material. This can have direct implications in the catalytic reaction, but only for diffusion-controlled reactions.

In any catalytic process, the rate of product formation can be controlled by either the diffusion of reactants from the solution to the catalytic active sites (diffusion-controlled reaction), or by the catalytic reaction taking place at the active sites (activation-controlled reaction). In this latter case, diffusion of the reactants is already fast enough (the rate limiting step is not the diffusion but the chemical transformation taking place at the active site). Therefore, any increase on the diffusion rate will not translate into an increase of the overall conversion rate.

Therefore, it is very important to determine in each particular case which is the limiting factor governing the reaction rate.

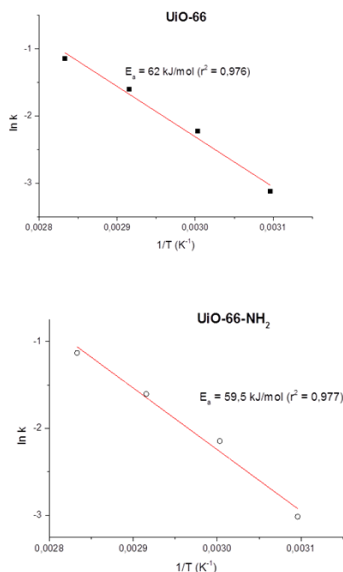
In the particular case of the esterification of levulinic acid (LA) with ethanol, we have carried out the following experiments to determine which type of reaction control operates:

- 1) External diffusion: To check whether external diffusion limitations were present during the esterification reaction of LA with ethanol, we carried out the reaction at various stirring rates (from

100–800 rpm) during preliminary screening of the catalysts. Since the mass-transfer coefficient depends on the fluid velocity around the catalyst, external limitations then would show by a change in conversion. If no external limitations exist, the resulting conversions should be the same. Our preliminary experiments revealed that there was no external mass transfer limitations for stirring rates >200 rpm. So all the data reported in this work were carried out at stirring rates well above this value (i.e., >400 rpm).

2) Internal diffusion: In order to determine whether the reaction is controlled by internal (intra-particle) diffusion or by the chemical reaction, in principle one can vary the particle dimensions of the material: for example, by crushing and sieving the catalyst. However, in the case of MOFs this can be tricky, because particle crushing might result in structural collapse. Alternatively, one can carry out the reaction at various reaction temperatures and evaluate the activation energy from the corresponding Arrhenius plot.

We thus carried out the esterification of LA with ethanol over UiO-66 and UiO-66-NH<sub>2</sub> at temperatures comprised between 323 and 353 K. The results obtained are summarized in Figure S16.



**Figure S16 :** Activation energy from the corresponding Arrhenius plot for the esterification of LA with ethanol over UiO-66 and UiO-66-NH<sub>2</sub> at temperatures comprised between 323 and 353 K.

In both cases, the calculated activation energies are relatively high (~60 kJ/mol), which is a clear indication that the reaction is chemically controlled. A much lower activation energy (10-15 kJ/mol) would be expected for a diffusion-controlled reaction (see References [16-20]).

In summary, our experiments clearly demonstrate that in the case of LA esterification with ethanol, the reaction is controlled by the chemical process and that there are no diffusion limitations. Therefore, even if the presence of defects in the catalyst (either missing linkers or missing nodes) may increase the diffusion properties of the material, this would not translate into an improvement of the catalytic performance of the material for this particular reaction. However, as we tried to stress in our previous reply, this holds true only for the particular case of the LA esterification with ethanol. For other (bulkier) substrates, diffusion limitations can become important, or even dominate predominantly the observed catalytic activity. In these latter cases, the role of missing nodes (although not directly involved in the reaction) may result in an indirect effect leading to an increase of the rate of product formation. It is evident that diffusion issues is not a minor subject when assessing the catalytic properties of a material. However, this is not the point of our present paper, which tries to shed light to understand the general mechanism of esterification of ANY carboxylic acids (not just levulinic acid) over defective Zr sites in UiO-66 materials. Therefore, we think that these particular details of the catalytic study (although important) go beyond the discussion considered in the present work and its inclusion in the revised manuscript would only deviate the attention of the reader.

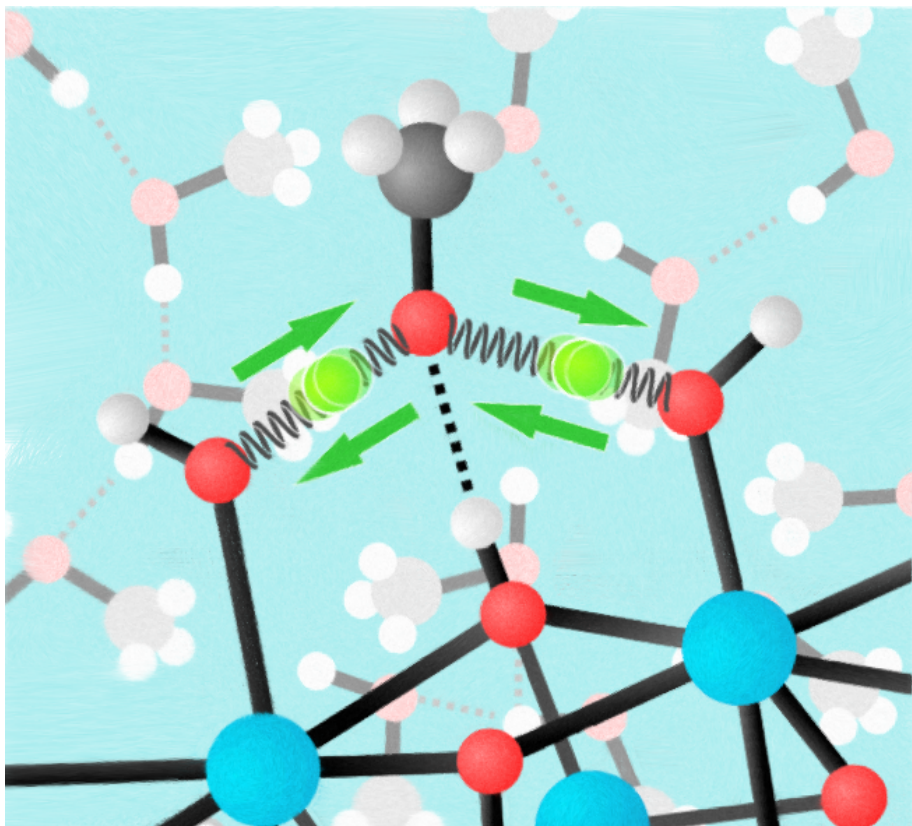
## References

- [1] T. Verstraelen, V. Van Speybroeck, M. Waroquier, ZEOBUILDER: A GUI toolkit for the construction of complex molecular structures on the nanoscale with building blocks, *Journal of Chemical Information and Modeling*, 48 (2008) 1530-1541.
- [2] R.A. Gaussian 09, Frisch, M. J.; Trucks, G. W.; Schlegel, H. B.; Scuseria, G. E.; Robb, M. A.; Cheeseman, J. R.; Scalmani, G.; Barone, V.; Mennucci, B.; Petersson, G. A.; Nakatsuji, H.; Caricato, M.; Li, X.; Hratchian, H. P.; Izmaylov, A. F.; Bloino, J.; Zheng, G.; Sonnenberg, J. L.; Hada, M.; Ehara, M.; Toyota, K.; Fukuda, R.; Hasegawa, J.; Ishida, M.; Nakajima, T.; Honda, Y.; Kitao, O.; Nakai, H.; Vreven, T.; Montgomery, Jr., J. A.; Peralta, J. E.; Ogliaro, F.; Bearpark, M.; Heyd, J. J.; Brothers, E.; Kudin, K. N.; Staroverov, V. N.; Kobayashi, R.; Normand, J.; Raghavachari, K.; Rendell, A.; Burant, J. C.; Iyengar, S. S.; Tomasi, J.; Cossi, M.; Rega, N.; Millam, J. M.; Klene, M.; Knox, J. E.; Cross, J. B.; Bakken, V.; Adamo, C.; Jaramillo, J.; Gomperts, R.; Stratmann, R. E.; Yazyev, O.; Austin, A. J.; Cammi, R.; Pomelli, C.; Ochterski, J. W.; Martin, R. L.; Morokuma, K.; Zakrzewski, V. G.; Voth, G. A.; Salvador, P.; Dannenberg, J. J.; Dapprich, S.; Daniels, A. D.; Farkas, Ö.; Foresman, J. B.; Ortiz, J. V.; Cioslowski, J.; Fox, D. J. Gaussian, Inc., Wallingford CT, 2009., in.
- [3] A.D. Becke, Density-functional exchange-energy approximation with correct asymptotic behavior, *Physical Review A*, 38 (1988) 3098-3100.
- [4] A.D. Becke, DENSITY-FUNCTIONAL THERMOCHEMISTRY .3. THE ROLE OF EXACT EXCHANGE, *Journal of Chemical Physics*, 98 (1993) 5648-5652.
- [5] C.T. Lee, W.T. Yang, R.G. Parr, DEVELOPMENT OF THE COLLE-SALVETTI CORRELATION-ENERGY FORMULA INTO A FUNCTIONAL OF THE ELECTRON-DENSITY, *Physical Review B*, 37 (1988) 785-789.
- [6] P.J. Hay, W.R. Wadt, Ab-initio effective core potentials for molecular calculations - Potentials for the transition-metal atoms Sc to Hg, *Journal of Chemical Physics*, 82 (1985) 270-283.
- [7] P.J. Hay, W.R. Wadt, Abinitio Effective Core Potentials for Molecular Calculations - Potentials for K to Au Including the Outermost Core Orbitals, *Journal of Chemical Physics*, 82 (1985) 299-310.

- [8] W.R. Wadt, P.J. Hay, Ab initio Effective Core Potentials for Molecular Calculations - Potentials for Main Group Elements Na to Bi, *Journal of Chemical Physics*, 82 (1985) 284-298.
- [9] S. Grimme, J. Antony, S. Ehrlich, H. Krieg, A consistent and accurate ab initio parametrization of density functional dispersion correction (DFT-D) for the 94 elements H-Pu, *Journal of Chemical Physics*, 132 (2010).
- [10] F. Vermoortele, M. Vandichel, B. Van de Voorde, R. Ameloot, M. Waroquier, V. Van Speybroeck, D.E. De Vos, Electronic Effects of Linker Substitution on Lewis Acid Catalysis with Metal-Organic Frameworks, *Angewandte Chemie-International Edition*, 51 (2012) 4887-4890.
- [11] C. Chizallet, N. Bats, External Surface of Zeolite Imidazolate Frameworks Viewed Ab Initio: Multifunctionality at the Organic-Inorganic Interface, *Journal of Physical Chemistry Letters*, 1 (2010) 349-353.
- [12] C. Chizallet, S. Lazare, D. Bazer-Bachi, F. Bonnier, V. Lecocq, E. Soyer, A.A. Quoineaud, N. Bats, Catalysis of Transesterification by a Nonfunctionalized Metal-Organic Framework: Acido-Basicity at the External Surface of ZIF-8 Probed by FTIR and ab Initio Calculations, *Journal of the American Chemical Society*, 132 (2010) 12365-12377.
- [13] P. Dementyev, K.H. Dostert, F. Ivars-Barcelo, C.P. O'Brien, F. Mirabella, S. Schauermann, X.K. Li, J. Pailer, J. Sauer, H.J. Freund, Water Interaction with Iron Oxides, *Angewandte Chemie-International Edition*, 54 (2015) 13942-13946.
- [14] A. Ghysels, T. Verstraelen, K. Hemelsoet, M. Waroquier, V. Van Speybroeck, TAMkin: A Versatile Package for Vibrational Analysis and Chemical Kinetics, *Journal of Chemical Information and Modeling*, 50 (2010) 1736-1750.
- [15] M.R. DeStefano, T. Islamoglu, J.T. Hupp, O.K. Farha, Room-Temperature Synthesis of UiO-66 and Thermal Modulation of Densities of Defect Sites, *Chem. Mat.*, 29 (2017) 1357-1361.
- [16] J. Bedard, H. Chiang, A. Bhan, Kinetics and mechanism of acetic acid esterification with ethanol on zeolites, *Journal of Catalysis*, 290 (2012) 210-219.
- [17] K.Y. Nandiwale, P.S. Niphadkar, S.S. Deshpande, V.V. Bokade, Esterification of renewable levulinic acid to ethyl levulinate biodiesel catalyzed by highly active and reusable desilicated H-ZSM-5, *Journal of Chemical Technology and Biotechnology*, 89 (2014) 1507-1515.
- [18] A. Patel, V. Brahmkhatri, Kinetic study of oleic acid esterification over 12-tungstophosphoric acid catalyst anchored to different mesoporous silica supports, *Fuel Processing Technology*, 113 (2013) 141-149.
- [19] W.Y. Shi, B.Q. He, J.X. Li, Esterification of acidified oil with methanol by SPES/PES catalytic membrane, *Bioresource Technology*, 102 (2011) 5389-5393.
- [20] X.-Q. Zhang, R.A. van Santen, A.P.J. Jansen, Kinetic Monte Carlo modeling of silicate oligomerization and early gelation, *Physical Chemistry Chemical Physics*, 14 (2012) 11969-11973.

## Paper II

### Influence of a confined methanol solvent on the reactivity of active sites in UiO–66



C. Caratelli, J. Hajek, S.M.J. Rogge, S. Vandenbrande, E.J. Meijer, M. Waroquier, V. Van Speybroeck, *ChemPhysChem*, **19**, 420–4290 (2018)

C. Caratelli performed all the calculations and prepared the manuscript.

©2018 Wiley-VCH Verlag GmbH & Co  
Reprinted with permission from Wiley-VCH Verlag.



# Influence of a Confined Methanol Solvent on the Reactivity of Active Sites in UiO-66

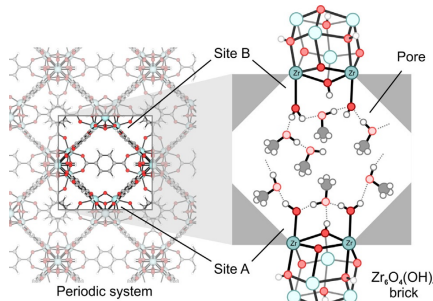
Chiara Caratelli,<sup>[a]</sup> Julianna Hajek,<sup>[a]</sup> Sven M. J. Rogge,<sup>[a]</sup> Steven Vandenbrande,<sup>[a]</sup> Evert Jan Meijer,<sup>[b]</sup> Michel Waroquier,<sup>[a]</sup> and Veronique Van Speybroeck<sup>\*[a]</sup>

UiO-66, composed of Zr-oxide bricks and terephthalate linkers, is currently one of the most studied metal–organic frameworks due to its exceptional stability. Defects can be introduced in the structure, creating undercoordinated Zr atoms which are Lewis acid sites. Here, additional Brønsted sites can be generated by coordinated protic species from the solvent. In this Article, a multilevel modeling approach was applied to unravel the effect of a confined methanol solvent on the active sites in UiO-66. First, active sites were explored with static periodic density functional theory calculations to investigate adsorption of water and methanol. Solvent was then introduced in the pores with grand canonical Monte Carlo simulations, followed by a series of molecular dynamics simulations at operating

conditions. A hydrogen-bonded network of methanol molecules is formed, allowing the protons to shuttle between solvent methanol, adsorbed water, and the inorganic brick. Upon deprotonation of an active site, the methanol solvent aids the transfer of protons and stabilizes charged configurations via hydrogen bonding, which could be crucial in stabilizing reactive intermediates. The multilevel modeling approach adopted here sheds light on the important role of a confined solvent on the active sites in the UiO-66 material, introducing dynamic acidity in the system at finite temperatures by which protons may be easily shuttled from various positions at the active sites.

## 1. Introduction

UiO-66 is a metal–organic framework (MOF) which has received significant attention from both experimental and theoretical researchers since its discovery in 2008.<sup>[1]</sup> Its attractiveness can be mainly traced back to its exceptional thermal, chemical and mechanical stability<sup>[2]</sup> and to the relative facility by which (linker) defects can be induced in the structure.<sup>[3]</sup> These linker defects create under-coordinated metal sites which act as Lewis acid sites that can be used for catalysis.<sup>[4]</sup> The chemical formula for a defect-free UiO-66 unit cell is  $[Zr_6O_4(OH)_4][C_6H_4(COO)_2]_6$ , as displayed in Figure 1. Each Zr-brick represents a six-centered zirconium oxyhydroxide cluster



**Figure 1.** Schematic representation of a pore in UiO-66. Left: periodic lattice; right: the pore where the missing linker defect is located, with included guest molecules. The active sites site A and B are indicated on the left.

[a] C. Caratelli, J. Hajek, S. M. J. Rogge, S. Vandenbrande, Prof. Dr. em. M. Waroquier, Prof. Dr. ir. V. Van Speybroeck  
Center for Molecular Modeling (CMM)  
Ghent University  
Technologiepark 903, 9052 Zwijnaarde (Belgium)  
E-mail: veronique.vanspeybroeck@ugent.be

[b] Prof. Dr. E. J. Meijer  
Amsterdam Center for Multiscale Modeling  
and van ‘t Hoff Institute for Molecular Sciences  
University of Amsterdam  
Science Park 904, 1098 XH Amsterdam (The Netherlands)

Supporting Information for this article can be found under:  
<https://doi.org/10.1002/cphc.201701109>.

© 2018 The Authors. Published by Wiley-VCH Verlag GmbH & Co. KGaA. This is an open access article under the terms of the Creative Commons Attribution-NonCommercial License, which permits use, distribution and reproduction in any medium, provided the original work is properly cited and is not used for commercial purposes.

An invited contribution to a Special Issue on Reactions in Confined Spaces

(octahedron of Zr atoms whose faces are capped by  $\mu_3$ -oxo and  $\mu_3$ -hydroxyl groups in an alternating fashion), linked via terephthalate or benzenedicarboxylate (bdc) linkers to form a face-centered-cubic net (**fcu-a** topology). As has been reported by Lillerud and co-workers,<sup>[1]</sup> each Zr metal is fully coordinated by 12 organic linkers to form a highly connected framework if no linker defects are present. This high connectivity lies on the basis of its exceptional structural stability and rigidity.

Another feature that makes UiO-66 very attractive for catalysis is the presence of both acid and basic centers within molecular distances, yielding active sites with bifunctional behavior.<sup>[5]</sup> In addition, the presence of water has a distinct influence on

the acidity and basicity of the active sites. Recently, Ling and Slater<sup>[6]</sup> used molecular dynamics simulations to show the existence of some dynamic acidity, created by a double proton transfer involving two physisorbed water molecules and a hydroxide anion in the defect structure. The findings of Ling and Slater have been confirmed independently by some of the present authors.<sup>[7]</sup> Its remarkable properties lie on the basis of the numerous coordination bonds of the linkers with the metal centers. When focusing on the catalytic behavior of the UiO-66 material, knowledge of the molecular structure of the active sites created by linker defects is an essential ingredient to understand the reactivity of the node with coordinating species such as water and methanol, and eventually to tune its catalytic properties. These species introduce additional Brønsted sites which can play a role in reactions catalyzed by the material. A combined experimental-theoretical work<sup>[8]</sup> demonstrated that the topology of the OH/OH<sub>2</sub> defect coordinating species on the Zr<sub>6</sub> node-face can be tuned with intermediate steps in which methanol replaces water on the Zr sites. Insight in the nature of active sites and the methanol substitution process was obtained, indicating that the thermodynamically most favorable structure was obtained with a node-face containing a methoxide and an open Zr metal site.<sup>[8]</sup> Further understanding of the broad variety of defect structures in the UiO-66 material was obtained by several recent theoretical works,<sup>[6–9]</sup> investigating possible structures where up to three defect coordinating molecules are involved. These metal-oxide-like nodes of UiO-66 unveil acid-base properties which are beneficial for a series of catalytic reactions such as the jasminaldehyde condensation, the Oppenauer oxidation<sup>[5,10]</sup> and the Fischer esterification of carboxylic acids with alcohols.<sup>[9]</sup> More precisely, special attention was given to the role of coordinated species to generate additional Brønsted acid and base sites in the UiO-66 material. Water was shown to have a beneficial effect on the reactivity by providing additional Brønsted sites and extra stabilization for various intermediates through hydrogen bonding. The bifunctional character of the catalyst has been highlighted. This conclusion was based on a concerted acid-base reaction mechanism that was found for the esterification reaction of propionic acid with methanol, in which water formed a combined Lewis/Brønsted network in defective UiO-66 material. However, it may be anticipated that such behavior is not restricted to water only but may also be extended to other protic molecules, such as methanol. This is especially important as many reactions take place in protic solvents like alcohols.

Herein we investigate the remarkable dynamic complexity of defect termination of UiO-66 in a methanol solution. This is of high importance as many heterogeneous catalytic reactions are performed in solution, where the solvent can play a notable role in facilitating or hindering the reaction due to its interactions with the catalyst and the solute. We particularly study the role of the solvent present in the confined cavities of the material and its interaction with the active sites, as displayed schematically in Figure 1. A major unresolved challenge lies in the characterization of the active sites at operating conditions when more molecules are confined in the pores of the materi-

al. It remains unclear in how far the presence of extra methanol molecules in the pores of the material affects the accessibility and nature of the active sites. For instance, solvent molecules can play a role by connecting the two active sites that are generated by local defects by means of linker vacancies and can shuttle protons of reactive species from one site to the other. The simplest theoretical model includes only species that are directly bonded to the Zr atoms. A more complex system could be generated by introducing additional molecules to reproduce the first solvation spheres. However, a more realistic behavior of the system at operating conditions can only be obtained by following the system in time under realistic temperatures and pressures and taking the full solvent environment in the pores of the material into account.

In this work, we study the nature of the active sites in the UiO-66 material at operating conditions in the presence of a realistic loading of methanol molecules confined in the pores of the material. To this end, a multistep modeling approach is used. First, a series of static periodic density functional theory (DFT) calculations were performed to estimate structures of the active sites with coordinated water or methanol molecules. Second, a full loading of the unit cell with methanol was considered. The number of methanol molecules was estimated by means of a series of grand canonical Monte Carlo (GCMC) calculations. In these simulations, we estimated the maximum uptake of solvent molecules in the pores of the defective hydrated UiO-66 unit cell with two water molecules capping the Zr metal sites at each defect site. Then, a series of molecular dynamics simulations was performed in the NVT ensemble, after an equilibration run in the NPT ensemble at 330 K, which is below the boiling point of methanol. The followed modeling approach yields insight into the role of a confined methanol solvent in the pores of the UiO-66 framework and its influence on the nature of the active sites. We will show that the active sites show a remarkable dynamic behavior where protons can be easily shuttled among various position on the defective sites.

## Computational Methods

To estimate the influence of a methanol solvent loading on the active sites in the UiO-66 material, a multistep modeling approach was used. First, the active sites were explored with static periodic calculations, investigating the role of defect capping species with different topologies. These calculations are necessary in order to get realistic starting structures and to obtain insight on the species directly coordinated to the Zr atoms. In a second step, a full loading of methanol solvent was considered. The initial loading in the pores was estimated by means of grand canonical Monte Carlo simulations, using an empirical force-field model. Subsequently, DFT-based molecular dynamics simulations were performed on a defective UiO-66 where Zr atoms are capped with water molecules. For our study, it is crucial to model hydrogen bonding and proton transfer mechanisms. These phenomena involve bonds being broken and formed and need an electronic level treatment in order to be correctly reproduced. Force-field based molecular dynamics would never capture these features even after long simulation times. Therefore, an ab initio treatment is required. The computational details for each of these calculations are outlined below.

## Static DFT Calculations

The various structures at the active site were investigated with a static DFT approach using a periodic model to correctly describe the environment surrounding the active sites. In this work, the same methodology and level of theory of previous work of the authors are adopted.<sup>[9–10]</sup> The calculations were performed with the Vienna Ab Initio Software Package (VASP),<sup>[11]</sup> applying the projector augmented wave approximation (PAW),<sup>[12]</sup> and limiting the sampling of the Brillouin zone to the  $\Gamma$  point. The structures were optimized with PBE exchange-correlation functional<sup>[13]</sup> complemented by the Grimme D3<sup>[14]</sup> dispersion corrections. The energy cutoff for the plane waves was set to 700 eV, and the convergence threshold for the electronic self-consistent field (SCF) calculations was fixed to  $10^{-5}$  eV. To improve convergence, a Gaussian smearing of 0.025 eV was also included. The used periodic unit cell is built following the crystallographic structure provided by Cavka et al.<sup>[1]</sup> Following a methodology already established in earlier works of present authors,<sup>[5,7,9–10,15]</sup> frequency calculations were performed on each periodic structure with a partial Hessian approach.<sup>[16]</sup> Firstly, they indicate if all structures were correctly optimized. Only positive values for the frequencies of the reported states ensure that they correspond to minima in the potential energy surface. Secondly, frequencies are used to account for the finite temperature effects in the calculation of free energy differences. For this purpose, thermal corrections were computed using the in-house developed processing toolkit TAMkin.<sup>[17]</sup>

## Active Sites in the Defective UiO-66 Unit Cell

In this work, we will restrict ourselves to active sites which are created by the removal of two terephthalate linkers in the conventional unit cell of four inorganic Zr-bricks. Many possibilities exist to remove two linkers. A rationalization of these two-linker defects has been done in Ref. [18]. The defect structure denoted as **type 6** in the work of Rogge<sup>[18b]</sup> was chosen here, as this structure ensures the highest accessibility for guest species, as shown in our earlier work.<sup>[5,9–10]</sup> We gave preference to the situation where active sites were created showing the best perspective for guest intrusion and accessibility of the metal center. In addition, the symmetry of this linker deficiency allows to reduce the dimension of the unit cell to two bricks. The structure of these active sites has been extensively outlined in previous works of the authors.<sup>[5,7,9,15]</sup>

The defective brick  $\langle \text{Zr}_6\text{O}_6(\text{OH})_2 \rangle^{10+}$  is tenfold coordinated, and shows two distinct active sites which lie on opposite sides of the brick, as displayed in Figure 1. We will refer to these sites as **site A** and **B**. When atmospheric water is present, the Zr-brick becomes hydrated: water molecules physisorb on the coordinatively unsaturated metal centers. One of the water molecules then dissociates into a hydroxyl group adsorbed on the Zr-atom and a proton is adsorbed on the adjacent  $\mu_3$ -oxygen, to give a more stable structure, as discussed in literature.<sup>[6–9]</sup> The unit cell of this hydrated UiO-66 material with two missing terephthalate linkers is displayed in Figure 1. The two hydrated node surface sites **A** and **B** exhibit the same structure. Further static periodic DFT calculations are performed with different types of coordination with water and methanol on **site A** while keeping the hydrated **site B** as passive.

## Grand Canonical Monte Carlo

To estimate the number of methanol molecules which can be inserted in the UiO-66 framework, we used Grand Canonical Monte Carlo (GCMC) simulations as implemented in the RASPA software

package.<sup>[19]</sup> The employed force field describes the short-range repulsion and long-range van der Waals attraction by a Lennard-Jones potential, and electrostatics via point-charge Coulombic interactions. The methodology is the same as used by Ghosh et al.<sup>[20]</sup> to describe water and CO<sub>2</sub> adsorption in UiO-66. The Lennard-Jones parameters of the framework atoms are obtained from Dreiding<sup>[21]</sup> (except for Zr for which the UFF<sup>[22]</sup> parameters are used) and framework charges are computed using the Extended Charge Equilibration method.<sup>[23]</sup> The TraPPE<sup>[24]</sup> model is used for the methanol guest atoms. In the GCMC simulations, van der Waals interactions are truncated beyond a distance of 12.8 Å, which is compensated by analytical tail corrections. For the electrostatic interaction, the Ewald summation to account for the long-range nature of this interaction is used. Each run consists of 10 000 equilibration cycles and 20 million production cycles, where a cycle consists of at least 20 Monte Carlo move attempts. The concept of a 2-brick unit cell is systematically employed in all calculations performed in the frame of this work. It implies that structures are easily interchangeable between the different approaches. Snapshots belonging to GCMC runs can be directly used as starting configurations for the ab initio molecular dynamics simulations. A temperature of 330 K and a pressure of 50 atm is applied and it is verified that methanol in UiO-66 shows liquid behavior under these conditions.<sup>[25]</sup>

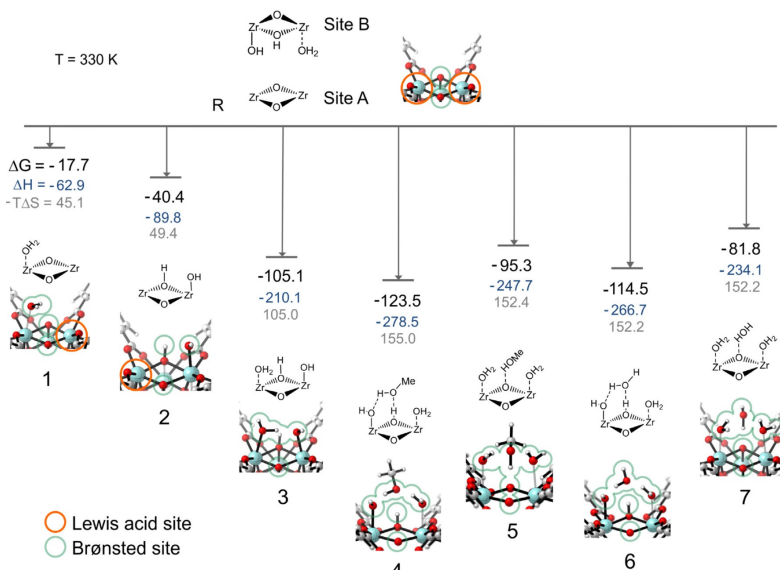
## Molecular Dynamics

DFT-based molecular dynamics simulations were performed with the CP2K software package,<sup>[26]</sup> that employs a hybrid Gaussian Plane Wave basis sets approach.<sup>[27]</sup> The DFT functional is taken to be the PBE<sup>[13]</sup> which was supplemented by Grimme D3 dispersion corrections.<sup>[14b]</sup> A DZVP-GTH basis set was used for C, O and H atoms together with pseudopotentials.<sup>[28]</sup> For Zr the DZVP-MOLOPT-SR basis set was taken into account. The time step for integration of the equation of motion was set to 0.5 fs, and the temperature was controlled by a Nosé-Hoover chain thermostat consisting of five beads and a time constant of 0.3 ps.<sup>[29]</sup> The unit cell used was taken from the static calculations and the methanol configurations were extracted from the GCMC simulation. A first simulation of 25 ps was performed in the NPT ensemble at 330 K and 1 bar, using a MTK barostat with a time constant of 0.1 ps.<sup>[30]</sup> The final structure is then used as starting configuration in an NVT simulation of 50 ps keeping the unit cell parameters fixed.

## 2. Results and Discussion

### 2.1. Free-Energy Balance—Water and Methanol Coordination on Defective Metal Sites

A first step towards a thorough understanding of the influence of methanol on the active sites in the UiO-66 material may be done by studying the stability of the various coordinated systems, involving physisorbed and chemisorbed water and methanol molecules on the active Zr sites. This first step can best be accomplished by means of static periodic calculations, as already done for the case of water in a recent paper of some of the authors.<sup>[9]</sup> As a result, insight is obtained into the structural topology of the Zr<sub>6</sub> node and the associated chemistry. To allow for a comparative discussion on coordination energies, the structure of **site B** (facing **site A** at the opposite brick (Figure 1)) is kept fixed in all structure calculations and is as-



**Figure 2.** Coordination free energies at temperature of 330 K of water and methanol at coordinatively unsaturated Zr-oxide bricks in defective UiO-66, with respect to a water coordination free node face R. We assume a hydrated site B which is kept fixed in the static calculations for the different structures of site A. Free energies in black are given in kJ mol<sup>-1</sup> and their decompositions into enthalpic (blue) and entropic contributions (grey). Energies resulting from periodic calculations at PBE-D3 level of theory.

sumed to show a hydrated node surface. The results of these static periodic calculations are shown in Figure 2.

In an environment with atmospheric water, the bare  $Zr_2O_5$  face will be hydrated immediately. The stabilization caused by one water molecule physisorbed to one of the undercoordinated Zr-atoms amounts to 17.7 kJ mol<sup>-1</sup> at 330 K (structure 1 of Figure 2). The molecule can be deprotonated to the  $\mu_3$ -oxygen atom (structure 2), lowering the free energy with an additional 22.7 kJ mol<sup>-1</sup>. The remaining open metal site acts as a Lewis acid center while a Brønsted acid and basic site arise on the  $\mu_3$ -hydroxyl and the hydroxyl bonded to the metal. The most stable configurations at 330 K are complexes with two or three water molecules. In configuration 3, both Zr sites are capped with a physisorbed and a chemisorbed water molecule, respectively, stabilizing the complex with an extra 64.7 kJ mol<sup>-1</sup>. Adding a third molecule yields a complex (structure 6 in Figure 2) which is slightly more stabilized ( $\approx$  9.4 kJ mol<sup>-1</sup>) than the complex with two coordinated water molecules. The additional water molecule is coordinated to the  $\mu_3$ -hydroxyl group and the Zr-OH group in accordance with what has been reported by Ling and Slater<sup>[6]</sup> and Vandichel et al.<sup>[7]</sup> However, the small additional coordination energy will lead to a spontaneous decoordination of this water molecule from the active site. With the presence of a solvent molecule like methanol in the vicinity of the active site, one could expect that water can

be displaced to allow for coordination by methanol. This may be important for reactions where methanol takes an active role in the chemical conversion which is for example, the case for esterification. Configuration 4 in Figure 2 is characterized by methanol which is settled along the hydrated face (structure 3) by means of hydrogen bonds with the Zr adsorbed water and hydroxide anion and with the  $\mu_3$ -hydroxyl group. This complex has an extra stabilization energy of 18.4 kJ mol<sup>-1</sup> compared to the well-known configuration 3. Another possible arrangement is structure 5, with two water molecules physisorbed to the two adjacent under-coordinated Zr-centers and a methanol coordinated to the  $\mu_3$ -oxygen atom. Summarizing, the static calculations give a good picture of how the active sites created by linker deficiencies are capped with water in atmospheric conditions, and how methanol can easily replace water when coordinated to the hydrated site. Structure 4, in which methanol is hydrogen-bonded with the  $\mu_3$ -hydroxyl group and Zr-OH, is even the most stable. Therefore, based on the static calculations one could predict that configuration 4 will be the most visited configuration in a MD simulation at operating conditions and with the pores filled with liquid methanol. Further in this paper, as part of our multilevel modeling approach, we will elaborate in how far these initial results correspond to a dynamic loading of the pores at operating conditions.

## 2.2. GCMC Calculations to Estimate the Loading of Methanol in the Pores of Defective UiO-66

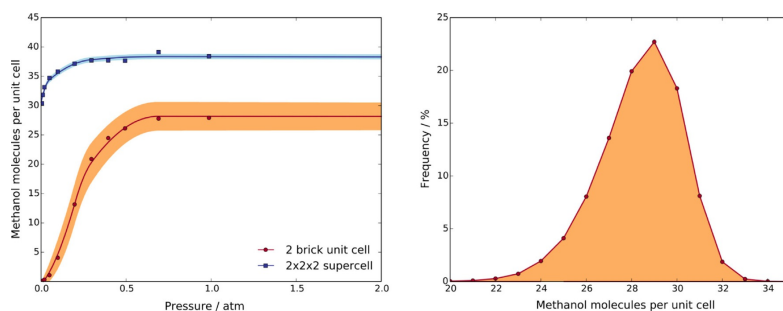
As a next step of our multilevel approach, we estimate the number of methanol molecules in the pores of the UiO-66 material at a temperature of 330 K and a pressure of 50 atmospheres, where methanol is in liquid phase. To this end, a series of GCMC calculations have been performed at various pressures. This yields a methanol adsorption isotherm for defective UiO-66 displayed in Figure 3a at a temperature of 330 K. Convergence is almost reached at 1 atm. Probability distributions for the uptake of methanol molecules at a high pressure of 50 atm (convergence is now absolutely assured) are plotted in Figure 3b and a maximum probability is reached at an uptake of 29 molecules in the pores of the unit cell (restricted to two bricks) with a spreading of  $\pm 3$  molecules. For the sake of completeness GCMC calculations have also been performed in a  $2 \times 2 \times 2$  supercell. The maximum loading becomes now 38 molecules (Figure 3a). This higher number is expected since in the small simulation cell a lot of space is lost in the boundaries, which could host additional methanol molecules. To compensate for the usage of a reduced unit cell, a maximum loading of 32 methanol molecules is considered in the following NPT and NVT molecular dynamics simulations. The impact of this number on the structure of the active site and immediate vicinity is scarcely visible, since the number of methanol molecules surrounding the active sites is constant and stabilized by hydrogen bonds, while other molecules occupy the adjacent pores.

## 2.3. Molecular Dynamics: Active Sites at Operating Conditions

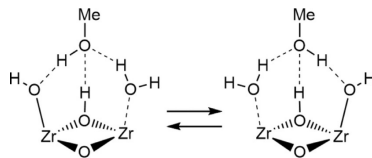
In previous work of some of the present authors, reactions were modeled at the active site of defective UiO-66 taking into account only the molecular species which are directly included in the reaction and possibly some directly coordinating protic molecules. However, at real catalytic operating conditions, a solvent is present in the pores of the material. Even when the solvent molecules do not play an active role in the reaction

mechanism, they frequently affect the reaction rate in a substantial and beneficial manner. We have shown in the GCMC calculations that the methanol solvent in the pores can be represented by an uptake of about 29–32 methanol molecules per unit cell (restricted to two bricks). To describe the active (hydrated) site and its immediate surroundings at operating conditions we perform a series of MD simulations starting from some random structures encountered at the end of the GCMC calculations near convergence. In particular, first an NPT simulation has been run with full loading of methanol during 25 ps to equilibrate the system, with two water molecules at each active site A and B (structure 3 of Figure 2). The empty framework has been kept fixed during the loading of the solvent molecules in the GCMC procedure, and the NPT simulation allows the system to relax which is clearly visible when examining the change of the unit cell volume, as visualized in Figure S2.

The final configuration of the NPT simulation is used as initial structure of the NVT simulation. During this simulation, attention is drawn to the mobility of the methanol molecules and its concentration and network formation in the pores of the unit cell. In the starting hydrated configuration, two water molecules are coordinated to each of the two active sites A and B (structure 3 in Figure 2). During the timescale of our simulations, the methanol solvent does not succeed in replacing a water molecule coordinated to the metal. At the beginning of the simulation, the two active sites A and B are equivalent, but at a certain moment a methanol is nestled between the water coordinated to the metal and the hydroxyl group bonded to the other Zr-center, bridging the two Zr-atoms and forming three hydrogen bonds with the node face. In this configuration, the aqua ligands give rise to a highly stabilized complex, as shown in Figure 4. This behavior takes place at the beginning of the simulation and breaks the symmetry of the two sites. In a completely arbitrary way we associate the appearance of this trigonal network with the water-hydroxo pair to site A. The system remains in this structure during the whole simulation (displayed in Figure 4). In the static calculations, it is also found that this configuration is the most stable (structure 4 in Figure 2). This trigonal network obviously interacts with



**Figure 3.** a) Methanol adsorption isotherm in defective UiO-66 at 330 K indicating also the 1 $\sigma$  width of the probability distribution; b) Probability distribution at different loading of methanol molecules as predicted by GCMC at 330 K and a pressure of 50 atm.



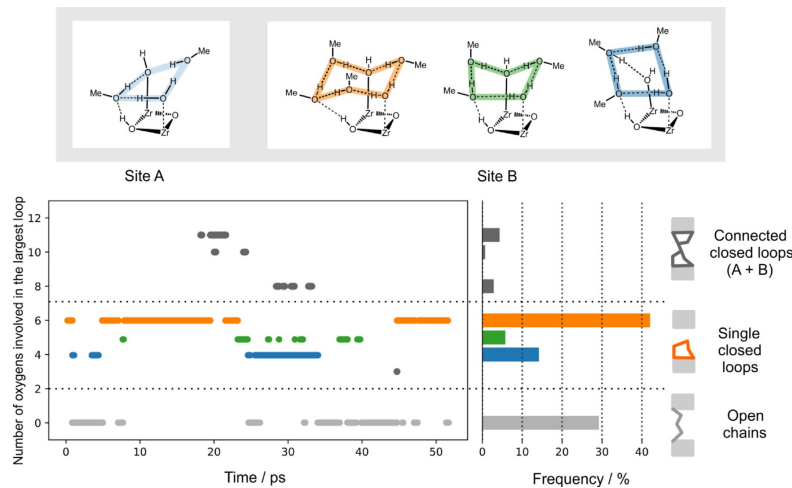
**Figure 4.** Dynamic Brønsted acidity in one of the structures established on the active site in defective UIO-66 and liquid methanol in the pores.

other methanol molecules of the pore, but they do not succeed in breaking this bridge. One may expect that the replacement of the water by a methanol molecule is to some extent activated. An important and interesting aspect is the continuous proton shuttle observed between one Zr-bound water and the other via the connecting methanol molecule. We are here confronted with a dynamic Brønsted acidity: the role of the acid proton of the water and the OH-anion is similar as there is a systematic switch between the two configurations, as clearly visualized in Figure 4. The observed dynamic acidity resembles that of Ling and Slater<sup>[6]</sup> but in the latter no methanol is present between the two groups.

At **site B** (opposite to **site A**) we observe a more complex variation of structures, going from single closed loops of hydrogen bonded methanol and water molecules to connected loops and open methanol chains with a length of 5–6 molecules. The total time of appearance of these three types of networks and the probability of occurrence during the 50 ps of simulation are displayed in Figure 5. These loops and chains are formed and disappear in a completely random way. The

size of the loops and chains varies dynamically and may easily amount to a network of 6 oxygens tied together with hydrogen bonds. Three of the possible and distinct patterns that are observed are shown in the top pane of Figure 5. In all these patterns, the node-ligated-aqua and hydroxyl species remain intact. None of these species have been replaced by methanol. One of the patterns at **site B** which appears the most frequently, is the six-membered ring formed by four methanol molecules and the two capping water molecules. We clearly see a boat or chair conformation for the six-membered ring analogous to the cyclohexane molecule. One methanol lies between the two water molecules, forming a hydrogen bond with the  $\mu_3$ -oxygen atom, while other three methanol molecules are located on the same site of the  $\mu_3\text{-OH}$  group. This configuration is stable for a part of the simulation time, with the position of the oxygens kept fixed in a network of hydrogen bonds, while some of the hydrogens are shuttled by the methanol molecules. The system then, after about 22 ps (Figure 5), evolves to an open 5-membered ring structure as a methanol molecule decoordinates from the Zr-OH group. The open ring structure further arranges to form a 4 or 5-membered ring as shown in the Figure. This structure allows a methanol molecule to come closer to the  $\mu_3\text{-OH}$  group, presumably enhancing the stability by forming tighter hydrogen bonds.

It is instructive to verify possible similarities with the microscopic structure of liquid methanol in bulk. It is unambiguously shown in a combined experimental-theoretical paper<sup>[31]</sup> that liquid methanol in bulk is a mixture of ring and chain structures dominated by six and eight methanol units. However, in bulk the methanol molecules are not hindered by any boundary effects. In general, the influence of the internal surfaces of



**Figure 5.** Top: Ring configurations observed at site A and site B originating from the interaction between the Zr-bonded hydroxyl and water and the solvent molecules. Bottom: Appearance of the various structures during the simulation. The frequency of occurrence of the different structures is also reported. A threshold of 2.2 Å for the donor-acceptor distance was chosen to determine a hydrogen bond and observations were smoothed over 0.5 ps.

the pores of a nanoporous material disturbs the presence of regular patterns in the structure of the methanol liquid. Here, boundary and surface effects will have a substantial influence on the length of the chain and ring structure. Nevertheless, the tendency to form chains of 4 methanol molecules which are eventually hydrogen-bonded to the coordinated water is clearly present. It is interesting to observe that the structure of bulk methanol has similarities with the structure in a confined environment. It must however be emphasized that such behavior will be critically dependent on the particular cavity and channel structure of this nanoporous material. The pores on UiO-66, where the included sphere diameter ranges from 6 to 9 Å<sup>[18b]</sup> are large enough to enable structuring of the methanol molecules, certainly when defects are present.

Besides single closed loops also open chains of hydrogen-bonded methanol molecules are occurring during the simulation (for at least 30% of the simulation time), as displayed in the bottom line of Figure 5. In some events these chains connect the two opposite sites, but no proton transfer has been observed through this chain of methanol molecules. It is striking that all the different patterns that have been observed involve methanol molecules that are located in the space between the two active sites. Assuming a total loading of 32 methanol molecules in the pore of the unit cell, many other molecules are not part of the observed patterns around the active sites. They also form chains of hydrogen bonds, which are generally of short length and which show similarities with those that have been observed in bulk methanol solution.<sup>[32]</sup>

In all these scenarios which take place during the NVT simulation, we observe a rather peculiar role of the acid proton on the  $\mu_3\text{-OH}$  group. It does not only play a fundamental role in the formation of the ring structures, as already noticed, but it also provides an additional stabilization. This is certainly also the case in the structure on **site A** where a single methanol molecule is coordinated to the  $\mu_3\text{-OH}$ , Zr-OH and Zr-OH<sub>2</sub> group, acting as an intermediary in the proton transfer between the Zr-OH and Zr-OH<sub>2</sub> groups. The proton of the  $\mu_3\text{-OH}$  group prefers to stay in its protonated state and only participates in the network by forming a hydrogen bond with a methanol molecule. Summarizing, the presence of liquid methanol in the pores of defective UiO-66 gives rise to a dynamic network of hydrogen bonds which surround the active sites and directly involve Brønsted sites, which could take part in reactive processes.

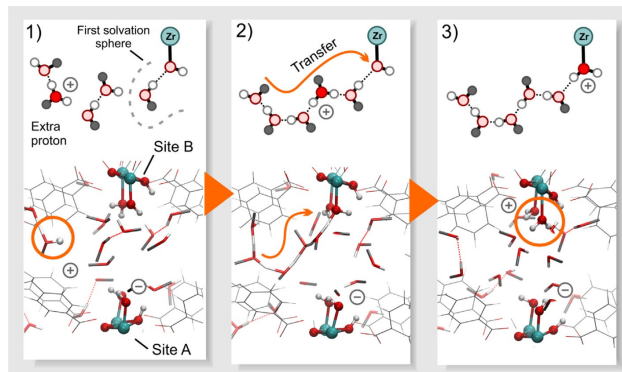
No proton transfer has been observed between the two opposite sites (**site A** and **site B**) during the simulation time. The distance between the two sites can easily be bridged by two methanol molecules forming a hydrogen bond with the waters coordinated at the Zr-centers in both opposite sites. During the simulation, such a bridge is formed several times, but there was no driving force to induce a proton transfer. During the simulation, we never saw a replacement of a water molecule coordinated to the metal by a methanol and also reversely, no replacement of a methanol by a water molecule has been observed. In configuration 5 of Figure 2 we see that deprotonation of the  $\mu_3\text{OH}$  group at **site A** is energetically not favored, as it is 30 kJ mol<sup>-1</sup> less stable than configuration 4. This

transition 4 → 5 needs breaking of two chemical bonds and is probably highly activated. We have not estimated this barrier but we never encountered the occurrence of configuration 5 during the NVT simulations. Another striking feature is the breaking of the symmetry in the structures formed at the two active sites. At one of the two sites, a methanol molecule acts as bridge to allow a proton shuttle between the terminating water and hydroxide, creating a dynamic Brønsted acidity center. These simulations shed light on a series of dynamic processes that cannot be observed with static calculations. Herein, we see that methanol molecules actively take part in the active sites via dynamic hydrogen bonds, and change the behavior of the Brønsted sites at the defect level, by exchanging protons with the water molecules. In general, the multilevel modeling approach allows to go one step beyond the static representation of the active sites by adding a realistic loading of solvent, making it possible to model the system at operating conditions.

#### 2.4. Proton Mobility in Liquid Methanol Confined in the Pores of UIO-66

So far, we have seen how protons are dynamically shuttled by methanol from one Zr-bound water to the other. It is however also interesting to investigate the transport mechanism of charged defects in a protic environment. Transport dynamics of charged defects in hydrogen-bonded liquids have their importance in numerous biological and technological systems [Ref<sup>[32b]</sup> and refs therein]. A substantial amount of theoretical and computational studies has addressed this topic. They all support the structural diffusion or Grotthuss mechanism in which a charge defect migrates through a hydrogen bond network via a series of proton transfer steps. All this work was restricted to liquids in bulk. The present simulations allow to extract information about the way a proton or charge can move through a confined liquid, by removing a proton artificially from the active site and inserting it elsewhere in the pore, as displayed in Figure 6. This way, one creates a positively and a negatively charged site in the pore of the unit cell and can investigate how the system responds to this charged defect in the pore of the material.

In a methanol solvent, a particular charge transfer mechanism was detected, which involve a series of subsequent hydrogen bonds, as displayed in Figure 6. In this context, it is interesting to see whether methanol in the pores of a nanoporous material shows similarities with the earlier observations. A proton shuttle generates transfer of charge. The proton transfer occurs through a hydrogen bonded network and implies a shuffle of a hydrogen between two neighboring oxygens. In a methanol chain or ring each non-terminating oxygen atom can play a role as hydrogen acceptor and donor, via hydrogen bonds. The positive charge is transferred from the acceptor to the donor since CH<sub>3</sub>OH<sup>+</sup> owns a coordination pattern which is similar to that of CH<sub>3</sub>OH. If we assume a proton transfer from A to B over a chain of methanol molecules tight together with hydrogen bonds, a charge displacement is generated yielding a change in the electrical potential



**Figure 6.** Three snapshots of the molecular dynamics simulation which starts from a deprotonated site A and a protonated methanol molecule, with corresponding schematic representation of the process (above). 1) starting structure with protonated solvent; 2) a snake-like chain of hydrogen bonds is formed which leads a proton to site B; 3) site B is protonated, while site A is missing a proton.

between **A** and **B**. The main pore in the reduced UiO-66 unit cell shows two opposite sites **A** and **B** filled with methanol liquid in between. Starting from a neutral system with no charged species we may assume that the two active sites **A** and **B** have the same electrical potential, and thus no proton transfer is indeed observed between these sites even when some network of methanol molecules appears in the simulation connecting the two sites. This was indeed observed in the previous section.

To study the effect of charge mobility in the UiO-66 material, three NVT simulations were performed, where in each of the simulations, a hydrogen atom was removed from **site A** and donated to one of the methanol molecules outside the first solvation sphere, as schematically shown in Figure 6. This creates a charge separation in the system. If the proton is allowed to move without restraints, the system will eventually seek to stabilize the charge. In two of the simulations, the protonated methanol is stabilized by the surrounding solvent molecules. In the third simulation, a chain of hydrogen bonds acts as a backbone for a cascade of exchange of protons, which leads to the donation of a proton from the solvent to the active site **B**. Snapshots of this path are displayed in Figure 6. **Site A**, therefore, remains deprotonated, while there is an extra proton on **site B**. This configuration is retained for the whole time of the simulation, and is apparently stabilized by the presence of solvent molecules. Static periodic calculations in the absence of any solvent molecules show a difference in free energy of  $89.6 \text{ kJ mol}^{-1}$  in favor of the structure with neutral sites (structure 3 of Figure 2) with respect to the structure where one proton is moved from **site A** to **site B** (Supporting Information, Figure S5). The observation that these protonated/deprotonated sites are maintained in the molecular dynamics simulations is an indication that solvent molecules have a decisive role in the stabilization of these charged configurations. Moreover, the active sites undergo also changes in the

geometry. On **site B**, in particular, the orientation of the two Zr bonded water molecules are slightly altered by the presence of an extra proton. The distance between the oxygens and the Zr atoms increases, and they become more loosely bonded. Moreover, the distance between the two oxygens themselves is larger, and has large fluctuations (up to  $2 \text{ \AA}$ ). This could be related to a higher tendency of water to leave the active site, and such a process could be the initiator of the substitution process of a water molecule with a methanol molecule, or with a generic reactant present in solution. The methanol substitution process in UiO-66 has been investigated by Yang et al.<sup>[8]</sup> showing that at room temperature the interexchange of one water molecule by one methanol molecule is not thermodynamically favorable. Proton mobility has also been studied in liquid methanol by inducing an excess proton as a defect structure.<sup>[32b]</sup> It is found that the defect structure associated with the excess proton is a hydrogen-bonded cationic chain whose length may exceed the average chain length in pure liquid methanol. This agrees perfectly with what we observed in the path discussed in Figure 6 where the excess proton as defect structure migrates/diffuses through the hydrogen-bonded network. The proton transfer satisfies a "snake-like" mechanism, as suggested by Morrone et al.<sup>[32b]</sup>

### 3. Conclusions

In this work, we investigated static and dynamic properties of the active sites on the hydrated UiO-66 in the presence of a realistic loading of methanol solvent. The behavior of a liquid in a confined space is substantially different from the one in bulk. The methanol molecules of the solvent mediate and aid proton transfers and are kept in stable configurations near the active sites by a network of hydrogen bonds. Moreover, the solvent has the capability of transferring protons to the active sites. The presence of a solvent like methanol assists in the

proton mobility, which is observed in the case of a deprotonation of the active site. When an excess proton is introduced in the solution, it can be transferred to the active site via the methanol molecules. In this case, we show that the solvent can stabilize a charge on the active site, with dynamic interactions that are impossible to consider in static calculations. This could also play a role in reactions where charged intermediates are present and can be stabilized by the solvent. The interaction with the solvent sheds light on the relative stability of both Brønsted acid and base sites of the material. The  $\mu_2$ -hydroxo group is involved in the solvent network, but does not exchange protons during the simulation time, which indicates that protons from water and hydroxyl group are preferential donors and show higher acidity. This remarkable behavior of the protons on these sites may have a substantial impact on many heterogeneous catalytic reactions which take place in protic solvents, such as Fischer esterification or hydrogenation reactions and could also affect the rearrangement of the framework itself, such as in the linker exchange process. A solvent can activate or deactivate the reaction, can serve as a substrate, influence the formation of different isomers, affect reaction mechanism and even influence the rate and selectivity due to its interactions with the starting materials or products. Hydrogen bonds between solvents and substrates can strongly influence the reaction, revealing the important role of solvent-stabilized catalytic intermediates, thus going far beyond the solvation alone. In general, this multilevel modeling approach brings insights on the interactions of the solvent in the confined pores of the material and how the active sites are modulated via these dynamic interactions.

## Acknowledgements

This work is supported by the Fund for Scientific Research Flanders (FWO) (project number 3G048612), the Research Board of Ghent University (BOF) and BELSPO in the frame of IAP/7/05. This project has received funding from the European Union's Horizon 2020 research and innovation programme under the Marie Skłodowska-Curie grant agreement No 641887 (project acronym: DEFNET). Funding was also received from the European Union's Horizon 2020 research and innovation programme [consolidator ERC grant agreement no. 647755-DYNPOR (2015–2020)]. The computational resources and services used in this work were provided by the VSC (Flemish Supercomputer Center), funded by the Research Foundation—Flanders (FWO). Molecular visualizations were produced with VMD software support. VMD is developed with NIH support by the Theoretical and Computational Biophysics group at the Beckman Institute, University of Illinois at Urbana-Champaign. We acknowledge Wim Dewitte for technical support with the table of contents Figure.

**Keywords:** ab initio calculations • hydrogen transfer • molecular dynamics • solvent effects • UiO-66

- [1] J. H. Cavka, S. Jakobsen, U. Olsbye, N. Guillou, C. Lamberti, S. Bordiga, K. P. Lillerud, *J. Am. Chem. Soc.* **2008**, *130*, 13850–13851.

- [2] a) Y. Bai, Y. Dou, L.-H. Xie, W. Rutledge, J.-R. Li, H.-C. Zhou, *Chem. Soc. Rev.* **2016**, *45*, 2327–2367; b) K. Leus, T. Bogaerts, J. De Decker, H. Depauw, K. Hendrickx, H. Vrielinck, V. Van Speybroeck, P. Van Der Voort, *Microporous Mesoporous Mater.* **2016**, *226*, 110–116; c) L. Valenzano, B. Civalieri, S. Chavan, S. Bordiga, M. H. Nilsen, S. Jakobsen, K. P. Lillerud, C. Lamberti, *Chem. Mater.* **2011**, *23*, 1700–1718.
- [3] a) O. V. Gutov, M. G. Hevia, E. C. Escudero-Adán, A. Shahaf, *Inorg. Chem.* **2015**, *54*, 8396–8400; b) G. C. Shearer, S. Chavan, S. Bordiga, S. Svelle, U. Olsbye, K. P. Lillerud, *Chem. Mater.* **2016**, *28*, 3749–3761; c) G. C. Shearer, S. Chavan, J. Ethiraj, J. G. Villalobos, S. Svelle, U. Olsbye, C. Lamberti, S. Bordiga, K. P. Lillerud, *Chem. Mater.* **2014**, *26*, 4068–4071; d) P. Valvekens, F. Vermoortele, D. De Vos, *Catal. Sci. Technol.* **2013**, *3*, 1435–1445.
- [4] S. M. J. Rogge, A. Bayvkina, J. Hajek, H. Garcia, A. I. Olivos-Suarez, A. Sepulveda-Escribano, A. Vimon, G. Clet, P. Bazin, F. Kaptein, M. Daturi, E. V. Ramos-Fernandez, F. X. Llabrés i Xamena, V. Van Speybroeck, *J. Gascon, Chem. Soc. Rev.* **2017**, *46*, 3134–3184.
- [5] J. Hajek, B. Bueken, M. Waroquier, D. De Vos, V. Van Speybroeck, *ChemCatChem* **2017**, *9*, 2203–2210.
- [6] S. L. Ling, B. Slater, *Chem. Sci.* **2016**, *7*, 4706–4712.
- [7] M. Vandichel, J. Hajek, A. Ghysels, A. De Vos, M. Waroquier, V. Van Speybroeck, *CrysEngComm* **2016**, *18*, 7056–7069.
- [8] D. Yang, V. Bernales, T. Islamoglu, O. K. Farha, J. T. Hupp, C. J. Cramer, L. Galgani, B. C. Gates, *J. Am. Chem. Soc.* **2016**, *138*, 15189–15196.
- [9] C. Caratelli, J. Hajek, F. G. Cirujano, M. Waroquier, F. X. Llabrés i Xamena, V. Van Speybroeck, *J. Catal.* **2017**, *352*, 401–414.
- [10] J. Hajek, M. Vandichel, B. Van de Voerde, B. Bueken, D. De Vos, M. Waroquier, V. Van Speybroeck, *J. Catal.* **2015**, *331*, 1–12.
- [11] a) G. Kresse, J. Furthmüller, *Phys. Rev. B* **1996**, *54*, 11169–11186; b) G. Kresse, J. Furthmüller, *Comput. Mater. Sci.* **1996**, *6*, 15–50; c) G. Kresse, J. Hafner, *Phys. Rev. B Condens Matter* **1993**, *47*, 558–561; d) G. Kresse, J. Hafner, *Phys. Rev. B Condens Matter* **1994**, *49*, 14251–14269; e) G. Kresse, D. Joubert, *Phys. Rev. B* **1999**, *59*, 1758–1775.
- [12] P. E. Blochl, *Phys. Rev. B* **1994**, *50*, 17953–17979.
- [13] a) J. P. Perdew, K. Burke, M. Ernzerhof, *Phys. Rev. Lett.* **1996**, *77*, 3865–3868; b) J. P. Perdew, K. Burke, M. Ernzerhof, *Phys. Rev. Lett.* **1997**, *78*, 1396.
- [14] a) S. Grimme, *J. Comput. Chem.* **2004**, *25*, 1463–1473; b) S. Grimme, J. Antony, S. Ehrlich, H. Krieg, *J. Am. Chem. Soc.* **2010**, *132*, 154104.
- [15] M. Vandichel, J. Hajek, F. Vermoortele, M. Waroquier, D. E. De Vos, V. Van Speybroeck, *CrysEngComm* **2015**, *17*, 395–406.
- [16] A. Ghysels, D. Van Neck, M. Waroquier, *J. Chem. Phys.* **2007**, *127*, 164108.
- [17] A. Ghysels, T. Verstraeten, K. Hemelsoet, M. Waroquier, V. Van Speybroeck, *J. Chem. Phys. Model.* **2010**, *50*, 1736–1750.
- [18] a) D. De Vos, K. Hendrickx, P. Van Der Voort, V. Van Speybroeck, K. Lejaeghere, *Chem. Mater.* **2017**, *29*, 3006–3019; b) S. M. J. Rogge, J. Wieme, L. Vanduyfhuys, B. Vandembande, G. Maurin, T. Verstraeten, M. Waroquier, V. Van Speybroeck, *Chem. Mater.* **2016**, *28*, 5721–5732.
- [19] a) D. Dubbeldam, S. Calero, D. E. Ellis, R. Q. Snurr, *Molecules Molecular Simulation* **2016**, *42*, 81–101; b) D. Dubbeldam, A. Torres-Knoop, K. S. Walton, *Molecular Simulation* **2013**, *39*, 1253–1292.
- [20] P. Ghosh, Y. J. Colon, R. Q. Snurr, *Chem. Commun.* **2014**, *50*, 11329–11331.
- [21] S. L. Mayo, B. D. Olafson, W. A. Goddard, *J. Phys. Chem.-Us* **1990**, *94*, 8897–8909.
- [22] A. K. Rappe, C. J. Casewit, K. S. Colwell, W. A. Goddard, W. M. Skiff, *J. Am. Chem. Soc.* **1992**, *114*, 10024–10035.
- [23] C. E. Wilmer, K. C. Kim, R. Q. Snurr, *J. Phys. Chem. Lett.* **2012**, *3*, 2506–2511.
- [24] B. Chen, J. J. Potoff, J. I. Siepmann, *J. Phys. Chem. B* **2001**, *105*, 3093–3104.
- [25] R. D. Goodwin, *J. Phys. Chem. Ref. Data* **1987**, *16*, 799–892.
- [26] J. VandeVondele, M. Krack, F. Mohamed, M. Parrinello, T. Chassaing, J. Hutter, *Comput. Phys. Commun.* **2005**, *167*, 103–128.
- [27] a) G. Lippert, J. Hutter, M. Parrinello, *Theor. Chem. Acc.* **1999**, *103*, 124–140; b) G. Lippert, J. Hutter, M. Parrinello, *Molecular Physics* **1997**, *92*, 477–487.
- [28] S. Goedecker, M. Teter, J. Hutter, *Phys. Rev. B Condens Matter* **1996**, *54*, 1703–1710.
- [29] D. Frenkel, B. Smit, *Understanding Molecular Simulation*, Academic Press, 2001.

- [30] G. J. Martyna, D. J. Tobias, M. L. Klein, *J. Chem. Phys.* **1994**, *101*, 4177–4189.
- [31] S. Kashtanov, A. Augustson, J.-E. Rubensson, J. Nordgren, H. Ågren, J.-H. Guo, Y. Luo, *Phys. Rev. B* **2005**, *71*, 104205.
- [32] a) M. Pagliai, G. Cardini, R. Righini, V. Schettino, *J. Chem. Phys.* **2003**, *119*, 6655–6662; b) J. A. Morrone, M. E. Tuckerman, *J. Chem. Phys.* **2002**, *117*, 4403–4413.

---

Manuscript received: October 12, 2017

Revised manuscript received: December 12, 2017

Accepted manuscript online: December 14, 2017

Version of record online: January 9, 2018

---

**Supporting Information****Influence of a Confined Methanol Solvent on the Reactivity of Active Sites in UiO-66**

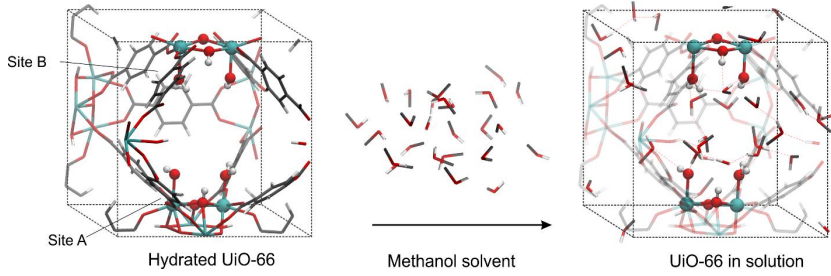
Chiara Caratelli,<sup>[a]</sup> Julianna Hajek,<sup>[a]</sup> Sven M. J. Rogge,<sup>[a]</sup> Steven Vandenbrande,<sup>[a]</sup>  
Evert Jan Meijer,<sup>[b]</sup> Michel Waroquier,<sup>[a]</sup> and Veronique Van Speybroeck<sup>\*[a]</sup>

cphc\_201701109\_sm\_miscellaneous\_information.pdf

## SUPPORTING INFORMATION

### GCMC

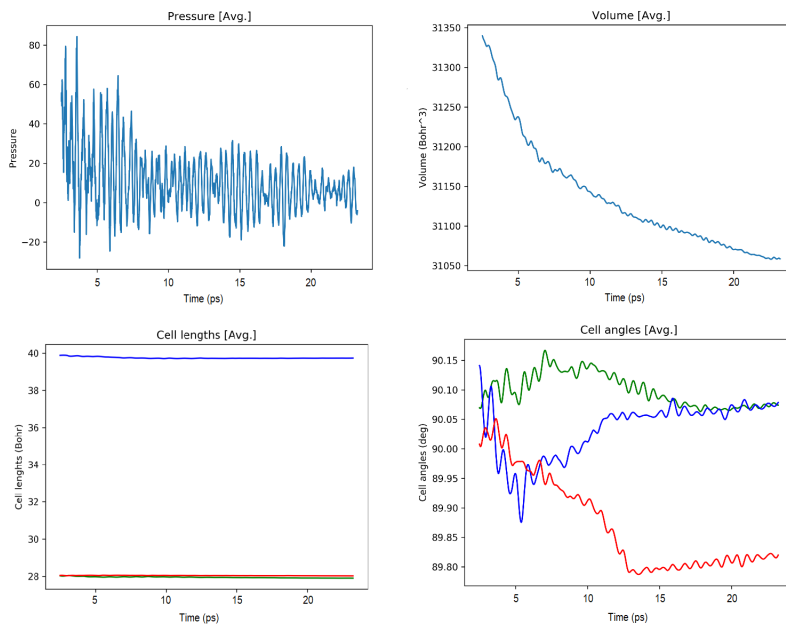
The procedure embedded in RASPA [1, 2] to perform GCMC calculations is based on the extraction of the potential energy grid which can be constructed from the structure of the empty framework. This structure has been optimized in VASP and in RASPA converted to a grid of potential energy values. At each point of the grid corresponds a value of the potential energy and on places where framework atoms are expected to be present a high potential energy value is assumed prohibiting overlap between a solvent molecule and a frame atom. The GCMC protocol makes a guess of the position of the methanol molecules on the potential energy grid. In a later phase the atomic positions are visualized and we came to the right figure in Figure S1.



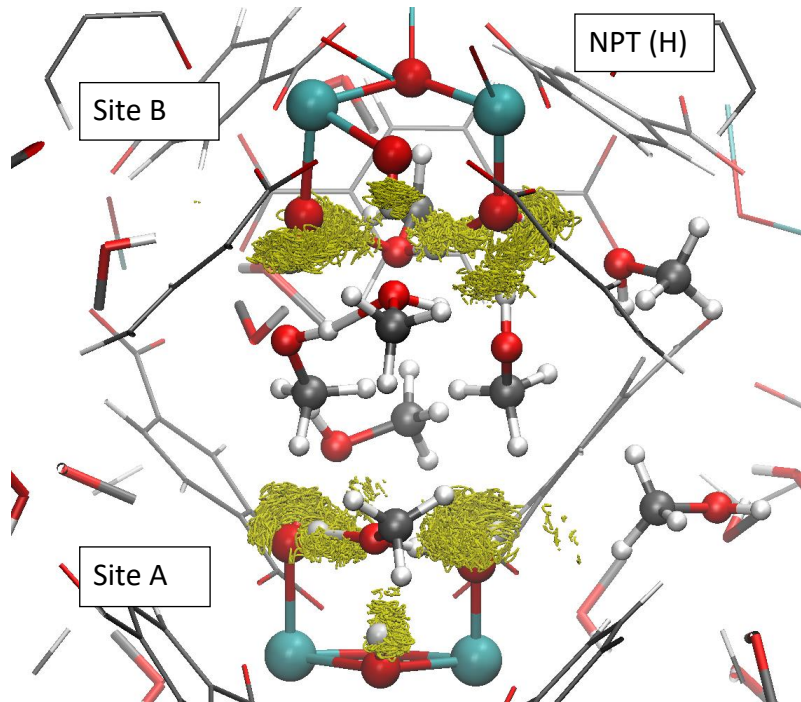
**Figure S1:** left : unit cell of hydrated and defective UiO-66 without solvent, optimized within a static periodic model; right : solvent molecules (methanol) embedded in the frame. The active sites A and B are indicated on the left.

### NPT simulation

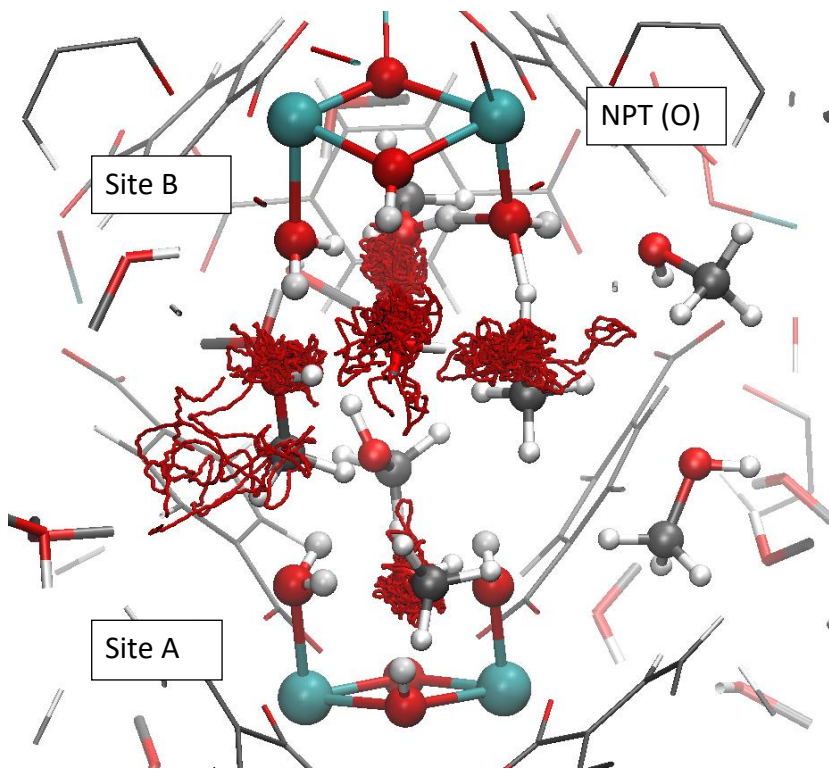
Starting configuration for the NPT comes from a random structure taken from the GCMC near convergence. NPT is performed with a maximum loading of methanol from GCMC and estimated to 32 taking into account the various comments made. Pressure is 1 atm , temperature = 330 K . The evolution of the pressure and volume during the simulation of 25 ps is given in **Figure S1**. Parameters are the same as used for the simulations done without solvent, except for the thermostat ( $T=330\text{ K}$  / Timestep: 0.5 fs / Thermostat: NH chain / Level of theory: rev-PBE + D3 / Basis set: DZVP-MOLOPT for Zr, and DZVP-GTH for H, C and O / Pseudo: GTH). The behavior of the volume of the unit cell during the simulation merits some additional comments. The volume shrinks and after 25 ps it reaches a value of  $4600\text{ \AA}^3$  which is close to the estimate of  $4669\text{ \AA}^3$  for a type 6 two-linker defect predicted by Rogge [3].



**Figure S2:** Pressure, volume, lengths and angles of the unit cell as a function of the step number.



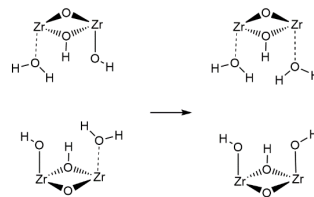
**Figure S3:** Snapshot from the NPT simulation. In yellow, the positions visited by the protons of the active sites or directly coordinated to it



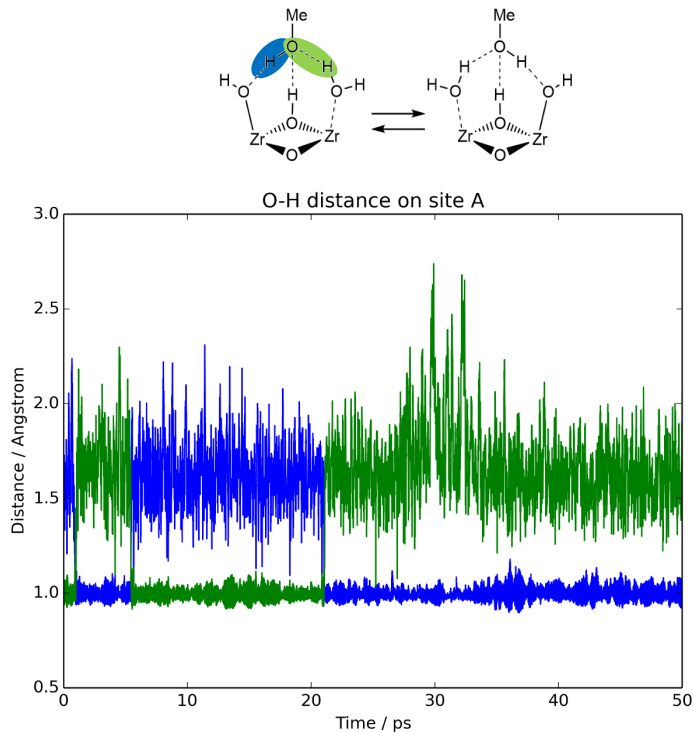
**Figure S4:** Snapshot from the NPT simulation. In red, the positions visited by the oxygens of the methanol molecules directly coordinated to the active site.

### Protonated and deprotonated active sites

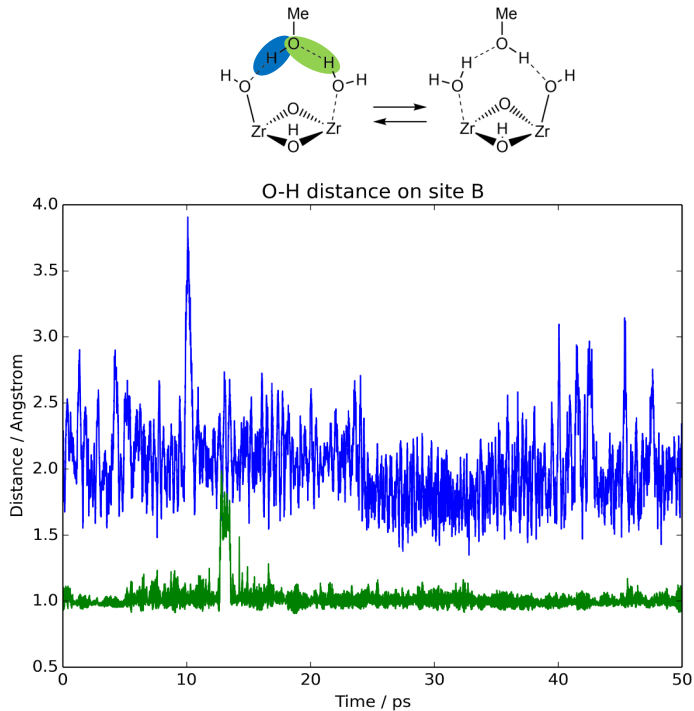
Difference in stabilization between neutral sites and protonated/deprotonated sites A and B is given by the free energy difference of the two systems at 330 K by means of static periodic calculations. The two systems are displayed in **Figure S5**. At 330 K, a free-energy difference of 89.6 kJ/mol is found.



**Figure S5:** Schematic representation of the neutral and protonated/deprotonated sites A and B

**O-H bond distances**

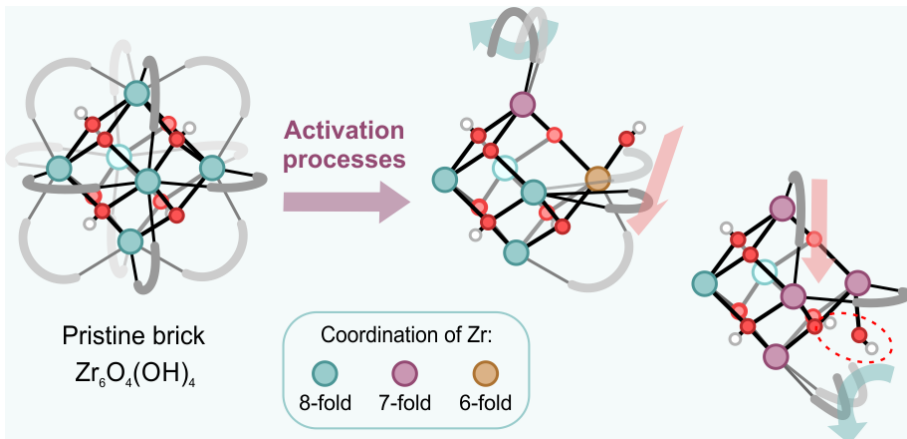
**Figure S6:** Distance between closest hydrons and oxygen of methanol on site A



**Figure S7:** Distances between closest hydrogens and oxygen of methanol on site B

## Paper III

### On the intrinsic dynamic nature of the rigid UiO–66 metal–organic framework



J. Hajek, C. Caratelli, R. Demuynck, K. De Wispelaere, L. Vanduyfhuys, M. Waroquier, V. Van Speybroeck, *Chemical Science*, **8**, 2723–2732 (2018)

C. Caratelli was involved in the manuscript preparation.

©2018 Royal Society of Chemistry.

Reprinted with permission from the Royal Society of Chemistry.





Cite this: *Chem. Sci.*, 2018, **9**, 2723



## On the intrinsic dynamic nature of the rigid UiO-66 metal–organic framework†

Julianna Hajek, Chiara Caratelli, Ruben Demuyncck, Kristof De Wispelaere, Louis Vanduyfhuys, Michel Waroquier and Veronique Van Speybroeck \*

UiO-66 is a showcase example of an extremely stable metal–organic framework, which maintains its structural integrity during activation processes such as linker exchange and dehydration. The framework can even accommodate a substantial number of defects without compromising its stability. These observations point to an intrinsic dynamic flexibility of the framework, related to changes in the coordination number of the zirconium atoms. Herein we follow the dynamics of the framework *in situ*, by means of enhanced sampling molecular dynamics simulations such as umbrella sampling, during an activation process, where the coordination number of the bridging hydroxyl groups capped in the inorganic  $Zr_6(\mu_3-O)_4(\mu_3-OH)_4$  brick is reduced from three to one. Such a reduction in the coordination number occurs during the dehydration process and in other processes where defects are formed. We observe a remarkable fast response of the system upon structural changes of the hydroxyl group. Internal deformation modes are detected, which point to linker decoordination and recoordination. Detached linkers may be stabilized by hydrogen bonds with hydroxyl groups of the inorganic brick, which gives evidence for an intrinsic dynamic acidity even in the absence of protic guest molecules. Our observations yield a major step forward in the understanding on the molecular level of activation processes realized experimentally but that is hard to track on a purely experimental basis.

Received 17th November 2017  
Accepted 26th January 2018

DOI: 10.1039/c7sc04947a  
[rsc.li/chemical-science](http://rsc.li/chemical-science)

## Introduction

Metal–organic frameworks (MOFs), among the most intriguing materials of current science, are hybrid materials constructed from metal ions or metal clusters linked together by multitopic organic linkers.<sup>1–3</sup> The building block concept gives nearly infinite possibilities to vary the chemical composition of MOFs and make these materials very appealing for a broad set of applications such as gas storage and separation,<sup>4</sup> detection and decomposition of warfare agents,<sup>5</sup> drug delivery<sup>6</sup> and catalysis.<sup>7–12</sup> The main drawback of most MOFs is their weak stability under reaction conditions.<sup>13,14</sup> However, to date, the amount of synthesized MOF structures has grown substantially, giving rise to chemically and thermally stable MOFs.<sup>14,15</sup>

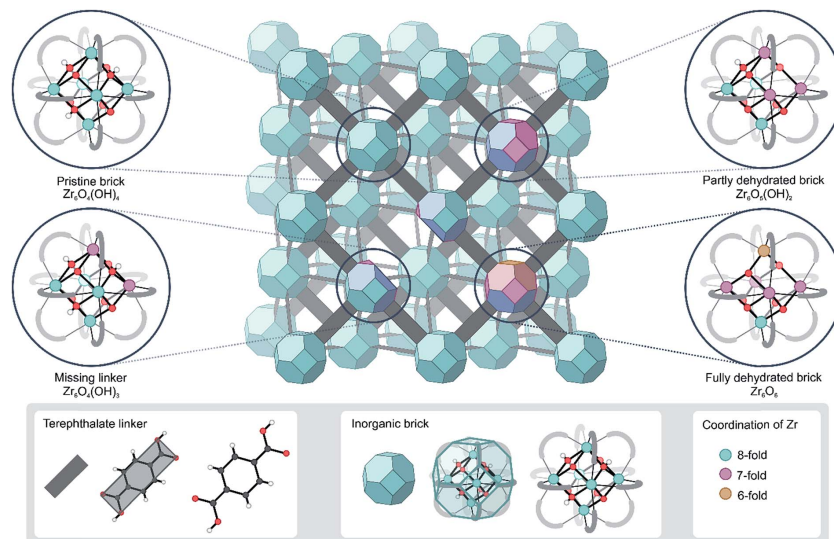
In this respect, UiO-66 has received considerable attention due to its exceptional thermal, mechanical and chemical stability, which is not typically found in other MOFs.<sup>16–19</sup> Pristine UiO-66 is composed of inorganic  $Zr_6(\mu_3-O)_4(\mu_3-OH)_4$  (Fig. 1) bricks connected through ditopic organic ligands and was first synthesized by Lillerud and co-workers.<sup>20</sup> In the inorganic brick, four three-fold bridging hydroxyl groups are symmetrically

distributed around the building block such that the oxide and hydroxide anions are capping the faces of the  $Zr_6$  octahedron alternately to achieve minimum repulsion (Fig. 1, pristine brick).<sup>21,22</sup> As will be shown here, the lability of the species that make up UiO-66 may play a critical role in processes where the coordination number of the Zr atoms changes, such as dehydration or exchange of either metal or linker ligands, and has a direct consequence in the formation of defects.

The key to the exceptional stability can be traced back to the inherent composition of the framework, where each Zr atom is 8-fold coordinated by oxygen atoms and each inorganic brick is 12-fold coordinated by organic linkers in the defect-free material. Despite being exceptionally rigid, there are various indications that the structure is far more dynamic than originally believed.<sup>24</sup> Dynamic behavior in this context should not be confused with the properties of flexible or dynamic frameworks, which have the ability to undergo large structural deformations while retaining their crystallinity upon exposure to external stimuli, such as light, temperature, pressure, and adsorption of guest molecules. Such materials are classified as third-generation soft porous crystals by Kitagawa and collaborators.<sup>25,26</sup> The dynamic behavior explored here refers to the flexibility introduced by changing the coordination number of the metal, which affords to modify the framework by temporarily breaking the metal–ligand (M–L) bonds. The M–L bond is generally perceived as the weakest link in MOFs, both

Center for Molecular Modeling (CMM), Ghent University, Technologiepark 903, B-9052 Zwijnaarde, Belgium. E-mail: veronique.vanspeybroeck@ugent.be

† Electronic supplementary information (ESI) available. See DOI: 10.1039/c7sc04947a



**Fig. 1** Schematic representation of the UiO-66 structure with possible configurations of the bricks that give rise to coordinatively unsaturated Zr atoms. The representation of the UiO-66 unit cell has been adapted from ref. 23.

thermodynamically and kinetically.<sup>15</sup> This has a negative effect on the thermal stability, but the ease of coordination change may also be used as an opportunity to modify the structure. In Zr-based MOFs, like UiO-66, M–L bonds are particularly stable as Zr is one of the most oxophilic metal elements,<sup>27</sup> but such post-synthetic modifications have recently been realized experimentally in UiO-66.<sup>28–30</sup>

First of all, it has been found that the  $\text{Zr}_6\text{O}_4(\text{OH})_4$  inorganic brick has the ability to be dehydrated reversibly, thereby changing the coordination number of the Zr metal centers between the hydrated and dehydrated forms.<sup>18,21,31,32</sup> The dehydration and rehydration process of the inorganic Zr-brick in UiO-66 has been experimentally studied using *in situ* infrared (IR) spectroscopy and gravimetric techniques.<sup>31</sup> The dehydration starts at 523 K and is completed at 573 K with the removal of two water molecules resulting in a cornerstone composition of  $\text{Zr}_6\text{O}_6$  (Fig. 1, fully dehydrated brick). When starting from the defect-free material, the dehydration process is initiated by the first water removal and results in a  $\text{Zr}_6\text{O}_5(\text{OH})_2$  brick, where the coordination number of the three Zr atoms is reduced from 8 to 7 (Fig. 1, partly dehydrated brick). A further reduction in the Zr coordination number takes place with the second removal of a water molecule. Fully dehydrated UiO-66 is composed of  $\text{Zr}_6\text{O}_6$  distorted units and has variously coordinated Zr atoms, with coordination numbers ranging from 8 to 6 (Fig. 1). Despite these significant deformations in the inorganic brick, the original structure of UiO-66 is almost preserved and maintains the robustness of the brick, which was confirmed by PXRD

patterns, *in situ* DRIFT spectra and gravimetric characterization techniques (TG-DSC).<sup>21,31</sup> Moreover, a rehydration process can restore the material to its initial structure, with the hydrated  $\text{Zr}_6\text{O}_4(\text{OH})_4$  inorganic cornerstone. This is a remarkable property of this MOF, giving an indication of the existence of mobile  $\mu_3\text{-OH}$  hydroxyl groups in the brick. By performing IR experiments on UiO-66, in which the temperature was gradually increased, Shearer *et al.*<sup>31</sup> observed the isolated hydroxyl region by the presence of additional bands at 3600–3700  $\text{cm}^{-1}$ . Furthermore, recent experimental findings pointed towards a significant structural mobility in frameworks that are classified as rigid. By applying ultrafast 2D IR spectroscopy, structural fluctuations have been shown in functionalized Zr-based MOFs.<sup>33</sup> These fast dynamics of the framework have a direct effect on an MOF's lability, flexibility and coordination changes. Furthermore, recent synthesis procedures have reached a higher level of perfection, allowing engineering of frameworks by concepts such as post-synthetic ligand exchange or solvent-assisted linker exchange.<sup>29</sup> Within the UiO-66 framework, unfunctionalized linkers have been replaced by functionalized ones without compromising the MOF crystallinity or porosity.<sup>28</sup>

All these observed features in UiO-66 point towards an intrinsic dynamic flexibility of the material and are related to changes in the coordination number of the metal ions making up the inorganic bricks.<sup>26,34</sup> A more general discussion on these aspects has been recently reviewed by Morris and Brammer.<sup>24</sup> The ease of coordination change and ability to modify the structure without compromising its hydrothermal stability has

shown to be extremely useful for adsorption and catalysis.<sup>12,35</sup> However, despite this application-driven importance, the understanding of rearrangement of linkers, hydroxyl groups and other labile species on the molecular level is fairly limited. It poses a huge challenge for experimentalists to trace this intrinsic dynamic flexibility *in situ* during an activation process. In this sense, computational techniques offer an indispensable alternative to follow the dynamics of the system, as was suggested by Ling and Slater, who showed a dynamic acidity of the defective UiO-66 framework.<sup>36</sup> Based on first-principles molecular dynamics simulations, proton shuttles have been observed between water molecules coordinated to the metals and charge-balancing hydroxide anions, which compensate for the missing linkers in defective UiO-66.<sup>36</sup> Such proton shuttles may also be facilitated by the presence of other guest species in the pores, such as methanol.<sup>37</sup>

Herein, we take a major step forward in the structural understanding of the UiO-66 by using advanced or enhanced sampling molecular dynamics simulations, which allow to follow *in situ* the fast dynamics of the UiO-66 framework during activation processes. Typical molecular dynamics simulations only sample stable regions of the free energy surface, whereas enhanced sampling techniques allow visiting activated regions of the free energy surface, typically encountered during activation processes. More elaborate reviews on these advanced molecular dynamics simulations may be found in the work of Valsson and references therein.<sup>38</sup> Such techniques have only recently found their way in the field of heterogeneous catalysis and have been successfully used to study chemical reactions at true operating conditions of temperature and pressure.<sup>39–45</sup> A good overview of the recent advances in computational techniques for nanoporous materials is given in ref. 46 and 47 by the Coudert group. In this contribution, we study the UiO-66 framework along the activation path where one of the hydroxyl groups bridging the Zr atoms in the brick lowers its coordination number from 3 to 1, which is a crucial step in the dehydration process.<sup>32</sup> Preliminary molecular insights are obtained from static calculations, neglecting the dynamic behavior of the system, and reveal the presence of transition states with loose hydroxyl groups and dangling linkers along the dehydration pathway (Reaction scheme depicted in Fig. S2 of the ESI†).<sup>48</sup> The results here show a highly dynamic behavior of M–L bonding, whose lability changes the degree of network connectivity and coordination that leads to open metal sites. Linkers can easily decoordinate, translate, rotate and re-coordinate, and hydroxyl groups show a high degree of mobility, even in the absence of external water or solvent molecules. All these rearrangements occur without deterioration of the structural integrity of the material. Our simulations show that even very stable MOFs like UiO-66 are much more dynamic than originally expected.

## Results and discussion

Herein, dynamical structural rearrangements of the UiO-66 framework are studied by lowering the coordination number of the hydroxyl groups bridging the Zr atoms from 3 to 1. This

reshuffling is typically encountered during dehydration, which is a commonly applied activation procedure upon thermal treatment. Exploration of higher free energy regions requires usage of enhanced molecular dynamics simulations.<sup>49–53</sup> Herein the umbrella sampling (US) methodology is used, whereby an external potential is added to the true Hamiltonian to enhance the sampling of low probability regions along certain coordinates of the system.<sup>53,54</sup> These degrees of freedom are called collective variables and may be complicated functions of all internal degrees of freedom. An appropriate choice of these coordinates is far from trivial,<sup>57</sup> but here we chose the coordination number of the hydroxyl oxygen to the three Zr atoms as a collective variable.<sup>58</sup> This choice is inspired by the experimental observation of dangling, asymmetric hydroxyl groups in intermediate states during dehydration,<sup>31</sup> and the theoretical reaction mechanism proposed in ref. 32. The coordination number is defined based on the distance between the hydroxyl group and the three surrounding Zr atoms, as schematically shown in Fig. 2.

With this choice, the coordination number at a value of about 2.17 represents the Zr brick in its equilibrium configuration, denoted as configuration 1 in Fig. 3, and reaches a value of about 0.9 when the hydroxyl group is covalently connected to only one Zr atom, giving rise to a bridging  $\mu_3$ -OH hydroxyl group (configuration 5). Partitioning the entire range of the reaction coordinate ( $1.7 \leq CV \leq 2.4$ ) into 36 windows following the procedure of US as outlined in the Methodology section and in the ESI† an umbrella sampling simulation has been performed in each window. The quality of the selection of the 36 windows along the reaction path and the magnitude of the spring constant characterizing the harmonic bias potential are assessed by sufficient overlap of the umbrellas covering the various windows (Fig. S1 of the ESI†), which is an indication that the sum of the three coordination numbers as CV is a well-suited choice in the reaction path towards the first dehydroxylation. Along the reaction path, five classes of configurations are distinguished, which differ in the degree of coordination of the hydroxyl group with the three neighboring Zr atoms going from a 3-fold to a 1-fold coordination (Fig. 3).

Configuration 1 in Fig. 3 at 573 K shows the equilibrium structure, where the four  $\mu_3$ -OH groups are ordered symmetrically in a tetrahedral fashion and each Zr atom is 8-fold coordinated (Table S2 of the ESI†). When slightly activating the

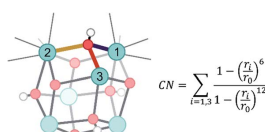
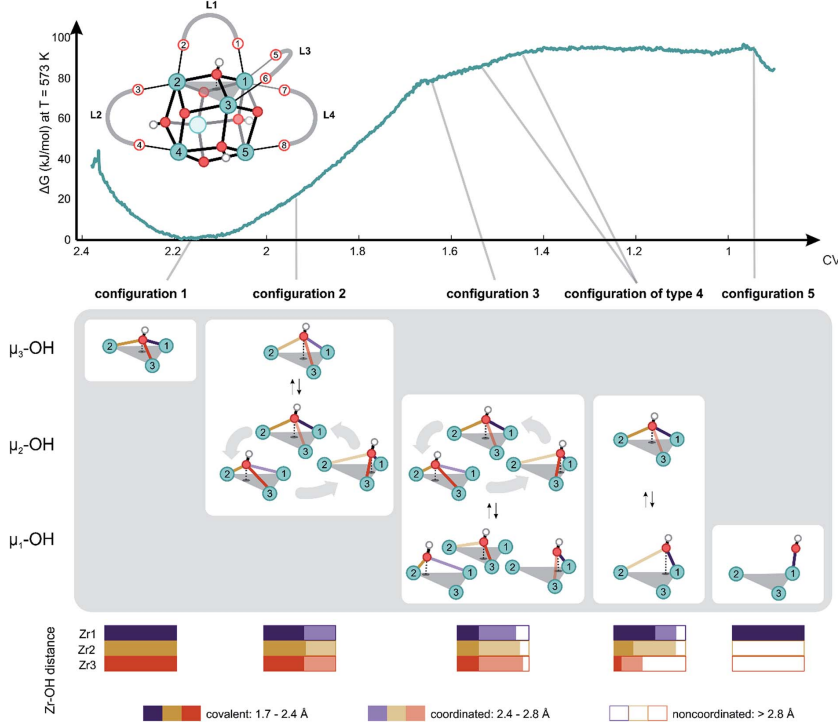


Fig. 2 Schematic representation of the applied collective variable. Three critical Zr–O distances, represented with solid yellow, red and purple lines, are used as input in the formal definition of the collective variable. The index labels each of the three Zr atoms surrounding the hydroxyl groups.





**Fig. 3** Free energy profile at 573 K along the reaction path of dehydration with the collective variable defined, as given by the equation in Fig. 2, as the reaction coordinate. Reference representation of the brick taken from configuration 1 is shown above the free energy profile, with labeling of all relevant linkers, carboxylate oxygens, hydroxyls and Zr atoms needed to describe the chemical transformation. Some essential turning points on the profile are indicated with a schematic display of their respective configurations. Probability distributions regarding the type of coordination of the hydroxyl group with respect to the Zr centers measured during the US simulation are reported in the bottom.

system towards configuration 2, which is characterized by a collective variable of 1.96, it becomes clear that the hydroxyl group is relatively mobile, changing its position equally between the three Zr atoms. The average position of the hydroxyl group remains centrally located between three Zr atoms in a  $\mu_3\text{-OH}$  configuration (Table S2 of the ESI†). Nevertheless, as the coordination number decreases, the mobility of the hydroxyl group becomes more distinct. Alternatively, the hydroxyl group makes a stronger connection to two out of three Zr atoms, breaking the trigonal symmetry ( $\mu_2\text{-OH}$  structure). The increase in free energy to reach this point is relatively modest with a value of about 20 kJ mol<sup>-1</sup> from configuration 1. To obtain more information on the type of connection between the oxygen and the three Zr atoms, we also constructed probability distributions for each of the configurations (Fig. 3, bottom). Interestingly, at configuration 2, the probability of observing a looser OH-bond with one of the Zr atoms is the

same for the three Zr atoms, which underlines the relatively mobile nature of the  $\mu_3\text{-OH}$  hydroxyl group in the pristine material. Additional inspection of the free energy profile shows that the dehydration process is initiated by configuration 2, as further progression towards lower coordination numbers does not reveal any more  $\mu_3\text{-OH}$  configurations.

A critical point along the reaction path is encountered at configuration 3 corresponding to a collective variable of 1.64, where the hydroxyl group is covalently bonded to only one of the Zr atoms. Nevertheless, some coordination with another metal is maintained, but the coordination with the third Zr atom is no longer observed. Interestingly, even for such lower coordinated structures, where the hydroxyl group changes substantially its position, there is no clear preference for the coordination of the hydroxyl group to one of the three Zr atoms and there is still a complete symmetry in the average coordination behavior of the hydroxyl group with the three Zr atoms (Table S2 of the



ESI<sup>†</sup>). Note that this region is already substantially highly activated with a value of about 80 kJ mol<sup>-1</sup> that is typically reached during the activation processes. During the simulation, the hydroxyl group travels from one position to the other, systematically establishing a covalent bond with one of the three adjacent Zr atoms to create open metal sites that are 7-fold coordinated. For the first time along the trajectory, we observe a tendency of the linkers to elongate the M-L bond and deform the phenyl ring out-of-plane to make space for the traveling hydroxyl group. Such elongations and deformations indicate that the system enters the transition state region, explaining the increased free energy.

All structures encountered after configuration 3, are situated in a higher energy plateau. They are almost isoenergetic since the collective variable only reflects the degree of coordination of the hydroxyl group to the three Zr atoms to which it was originally attached. The broad set of structures encountered in this window of the collective variable show new internal deformation modes, which include decoordination, translation, rotation, and recoordination of the linkers and hydroxyl group bond cleavages. Each of the structures of configuration of type 4 has a clear preference to form  $\mu_1$ -OH configuration with one of the three Zr atoms. However, the hydroxyl group seeks stabilizing interactions with the other Zr atoms. For configurations of type 4, the probability distributions for the various Zr-O bonds show a clear asymmetry for the three Zr atoms. A strong covalent bond is observed between the hydroxyl group and a Zr atom from which a linker has been decoordinated (*vide infra*). Indeed, substantial mobility of linkers is observed in this region, with strong deformation modes of four linkers. This is explained in greater detail hereafter for configurations of type 4 and 5. For the labeling pattern of the various linkers and atoms, we refer to the reference structure as displayed in Fig. 3 above of the free energy profile.

For configurations of type 4, in which one Zr atom (Zr1) makes a strong, covalent bond with the hydroxyl group, two possible motions of the BDC linker are observed, which are further illustrated in Fig. 4. The first defined motion (Fig. 4, left column) corresponds to a translation of the linker along the axis of the two Zr atoms to which it is bonded (Movie S1 of the ESI<sup>†</sup>). In this case, the linker decoordination starts on the Zr with the  $\mu_1$ -OH configuration and is induced by the steric interactions, which are directly correlated to the position of the hydroxyl group. The linker (L1) decoordinates from Zr (O1 from Zr1) and further forms an intermediary chelated structure in which both carboxylic oxygens are connected to the same Zr atom (Zr2 and O1, O2). The chelated structure is a short-living metastable state from which one oxygen of the linker (O2) subsequently decoordinates from Zr2 (configuration 4t in Fig. 4), thereby changing the parent connectivity between the metal ion and the carboxylic oxygen from the linker (Zr2 is now connected to O1 instead of O2). During the simulation of this configuration, the hydroxyl group keeps its bond with Zr1 and systematically switches between  $\mu_2$  and  $\mu_1$  connectivity by establishing a coordination with the Zr atom (Zr2) to which the linker is  $\eta^1$  chemically bonded. Another significant aspect of configuration of type 4 that exhibits the translation mode is the progressive

change in the coordination number of the two Zr atoms. Firstly, linker decoordination lowers the coordination number of Zr1 from 8 to 7. Secondly, in the starting configuration of type 4 and final configuration 4t, Zr2 is 7-fold coordinated, but during the process of linker translation, an intermediary coordination of 8 is present in the chelated structure. This evidence of the presence of an intermediary chelated structure has also been observed by Puchberger *et al.*<sup>59</sup> in the case of an isolated Zr<sub>6</sub> cluster. The change in coordination number of the various Zr atoms is schematically represented by a color code in Fig. 4.

The second defined motion observed in configurations of type 4 corresponds to a rotation mode of the linker (Fig. 4, right column), which is again prompted by the  $\mu_1$ -OH hydroxyl group dislocation. At this case, the linker breaks a bond with a Zr atom (O1 with Zr1) and rotates along the Zr2-O2 bond (Movie S2 of the ESI<sup>†</sup>). The rearrangement of this linker (L1), with its steric hindrance, influences the coordination pattern of another linker connected to the same Zr (L2 to Zr2), which is pushed away by linker L1 and detaches from Zr2. This second linker (L2) immediately stabilizes itself by coordinating to the closest  $\mu_3$ -OH group (originally attached in between Zr2 and Zr4). This linker decoordination is clearly visible in the probability distribution of the O3 and Zr2 bond. In the remaining part of the simulation, the proton of the hydroxyl group travels from the  $\mu_3$ -O atom to the carboxylic oxygen O3 and is donated to the linker. The appearance of phenomena such as proton transfer processes between partly decoordinated carboxylic ligands and hydroxyl groups generates an intrinsic dynamic acidity. Proton mobility in UiO-66 was reported earlier by Ling and Slater,<sup>36</sup> but in that work, the dynamic acidity was caused by shuttling protons between water molecules coordinated to the metals and charge balancing hydroxide anions, which compensate for the missing linkers in the defective material. This proton transfer process is reversible and elucidates the unusual simultaneous action of carboxylic ligands as hydrogen donors and hydrogen acceptors, which is an indication of the existence of an intrinsic dynamic acidity in defect-free UiO-66. During the rotational deformation mode observed for configuration of type 4, substantial rearrangements of the coordination numbers of the various Zr atoms are observed. The linker decoordination leaves an open metal site on Zr1, which changes the chemical bonding pattern of this atom from 8 to 7. Additionally, the rotation of the linker around Zr2 results in the second decoordination from this site, decreasing the Zr coordination number from 7 to 6, as shown in configuration 4r in Fig. 4.

The reversible proton shuttles observed in configuration 4r require some additional attention. First, a similar pattern has been noticed by Haigis *et al.*<sup>44</sup> in metadynamics simulations performed at high temperatures on MIL-53(Ga), where the hydroxyl group of the inorganic chain is hydrogen bonded with the carboxylic oxygen of the BDC linker, forming an intermediate structure. Second, the ability to reversibly protonate the carboxylate groups of linker ligands in UiO-66 has been experimentally evidenced by DeCoste *et al.*<sup>14</sup> by observing some specific peaks of C=O in the IR spectrum when adding hydrochloric acid to the material. The simulations performed here give evidence of an intrinsic dynamic acidity with rapid

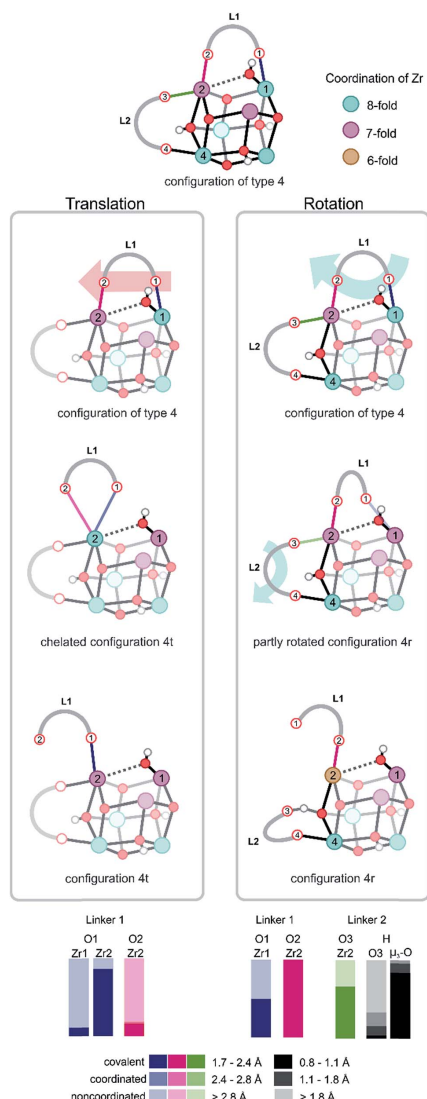


Fig. 4 Umbrella sampling in two windows of  $\text{CV} = 1.45$  and  $1.51$ , showing two distinct motions of the linkers. On the left column, a translation of the linker L1 generates a chelated structure and a subsequent shift in the carboxylic oxygen connected to Zr2 (configuration 4t). On the right column, a rotation of the linker L1 and a partial decoordination of linker L2 forming a hydrogen bond with an  $\mu_3\text{-OH}$  hydroxyl group is shown (configuration 4r). A proton transfer

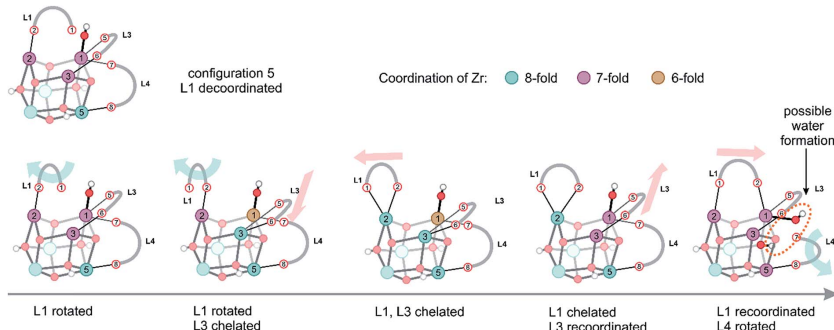
proton transfers between the hydroxyl groups and linkers, even in the absence of protic molecules in the pores of the material. This aspect gives evidence for a similar linker, and hydrogen bond stabilization during the reactions in which  $\text{UiO-66}$  undergoes chemical transformations, like in the case of ligand exchange process and substantiates the structural stability.

Configurations of type 5, encountered in the window with collective variables smaller than 1.0, are typical for processes, where eventually water could also be formed. However, one should be careful; there is not one single water formation mode, but the system can assume a plethora of configurations of almost equal free energy, which are characterized by a large mobility of both linkers and protons originally connected to the inorganic brick. Herein, we demonstrate the presence of complex, fast structural fluctuations that can be rationalized as a combination of the two previously described motions of linker translation and rotation. In all these configurations located in the configuration 5 region (Fig. 5), which is characterized by an initial collective variable of 0.94, the hydroxyl group is bonded to a Zr atom in a stable  $\mu_1\text{-OH}$  position (Movie S3 of the ESI†). The starting configuration of the inorganic brick is composed of three 7-fold and three 8-fold coordinated Zr atoms, but the coordination pattern of the Zr atoms rapidly evolves, giving different types of open metal sites. During the simulation, two linkers (L1 and L3) undergo translational and rotational motions at the same time, modifying the chemical properties of four Zr sites by changing the coordination number between 8 and 6. In addition, it is important to notice that linker decoordination occurs from the same metal ion, which can lead to linker vacancies. Interestingly, linkers also recoordinate to their parent position, providing an explanation for the remarkable stability of  $\text{UiO-66}$ . The ability of the linkers to reversibly decoordinate and coordinate to the Zr atoms is intrinsically related to the oxophilic character of the metal. Upon linker recoordination, the hydroxyl group travels to the other side of the brick with spontaneous decoordination of another linker (L4) (Fig. 5). These intrinsic motions show the ability of the structure to easily respond to deformations of linkers and hydroxyl groups. Water formation can eventually occur by a process where a deordinated hydroxyl group captures a proton from the  $\mu_3\text{-OH}$  group (Fig. 5, last configuration). All structural reorganizations observed so far give rise to the final configuration, which is made up of four 7-fold and two 8-fold coordinated Zr atoms.

At this point, it is also interesting to note the differences between the chemical features shown in this study and the earlier reaction profile determined with static NEB calculations. The earlier static calculations allow two transition states to be located with barriers of  $121.3$  and  $178.7 \text{ kJ mol}^{-1}$  at  $593 \text{ K}$ .<sup>48</sup> The processes observed here consist translation and rotation of

between the carboxylic oxygen O3 and the bridging  $\mu_3\text{-O}$  is also observed and is evidenced by the measured probability distribution (bottom). It is an indication of the occurrence of an intrinsic dynamic acidity. Colors indicate the coordination number of Zr atoms.





**Fig. 5** Different structures observed in the simulation window of configuration 5, which are rationalized by the two motions presented in Fig. 4. The colors of the Zr atoms indicate their coordination number.

a linker attached originally to two Zr atoms with the hydroxyl group in a  $\mu_1\text{-OH}$  configuration and situated on a multidimensional free energy plateau at about  $90 \text{ kJ mol}^{-1}$ . The simulations shown here reveal that deformations in one linker induces the mobility of various nearby linkers and another hydroxyl group in the inorganic brick. Such metastable configurations are stabilized by the presence of hydrogen bonds and are maintained for a consistent part of the simulation. This has been further validated by an additional set of regular MD simulations of 50 ps without the presence of activated umbrellas starting from the final configuration obtained in the last window. This regular MD simulation confirms the mobility of the hydroxyl groups and supports the hypothesis of a strongly varying intrinsic dynamic proton acidity (Fig. S3 of the ESI†).

Overall, our simulations show that linkers are much more mobile than originally anticipated. During an activation process, they can easily change their position *via* decoordinations, translations, rotations and recoordinations, while the inorganic brick shows no major distortions. The latter is shown in the distribution of the Zr–Zr and Zr–O distances in the brick (Fig. S4 of the ESI†). Such effects point towards a remarkable intrinsic flexibility of the framework, where the coordination numbers can easily vary between 8 and 6. Defects on the structure are crucial for the catalytic activity and the dehydration mechanism may have a decisive effect on certain catalytic reactions, where next to the Lewis acid site also, the neighboring Brønsted base or acid sites may take an interactive role in the reaction mechanism.<sup>60,61</sup> Examples of such reactions are jasminaldehyde condensation,<sup>62</sup> in which first the C–C coupling product gets protonated by the hydrogen attached to the  $\mu_3$ -oxygen atom and this leads to the aldol product. Also, in the case of esterification reaction, the hydrogen bond with the  $\mu_3$ -oxygen atom plays a crucial role in the proposed reaction mechanism.<sup>60</sup> For the Oppenauer oxidation studied in ref. 61, Lewis and dynamic Brønsted sites are required. For this reaction, a conversion of 68% was found to the desired product for an almost ideal UiO-66 material (11.6 linker per brick). The

mobility of the linkers observed in this study could explain these findings, as linkers might temporarily decoordinate from the Zr atoms and be stabilized by protons from the framework, giving more accessible Lewis acid sites.<sup>64</sup> The unraveled dynamic behavior of UiO-66 can serve as a platform to rationalize the dynamic coordination change and accessibility of active sites in other ‘inert’ MOFs characterized by exceptional stability and higher surface-to-volume ratio.

The energy required to induce such internal rearrangements are easily accessible with common experimental activation procedures such as a temperature increase and can be accommodated with this exceptionally stable material. Furthermore, hydrogen bonding appears to be an important part of the interaction between hydroxyl group and the decoordinated linkers. The hydrogen-bonding pattern observed during dehydration is remarkable and can stabilize the structure in processes that involve decoordination of the linkers. One may anticipate that further stabilization patterns might occur when a solvent such as methanol would be present. The observed structural dynamic flexibility of robust UiO-66 is unique and our results confirmed that the chemistry of M–L bond is reversible, as was indicated by Kim *et al.*<sup>28</sup> in the linker exchange reaction. This demonstrates that in all chemical processes where the coordination number of the metal ion changes, there is fast structural evolution in which the linkers play a major role, constantly switching their position. Experimentally, the characteristics of structural dynamic motions on the picosecond timescale have been seen in the case of functionalized MOFs by applying ultrafast 2D IR spectroscopy<sup>33</sup> and can be expanded to track changes during reversible dehydration process of UiO-66.

## Conclusions

The UiO-66 framework is archetypal for its structural stability, but also allows structural deformations by processes such as dehydration, linker exchange, and defect formation while maintaining its structural integrity. Herein, we tried by means





of enhanced sampling molecular dynamics simulations such as umbrella sampling techniques to give a better insight in the factors based on the observed intrinsic dynamic flexibility of the framework, whereby the coordination number of the Zr atoms can easily change between 8 and 6. By following the system on the fly at 573 K, during an activated process where the coordination number of the hydroxyl group bridging the Zr atoms of the inorganic brick varies from 3 to 1, a remarkable fast dynamics of the system is observed. Depending on the free energy window explored, major rearrangements are observed for the hydroxyl group, which induce a strong mobile behavior of various connecting linkers. In lower activated regions, the hydroxyl group can easily travel among the three Zr atoms to which it is originally connected in a  $\mu_3\text{-OH}$  configuration. Once higher activated plateau is reached at about 90  $\text{kJ mol}^{-1}$ , reversible mobility of the linkers is observed, while the rigidity of the inorganic brick is retained. We observe the processes of proton shuttling even in defect-free UiO-66 at elevated temperature, where a proton transfer occurs between a  $\mu_3\text{-OH}$  and carboxylic oxygen of a partly decoordination linker. These results expand the earlier concept of dynamic acidity introduced by Ling and Slater<sup>66</sup> to defect-free UiO-66, even in the absence of protic species. General deformation modes are detected for the linkers during activation, which correspond to translational and rotational modes. The system has a remarkable intrinsic dynamic ability to respond to deformations, where closely connected linkers decoordinate and are eventually stabilized by hydrogen bonding interactions with adjacent hydroxyl groups. We can safely assume that partly decoordination linkers would also be stabilized by hydrogen bonding interactions with other solvent species during processes such as solvent assisted ligand exchange. The change in coordination of the hydroxyl group simulated here is an essential step during the dehydroxylation process. Furthermore, our observations are based on simulations in defect-free UiO-66, but these rearrangements may be expected to take place in defective UiO-66, as we have already established similar dehydration pathways in defective materials. The understanding of rearrangements of linker ligands or bridging hydroxyl groups in the inorganic node during activation has so far been insufficient, as it poses a huge challenge to follow the system *in situ* during activation based on a purely experimental basis. Herein, we took a major step forward for the structural understanding in the intrinsic dynamic behavior of UiO-66.

## Methodology

The *ab initio* molecular dynamics (AIMD) simulations were performed within the DFT level of theory in a full periodic defect-free UiO-66 in the NPT ensemble using the CP2K simulation package interfaced with the advanced simulation library PLUMED.<sup>63,64</sup> The revPBE functional<sup>65</sup> with inclusion of Grimme D3 dispersion corrections<sup>66</sup> was chosen using the DZVP-GTH basis sets for C, O and H atoms, which is a combination of Gaussian basis functions and plane waves (GPW)<sup>67</sup> with a cut-off energy of 350 Ry. For Zr, the DZVP-MOLOPT-SR basis set has been applied. Along the reaction path, we performed advanced

molecular dynamic simulations by means of umbrella sampling (US). The crucial step in the US methodology was the selection of the various windows on the reaction path along the collective variable (CV) and determination of the initial structures in each of these windows. We applied a protocol in the form of a moving umbrella, which during the duration of the molecular dynamics crosses the entire range of CV with a constant velocity. This constrained MD concept was introduced by Grubmüller *et al.*<sup>68</sup> but it was not applied in this context. 36 snapshots were extracted from this moving umbrella simulation, and in each of those, an MD simulation with a static harmonic bias was initiated. Those MD simulations were run for 25 ps and the frequently visited configurations in each umbrella sampling were stored and their specific features were discussed. The free energy profile was constructed by application of the WHAM methodology.<sup>69,70</sup> More details of the calculations were included in the ESI.†

## Conflicts of interest

There are no conflicts of interest to declare.

## Acknowledgements

This work is supported by the Research Foundation Flanders (FWO), the Research Board of Ghent University (BOF) and BELSPO in the frame of IAP/7/05. This project received funding from the European Union's Horizon 2020 research and innovation programme under the Marie Skłodowska-Curie grant agreement No. 641887 (project acronym: DEFNET). Funding was also received from the European Union's Horizon 2020 research and innovation programme [consolidator ERC grant agreement no. 647755-DYNPOR (2015–2020)]. The computational resources and services used in this work were provided by the VSC (Flemish Supercomputer Center), funded by the FWO. Molecular visualizations were produced with VMD software support. VMD is developed with NIH support by the Theoretical and Computational Biophysics group at the Beckman Institute, University of Illinois, at Urbana-Champaign.

## References

- 1 J. L. C. Rowsell and O. M. Yaghi, *Microporous Mesoporous Mater.*, 2004, **73**, 3–14.
- 2 G. Férey, *Chem. Soc. Rev.*, 2008, **37**, 191–214.
- 3 H. C. Zhou and S. Kitagawa, *Chem. Soc. Rev.*, 2014, **43**, 5415–5418.
- 4 J. R. Li, R. J. Kuppler and H. C. Zhou, *Chem. Soc. Rev.*, 2009, **38**, 1477–1504.
- 5 J. E. Mondloch, M. J. Katz, W. C. Isley III, P. Ghosh, P. Liao, W. Bury, G. W. Wagner, M. G. Hall, J. B. DeCoste, G. W. Peterson, R. Q. Snurr, C. J. Cramer, J. T. Hupp and O. K. Farha, *Nat. Mater.*, 2015, **14**, 512–516.
- 6 P. Horcajada, R. Gref, T. Baati, P. K. Allan, G. Maurin, P. Couvreur, G. Férey, R. E. Morris and C. Serre, *Chem. Rev.*, 2012, **112**, 1232–1268.



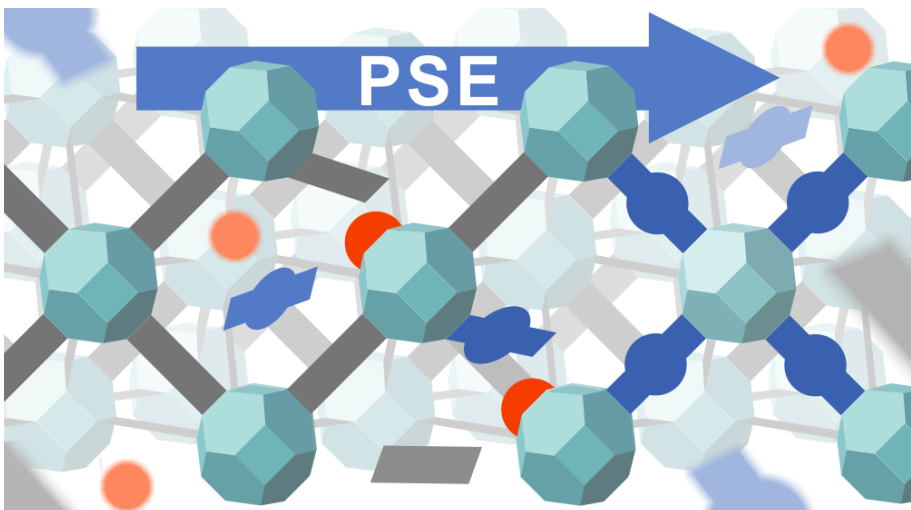
- 7 J. Gascon, A. Corma, F. Kapteijn and F. X. Llabrés i Xamena, *ACS Catal.*, 2014, **4**, 361–378.
- 8 J. Lee, O. K. Farha, J. Roberts, K. A. Scheidt, S. T. Nguyen and J. T. Hupp, *Chem. Soc. Rev.*, 2009, **38**, 1450–1459.
- 9 M. Ranocchiari and J. A. v. Bokhoven, *Phys. Chem. Chem. Phys.*, 2011, **13**, 6388–6396.
- 10 P. Valvelens, F. Vermoortele and D. De Vos, *Catal. Sci. Technol.*, 2013, **3**, 1435–1445.
- 11 A. Corma, H. Garcia and F. X. Llabrés i Xamena, *Chem. Rev.*, 2010, **110**, 4606–4655.
- 12 S. M. J. Rogge, A. Baykina, J. Hajek, H. Garcia, A. I. Olivos-Suarez, A. Sepúlveda-Escribano, A. Vimont, G. Clet, P. Bazin, F. Kapteijn, M. Daturi, E. V. Ramos-Fernandez, F. X. Llabrés i Xamena, V. Van Speybroeck and J. Gascon, *Chem. Soc. Rev.*, 2017, **46**, 3134–3184.
- 13 K. Leus, T. Bogaerts, J. De Decker, H. Depauw, K. Hendrickx, H. Vrielinck, Van Speybroeck and P. Van Der Voort, *Microporous Mesoporous Mater.*, 2016, **226**, 110–116.
- 14 A. J. Howarth, Y. Liu, P. Li, Z. Li, T. C. Wang, J. T. Hupp and O. K. Farha, *Nat. Rev. Mater.*, 2016, **1**, 15018.
- 15 N. C. Burtch, H. Jasuja and K. S. Walton, *Chem. Rev.*, 2014, **114**, 10575–10612.
- 16 S. M. J. Rogge, J. Wieme, L. Vanduyfhuys, S. Vandenbrande, G. Maurin, T. Verstraeten, M. Waroquier and V. Van Speybroeck, *Chem. Mater.*, 2016, **28**, 5721–5732.
- 17 M. Kandiah, M. H. Nilsen, S. Usseglio, S. Jakobsen, U. Olsbye, M. Tilset, C. Larabi, E. A. Quadrelli, F. Bonino and K. P. Lillerud, *Chem. Mater.*, 2010, **22**, 6632–6640.
- 18 J. B. DeCoste, G. W. Peterson, H. Jasuja, T. G. Glover, Y.-g. Huang and K. S. Walton, *J. Mater. Chem. A*, 2013, **1**, 5642–5650.
- 19 A. De Vos, K. Hendrickx, P. Van Der Voort, V. Van Speybroeck and K. Lejaeghere, *Chem. Mater.*, 2017, **29**, 3006–3019.
- 20 J. H. Cavka, S. Jakobsen, U. Olsbye, N. Guillou, C. Lamberti, S. Bordiga and K. P. Lillerud, *J. Am. Chem. Soc.*, 2008, **130**, 13850–13851.
- 21 L. Valenzano, B. Civalleri, S. Chavan, S. Bordiga, M. H. Nilsen, S. Jakobsen, K. P. Lillerud and C. Lamberti, *Chem. Mater.*, 2011, **23**, 1700–1718.
- 22 H. Wu, Y. S. Chua, V. Krungleviciute, M. Tyagi, P. Chen, T. Yildirim and W. Zhou, *J. Am. Chem. Soc.*, 2013, **135**, 10525–10532.
- 23 M. J. Cliffe, W. Wan, X. D. Zou, P. A. Chater, A. K. Kleppe, M. G. Tucker, H. Wilhelm, N. P. Funnell, F. X. Couder and A. L. Goodwin, *Nat. Commun.*, 2014, **5**, 4176.
- 24 R. E. Morris and L. Brammer, *Chem. Soc. Rev.*, 2017, **46**, 5444–5462.
- 25 S. Horike, S. Shimomura and S. Kitagawa, *Nat. Chem.*, 2009, **1**, 695–704.
- 26 A. Schneemann, V. Bon, I. Schwedler, I. Senkovska, S. Kaskel and R. A. Fischer, *Chem. Soc. Rev.*, 2014, **43**, 6062–6096.
- 27 Y. Bai, Y. Dou, L.-H. Xie, W. Rutledge, J.-R. Li and H.-C. Zhou, *Chem. Soc. Rev.*, 2016, **45**, 2327–2367.
- 28 M. Kim, J. F. Cahill, Y. Su, K. A. Prather and S. M. Cohen, *Chem. Sci.*, 2012, **3**, 126–130.
- 29 K. K. Tanabe and S. M. Cohen, *Chem. Soc. Rev.*, 2011, **40**, 498–519.
- 30 S. M. Cohen, *J. Am. Chem. Soc.*, 2017, **139**, 2855–2863.
- 31 G. C. Shearer, S. Forslev, S. Chavan, S. Bordiga, K. Mathisen, M. Bjorgen, S. Svelle and K. P. Lillerud, *Top. Catal.*, 2013, **56**, 770–782.
- 32 M. Vandichel, J. Hajek, F. Vermoortele, M. Waroquier, D. E. De Vos and V. Van Speybroeck, *CrystEngComm*, 2015, **17**, 395–406.
- 33 J. Nishida, A. Tamimi, H. Fei, S. Pullen, S. Ott, S. M. Cohen and M. D. Fayer, *Proc. Natl. Acad. Sci. U. S. A.*, 2014, **111**, 18442–18447.
- 34 T. D. Bennett, A. K. Cheetham, A. H. Fuchs and F.-X. Coudert, *Nat. Chem.*, 2017, **9**, 11–16.
- 35 A. D. Wiersum, E. Soubeiran-Lenoir, Q. Yang, B. Moulin, V. Guillerm, M. B. Yahia, S. Bourrelly, A. Vimont, S. Miller, C. Vagner, M. Daturi, G. Clet, C. Serre, G. Maurin and P. Llewellyn, *Chem.-Asian J.*, 2011, **6**, 3270–3280.
- 36 S. Ling and B. Slater, *Chem. Sci.*, 2016, **7**, 4706–4712.
- 37 C. Caratelli, J. Hajek, S. M. J. Rogge, S. Vandenbrande, E. J. Meijer, M. Waroquier and V. Van Speybroeck, *ChemPhysChem*, DOI: 10.1002/cphc.201701109.
- 38 O. Valsson, P. Tiwary and M. Parrinello, in *Annual Review of Physical Chemistry*, Vol. 67, ed. M. A. Johnson and T. J. Martinez, 2016, vol. 67, pp. 159–184.
- 39 K. De Wispelaere, S. Bailleul and V. Van Speybroeck, *Catal. Sci. Technol.*, 2016, **6**, 2686–2705.
- 40 K. De Wispelaere, B. Ensing, A. Ghysels, E. J. Meijer and V. Van Speybroeck, *Chem.-Eur. J.*, 2015, **21**, 9385–9396.
- 41 P. Cnudde, K. De Wispelaere, J. Van der Mynsbrugge, M. Waroquier and V. Van Speybroeck, *J. Catal.*, 2017, **345**, 53–69.
- 42 J. Hajek, J. Van der Mynsbrugge, K. De Wispelaere, P. Cnudde, L. Vanduyfhuys, M. Waroquier and V. Van Speybroeck, *J. Catal.*, 2016, **340**, 227–235.
- 43 V. Van Speybroeck, K. De Wispelaere, J. Van der Mynsbrugge, M. Vandichel, K. Hemelsoet and M. Waroquier, *Chem. Soc. Rev.*, 2014, **43**, 7326–7357.
- 44 V. Haigis, F.-X. Coudert, R. Vuilleumier, A. Boutin and A. H. Fuchs, *J. Phys. Chem. Lett.*, 2015, **6**, 4365–4370.
- 45 T. Bučko, L. Benco, J. Hafner and J. G. Angyan, *J. Catal.*, 2011, **279**, 220–228.
- 46 J. D. Evans, G. Fraux, R. Gaillac, D. Kohen, F. Trouselet, J. M. Vanson and F. X. Couder, *Chem. Mater.*, 2017, **29**, 199–212.
- 47 G. Fraux and F. X. Couder, *Chem. Commun.*, 2017, **53**, 7211–7221.
- 48 M. Vandichel, J. Hajek, A. Ghysels, A. De Vos, M. Waroquier and V. Van Speybroeck, *CrystEngComm*, 2016, **18**, 7056–7069.
- 49 Y. Sugita and Y. Okamoto, *Chem. Phys. Lett.*, 1999, **314**, 141–151.
- 50 U. H. E. Hansmann, *Chem. Phys. Lett.*, 1997, **281**, 140–150.
- 51 L. Maragliano and E. Vanden-Eijnden, *Chem. Phys. Lett.*, 2006, **426**, 168–175.
- 52 R. W. Zwanzig, *J. Chem. Phys.*, 1954, **22**, 1420–1426.
- 53 J. G. Kirkwood, *J. Chem. Phys.*, 1935, **3**, 300–313.
- 54 A. Laio and M. Parrinello, *Proc. Natl. Acad. Sci. U. S. A.*, 2002, **99**, 12562–12566.
- 55 G. N. Patey and J. P. Valleau, *J. Chem. Phys.*, 1975, **63**, 2334–2339.

- 56 G. M. Torrie and J. P. Valleau, *J. Comput. Phys.*, 1977, **23**, 187–199.
- 57 M. A. Rohrdanz, W. Zheng and C. Clementi, *Annu. Rev. Phys. Chem.*, 2013, **64**, 295–316.
- 58 R. Demuynck, S. M. J. Rogge, L. Vanduyfhuys, J. Wieme, M. Waroquier and V. Van Speybroeck, *J. Chem. Theory Comput.*, 2017, **13**, 5861–5873.
- 59 M. Puchberger, F. R. Kogler, M. Jupa, S. Gross, H. Fric, G. Kickelbich and U. Schubert, *Eur. J. Inorg. Chem.*, 2006, **2006**, 3283–3293.
- 60 C. Caratelli, J. Hajek, F. G. Cirujano, M. Waroquier, F. X. Llabrés i Xamena and V. Van Speybroeck, *J. Catal.*, 2017, **352**, 401–414.
- 61 J. Hajek, B. Bueken, M. Waroquier, D. De Vos and V. Van Speybroeck, *ChemCatChem*, 2017, **9**, 2203–2210.
- 62 J. Hajek, M. Vandichel, B. Van de Voorde, B. Bueken, D. De Vos, M. Waroquier and V. Van Speybroeck, *J. Catal.*, 2015, **331**, 1–12.
- 63 J. VandeVondele, M. Krack, F. Mohamed, M. Parrinello, T. Chassaing and J. Hutter, *Comput. Phys. Commun.*, 2005, **167**, 103–128.
- 64 G. A. Tribello, M. Bonomi, D. Branduardi, C. Camilloni and G. Bussi, *Comput. Phys. Commun.*, 2014, **185**, 604–613.
- 65 K. Yang, J.-J. Zheng, Y. Zhao and D. G. Truhlar, *J. Chem. Phys.*, 2010, **132**, 10.
- 66 S. Grimme, J. Antony, S. Ehrlich and H. Krieg, *J. Chem. Phys.*, 2010, **132**, 154104.
- 67 G. Lippert, J. Hutter and M. Parrinello, *Theor. Chem. Acc.*, 1999, **103**, 124–140.
- 68 H. Grubmüller, B. Heymann and P. Tavan, *Science*, 1996, **271**, 997–999.
- 69 A. Grossfield, <http://membrane.urmc.rochester.edu/content/wham>.
- 70 S. Kumar, J. M. Rosenberg, D. Bouzida, R. H. Swendsen and P. A. Kollman, *J. Comput. Chem.*, 1992, **13**, 1011–1021.



## Paper IV

### Active Role of Methanol in Post-Synthetic Linker Exchange in the Metal–Organic Framework UiO–66



J. Marreiros, C. Caratelli, J. Hajek, A. Krajnc, G. Fleury, B. Bueken, D. De Vos, G. Mali, M. Roeffaers, V. Van Speybroeck, R. Ameloot, *Chemistry of Materials*, **31**, 4, 1359–1369 (2019)

C. Caratelli performed the computational research and was involved in the manuscript preparation.

©2019 American Chemical Society.

Reprinted with permission from the American Chemical Society.



## Active Role of Methanol in Post-Synthetic Linker Exchange in the Metal–Organic Framework UiO-66

Joao Marreiros,<sup>†</sup> Chiara Caratelli,<sup>‡</sup> Julianna Hajek,<sup>‡</sup> Andraž Krajnc,<sup>§</sup> Guillaume Fleury,<sup>†</sup><sup>¶</sup> Bart Bueken,<sup>†</sup> Dirk E. De Vos,<sup>†</sup> Gregor Mali,<sup>§</sup> Maarten B. J. Roeffaers,<sup>†</sup><sup>¶</sup> Veronique Van Speybroeck,<sup>‡</sup> and Rob Ameloot<sup>\*,†</sup><sup>¶</sup>

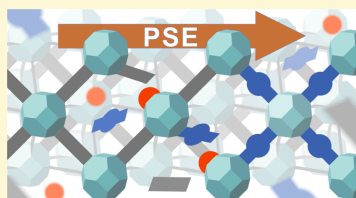
<sup>†</sup>Centre for Surface Chemistry and Catalysis, KU Leuven, Celestijnenlaan 200F, P.O. Box 2461, 3001 Leuven, Belgium

<sup>‡</sup>Center for Molecular Modeling, Universiteit Gent, Technologiepark 903, B-9052 Zwijnaarde, Belgium

<sup>§</sup>Department of Inorganic Chemistry and Technology, National Institute of Chemistry, Hajdrihova 19, 1001 Ljubljana, Slovenia

### Supporting Information

**ABSTRACT:** UiO-66 is known as one of the most robust metal–organic framework materials. Nevertheless, UiO-66 has also been shown to undergo postsynthetic exchange of structural linkers with surprising ease in some solvents. To date, the exchange mechanism has not yet been fully elucidated. Here, we show how time-resolved monitoring grants insight into the selected case of exchanging 2-aminoterephthalate into UiO-66 in methanol. Analysis of both the solid and liquid phases, complemented by computational insights, revealed the active role of methanol in the creation and stabilization of dangling linkers. Similar to monocarboxylate defects that can be introduced during UiO-66 synthesis, such dangling linkers undergo fast exchange. The presence of missing-linker or missing-cluster defects at the start of the exchange process was shown to have no considerable impact on the equilibrium composition. After the exchange process, the incoming 2-aminoterephthalate and remaining terephthalate linkers were distributed homogeneously in the framework for the typical submicron size of UiO-66 crystallites.



Metal–organic frameworks (MOFs) are porous crystalline materials currently at the forefront of materials chemistry because of their high internal surface area and tunable nature. MOFs are constructed from metal ion nodes connected by multitopic organic linkers. One of the most promising MOF materials, because of its high stability, is the widely studied UiO-66, composed of 12-coordinated  $[Zr_6(\mu_3-O)_4(\mu_3-OH)_4]^{12+}$  clusters connected through 1,4-benzenedicarboxylate (BDC) linkers.<sup>1</sup> UiO-66 presents high framework connectivity combined with strong coordination bonds between the oxophilic  $Zr^{4+}$ -based clusters and the BDC carboxylate groups.<sup>2</sup> Moreover, because of its high connectivity, the UiO-66 framework has a high tolerance for structural defects,<sup>3</sup> a property that has been explored in catalysis,<sup>4,5</sup> gas storage and separation,<sup>6,7</sup> sensing,<sup>8</sup> drug delivery,<sup>9</sup> and so forth. Despite their presumed robust and inert nature, UiO-66 and other Zr-MOFs have been found to be susceptible to a range of post-synthetic modification processes. For instance, Farha and co-workers reported the post-synthetic grafting of linkers onto coordinatively unsaturated sites in the MOF material NU-1000.<sup>10,11</sup> Kim et al. demonstrated that the BDC linker in UiO-66 can be exchanged with a differently functionalized analogue without a loss in crystallinity, in a process termed “post-synthetic ligand exchange” (PSE, Figure 1).<sup>12</sup>

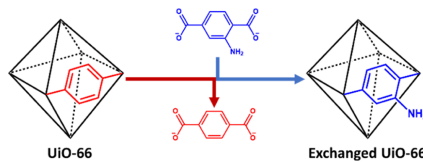


Figure 1. PSE in UiO-66. The structural linker in the framework is replaced and released into the surrounding solution.

Since its introduction, PSE has become a well-established procedure in the preparation of UiO-66 materials with specific chemical functionalities, often inaccessible through direct synthesis.<sup>13,14</sup> Nevertheless, a fundamental understanding of the PSE process is still lacking. Furthermore, different reported exchange protocols lead to seemingly contradictory results, in terms of the extent of linker exchange and distribution. Recently, a number of studies have demonstrated how the particle size can impact whether or not the incoming linker will be distributed homogeneously in the modified framework.<sup>14,15</sup>

Received: November 12, 2018

Revised: February 6, 2019

Published: February 6, 2019

## Chemistry of Materials

## Article

Shearer et al. and Taddei et al. demonstrated how defect sites are more prone to exchange than the structural linker of the parent framework.<sup>16,17</sup> Both reports show that when performed in dimethylformamide (DMF), incoming monodentate ligands or bidentate linkers end up predominantly at defect sites capped by monocarboxylates. The latter are often introduced during synthesis through the use of "modulators" and are more easily displaced than the doubly anchored dicarboxylate linkers during PSE. Kim et al. described PSE in UiO-66 for a selection of solvents ( $\text{H}_2\text{O}$ , DMF, MeOH, and  $\text{CHCl}_3$ ), resulting in different linker exchange yields.<sup>13,18</sup> In the reports cited above, both defect generation plus healing as well as direct linker replacement are suggested as PSE mechanisms.

With some exceptions,<sup>17</sup> the PSE studies reported thus far focused on comparing the parent material and the exchanged samples, with little insight into the process at the molecular level. Therefore, many questions regarding the ligand exchange mechanism remain unanswered, including its kinetics, the changes in the cluster coordination, the ratio of outgoing and incoming linkers, as well as the role of framework defects and solvent interactions. Nevertheless, as the examples above illustrate,<sup>13</sup> parameters such as solvent composition clearly play a determining role in the exchange process.<sup>12</sup> To address the remaining questions, we studied PSE in UiO-66 via time-resolved monitoring of both the exchange solution and the modified MOF materials. The combination of this approach with computational modeling and spectroscopic techniques provides direct insights into the ligand exchange mechanism and the parameters determining its outcome.

## ■ EXPERIMENTAL DETAILS

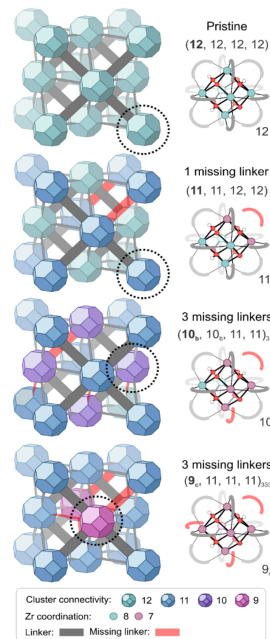
**Synthesis of UiO-66 and Ligand Exchange.** Reference UiO-66 material was prepared using a solvothermal protocol reported to afford materials with the near-perfect coordination of 12 BDC linkers per cluster, further referred to as "modulator-free synthesis".<sup>19</sup> This material was activated through several solvent washing steps in DMF and ethanol (EtOH), followed by drying under dynamic vacuum at 473 K for 24 h. After drying, this reference UiO-66 material was found to have 11.8 linkers per cluster. The Brunauer–Emmett–Teller (BET) surface area determined by  $\text{N}_2$  physisorption was found to be  $1273 \text{ m}^2 \text{ g}^{-1}$ . The particle size was approximately 500 nm, based on electron micrographs. The ligand exchange procedure followed that of Kim et al.:<sup>12</sup> 28 mg of UiO-66 (containing 0.1 mmol of BDC) was suspended in a solution of 18 mg (0.1 mmol) of 2-aminoterephthalic acid ( $\text{NH}_2\text{--H}_2\text{BDC}$ ) in 10 mL of methanol (MeOH) at 313 K. Under these conditions, equal amounts of both linkers are present in the mixture. The concentration of 10 mM was selected to not exceed the experimentally determined solubility limit of either linker, namely, 12 and 18 mM in MeOH at room temperature for  $\text{H}_2\text{BDC}$  and  $\text{NH}_2\text{--H}_2\text{BDC}$ , respectively.

**Time-Resolved PSE Monitoring.** High-performance liquid chromatography (HPLC) monitoring of the exchange solution was performed by injecting 1  $\mu\text{L}$  of sample on an Agilent 1260 HPLC with a  $1 \text{ mL min}^{-1}$  eluent flow (95:5 water/acetonitrile isocratic mixture) and equipped with a ZORBAX Eclipse XDB C18 column and DAD detector tuned to the maximum absorbance wavelength of 240 nm.<sup>20</sup> Analysis of the exchange solution confirmed the absence of side reactions during ligand exchange (e.g., esterification). The solid-phase characterization was adapted from Shearer et al.<sup>21</sup> and complemented via thermogravimetric analysis (TGA) and  $^1\text{H}$  NMR analysis of the number of linkers per cluster, a measure of defect density. TGA analysis under  $\text{O}_2$  yields a quantitative measure of the organic/inorganic ratio in the framework by assuming full conversion to  $\text{ZrO}_2$  upon decomposition. Quantitative solution  $^1\text{H}$  NMR of acid-digested MOF samples enables quantitative identification of the organic composition of the framework. Solution NMR and HPLC were both

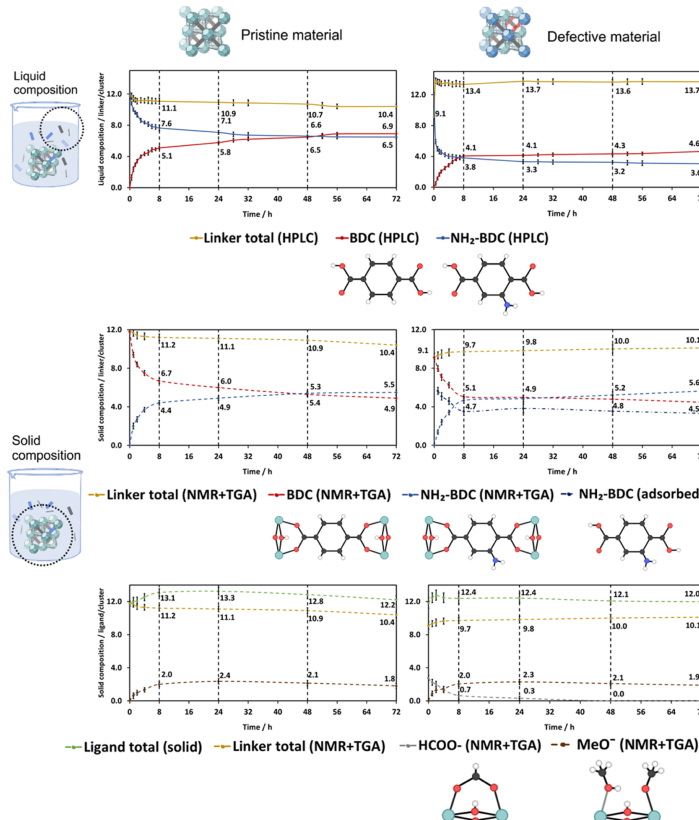
calibrated using standard solutions of  $\text{H}_2\text{BDC}$  and  $\text{NH}_2\text{--H}_2\text{BDC}$ . Reproducibility was assessed through triplicate trials, revealing standard deviations of 0.46–0.78, 0.28–0.89, and 0.49–1.2 linkers/cluster for HPLC, NMR, and TGA, respectively. Further details on the experimental and characterization methods are provided in the Supporting Information (Section III).

**Computational Methodology.** Defective structure models were obtained from De Vos et al.<sup>22</sup> by removal of linkers from the UiO-66 unit cell containing four  $[\text{Zr}_6(\mu_3\text{O})_4(\mu_3\text{OH})]^{12+}$  clusters.<sup>1</sup> A low number of defects are represented by a unit cell with one missing linker, resulting in two 12-fold and two 11-fold coordinated clusters. To model a higher number of defects, 3 linkers are removed, resulting in an average of 10.5 linkers per cluster. Of the many possible ways to remove three linkers,<sup>22,23</sup> we chose two cases denoted as  $(10_b, 10_b, 11, 11)_{334}$  and  $(9_c, 11, 11, 11)_{333}$ , where the numbers indicate the connectivity of each brick and the subscripts are determined by the symmetry of the unit cell.<sup>23</sup> In the first case, two clusters are 10-fold coordinated and two are 11-fold coordinated. In the second, one 9-fold and three 11-fold coordinated clusters are present. A representation of the unit cells is given in Figure 2. With each removed linker, four Zr atoms become coordinatively unsaturated and two positive charges on the inorganic node need to be compensated.

Charges at the defect sites can be compensated by adsorption of a negative species or removal of a proton. However, the latter



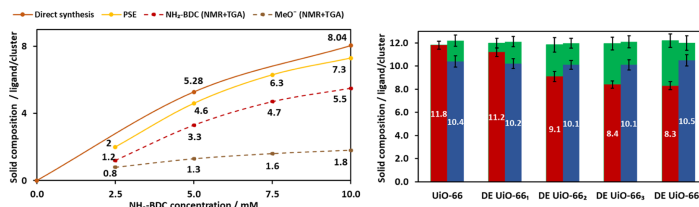
**Figure 2.** Structural models of defect-free and defective UiO-66. Left: the four UiO-66 unit cells used for computational modeling, with the missing linkers indicated in red. For clarity, the clusters and linkers at the border of the unit cell are represented in their entirety. Right: the four clusters that make up the unit cells, with connectivity ranging from 12 to 9.



**Figure 3.** Time-resolved monitoring of PSE in defect-free UiO-66 (left) and defect-rich UiO-66 (right). Top: Exchange solution composition as determined by HPLC, with  $\text{H}_2\text{BDC}$  and  $\text{NH}_2\text{-H}_2\text{BDC}$  concentrations (expressed per inorganic cluster) shown in red and blue, respectively. The total number of linkers in the solid (yellow) is calculated based on the difference between BDC coming out and  $\text{NH}_2\text{-BDC}$  going in. Middle: Linker content of the MOF material during PSE as determined by analysis of the solid by TGA and quantitative  $^1\text{H}$  NMR of acid-digested samples. The measured  $\text{H}_2\text{BDC}$  and  $\text{NH}_2\text{-H}_2\text{BDC}$  contents are shown in dashed red and blue, respectively; the calculated number of linkers per cluster in the solid in dashed yellow. Bottom: The  $\text{MeO}^-$  and  $\text{HCOO}^-$  contents in the MOF material during PSE, as determined by TGA and quantitative  $^1\text{H}$  NMR, of acid-digested samples, are shown in dashed brown and dashed gray, respectively. The total number of ligands per cluster (dashed green) is calculated as the sum of the linkers (dashed yellow, same curve as in middle panel) and the  $\text{MeO}^-$  content. The NMR, TGA, and HPLC measurements at each time instance were performed in triplicate. The error bars are based on these nine data points. The analysis results are presented in more detail in Figures S9 and S13.

configurations are higher in energy.<sup>24,25</sup> In our models, the Zr atoms at the defect sites are capped by species likely present in the pores:  $\text{H}_2\text{O}$ ,  $\text{OH}^-$ ,  $\text{MeOH}$ ,  $\text{MeO}^-$ , and  $\text{HCOO}^-$ . Taking into account the symmetry of the unit cell, multiple positions of the charge-compensating species were compared. All calculations were performed with periodic density functional theory to fully represent the crystal environment. We made use of the periodic Vienna Ab initio Simulation Package (VASP) code,<sup>26–30</sup> applying the projector augmented wave approach<sup>31</sup> and  $\Gamma$ -point approximation at Perdew–Burke–Eenzerhof level of theory<sup>32</sup> including GrimmeD3 dispersion

corrections.<sup>33,34</sup> The kinetic energy cutoff for the plane waves was set to 700 eV, and the convergence threshold for the electronic self-consistent field calculations was fixed to  $10^{-5}$  eV. A Gaussian smearing of 0.025 eV was included to improve convergence. The volume for each unit cell (Figure 2) was optimized by fitting a Birch–Murnaghan equation of state. In the calculation of energies, to account for the finite temperature, thermal corrections were performed using the calculated frequencies. Enthalpic and entropic contributions were calculated with the TAMkin processing toolkit.<sup>35</sup> A partial Hessian



**Figure 4.** Equilibrium nature of the PSE process in MeOH. Left: Cluster coordination as a function of the NH<sub>2</sub>-BDC fraction offered either in modulator-free, direct synthesis or PSE (72 h in MeOH). For the direct synthesis case, the number of NH<sub>2</sub>-BDC linkers per cluster is indicated (orange full line). For the PSE case, the sum of the NH<sub>2</sub>-BDC linkers and the MeO<sup>-</sup> ligands is indicated (yellow full line). Right: The effect of PSE on cluster coordination for UiO-66 materials with different initial defect densities. The “defect-engineered” samples are indicated with the prefix “DE”. The materials termed “UiO-66” and “DE UiO-66”, correspond to the MOFs studied in Figure 3. The number of structural linkers per cluster before and after PSE is indicated in red and blue, respectively. The total cluster coordination, including both structural terephthalates and other charged species, is indicated in green. After PSE, the height of the green bar corresponds to the amount of incorporated MeO<sup>-</sup>. Error bars are based on solid-phase analyses performed in triplicate.

vibrational analysis approach was used<sup>36</sup> as this does not substantially affect entropy and enthalpy differences.

## ■ RESULTS AND DISCUSSION

**Monitoring the PSE Process.** By monitoring both the MOF and exchange medium over time, we aimed at filling in the remaining gaps in the understanding of PSE in UiO-66. To facilitate data interpretation, linker concentrations in both the liquid and solid phases are reported as the number of BDC or NH<sub>2</sub>-BDC carboxylate groups per cluster, that is, 12 in the fully connected, defect-free UiO-66 network. Uptake of NH<sub>2</sub>-BDC from and release of H<sub>2</sub>BDC into the exchange medium was monitored by HPLC (Figure 3, top). The most pronounced changes are observed in the initial 8 h of exchange, followed by equilibration. After 72 h of PSE, a BDC/NH<sub>2</sub>-BDC ratio of 0.9:1 is observed in the framework, indicating a slight preference for the latter linker. Although the composition of the framework changes dramatically during PSE, the UiO-66 crystallinity is preserved throughout the treatment as shown by powder X-ray diffraction (Figure S8). To exclude crystal dissolution and recrystallization, control experiments with mixtures of linker and ZrCl<sub>4</sub> in MeOH in the concentration ranges relevant to PSE were performed (Table S2). No precipitate was formed with either linker after incubation at the exchange temperature. Additionally, UiO-66 crystals before and after exchange show no variation in particle size or shape (Figure S10).

In contrast to the PSE behavior commonly assumed, close analysis of the HPLC data shows nonstoichiometric linker exchange: more H<sub>2</sub>BDC is released than NH<sub>2</sub>-H<sub>2</sub>BDC is incorporated. Since the exchange conditions avoid solubility issues of either linker, these measurements indicate an actual decrease from 11.8 to 10.4 linkers per cluster during PSE, for the pristine UiO-66. To cross-check these observations with the changes in the solid phase, MOF samples were collected at selected instances and characterized for composition and structure (Figure 3, middle and bottom). Analysis of the linker ratio was performed via quantitative solution <sup>1</sup>H NMR after extensive washing with EtOH. The total organic content was determined by TGA and used as a reference for the NMR measurements. The solid-phase data mirrors the observations from the solution data, with the most pronounced changes to the framework composition in the initial 8 h. Moreover, these

results reveal the same decline in the number of linkers per cluster as determined by HPLC, consistent with the generation of defects in the UiO-66 treated samples. As defects are necessarily formed by the net removal of linkers, negatively charged species different from BDC or NH<sub>2</sub>-BDC have to be incorporated in the framework. A clear distinction is made between *linkers* and *ligands*: the former term addresses the structural terephthalates that build up the framework, the latter includes all cluster-bound species, including terephthalates as well as other charged organic species responsible for charge compensation. To facilitate data interpretation, linker and ligand concentrations are both reported on a per-cluster basis.

A closer look at the NMR spectra of PSE UiO-66 samples digested with CsF and DCl in DMSO-*d*<sub>6</sub> reveals a characteristic MeOH signal. Given that all samples were extensively washed with EtOH and vacuum dried at temperatures exceeding 373 K before analysis, this observation indicates a strong interaction between MeOH solvent species and the inorganic clusters. Because no EtOH could be detected, the two alcohols seem to have a different affinity for UiO-66. To better assess the effect of MeOH, pristine UiO-66 was suspended in pure MeOH at the same temperature as used for PSE. Combined TGA analysis showed the loss of approximately one BDC linker per cluster, accompanied by an increasing MeOH NMR signal for acid-digested samples (Figure S6). Interestingly, Shearer et al. previously reported a decrease in the linker content for UiO-66 washed with MeOH.<sup>19</sup> Recently, the coordination of MeO<sup>-</sup> to [Zr<sub>6</sub>(μ<sub>3</sub>O)<sub>4</sub>(μ<sub>3</sub>-OH)<sub>4</sub>]<sup>12+</sup> clusters was proposed by Yang et al. as a mechanism to stabilize missing-linker defects.<sup>37</sup> These observations indicate that even under mild conditions MeOH generates defects, most likely of the missing-linker type, in the otherwise robust UiO-66 framework.

Adding monocarboxylic acids as “modulators” is a common strategy to control the particle size or defectivity of Zr-based MOFs.<sup>38</sup> In UiO-66, part of these monocarboxylates end up in the framework where they form missing-linker and/or missing-cluster defect sites that might affect PSE.<sup>16,17</sup> To study the effect of such sites, defect-rich UiO-66 was prepared solvothermally in the presence of formic acid. The inorganic clusters in the resulting material are coordinated on average by 9.1 BDC linkers and 2.7 formate ligands.

## Chemistry of Materials

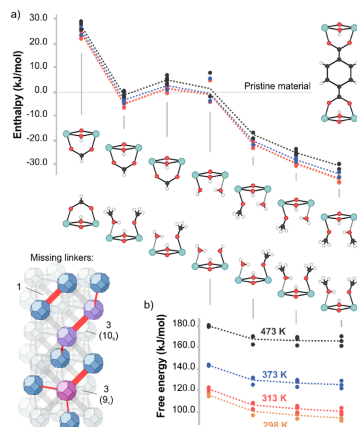
## Article

The material showed a slightly larger average particle size than the defect-free UiO-66 prepared in the absence of a modulator ( $2\ \mu\text{m}$  vs  $500\ \text{nm}$ ). As expected from the presence of defect sites, an increased BET surface area was measured,  $1538\ \text{m}^2\ \text{g}^{-1}$  compared with  $1273\ \text{m}^2\ \text{g}^{-1}$ .<sup>21</sup> When subjected to linker exchange, the defective material shows a rapid change in composition in the first 8 h followed by equilibration, similar to the reference UiO-66 material (Figure 3, top and middle). Solid-phase analysis shows that  $\text{HCOO}^-$  is rapidly removed from the framework and can no longer be detected after 48 h (Figure 3, bottom, dashed gray line). At the same time, MeOH is incorporated, likely in the form of  $\text{MeO}^-$  for charge compensation, at defect sites previously capped by  $\text{HCOO}^-$ . However, after PSE, this  $\text{MeO}^-$  content is lower than the amount of  $\text{HCOO}^-$  initially present (1.9 vs 2.7 per cluster), which hints at healing of a fraction of the defects (vide infra).

While PSE in MeOH differs in details for defect-free and defect-rich UiO-66, the evolution and outcome of the process seem to be very similar for both materials. An exchange of structural linkers is detected in both cases, in contrast to what is observed for PSE in DMF.<sup>17</sup> After exchange, virtually the same numbers of dicarboxylate linkers per cluster are observed in the defective and nondefective material, 10.1 versus 10.4, with a BDC/ $\text{NH}_2\text{-BDC}$  ratio of 0.8 and 0.9, respectively. Also, approximately the same amount of  $\text{MeO}^-$  is eventually incorporated, 1.9 versus 1.8 per cluster, respectively. These very similar compositions strongly hint at an equilibrium process at the inorganic cluster level. To further explore this hypothesis, PSE trials were conducted with different  $\text{NH}_2\text{-BDC}/\text{BDC}$  concentrations, 2.5–10 mM, corresponding to a  $\text{NH}_2\text{-BDC}/\text{BDC}$  linker ratio of 1:4–1:1. The PSE results for a defect-free starting material are summarized in Figure 4, left. For comparison, the composition of a UiO-66 obtained through a direct, modulator-free synthesis with the same  $\text{NH}_2\text{-BDC}/\text{BDC}$  ratios is given as well. As expected when the final composition would be equilibrium-controlled, the materials obtained through these different preparation routes show a similar trend, with more  $\text{NH}_2\text{-BDC}$  ending up in the framework when a higher concentration is present in the synthesis mixture or exchange solution. The difference in composition between both materials seems mainly to be due to the incorporation of  $\text{MeO}^-$  during PSE.

To further test the idea of PSE as an equilibrium process, the composition after linker exchange was compared for UiO-66 samples with different initial defect densities. Through the use of different monocarboxylic acid modulators and concentrations, these materials covered a broad range of defectivity. The number of linkers per cluster ranged from 11.2 to 8.3, with the rest of the cluster coordination completed by monocarboxylate ligands. Strikingly, however, when subjected to identical PSE conditions, all samples were found to contain approximately 10 linkers and 2  $\text{MeO}^-$  per cluster (Figure 4, right). These near-identical compositions, irrespective of the initial framework defect density, underline the equilibrium nature of the PSE process in MeOH.

**Nature of the Defect Sites in MeOH.** To understand the nature of the defects created by the net linker loss during PSE, the stability of these sites capped with different species was computationally investigated and compared with the defect-free material. Apart from MeOH and  $\text{MeO}^-$ , also  $\text{H}_2\text{O}$ ,  $\text{OH}^-$ , and  $\text{HCOO}^-$  were included because of their possible presence as a result of synthesis solvent contamination or decomposition.<sup>21</sup> The calculated enthalpy differences (Figure 5a)



**Figure 5.** Energy diagrams for defective UiO-66 unit cells. Each dot represents a possible distribution of missing-linker defects (1 or 3 in total) within the unit cell; the connecting dotted line represents a weighted average (see the Supporting Information). Values are normalized by the number of missing linkers in the unit cell. (a) Enthalpy difference between defect sites capped in different ways versus the nondefective material at  $T = 298, 313, 373, 473\ \text{K}$ . (b) Temperature-dependence of the free-energy difference of the defective structures indicated above (capped with  $\text{H}_2\text{O}/\text{OH}^-$ ,  $\text{H}_2\text{O}/\text{MeO}^-$  and  $\text{MeOH}/\text{MeO}^-$ ) versus the nondefective structure. A representation of the clusters with different missing-linker connectivities is also provided.

indicate a clear preference for capping missing-linker defects with a  $\text{MeOH}/\text{MeO}^-$  pair, in line with the previous report by Yang et al.<sup>37</sup> Note that the protonated MeOH molecule is removed during vacuum-drying and only the  $\text{MeO}^-$  species is detected in NMR analysis of digested samples. Entropic contributions and dynamic solvent effects may further play a role in the stabilization of both the defective and nondefective structures.<sup>38</sup> Furthermore, free-energy calculations that take entropic effects into account indicate that the formation of  $\text{MeOH}/\text{MeO}^-$ -terminated defects becomes more favorable at lower temperatures because the entropic penalty associated with adsorption decreases (Figure 5b). Because PSE is performed at much lower temperatures than UiO-66 synthesis, the formation of missing-linker defects can be rationalized through this lower free energy penalty. Vice versa, this computational result agrees well with the experimentally observed preference for forming nondefective UiO-66 at high synthesis temperatures.<sup>19</sup> Knowing the nature of the ligands that balance the charge of the inorganic clusters also provides insight into the connectivity of the linkers and clusters. Quantification of the structural linkers and other charged ligands (i.e., BDC,  $\text{NH}_2\text{-BDC}$ , and  $\text{MeO}^-$ ) reveals that during PSE, there are more than the required 12 ligating groups present per cluster (Figure 3, bottom, green dashed line). Most likely, this apparent “overcoordination” can be caused by the presence of dicarboxylic linkers that are connected only through one end to an inorganic cluster, leaving the other end

## Chemistry of Materials

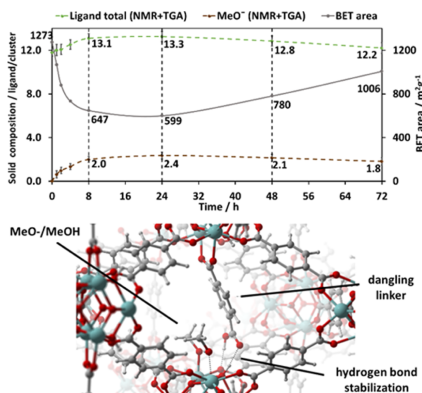
## Article

dangling in the pore, thus not contributing to charge compensation.

The framework composition reveals that this overcoordination is predominantly because of the incorporation of more than two  $\text{MeO}^-$  groups per cluster (Figure 3, bottom). The total of over 13 ligands per cluster observed for pristine UiO-66 implies that on average each cluster has at least one dangling BDC or  $\text{NH}_2\text{-BDC}$  linker connected to it. Interestingly, throughout the PSE process, the degree of overcoordination first rises and then falls (Figure 3, bottom, green curve). Initially, the total number of ligands per cluster climbs to over 13 after 8 h. Eventually, after 72 h of ligand exchange, almost no overcoordination is observed and approximately 12 ligands per cluster are present. This two-step variation is counterintuitive and hints at the combined contribution of several processes occurring on a different timescale.

The lack of overcoordination at the end of the exchange process (72 h) indicates that there are few dangling linkers left. At the same time,  $\text{MeO}^-$  species remain present in the structure (1.8 per cluster), presumably as  $\text{MeOH}/\text{MeO}^-$  pairs. Combined, these two observations imply that at the end of the PSE process, most defects in the lattice take the form of a missing linker that has been replaced by two  $\text{MeOH}/\text{MeO}^-$  pairs directly opposite to each other, as displayed in Figure 5. In other words, the changes in overcoordination during PSE are due to  $\text{MeOH}/\text{MeO}^-$  pairs or alternatively the associated dangling linker sites, moving through the crystal lattice. As can be expected, this process is rather slow to come to an equilibrium. It was experimentally confirmed that longer PSE times do not further alter the framework composition. On the basis of the above observations, it can be hypothesized that (i) during PSE of UiO-66 in MeOH, the solvent continuously generates dangling linker defects through the formation of  $\text{MeOH}/\text{MeO}^-$  pairs and that (ii) eventually a state is reached in which  $\text{MeO}^-$  ligands are still present, but in the form of double  $\text{MeOH}/\text{MeO}^-$  pairs, as indicated by the absence of dangling linkers.

**Monitoring the Porosity throughout PSE.** Because dangling linkers affect the accessible pore volume, their appearance can be monitored through physisorption measurements. The BET surface areas determined for samples isolated at different moments during PSE show an abrupt drop in the initial 24 h, from over  $1200 \text{ m}^2 \text{ g}^{-1}$  to below  $600 \text{ m}^2 \text{ g}^{-1}$ , followed by a gradual recovery to  $1006 \text{ m}^2 \text{ g}^{-1}$  (Figure 6, top). Composition analysis shows that the time instances where overcoordination is the highest coincide with the lowest specific surface area values. To further establish the relation between the measured surface area and the expected defect sites, theoretical BET surface areas were calculated for frameworks containing (i) dangling linkers and (ii) double  $\text{MeOH}/\text{MeO}^-$  pairs. Energy-optimized framework models with these defect sites are, respectively, thought of as representative of the intermediate regime with high overcoordination (and low surface area) and the final state without overcoordination (and partially recovered surface area). Zeo+<sup>40</sup> calculations estimate a surface area of  $868 \text{ m}^2 \text{ g}^{-1}$  for a UiO-66 material that contains on average one dangling BDC linker and one  $\text{MeOH}/\text{MeO}^-$  pair per cluster. Not surprisingly, this value is significantly lower compared with the theoretical surface area calculated for a defect-free UiO-66 that would be similar to the starting material before PSE ( $1147 \text{ m}^2 \text{ g}^{-1}$ ). Interestingly, when the dangling linker is replaced by a

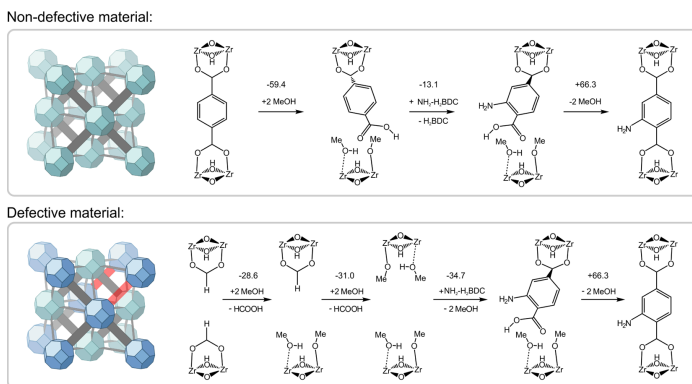


**Figure 6.** Porosity evolution during PSE of UiO-66. Top:  $\text{MeO}^-$  content in the MOF material during PSE (dashed brown) as determined by NMR and TGA. The total number of ligands per cluster is shown in dashed green. The evolution of BET areas measured for samples collected at selected instances is shown in gray. Bottom: Representation of an energy-optimized UiO-66 structure with both dangling linkers and  $\text{MeO}^-/\text{MeOH}$  pairs.

second  $\text{MeOH}/\text{MeO}^-$  pair, the calculated surface area rises to  $1057 \text{ m}^2 \text{ g}^{-1}$ . The correspondence between the calculated and measured surface areas, especially in combination with observed overcoordination, supports the hypothesis of the initial creation of dangling linkers, followed by the slow movement of defect sites.

In the defect-rich UiO-66 sample, no dangling linkers are observed (Figure 3, bottom, green dashed line). Together with the observation that the  $\text{MeO}^-$  content after PSE is lower than the initial  $\text{HCOO}^-$  content, this observation has two implications: (i) part of the  $\text{HCOO}^-$  initially present at defect sites is replaced by BDC or  $\text{NH}_2\text{-BDC}$  structural linkers that are connected on both ends. It is our hypothesis that the extent of this “healing”, that is, eliminating two adjacent monocarboxylate-capped sites in favor of a structural linker, corresponds to a small fraction of missing-linker defects that exists next to a larger number of missing-cluster sites;<sup>17</sup> (ii) the sites adjacent to the predominant missing-cluster defects are capped almost exclusively with  $\text{MeO}^-/\text{MeOH}$ . Likely, the high number of these “edge” sites lining a defect causes the overcoordination during PSE to be much less pronounced than in the defect-free material where two  $\text{MeOH}/\text{MeO}^-$  pairs eventually seem to find a position directly opposing each other. Also, in contrast to defect-free UiO-66, HPLC analysis of the PSE solution shows a considerably higher uptake of  $\text{NH}_2\text{-BDC}$  than BDC release (Figure 3, top). However, this excess of  $\text{NH}_2\text{-BDC}$  is not found when analyzing the solids after washing with EtOH. Given that the defective sample has a larger accessible pore volume because of missing-cluster defects,<sup>21</sup> this difference is likely due to weak  $\text{NH}_2\text{-BDC}$  adsorption in solution. This hypothesis is supported by the drop in the adsorbed amount together with the replacement of  $\text{HCOO}^-$  by the bulkier  $\text{MeOH}/\text{MeO}^-$  pairs.

**Mechanism of PSE in MeOH.** The exchange of structural linker, that is, the release of BDC in favor of  $\text{NH}_2\text{-BDC}$



**Figure 7.** Proposed PSE mechanism in nondefective and defective UiO-66. MeOH facilitates ligand exchange through the creation and stabilization of defects. Enthalpy differences are given in  $\text{kJ mol}^{-1}$  at 313 K (PSE temperature).

incorporation, occurs a lot faster in MeOH compared with some other reported PSE conditions. A recent time-resolved study of PSE in DMF found that after 8 h at 323 K the defect-free UiO-66 starting material had lost less than 1% of the BDC linkers.<sup>17</sup> In MeOH, about 40% of the BDC originally present in the framework has been released and replaced by  $\text{NH}_2\text{-BDC}$  (or  $\text{MeOH}/\text{MeO}^-$  pairs) at the same point in time, even though both the exchange temperature and the concentration of incoming linker were lower than in the aforementioned study. Likely, the PSE process is greatly facilitated by the dangling linker states that are generated and stabilized in MeOH but not in solvents such as DMF. Only two  $\text{Zr}-\text{O}$  bonds need to be broken to remove a dangling linker from the framework, whereas exchanging a fully bound BDC would require breaking a total of four  $\text{Zr}-\text{O}$  bonds, from two adjacent inorganic clusters. Indeed, under various PSE conditions, it has been observed that when monocarboxylates are present in the UiO-66 starting material, these are exchanged faster than the structural linker.<sup>15,17,41–43</sup> This preference is in line with static calculations, which show an enthalpy penalty of about  $25 \text{ kJ mol}^{-1}$  per cluster for  $\text{HCOO}^-$  with respect to BDC. Through the formation and stabilization of dangling states, MeOH enables the exchange of structural linkers with similar ease as for monocarboxylate ligands, an effect likely accredited to the solvent's acidic nature ( $\text{pK}_a = 15.5$ ) small kinetic diameter and hydrogen-bonding capacity.

On the basis of the above observations, a mechanism can be proposed for the ligand exchange of UiO-66 in MeOH, and the relative enthalpies can be calculated for each involved state (Figure 7). The process is initiated by fast chemisorption of MeOH as  $\text{MeO}^-$ , while a linker carboxylate group is protonated and detaches from the inorganic cluster. When  $\text{MeOH}/\text{MeO}^-$  pairs are formed at the defect site, this metastable dangling linker state is enthalpically favorable by  $59.4 \text{ kJ mol}^{-1}$  compared with the initial state. Hydrogen-bonding likely plays a key role in stabilizing the protonated linker, via the carboxylate oxygen atoms of other linkers and the cluster  $\mu_3\text{-OH}$  hydrogen.<sup>44</sup> The dangling linker partially blocks the pore, as experimentally confirmed through

initially steeply decreasing BET surface area. Exchange of the monocoordinated BDC linker with  $\text{NH}_2\text{-BDC}$  follows, with partial coordination of the incoming linker. This process is considerably faster than exchange in DMF, in which the linkers remain fully coordinated.<sup>17</sup> Next, MeOH is desorbed through reprotonation of the  $\text{MeO}^-$  ligand and the coordination of  $\text{NH}_2\text{-BDC}$  on both ends.

In defective UiO-66, the replacement of  $\text{HCOO}^-$  with  $\text{MeO}^-/\text{MeO}^+$  pairs results in an enthalpy decrease of  $59.6 \text{ kJ mol}^{-1}$  (Table S3). When  $\text{NH}_2\text{-H}_2\text{BDC}$  subsequently adsorbs at one of these defect sites, the cluster coordination becomes identical to the defect-free case. In both cases, dangling linkers in combination with  $\text{MeOH}/\text{MeO}^-$  sites continue to be created and the exchange process goes on until an equilibrium composition is achieved. The proposed reprotonation and partial decoordination of linkers throughout PSE is in complete agreement with a recent molecular dynamics study by some of the authors.<sup>44</sup> Unlike DMF, MeOH likely facilitates the required proton transfer and hydrogen bond stabilization, in addition to its role in capping the resulting defects in an energetically favorable way. These insights into the mechanism rely on solvent-free periodic static calculations; it is likely that further stabilization is possible through additional hydrogen bonds with the solvent.

Free-energy calculations (Tables S4 and S5) show that the PSE process is enthalpically driven. The net replacement of one BDC linker by  $\text{NH}_2\text{-BDC}$  lowers the enthalpy of about  $6.2 \text{ kJ mol}^{-1}$ . This slight preference is also observed in the equilibrium composition after both direct synthesis and PSE: more  $\text{NH}_2\text{-BDC}$  than BDC ends up in the framework when stoichiometric quantities are present. Furthermore, the introduction of dangling or missing-linker defects is more favorable at lower temperatures (Tables S4 and S5). In other words, the UiO-66 framework has a stronger preference for  $\text{MeOH}/\text{MeO}^-$ -capped defects at the mild PSE temperature. PSE tests starting with different  $\text{NH}_2\text{-BDC}$  concentrations show that the higher the framework  $\text{NH}_2\text{-BDC}$  content, the more the  $\text{MeOH}/\text{MeO}^-$  pairs are tolerated at equilibrium (Supporting Information S23). Calculations further show no

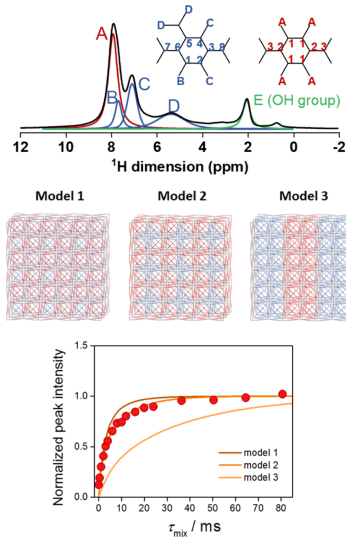
## Chemistry of Materials

## Article

substantial difference in enthalpy for unit cells with different amounts of defects, in agreement with the experimental observations.

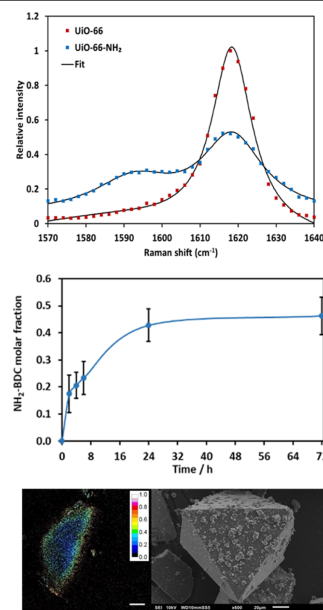
**Linker Distribution after PSE.** The linker distribution after PSE has been the topic of some debate in the literature, with some authors finding a homogeneous distribution while others observe a higher concentration of the incoming linker near the crystal surface.<sup>14,15,17,45</sup> In the small UiO-66 particles studied here (<1  $\mu\text{m}$ ), we expect defect generation by MeOH, and therefore exchange, to occur homogeneously throughout the particle. To test this hypothesis, the linker distribution after 72 h of PSE was determined through solid-state NMR (SSNMR), by monitoring spin diffusion between chemically distinct  $^1\text{H}$  nuclei. Because spin diffusion is governed by dipolar coupling, its rate is highly sensitive to the distance between the nuclei.<sup>46,47</sup> After distinct NMR signals for the  $\text{NH}_2$ -BDC and BDC protons were assigned (Figure 8, top),  $^1\text{H}$  spin diffusion experiments were performed for different mixing times.

In larger particles, the finite diffusion rate of the incoming linker could, depending on the exchange rate, result in the formation of enrichment near the crystal exterior.<sup>14,45</sup> We used stimulated Raman scattering (SRS) microscopy to visualize the



**Figure 8.** SSNMR analysis of the linker distribution after PSE. Top: SSNMR analysis of UiO-66 after PSE.  $^1\text{H}$  MAS NMR spectrum with assignment of individual signals to the inequivalent hydrogen nuclei A–E. Middle: Mixed-linker models ( $6 \times 6 \times 3$  unit cells) with different degrees of linker mixing for a BDC/ $\text{NH}_2$ -BDC ratio of 45:55. BDC and  $\text{NH}_2$ -BDC positions are indicated in red and blue, respectively. Bottom: SSNMR spin diffusion modeling. The calculated  $^1\text{H}$  spin diffusion curves for the polarization transfer from protons D to protons A are shown for each model with overlay of the experimental data.

linker distribution in large UiO-66 crystals ( $>50 \mu\text{m}$ ) after PSE in MeOH. SRS microscopy offers three-dimensional vibrational imaging with a spatial resolution of  $\sim 300 \text{ nm}$ .<sup>48,49</sup> Large enough UiO-66 crystals were prepared by using formic acid as a modulator (DE UiO-66). The parent UiO-66 material shows a characteristic Raman signal at  $1618 \text{ cm}^{-1}$ . The exchange of  $\text{NH}_2$ -BDC into UiO-66 can be observed through the appearance of a band at  $1592 \text{ cm}^{-1}$ , characteristic for UiO-66- $\text{NH}_2$  (Figure 9, top).<sup>50</sup> For the mixed-linker materials



**Figure 9.** Monitoring of PSE through SRS microscopy. Top: SRS spectra of UiO-66 (red) and UiO-66- $\text{NH}_2$  (blue). Middle: evolution of the  $\text{NH}_2$ -BDC content for smaller UiO-66 crystals ( $1\text{--}2 \mu\text{m}$  diameter) as measured by the signal intensity ratio of the signals at  $1592$  and  $1618 \text{ cm}^{-1}$  ( $I_{1592}/I_{1618}$ ). The error bars are based on measurements of five crystals at each exchange time. Bottom: Confocal SRS cross section of a large UiO-66 crystal ( $100 \mu\text{m}$  diameter) measured  $30 \mu\text{m}$  within the particle and a SEM micrograph of a crystal from the same batch. The intensity scale in confocal image corresponds to the ratio of the SRS signals at  $1592$  and  $1618 \text{ cm}^{-1}$ . Exchange time: 120 h. Scale bar: 10  $\mu\text{m}$ .

resulting from PSE, the extent of  $\text{NH}_2$ -BDC incorporation can be quantified by deconvolution of the spectra and taking the ratio of the signal intensities at  $1592$  and  $1618 \text{ cm}^{-1}$  ( $I_{1592}/I_{1618}$ ). To validate this approach, the PSE process for the defect-rich UiO-66 crystals studied above (Figure 3) was monitored through SRS microscopy by measuring the average signal ratio at each time instance for a number of crystals.

The resulting profile closely resembles the evolution determined by the bulk analysis of the liquid and solid phase

## Chemistry of Materials

Article

(Figure 9, middle). Next, the linker distribution in the large UiO-66 crystals was visualized by determining  $I_{1592}/I_{1618}$  in a spatially resolved fashion. One of the strengths of SRS is that such imaging is performed in a confocal way and can therefore visualize a cross section through the UiO-66 crystal without potentially interfering contributions of the top and bottom planes. After 120 h of PSE, a cross-sectional image taken at 30  $\mu\text{m}$  within the crystal clearly shows the presence of a gradient, with a gradually decreasing concentration of  $\text{NH}_2-\text{BDC}$  toward the crystal interior. These results are in agreement with the observations by Matzger and co-workers for large UiO-66 crystals.<sup>14</sup> We hypothesize that, in addition to diffusion effects, the dangling linkers intrinsic to PSE in MeOH further hamper the  $\text{NH}_2-\text{BDC}$  transport, either through a lowered accessible pore volume or via hydrogen bonding interactions. Therefore, the  $\text{NH}_2-\text{BDC}$  gradient that can persist even long after equilibrium would be reached in smaller crystals ( $<1-2 \mu\text{m}$ ). Whether the linker distribution after PSE is homogeneous or not likely not only depends on crystal size but might be solvent-dependent as well.

## CONCLUSION

In conclusion, we showed that time-resolved monitoring together with molecular modeling grants insight into PSE in UiO-66. The analysis of both solid and liquid phases grants for the first time unparalleled insight into the intricate nature of the interactions during PSE of UiO-66 in MeOH. The active role of MeOH was revealed, in the first place in the creation and stabilization of dangling linker defects. Similarly to monocarboxylates, dangling linkers undergo fast exchange. The presence of missing-linker or missing-cluster defects at the start of the PSE process was shown to have no considerable impact on the equilibrium composition. After the exchange process, both linkers are distributed homogeneously in the framework for small UiO-66 crystallites. The current study represent a significant step forward in understanding the behavior of the UiO-66 family and provides a reference for both rational design and applications of these and related materials.

## ASSOCIATED CONTENT

### Supporting Information

The Supporting Information is available free of charge on the ACS Publications website at DOI: [10.1021/acs.chemmater.8b04734](https://doi.org/10.1021/acs.chemmater.8b04734).

Full analytic details including XRD patterns, SEM images, TGA curves, sorption isotherms, NMR spectra, and all modeling results (PDF)

## AUTHOR INFORMATION

### Corresponding Author

\*E-mail: [rob.ameloot@biw.kuleuven.be](mailto:rob.ameloot@biw.kuleuven.be).

### ORCID

Joao Marreiros: [0000-0002-4898-2096](https://orcid.org/0000-0002-4898-2096)

Chiara Caratelli: [0000-0001-9070-6813](https://orcid.org/0000-0001-9070-6813)

Andraž Krajnc: [0000-0003-2249-602X](https://orcid.org/0000-0003-2249-602X)

Guillaume Fleury: [0000-0001-9480-3952](https://orcid.org/0000-0001-9480-3952)

Bart Bueken: [0000-0002-4610-7204](https://orcid.org/0000-0002-4610-7204)

Gregor Mali: [0000-0002-9012-2495](https://orcid.org/0000-0002-9012-2495)

Maarten B. J. Roeffaers: [0000-0001-6582-6514](https://orcid.org/0000-0001-6582-6514)

Veronique Van Speybroeck: [0000-0003-2206-178X](https://orcid.org/0000-0003-2206-178X)

Rob Ameloot: [0000-0003-3178-5480](https://orcid.org/0000-0003-3178-5480)

### Notes

The authors declare no competing financial interest.

## ACKNOWLEDGMENTS

This project has received funding from the European Union's Horizon 2020 research and innovation program under the Marie Skłodowska-Curie (grant agreement no. 641887, acronym: DEFNET). R.A. further acknowledges the funding from the European Research Council (grant agreement no. 716472, acronym: VAPORE), as well as the Research Foundation Flanders (FWO) for funding in the projects G083016N, 12R1217N and 1501618N. KU Leuven is acknowledged for funding in the project C32/16/019. V.-R.V.S. and J.H. further acknowledge the financial support from the European Research Council grant agreement Agency (research core funding no. 647755, acronym: DYNPOR) and the Research Board of Ghent University (BOF). The computational resources and services used in this work were provided by the VSC (Flemish Supercomputer Center) and funded by the FWO. A.K. and G.M. acknowledge the financial support from the Slovenian Research Agency (research core funding no. P1-0021 and project no. N1-0079). M.R. acknowledges the financial support from the Research Foundation-Flanders (FWO, G.0962.13, AKUL/15/15—GOH0816N), KU Leuven Research Fund (C14/15/053, OT/12/059), the Hercules foundation (HER/11/14), and funding from the European Research Council under the European Union's Seventh Framework Programme (FP/2007-2013)/ERC Grant agreement no. [307523], ERC-Stg LIGHT to M.B.J.R.

## REFERENCES

- (1) Cavka, J. H.; Jakobsen, S.; Olsbye, U.; Guillou, N.; Lamberti, C.; Bordiga, S.; Lillerud, K. P. A New Zirconium Inorganic Building Brick Forming Metal Organic Frameworks with Exceptional Stability. *J. Am. Chem. Soc.* **2008**, *130*, 13850–13851.
- (2) Wang, C.; Liu, X.; Keser Demir, N.; Chen, J. P.; Li, K. Applications of water stable metal-organic frameworks. *Chem. Soc. Rev.* **2016**, *45*, 5107–5134.
- (3) Van de Voorde, B.; Stassen, I.; Bueken, B.; Vermoortele, F.; De Vos, D.; Ameloot, R.; Tan, J.-C.; Bennett, T. D. Improving the mechanical stability of zirconium-based metal-organic frameworks by incorporation of acidic modulators. *J. Mater. Chem. A* **2015**, *3*, 1737–1742.
- (4) Vermoortele, F.; Bueken, B.; Le Bars, G.; Van de Voorde, B.; Vandichel, M.; Houthoofd, K.; Vimont, A.; Daturi, M.; Waroquier, M.; Van Speybroeck, V.; et al. Synthesis Modulation as a Tool To Increase the Catalytic Activity of Metal-Organic Frameworks: The Unique Case of UiO-66(Zr). *J. Am. Chem. Soc.* **2013**, *135*, 11465–11468.
- (5) Rogge, S. M. J.; Bavkina, A.; Hajek, J.; Garcia, H.; Olivos-Suarez, A. I.; Sepulveda-Escobar, A.; Vimont, A.; Clet, G.; Bazin, P.; Kapteijn, F.; et al. Metal-organic and covalent organic frameworks as single-site catalysts. *Chem. Soc. Rev.* **2017**, *46*, 3134–3184.
- (6) Wu, H.; Chua, Y. S.; Krungleviciute, V.; Tyagi, M.; Chen, P.; Yildirim, T.; Zhou, W. Unusual and Highly Tunable Missing-Linker Defects in Zirconium Metal-Organic Framework UiO-66 and Their Important Effects on Gas Adsorption. *J. Am. Chem. Soc.* **2013**, *135*, 10525–10532.
- (7) Ren, J.; Langmi, H. W.; North, B. C.; Mathe, M.; Bessarabov, D. Modulated Synthesis of Zirconium-Metal Organic Framework (Zr-MOF) for Hydrogen Storage Applications. *Int. J. Hydrg. Energy* **2014**, *39*, 890–895.
- (8) Stassen, I.; Bueken, B.; Reinsch, H.; Oudenoven, J. F. M.; Wouters, D.; Hajek, J.; Van Speybroeck, V.; Stock, N.; Vereecken, P.

## Chemistry of Materials

## Article

- M.; Van Schaijk, R.; et al. Towards Metal–Organic Framework Based Field Effect Chemical Sensors: UiO-66-NH<sub>2</sub> for Nerve Agent Detection. *Chem. Sci.* **2016**, *7*, S827–S832.
- (9) Cunha, D.; Ben Yahia, M.; Hall, S.; Miller, S. R.; Chevreau, H.; Elkaim, E.; Maurin, G.; Horcajada, P.; Serre, C. Rationale of Drug Encapsulation and Release from Biocompatible Porous Metal–Organic Frameworks. *Chem. Mater.* **2013**, *25*, 2767–2776.
- (10) Deria, P.; Mondloch, J. E.; Tylianakis, E.; Ghosh, P.; Bury, W.; Snurr, R. Q.; Hupp, J. T.; Farha, O. K. Perfluoroalkane Functionalization of NU-1000 via Solvent-Assisted Ligand Incorporation: Synthesis and CO<sub>2</sub> Adsorption Studies. *J. Am. Chem. Soc.* **2013**, *135*, 16801–16804.
- (11) Deria, P.; Chung, Y. G.; Snurr, R. Q.; Hupp, J. T.; Farha, O. K. Water Stabilization of Zr<sub>6</sub>-Based Metal–Organic Frameworks via Solvent-Assisted Ligand Incorporation. *Chem. Sci.* **2015**, *6*, S172–S176.
- (12) Kim, M.; Cahill, J. F.; Su, Y.; Prather, K. A.; Cohen, S. M. Postsynthetic Ligand Exchange as a Route to Functionalization of ‘Inert’ Metal–Organic Frameworks. *Chem. Sci.* **2012**, *3*, 126–130.
- (13) Kim, M.; Cahill, J. F.; Su, Y.; Prather, K. A.; Cohen, S. M. Postsynthetic ligand exchange as a route to functionalization of “inert” metal-organic frameworks. *Chem. Sci.* **2012**, *3*, 126–130.
- (14) Boissonnault, J. A.; Wong-Foy, A. G.; Matzger, A. J. Core-Shell Structures Arise Naturally During Ligand Exchange in Metal–Organic Frameworks. *J. Am. Chem. Soc.* **2017**, *139*, 14841–14844.
- (15) Fluch, U.; Paneta, V.; Primetzhofer, D.; Ott, S. Uniform distribution of post-synthetic linker exchange in metal-organic frameworks revealed by Rutherford backscattering spectrometry. *Chem. Commun.* **2017**, *53*, 6516–6519.
- (16) Shearer, G. C.; Vitillo, J. G.; Bordiga, S.; Svelle, S.; Olsbye, U.; Lillerud, K. P. Functionalizing the Defects: Postsynthetic Ligand Exchange in the Metal Organic Framework UiO-66. *Chem. Mater.* **2016**, *28*, 7190–7193.
- (17) Taddei, M.; Wakeham, R. J.; Koutsianos, A.; Andreoli, E.; Barron, A. R. Post-Synthetic Ligand Exchange in Zirconium-Based Metal–Organic Frameworks: Beware of the Defects! *Angew. Chem., Int. Ed.* **2018**, *57*, 11706–11710.
- (18) Kim, M.; Cahill, J. F.; Fei, H.; Prather, K. A.; Cohen, S. M. Postsynthetic Ligand and Cation Exchange in Robust Metal–Organic Frameworks. *J. Am. Chem. Soc.* **2012**, *134*, 18082–18088.
- (19) Shearer, G. C.; Chavan, S.; Ethiraj, J.; Vitillo, J. G.; Svelle, S.; Olsbye, U.; Lamberti, C.; Bordiga, S.; Lillerud, K. P. Tuned to Perfection: Ironing Out the Defects in Metal–Organic Framework UiO-66. *Chem. Mater.* **2014**, *26*, 4068–4071.
- (20) Liédana, N.; Lozano, P.; Galve, A.; Téllez, C.; Coronas, J. The template role of caffeine in its one-step encapsulation in MOF NH2-MIL-88B(Fe). *J. Mater. Chem. B* **2014**, *2*, 11442–11451.
- (21) Shearer, G. C.; Chavan, S.; Bordiga, S.; Svelle, S.; Olsbye, U.; Lillerud, K. P. Defect Engineering: Tuning the Porosity and Composition of the Metal-Organic Framework UiO-66 via Modulated Synthesis. *Chem. Mater.* **2016**, *28*, 3749–3761.
- (22) Rogge, S. M. J.; Wieme, J.; Vanduyfhuys, L.; Vandenbrande, S.; Maurin, G.; Verstraeten, T.; Waroquier, M.; Van Speybroeck, V. Thermodynamic Insight in the High-Pressure Behavior of UiO-66: Effect of Linker Defects and Linker Expansion. *Chem. Mater.* **2016**, *28*, 5721–5732.
- (23) De Vos, A.; Hendrickx, K.; Van Der Voort, P.; Van Speybroeck, V.; Lejaeghere, K. Missing Linkers: An Alternative Pathway to UiO-66 Electronic Structure Engineering. *Chem. Mater.* **2017**, *29*, 3006–3019.
- (24) Vandichel, M.; Hájek, J.; Ghysels, A.; De Vos, A.; Waroquier, M.; Van Speybroeck, V. Water Coordination and Dehydration Processes in Defective UiO-66 Type Metal–Organic Frameworks. *CrystEngComm* **2016**, *18*, 7056–7069.
- (25) Caratelli, C.; Hájek, J.; Cirujano, F. G.; Waroquier, M.; Llabrés i Xamena, F. X.; Van Speybroeck, V. Nature of Active Sites on UiO-66 and Beneficial Influence of Water in the Catalysis of Fischer Esterification. *J. Catal.* **2017**, *352*, 401–414.
- (26) Kresse, G.; Joubert, D. From Ultrasoft Pseudopotentials to the Projector Augmented-Wave Method. *Phys. Rev. B: Condens. Matter Mater. Phys.* **1999**, *59*, 1758–1775.
- (27) Kresse, G.; Furthmüller, J. Efficient iterative schemes for ab initio total-energy calculations using a plane-wave basis set. *Phys. Rev. B* **1996**, *54*, 11169–11186.
- (28) Kresse, G.; Furthmüller, J. Efficiency of Ab-Initio Total Energy Calculations for Metals and Semiconductors Using a Plane-Wave Basis Set. *Comput. Mater. Sci.* **1996**, *6*, 15–50.
- (29) Kresse, G.; Hafner, J. Ab initiomolecular-dynamics simulation of the liquid-metal-amorphous-semiconductor transition in germanium. *Phys. Rev. B* **1994**, *49*, 14251–14269.
- (30) Kresse, G.; Hafner, J. Ab initiomolecular dynamics for liquid metals. *Phys. Rev. B* **1993**, *47*, 558.
- (31) Blöchl, P. E. Projector Augmented-Wave Method. *Phys. Rev. B* **1994**, *50*, 17953–17979.
- (32) Perdew, J. P.; Burke, K.; Ernzerhof, M. Generalized Gradient Approximation Made Simple. *Phys. Rev. Lett.* **1996**, *77*, 3865–3868.
- (33) Grimme, S. Accurate Description of van Der Waals Complexes by Density Functional Theory Including Empirical Corrections. *J. Comput. Chem.* **2004**, *25*, 1463–1473.
- (34) Grimme, S.; Antony, J.; Ehrlich, S.; Krieg, H. A Consistent and Accurate Ab Initio Parametrization of Density Functional Dispersion Correction (DFT-D) for the 94 Elements H–Pu. *J. Chem. Phys.* **2010**, *132*, 154104.
- (35) Ghysels, A.; Verstraeten, T.; Hemelsoet, K.; Waroquier, M.; Van Speybroeck, V. TAMKIN: A Versatile Package for Vibrational Analysis and Chemical Kinetics. *J. Chem. Inf. Model.* **2010**, *50*, 1736–1750.
- (36) Ghysels, A.; Van Neck, D.; Waroquier, M. Cartesian Formulation of the Mobile Block Hessian Approach to Vibrational Analysis in Partially Optimized Systems. *J. Chem. Phys.* **2007**, *127*, 164108.
- (37) Yang, D.; Bernales, V.; Islamoglu, T.; Farha, O. K.; Hupp, J. T.; Cramer, C. J.; Gagliardi, L.; Gates, B. C. Tuning the Surface Chemistry of Metal Organic Framework Nodes: Proton Topology of the Metal-Oxide-Like Zr<sub>6</sub> Nodes of UiO-66 and NU-1000. *J. Am. Chem. Soc.* **2016**, *138*, 15189–15196.
- (38) Trickett, C. A.; Gagnon, K. J.; Lee, S.; Gándara, F.; Bürgi, H.-B.; Yaghi, O. M. Definitive Molecular Level Characterization of Defects in UiO-66 Crystals. *Angew. Chem.* **2015**, *127*, 11314–11319.
- (39) Caratelli, C.; Hájek, J.; Rogge, S. M. J.; Vandenbrande, S.; Meijer, E. J.; Waroquier, M.; Van Speybroeck, V. Influence of a Confined Methanol Solvent on the Reactivity of Active Sites in UiO-66. *ChemPhysChem* **2018**, *19*, 420–429.
- (40) Willems, T. F.; Rycroft, C. H.; Kazi, M.; Meza, J. C.; Haranczyk, M. Algorithms and Tools for High-Throughput Geometry-Based Analysis of Crystalline Porous Materials. *Microporous Mesoporous Mater.* **2012**, *149*, 134–141.
- (41) Shearer, G. C.; Chavan, S.; Bordiga, S.; Svelle, S.; Olsbye, U.; Lillerud, K. P. Defect Engineering: Tuning the Porosity and Composition of the Metal–Organic Framework UiO-66 via Modulated Synthesis. *Chem. Mater.* **2016**, *28*, 3749–3761.
- (42) Gutov, O. V.; Hevia, M. G.; Escudero-Adán, E. C.; Shafir, A. Metal–Organic Framework (MOF) Defects under Control: Insights into the Missing Linker Sites and Their Implication in the Reactivity of Zirconium-Based Frameworks. *Inorg. Chem.* **2015**, *54*, 8396–8400.
- (43) Gutov, O. V.; Molina, S.; Escudero-Adán, E. C.; Shafir, A. Modulation by Amino Acids: Toward Superior Control in the Synthesis of Zirconium Metal–Organic Frameworks. *Chem.—Eur. J.* **2016**, *22*, 13582–13587.
- (44) Hájek, J.; Caratelli, C.; Demuyck, R.; De Wispelaere, K.; Vanduyfhuys, L.; Waroquier, M.; Van Speybroeck, V. On the intrinsic dynamic nature of the rigid UiO-66 metal-organic framework. *Chem. Sci.* **2018**, *9*, 2723–2732.
- (45) Jayachandrababu, K. C.; Sholl, D. S.; Nair, S. Structural and Mechanistic Differences in Mixed-Linker Zeolitic Imidazolate Framework Synthesis by Solvent Assisted Linker Exchange and *de Novo* Routes. *J. Am. Chem. Soc.* **2017**, *139*, 5906–5915.

## Chemistry of Materials

## Article

- (46) Krajnc, A.; Kos, T.; Zubukovec Logar, N.; Mali, G. A Simple NMR-Based Method for Studying the Spatial Distribution of Linkers within Mixed-Linker Metal-Organic Frameworks. *Angew. Chem., Int. Ed.* **2015**, *54*, 10535–10538.
- (47) Krajnc, A.; Bueken, B.; De Vos, D.; Mali, G. Improved Resolution and Simplification of the Spin-Diffusion-Based NMR Method for the Structural Analysis of Mixed-Linker MOFs. *J. Magn. Reson.* **2017**, *279*, 22–28.
- (48) Freudiger, C. W.; Min, W.; Saar, B. G.; Lu, S.; Holtom, G. R.; He, C.; Tsai, J. C.; Kang, J. X.; Xie, X. S. Label-Free Biomedical Imaging with High Sensitivity by Stimulated Raman Scattering Microscopy. *Science* **2008**, *322*, 1857.
- (49) Liu, K.-L.; Kubarev, A. V.; Van Loon, J.; Uji-i, H.; De Vos, D. E.; Hofkens, J.; Roeffaers, M. B. J. Rationalizing Inter- and Intracrystalline Heterogeneities in Dealuminated Acid Mordenite Zeolites by Stimulated Raman Scattering Microscopy Correlated with Super-Resolution Fluorescence Microscopy. *ACS Nano* **2014**, *8*, 12650–12659.
- (50) Otal, E. H.; Kim, M. L.; Calvo, M. E.; Karvonen, L.; Fabregas, I. O.; Sierra, C. A.; Hinestroza, J. P. A panchromatic modification of the light absorption spectra of metal-organic frameworks. *Chem. Commun.* **2016**, *52*, 6665–6668.



## Supporting information

### The active role of methanol in post-synthetic linker exchange in the metal-organic framework UiO-66

Joao Marreiros<sup>†</sup>, Chiara Caratelli<sup>‡</sup>, Julianna Hajek<sup>‡</sup>, Andraž Krajnc<sup>§</sup>, Guillaume Fleury<sup>†</sup>, Bart Bueken<sup>†</sup>, Dirk De Vos<sup>†</sup>, Gregor Mali<sup>§</sup>, Maarten Roeffaers<sup>†</sup>, Veronique Van Speybroeck<sup>‡</sup>, Rob Ameloot<sup>†\*</sup>

<sup>†</sup>Centre for Surface Chemistry and Catalysis, KU Leuven, Celestijnenlaan 200F p.o. box 2461, 3001 Leuven, Belgium

<sup>‡</sup>Center for Molecular Modeling, Universiteit Gent, Technologiepark 903, B-9052 Zwijnaarde, Belgium

<sup>§</sup>Department of Inorganic Chemistry and Technology, National Institute of Chemistry, Hajdrihova 19, 1001 Ljubljana, Slovenia

## Theoretical calculations

### a. PSE & MeOH/MeO- framework coordination

Framework coordination:

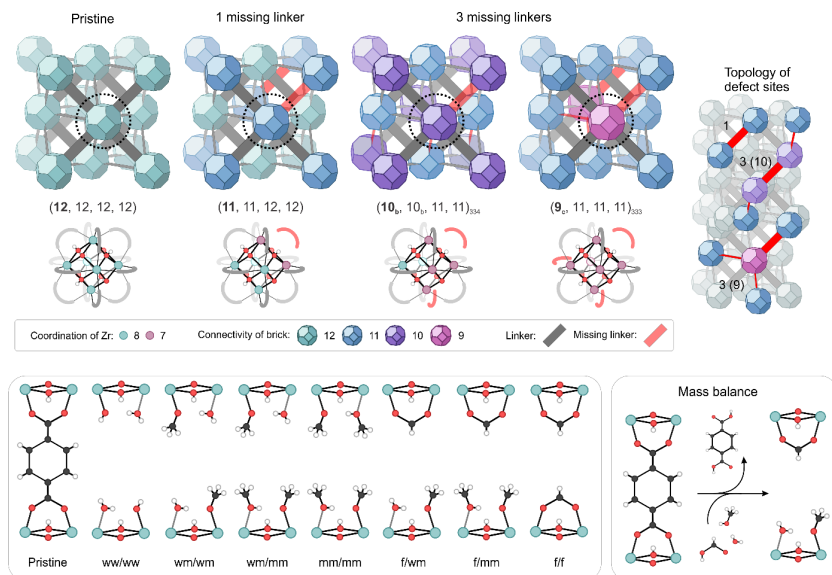


Figure S1 **Top:** the four 4-brick unit cells taken into consideration in the computational modeling, with the missing linkers indicated in red and the topology of the missing linker vacancies indicated on the right. For clarity, the bricks and linkers at the border of the unit cell are represented entirely. Below the bricks, the four types of bricks present in the unit cells. **Bottom:** possible adsorbates configurations upon linker removal which are reported in table. For each structure, thermodynamic data are obtained considering the right mass balance with gas phase reactants. On the right an example reaction.

In Table S3, the Free energy, enthalpic and entropic contribution for the defect coordinating species in the various unit cells are reported. For a comparison between unit cells with different amount of defects, the variation in energy compared to the pristine unit cell is divided by the number of missing linkers. Taking into account the symmetry of the unit cell, multiple positions of the charge-compensating species were compared. The average is done between the three defective unit cells, and in the case of multiple possible positions of the ligands within the unit cells, their energies are all averaged out to give a single contribution for that specific defective unit cell. Adsorption of methanol and hydroxide was also modeled, but the proton spontaneously detached to give the configuration with water and methoxide reported here.

Table S1 Difference in Free energy, enthalpy and entropy at 298 K, 313 K, 373 K and 473 K between the pristine structure and the defective structures with defect coordinating species reported in Figure S4. Energies are reported divided by the amount of missing linkers, at PBE-D3 level of theory. When possible, different possibilities for the adsorbates positions are reported.

Ads.	Defects	298 K			313 K			373 K			473 K		
		ΔG	ΔH	TAS									
<b>Pristine</b>													
ww /	1	115.8	4.2	111.6	121.4	4.3	117.1	143.8	5.1	138.7	180.7	7.4	173.3
ww	3 (9)	113.4	-4.5	117.9	119.3	-4.5	123.8	143.0	-4.2	147.2	182.3	-2.4	184.7
	3 (10)	112.9	-4.7	117.6	118.8	-4.7	123.5	142.5	-4.3	146.8	181.6	-2.5	184.1
	<b>Av.</b>	114.0	-1.6	115.7	119.8	-1.6	121.5	143.1	-1.2	144.3	181.5	0.8	180.7
wm /	1	95.3	-23.9	119.2	101.3	-23.6	124.9	125.1	-22.5	147.6	164.4	-19.8	184.2
wm	3 (9)	100.7	-21.4	122.1	106.8	-21.2	128.0	131.3	-20.1	151.4	171.5	-17.5	189.0
	3 (10)	101.0	-21.4	122.4	107.1	-21.2	128.4	131.6	-20.1	151.7	172.0	-17.4	189.4
	<b>Av.</b>	99.0	-22.2	121.2	105.1	-22.0	127.1	129.4	-20.9	150.2	169.3	-18.2	187.5
mm /	1	92.1	-31.3	123.4	98.3	-31.0	129.3	122.9	-29.6	152.5	163.5	-26.6	190.0
wm	3 (9)	97.9	-29.0	126.9	104.3	-28.7	133.0	129.6	-27.2	156.9	171.3	-24.3	195.6
	"	97.0	-29.9	126.9	103.4	-29.6	133.0	128.8	-28.3	157.1	170.5	-25.5	196.1
	3 (10)	96.2	-30.5	126.6	102.5	-30.2	132.7	127.9	-28.8	156.7	169.5	-26.0	195.5
	<b>Av.</b>	95.2	-30.4	125.6	101.6	-30.1	131.7	126.7	-28.7	155.4	168.0	-25.8	193.8
mm /	1	92.3	-38.2	130.5	98.9	-37.8	136.7	124.9	-36.0	160.9	167.6	-32.6	200.2
mm	3 (9)	95.9	-36.1	132.0	102.5	-35.7	138.2	128.8	-33.9	162.7	172.0	-30.5	202.5
	3 (10)	90.2	-36.1	126.4	96.6	-35.7	132.3	121.8	-33.9	155.6	163.0	-30.4	193.5
	<b>Av.</b>	92.8	-36.8	129.6	99.3	-36.4	135.7	125.2	-34.6	159.7	167.5	-31.2	198.7
f /	1	77.8	-1.1	78.9	81.7	-0.8	82.6	97.4	0.4	97.1	123.2	2.7	120.5
wm	3 (9)	88.7	3.4	85.3	92.9	3.6	89.4	110.0	4.5	105.5	138.0	6.4	131.6
	"	84.3	1.8	82.5	88.4	2.1	86.4	104.9	3.1	101.9	132.0	5.1	126.8
	"	84.5	1.3	83.2	88.7	1.5	87.1	105.3	2.6	102.7	132.5	4.8	127.8
	3 (10)	81.9	0.8	81.2	86.0	1.0	85.0	102.2	2.1	100.1	128.7	4.4	124.4
	"	85.4	1.6	83.8	89.6	1.8	87.8	106.4	2.9	103.5	133.8	5.1	128.7
	<b>Av.</b>	82.4	0.7	81.7	86.5	1.0	85.5	102.8	2.1	100.7	129.5	4.3	125.3
f /	1	65.2	-7.2	72.3	68.8	-6.8	75.6	83.1	-5.3	88.4	106.5	-2.6	109.1
mm	3 (9)	80.7	-5.3	85.9	85.0	-4.9	89.9	102.1	-3.4	105.5	130.1	-0.8	130.9
	"	84.9	-5.4	90.2	89.4	-5.1	94.5	107.4	-3.9	111.3	137.0	-1.7	138.7
	"	83.8	-4.7	88.6	88.3	-4.4	92.7	105.9	-3.0	108.9	134.8	-0.5	135.3
	3 (10)	82.1	-5.2	87.3	86.5	-4.8	91.3	103.9	-3.3	107.2	132.3	-0.7	132.9
	"	82.5	-4.4	86.9	86.8	-4.1	90.9	104.1	-2.7	106.8	132.4	-0.1	132.5
	<b>Av.</b>	76.9	-5.7	82.6	81.0	-5.4	86.4	97.4	-3.9	101.3	124.3	-1.3	125.6
f /	1	59.0	21.5	37.5	60.9	21.8	39.0	68.2	23.1	45.1	80.0	25.2	54.9
f	3 (9)	70.2	25.8	44.3	72.4	26.1	46.3	81.2	27.1	54.1	95.5	28.7	66.7
	3 (10)	67.0	24.7	42.4	69.2	24.9	44.2	77.5	26.0	51.5	91.1	27.8	63.3
	<b>Av.</b>	65.4	24.0	41.4	67.5	24.3	43.2	75.7	25.4	50.2	88.9	27.3	61.6

Energy profile for the PSE process:

Non-defective material:

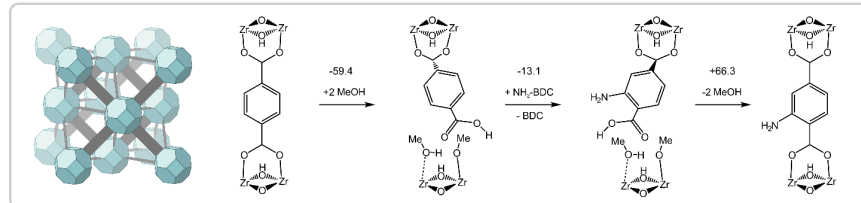


Figure S2 Schematic representation of the PSE process starting from the pristine material

Table S2 Free energy, enthalpic and entropic contributions at 298 K, 313 K, 373 K and 473 K for the structures involved in the PSE process. PBE-D3 level of theory. Values are referred to the pristine structure. In yellow, the values reported in the main text.

	298 K			313 K			373 K			473 K		
	ΔG	ΔH	TAS									
Pristine	0.0	0.0	0.0	0.0	0.0	0.0	0.0	0.0	0.0	0.0	0.0	0.0
Dangling BDC	39.7	-59.6	99.3	44.7	-59.4	104.0	64.5	-58.2	122.7	97.1	-56.1	153.2
Dangling (NH <sub>2</sub> )	28.1	-72.9	101.0	33.2	-72.5	105.7	53.3	-71.0	124.3	86.3	-68.2	154.5
Pristine (NH <sub>2</sub> )	-8.2	-6.4	-1.8	-8.3	-6.2	-2.1	-8.7	-5.7	-3.0	-9.7	-4.9	-4.8

Defective material:

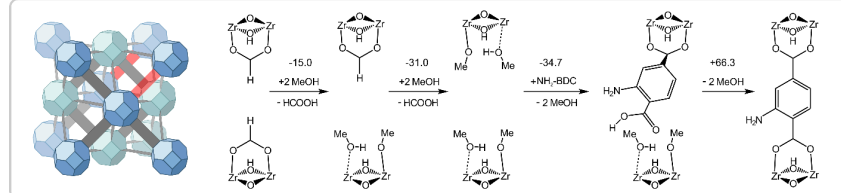


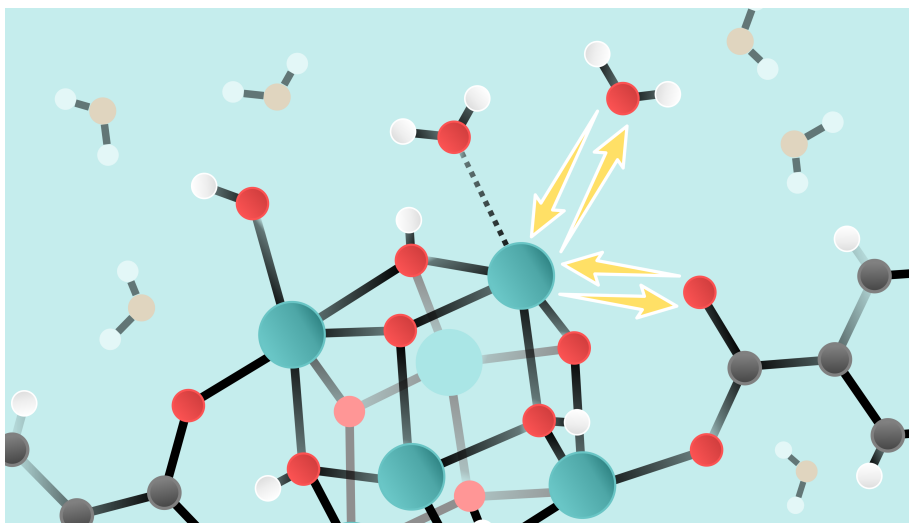
Figure S3 Schematic representation of the PSE process starting from the defective material.

Table S3 Free energy, enthalpic and entropic contributions at 298 K, 313 K, 373 K and 473 K for the structures involved in the PSE process. PBE-D3 level of theory. Values are referred to the pristine structure. In yellow, the values reported in the main text.

	298 K			313 K			373 K			473 K		
	ΔG	ΔH	TAS									
Pristine	0.0	0.0	0.0	0.0	0.0	0.0	0.0	0.0	0.0	0.0	0.0	0.0
1d – f/f	59.0	21.5	37.5	60.9	21.8	39.0	68.2	23.1	45.1	80.0	25.2	54.9
1d – f/mm	65.2	-7.2	72.3	68.8	-6.8	75.6	83.1	-5.3	88.4	106.5	-2.6	109.1
1d – mm/mm	92.3	-38.2	130.5	98.9	-37.8	136.7	124.9	-36.0	160.9	167.6	-32.6	200.2
Dangling (NH <sub>2</sub> )	28.1	-72.9	101.0	33.2	-72.5	105.7	53.3	-71.0	124.3	86.3	-68.2	154.5
Pristine (NH <sub>2</sub> )	-8.2	-6.4	-1.8	-8.3	-6.2	-2.1	-8.7	-5.7	-3.0	-9.7	-4.9	-4.8

## Paper V

### Dynamic interplay between defective UiO–66 and protic solvents in activated processes



C. Caratelli, J. Hajek, E.J. Meijer, M. Waroquier, V. Van Speybroeck, **Submitted**

C. Caratelli performed all the calculations and prepared the manuscript.



## Dynamic interplay between defective UiO-66 and protic solvents in activated processes

Chiara Caratelli<sup>1</sup>, Julianna Hajek<sup>1</sup>, Evert Jan Meijer<sup>2</sup>, Michel Waroquier<sup>1</sup>, Veronique Van Speybroeck<sup>1</sup>

<sup>1</sup>Center for Molecular Modeling, Ghent University, Technologiepark 46, 9052 Zwijnaarde, Belgium

<sup>2</sup>Van 't Hoff Institute for Molecular Sciences, University of Amsterdam, Science Park 904, 1098 XH Amsterdam, The Netherlands

### Abstract:

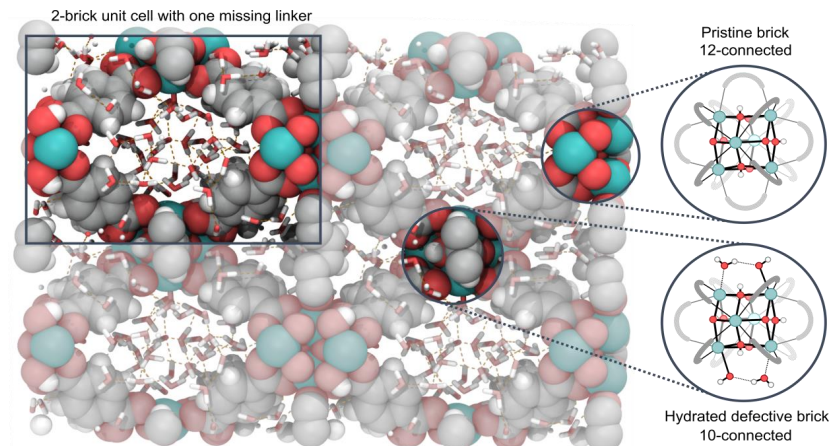
UiO-66, composed by Zr-oxide bricks and terephthalate linkers, is one of the most studied metal organic frameworks due to its exceptional stability, and the presence of structural disorder. The material has been explored to a large extent within catalysis, for which open metal sites with undercoordinated zirconium atoms need to be present. Without losing its stability, the structure is very versatile for linker exchange, which points towards an intrinsic dynamic flexibility to change the zirconium coordination number. Herein, we show by means of first principle molecular dynamics simulations at operating conditions how protic solvents like water and methanol may facilitate such changes in the metal coordination numbers. The solvent has both hydrophilic and hydrophobic interactions with the material, with repulsion from the linker and strong interactions with the inorganic brick. The dynamic interplay between solvent and inorganic brick allows the presence of temporarily undercoordinated but also overcoordinated zirconium atoms. During such processes linkers may be decoordinated, which is the onset for defect formation or for linker exchange processes. The approach followed here allows to track the intrinsic dynamics of the framework *in situ* and reveals molecular level insight into the activation of one of the most stable Metal-Organic Frameworks.

### Introduction:

Metal organic frameworks (MOFs) are hybrid nanoporous materials that lie at the intersection between inorganic and organic chemistry. Their peculiar building concept, based on metal or metal-oxo clusters and organic linkers, allows the creation of a plethora of structures with different topologies and functionalities. Moreover, these materials can further be tuned post synthetically via a process called post synthetic ligand exchange (PSLE)<sup>1-3</sup>, in which linkers are functionalized to allow finetuning of the properties<sup>4-5</sup>. This tunability, along with their high metal content and porosity, makes them very appealing for many possible industrial applications<sup>6</sup>, ranging from catalysis<sup>7</sup> to gas storage and separation<sup>8</sup>, or elimination of warfare agents<sup>9, 10</sup>. The main drawback of this family of materials is their rather poor stability under reaction conditions. However, to date, a range of new chemically and thermally stable materials have been proposed, such as the Zr MOF family<sup>11</sup>. Without any doubt, UiO-66<sup>12</sup> (displayed in **Figure 1**) composed by  $[Zr_6(\mu_3-O)_4(\mu_3-OH)_4]$  bricks and terephthalate (BDC) linkers, is currently one of the most studied MOFs due to its exceptional stability<sup>13, 14</sup>, that finds its origin in the high degree of connectivity of the framework. Each of the bricks in UiO-66 is connected to 12 ditopic BDC linkers, and within the brick, each of the 6 zirconium atoms is coordinated to four oxygen atoms

belonging to the brick, and four belonging to the linkers. In this perfect structure, zirconium atoms have an eight-fold coordination number. However, to activate these materials for catalysis, it is necessary to create open metal sites, and reduce the zirconium coordination number. In this sense, structural defects may be incorporated in the material in the form of missing linkers or clusters<sup>15-18</sup>, without compromising the structural integrity. Such defects arise spontaneously during synthesis but may also be tuned easily<sup>15, 17, 19</sup>. Apart from these on-purpose defect creation, the material may also be thermally activated by dehydration at temperatures in the range of 523-603 K<sup>20</sup>. Also in this case, the zirconium coordination number is reduced. Very recently, operando molecular dynamics simulations revealed that thermal activation of the brick leads to decoordination of linkers, which can in turn induce a domino-like process pushing other linkers away from the brick, leading to a cascade of zirconium active sites<sup>21</sup>. It was postulated that these dangling linkers might possibly be stabilized by solvent interactions.

Recently, it has been shown that a protic solvent can play a crucial role in the stabilization of charged intermediates<sup>22</sup>. However, the exact role of a confined solvent in the pores of the material is so far unknown. Experimentally it was observed that methanol actively participates during the PSLE process. Even at low temperatures UIO-66 is susceptible for ligand exchange with the aid of a solvent, without compromising the structural integrity of the material. It was postulated that intermediate metastable states are involved in the PSLE process, where linkers are dangling in the pores and remain only connected to one inorganic brick<sup>23</sup>. These rearrangements of the material point towards an active role and dynamic interplay of a confined protic solvent with the material<sup>22</sup>.



**Figure 1** Representation of the defective 2-brick unit cell of UiO-66 used in the simulations, with water in the pores of the material. The unit cell is composed by one 12-connected pristine brick and one 10-connected hydrated defective brick, which are displayed on the right.

Interestingly UiO-66 exhibits both hydrophilic and hydrophobic regions, which will most probably induce fundamentally different properties of a confined protic solvent with respect to the bulk. It is expected that protic solvents will have strong interactions with the inorganic brick and in particular with the defective sites. This was indeed confirmed by Ghosh et al.<sup>24</sup> who simulated adsorption isotherms for UiO-66 and indeed found a crucial role of the number of defects, their locations in the material and the loading of water molecules. Yang et al. showed that the water topology of these defect sites can be modified by modulation of methanol<sup>25</sup>. So far nanoscale insights into how the solvent may induce dynamic changes of the zirconium coordination number during activation processes are to a large extent missing. It poses a huge challenge to trace these intrinsic dynamics of the inorganic brick *in-situ* experimentally. First principle molecular dynamic simulations at operating conditions, thus taking into account realistic temperatures and solvent loadings have now become within reach<sup>26</sup>. Such approach is followed here and enabled us to reveal fundamentally new insights into the structural rearrangements of UiO-66.

With the aid of a protic solvent, zirconium undercoordinated and overcoordinated sites are observed. Overcoordination of the zirconium atom by a water solvent can trigger a decoordination of the adjacent linkers and may thus be the onset for linker exchange processes. Undercoordination on the other hand is crucial for catalysis, where these defective sites serve as adsorption sites for reactive species and are responsible for the catalytic activity of the material<sup>27-29</sup>. Especially Lewis acid catalysed reactions make profit of the accessibility of the metal site due to the defects generated by linker deficiencies. The catalytic activity of the material is clearly enhanced with the number and strength of the Lewis acid sites induced by the defects as demonstrated in earlier work of part of the authors with the citronellal cyclization as model reaction<sup>5, 19</sup>. The presence of protic solvents may furthermore induce a dual acid/base character of the catalyst by the appearance of Lewis and Brønsted sites. The latter sites inherently belonging to the Zr-oxide bricks can actively take part in the catalytic process, but their formation can even be enhanced by the presence of water molecules which can coordinate to the Zr-brick providing extra stabilization of various intermediates through hydrogen bonds<sup>22</sup>, as demonstrated in the study of the Fischer esterification of carboxylic acids with alcohols<sup>30</sup>.

In this contribution, *in-situ* molecular insight is obtained into the dynamic interactions between the defective UiO-66 material and a confined water and methanol loading, through usage of first principle molecular dynamics simulations at operating conditions. We show that the solvent is confined by hydrophobic interactions with the linkers but on the other hand strongly interacts with the bricks and in particular with the defective sites. On these sites, water is strongly adsorbed and can be exchanged via a stepwise mechanism where zirconium is undercoordinated, or through a concerted one, which proceeds via an overcoordination of zirconium. Moreover, the overcoordination of the zirconium atom by solvent water can trigger a decoordination of the adjacent linkers. Our simulations follow the interplay between solvent and material and unravel for the first time the key process that leads to creation of diverse active sites, linker exchange and defect formation at operating conditions.

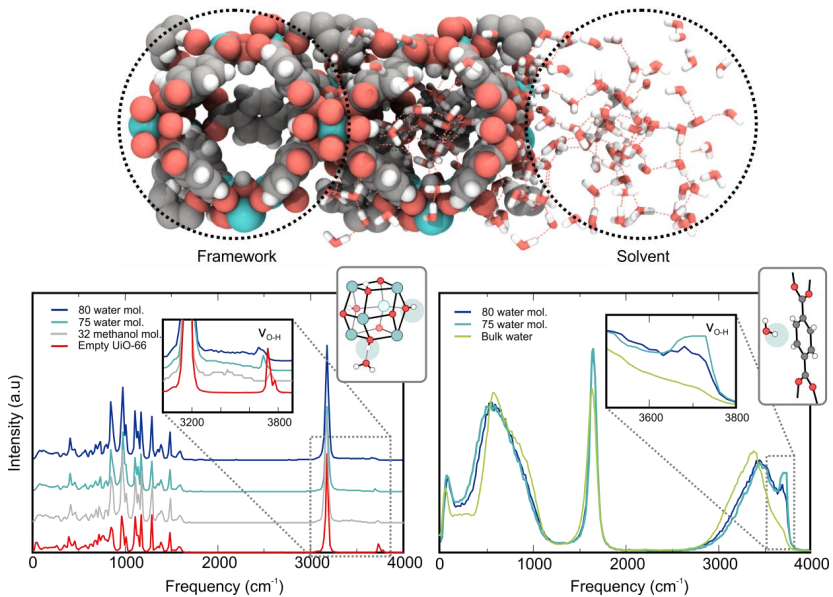
## Results and discussion

To fully unravel the interaction between protic solvents and the defective UiO-66 material, three model systems have been constructed. The defective UiO-66 material is represented by a unit cell with two zirconium bricks and one missing linker, as schematically shown in **Figure 1**, in which a full loading of methanol and two different loadings of water are considered. For further details about computations, we refer to the computational methodology. A first step in the analysis consists in clearly identifying the type of interactions the confined solvent exhibits with the material, which consists of hydrophobic and hydrophilic parts. It is furthermore essential to identify the impact of the confinement on the structure of the solvent<sup>31</sup>. The changes resulting from the interaction between the host and the confined solvent, are monitored by investigating the vibrational density of states and radial distribution functions (RDF) of the loaded framework, the empty framework and bulk water. To this end, regular molecular dynamics simulations are performed at working temperatures of 298 and 330 K.

At second instance, a series of enhanced sampling molecular dynamics simulations are performed at operating conditions, to mimic activated processes which might be assisted or even induced by interactions with the protic solvents. Such processes rely on dynamic changes in the zirconium coordination number, which may entail rearrangements of the inorganic brick, linker decoordination, or dynamic capping/decapping of defective sites with protic species. Such simulations may reveal molecular rearrangements which are hard to track from purely experimental point of view. In the defective UiO-66 material two opposing factors contribute to the solvent-material interaction. On the one hand, the interaction between organic linkers and solvent is dominated by hydrophobic effects that confine the solvent in the pores. On the other hand, the bricks offer hydrophilic Brønsted sites that interact via hydrogen bonding with the protic solvent and undercoordinated zirconium atoms that attract the solvent.

### **Interactions between protic solvents and hydrophobic and hydrophilic parts of the material**

To understand the nature of the interactions between material and solvent, the vibrational density of states was generated by calculating the power spectra of the velocity autocorrelation functions of the atoms in the unit cell. By selecting specific atoms in the unit cell, it is possible to decompose the density of states into its different contributions. As such, two different spectra were generated for each simulation, separating the contribution of the material and the solvent (spectra in **Figure 2**, bottom). Moreover, to assign the peaks in the vibrational spectra to the corresponding molecular motions, the spectrum was compared to the one obtained from total Hessian static calculations performed with the periodic VASP code<sup>32-36</sup> on the same unit cell without solvent and one hydroxyl group as charge balancing species on each defect site (**Figure S3**). By means of these static frequency calculations, it is possible to decompose the spectrum into the contributions of each single vibrational mode and this way giving insight into the changes which occur in the presence of a solvent.



**Figure 2** Top: schematic representation of the empty pore, pore with the solvent, and confined solvent without the material. Bottom: vibrational density of states obtained from the velocity autocorrelation function power spectra of selected atoms of the simulation. Bottom left: solvated material compared to the empty material. Bottom right: water in the pores compared to bulk water.

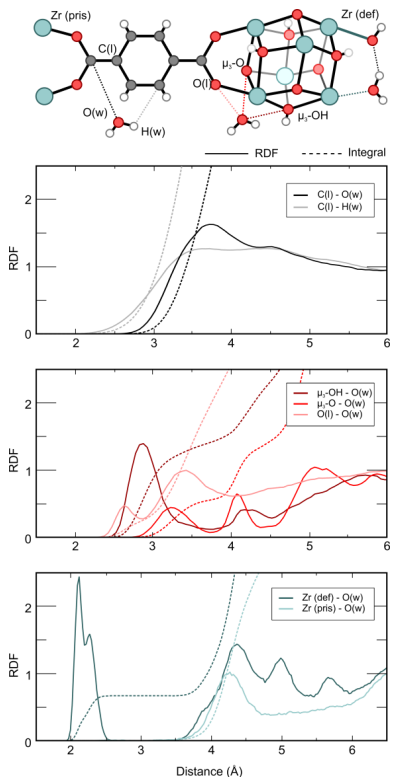
The vibrational density of states obtained from the velocity autocorrelation function power spectrum of the framework atoms is shown in **Figure 2** (bottom left). The results originate from molecular dynamics simulations performed with the CP2K code<sup>37</sup> at the PBE-D3 level of theory on the framework with and without water and/or methanol. It is immediately clear that a distinction can be made between the frequency range below 1700 cm<sup>-1</sup> and the range above 3000 cm<sup>-1</sup>. The low frequency spectrum is dominated by modes that involve deformations of the whole structure and motion of the linkers. This fingerprint region of the spectrum is characterized by vibrational modes that involve multiple parts of the system at the same time, therefore it is not always possible to assign peaks to isolated molecular motions. In this region, a small change in intensity between the empty (**Figure 2**, red curve) and solvated material (**Figure 2**, grey, blue curves) can be seen in the band at  $\nu < 500$  cm<sup>-1</sup>. According to the static decomposition of vibrational modes, this is due to the slow rotation of the linkers along the axis that connects the two bricks and to deformations that change the pore shape and size. These modes are slightly affected by the interaction with the solvent molecules. At higher frequencies, up to 800 cm<sup>-1</sup> motions that involve bonds with the zirconium atoms and the stretching of the  $\mu_3\text{-OH}$  groups in the bricks are present, while the peaks that go from 800-1600 cm<sup>-1</sup> are due to

combinations of C-O, C-C stretching and bending and C-H bending vibrations of the linker atoms. For more details, a dual computational-experimental characterization of this region in the case of the infrared spectrum has been reported by Valenzano *et al.*<sup>14</sup> This part of the spectrum corresponds almost exactly to the empty material, with only changes in intensity of the bands when solvent is included, but no shifts in frequency.

The high frequency region above 3000 cm<sup>-1</sup> is characterized by two sharp peaks related to C-H and O-H stretching. This part of the vibrational spectrum is clearly affected by the presence of a confined solvent (**Figure 2** left, inset). The first peak is due to the stretching of the aromatic C-H bonds of the linkers. This peak in the presence of a solvent is slightly broadened but does not change in frequency. This weak broadening is most likely due to improper hydrogen bond interactions<sup>38</sup> with the solvent. The most dramatic change in the spectrum can be seen in the peak at  $\nu \approx 3750$  cm<sup>-1</sup>. This peak in the empty material (**Figure 2** left, red curve) is due to the O-H stretching of the  $\mu_3$ -OH groups of the bricks and to the hydroxyl groups adsorbed on two of the defective zirconium atoms which serve as charge balancing species. Upon introduction of a solvent, we observe a spread of this peak to give a broadened band at lower frequencies, which is due to strong hydrogen bond interactions with the solvent. Previous results indicate that the lower vibrational spectrum, related to the structural part of the material is barely influenced by the presence of water, whereas the higher vibrational part related to O-H vibrational modes of the inorganic brick are very sensitive to the presence of protic solvents.

To specifically understand the impact of the material on the vibrational density of states of the solvent, we also analysed the vibrational density of states for the confined water solvent (**Figure 2** right, blue curves) and compared it to a bulk water simulation performed on the same unit cell at the same conditions (**Figure 2** right, green curve). The modes below 1000 cm<sup>-1</sup> associated to librations and diffusion modes seem to be slightly shifted towards lower frequencies in case of confinement, pointing towards slower rearrangements of the water molecules due to a tighter network of hydrogen bonds in case of a confined solvent<sup>39, 40</sup>. No changes seem to be present in the sharp bending peak at 1700 cm<sup>-1</sup>. The most striking feature in these spectra is the appearance in the confined liquid of a peak at  $\nu > 3700$  cm<sup>-1</sup>, which is due to O-H bonds which are not hydrogen bonded, in line with what is observed in case of a hydrophobic confinement<sup>31, 41-43</sup>. These should be identified as O-H bonds of water molecules pointing towards the hydrophobic linkers.

Previous interaction sites of water with hydrophobic and hydrophilic parts of the material can also be deduced from radial distribution functions (RDFs) which offer a measure on how the density of the particles varies as a function of the distance from another tagged particle and form important structural characteristics. In our study we calculate RDFs for pairs of atoms belonging to the material and the solvent in a unit cell with a loading of 80 water molecules. These are reported in **Figure 3**, along with their integrated values, which show the number of correlated pairs that give rise to each RDF peak, which are further discussed in the SI.



**Figure 3** Radial distribution functions between oxygen and hydrogen of water ( $O(w)$ ,  $H(w)$ ), and different atoms of the material obtained from the simulation with 80 water molecules in the unit cell. Full lines indicate the  $g(r)$ , dashed lines indicate its integral. Upper panel: RDFs between water and linker carbons  $C(l)$ ; middle panel: RDFs between water and oxygen atoms of the linkers and bricks ( $O(l)$ ,  $\mu_3\text{-OH}$ ,  $\mu_3\text{-O}$ ); lower panel: RDFs between water and zirconium atoms of defective and pristine bricks ( $Zr(\text{def})$ ,  $Zr(\text{pris})$ ).

RDFs between the linker atoms and the water atoms (shown in the upper panel of **Figure 3**) show a typical behaviour for a hydrophobic confinement and are similar to what has been observed in carbon nanotubes<sup>42</sup>. The RDF corresponding with the  $C(l)\text{-}O(w)$  pair (black curve) is nearly zero for distances before 3 Å after which it increases sharply, while the  $C(l)\text{-}H(w)$  RDF (light grey curve) starts at lower values. This is an indication that the hydrogens of the water molecules near the interface have a slight preference to orient themselves towards the aromatic carbons. On the other hand, the RDFs between water and oxygens of the brick and linkers in the middle panel of **Figure 3** are more structured due to stronger interactions between material and solvent. In particular, the water molecules interact strongly with the oxygens of the inorganic brick ( $\mu_3\text{-OH}$ , dark red curve and  $\mu_3\text{-O}$ , red curve). The correlation between a  $\mu_3\text{-OH}$  oxygen atom and an adjacent water molecule is stronger than with a  $\mu_3\text{-O}$ , in agreement with the weak acidity of the  $\mu_3\text{-OH}$  hydrogen reported for some reactions<sup>30, 44</sup>.

<sup>45</sup>. The RDF between the carboxylic oxygens of the linkers (pink curve) and the oxygens of the water molecules also shows a stronger interaction compared to the C(l) – O(w) RDF and formation of a network of hydrogen bonds with the water molecules. Finally, we investigate the coordination between the Zr-atoms of the brick and the water molecules. In the case of a defective brick the first peak at 2.1 – 2.3 Å is due to the adsorption of water or hydroxy species on the undercoordinated Zr-atom at the defect site. At the pristine brick the RDF starts at larger distances, as water molecules are rather coordinated to other parts of the brick such as the  $\mu_3$ -OH oxygen atoms.

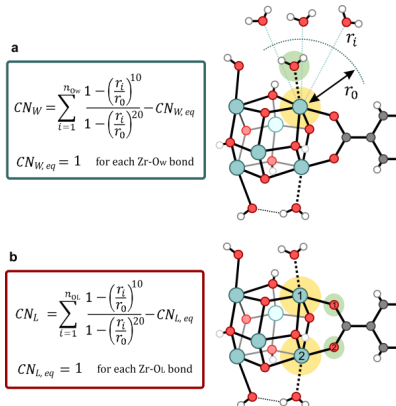
Summarizing, the various RDFs give valuable structural information on the confinement effect of water solvent in the pores of a defective UiO-66 material and the partition of hydrophilic and hydrophobic regions. However, the reported RDFs are average distributions measured over the whole simulation time and do not give a reflection of the dynamic processes which occur during the simulations. Processes such as dynamic proton acidity, decoordination of water from the active sites, or linker decoordination can lead to dynamic fluctuation of the coordination environment of the zirconium atoms. This can have a drastic effect on the nature, type and number of active sites, which in turn substantially affects the catalytic properties of the material. These fluctuations will be examined in detail in the next section.

#### Activated processes related to dynamic changes in the zirconium coordination number

Herein, we focus on the dynamic changes of the zirconium coordination numbers of the hydrated defective brick as displayed in **Figure 1**. In its hydrated form, each zirconium atom on the defect site has a total coordination number of eight. Previous regular MD simulations do not show any changes in the coordination numbers, neither in water nor in methanol solvent. The energetically favourable substitution of defect coordinating water by methanol postulated in previous works<sup>23, 25, 30</sup> was not observed. However, the radial distribution functions (**Figure 3**) point towards some large fluctuations of the zirconium-water coordination bonds. Breaking of zirconium-oxygen coordination bonds typically occurs during activation processes, such as dehydration, defect formation and PSLE. To simulate the behaviour of the material under these conditions, we need to apply enhanced sampling molecular dynamics simulations which allow to steer the system towards higher lying regions of the free energy surface<sup>46-51</sup>. In this case we performed a series of independent metadynamics (MTD) simulations, which enabled to enhance the sampling of some low probability regions along certain coordinates of the system, denoted as collective variables (CVs) which describe the coordination state of zirconium. We particularly focus on water as protic solvent in these simulations, as it possesses a higher number of mobile protons compared to methanol, thus better stabilizing intermediate configurations. Moreover, we can better follow the dynamics of the system as the defect coordinating species are the same as the rest of the solvent.

A first CV, displayed in **Figure 4a** represents the coordination  $CN_w$  between a zirconium atom on the defect site and the oxygen atoms of water. In the formula,  $r_i$  is the zirconium-oxygen distance, while  $r_0$  represents a cut-off distance of 2.9 Å, representative for a physisorbed water at the zirconium atom. This value may be derived readily from the RDF of **Figure 3**. Only the oxygen atoms that are inside this coordination sphere (represented in

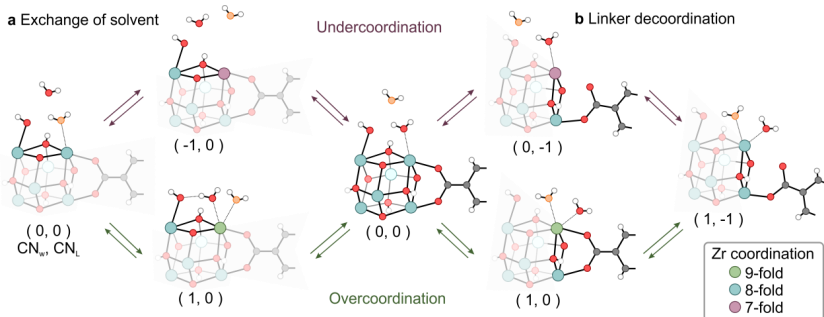
green) contribute to the coordination with the metal. To better monitor the variations, the coordination number is taken as relative with respect to the equilibrium value ( $CN_{W,eq} = 1$ ). For example, at equilibrium conditions, where the zirconium atom is 8-fold coordinated,  $CN_W = 0$ , whereas  $CN_W = -1$  when water decoordinates from the active site.



**Figure 4** Coordination numbers used in the simulation **a**: coordination number  $CN_W$  between zirconium and all water oxygens. Also the linker that induces changes in the zirconium coordination number is visualized. **b**: coordination number  $CN_L$  between each zirconium atom and linker oxygen atoms.  $n_{eq}$  and  $n_{OL}$  are the number of oxygen atoms considered in the two cases,  $r_i$  is the zirconium-oxygen distance,  $r_0$  a cutoff distance of 2.9 Å. In yellow, the zirconium atoms considered in the CN. In green, the oxygen atoms that have a weight close to one and substantially different from zero in the summation.

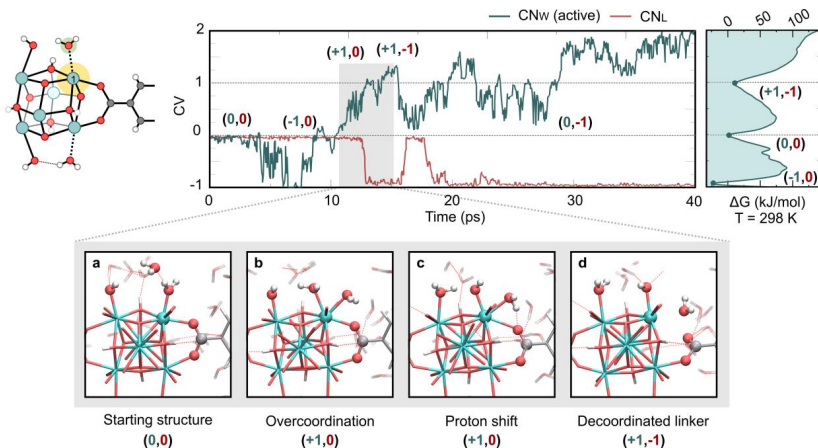
The second relevant CV is the coordination number  $CN_L$  that describes the coordination of the defect-bridging linker to the zirconium atoms of the brick. It is defined in a similar way, but with the coordination bond length  $r_i$  equal to the zirconium-carboxylate oxygen distance (**Figure 4b**). In this case, we also consider the CN as relative to the equilibrium value (for each  $Zr-O_L$  bond,  $CN_{L,eq} = 1$ ).  $CN_L = 0$  means that the linker is in the equilibrium configuration and is entirely coordinated to the two zirconium-atoms of the brick as displayed in **Figure 4b**. If one of the bonds is broken,  $CN_L = -1$ .

Various MTD simulations were performed which reveal how the system behaves when the zirconium coordination number changes upon enhanced sampling along one of these two collective variables. Using the coordination numbers  $CN_W$  and  $CN_L$  it is possible to describe many events which occur around the brick and which are reported schematically in **Figure 5**. In the equilibrated structure at operating conditions, each zirconium atom belonging to the defective brick is 8-fold coordinated, and we can define this state as **(0,0)**, where the first number refers to  $CN_W$  and the second to  $CN_L$ . The coordination changes of the zirconium atoms can be easily deduced by the values of the two collective variables: if  $CN_L + CN_W < 0$ , such as in the states **(-1,0)** or **(0,-1)** there is an undercoordination, whereas  $CN_L + CN_W > 0$  (such as in **(+1,0)**) means overcoordination.



**Figure 5** Coordination and value of the CV during (a) the exchange of solvent and (b) linker decoordination in the MTD simulations. top paths: stepwise pathway which goes through undercoordinated zirconium; bottom paths: concerted pathways which go through overcoordinated zirconium.

Undercoordinated zirconium states have already been reported in literature, for example in the work of Hajek et al<sup>21, 30</sup>. However, overcoordinated states have not been explicitly reported so far. Various possibilities for the rearrangements around the inorganic brick are shown in **Figure 5**. When inspecting the starting structure of the inorganic brick, the easiest way to induce undercoordination and creation of Lewis acid sites is the decoordination of one physisorbed water (state **(-1, 0)** in **Figure 5**). Another possibility is the breakage of a zirconium-oxygen bond with one of the organic linkers (state **(0, -1)** in **Figure 5**). Overcoordination might in principle occur when more water molecules are coordinated to the zirconium atoms (state **(1, 0)** in **Figure 5**). These are all events which may take place, however at this moment it is still unclear whether such processes actually take place during activation and what the effect of such events would be on the other coordination bonds of the inorganic brick, as well as how the solvent around the inorganic brick would respond to such rearrangements. Possible events are schematically shown in **Figure 5**. To estimate the occurrence of these events, a series of independent metadynamics simulations are performed as sketched below.



**Figure 6:** Top: time evolution of the collective variable and free energy profile for the first MTD simulation along the CV representing the coordination  $CN_w$  between the zirconium atom Zr1, highlighted in yellow, and all water molecules (green curve).  $CN_L$  between Zr1 and the neighbouring defect-bridging linker oxygen (red curve) is also monitored; bottom: snapshots of the linker decoordination triggered by overcoordination

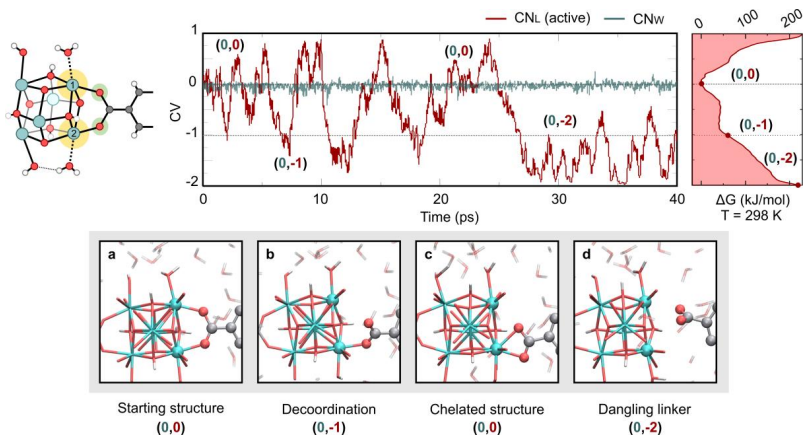
In a **first case study**, we consider the coordination number  $CN_w$  between one of the zirconium atoms of the defective site and water oxygens as CV, as already proposed by Lau and Ensing<sup>52</sup>.  $CN_w$ , as defined in **Figure 4**, allows to involve all solvent water molecules of the unit cell. In a dynamic process, water molecules can migrate in or outside the coordination sphere. The MTD calculation was started from an equilibrated structure obtained from the previous MD simulation with 80 water molecules in the unit cell. The time evolution of the collective variable is plotted in **Figure 6**, where 0 is taken as the reference where the zirconium atom is 8-fold coordinated. Negative values for the CV correspond to undercoordination of the zirconium atom, whereas positive values indicate an overcoordination. At the same time, the coordination number of the linker that induces changes in the coordination number with the same zirconium atom (Zr1, highlighted in yellow) is also monitored. In the beginning of the simulation at equilibrium, the coordination number between the zirconium atom and this linker is 1, therefore  $CN_L=0$ . In this sense, we start from an equilibrium configuration which is labelled **(0,0)**, referring to  $CN_w=0$  and  $CN_L=0$ . After 4 ps, the water molecule coordinated to the zirconium atom leaves the coordination sphere, creating a temporarily undercoordinated zirconium site (configuration **(-1,0)**). The large fluctuations of the CV between -1 and 0 after 4 ps suggest that water is dynamically re-entering the coordination sphere. The decoordination leads to the formation of a Lewis acid site where reactants can adsorb, and which may represent the active site in catalytic processes. The system dynamically explores configurations where temporarily the zirconium atom is undercoordinated and where another water molecule can then re-enter the coordination sphere. In this undercoordinated pathway, the dynamic exchange of a solvent molecule occurs after the metal site has been opened (**Figure 5a**), with a free energy barrier in the order of 70 kJ/mol. As the exact free energies may be quite dependent on various computational degrees of freedom, such as choice of the CV and level of theory, the values

given here should be interpreted as a qualitative measure rather than an exact quantitative estimate of the barrier. More details about the free energy profiles and the regions visited by the two collective variables are provided in the SI.

When further proceeding the MTD simulation, the system explores configurations where the zirconium atom is overcoordinated going to a 9-fold coordination. It is interesting to mechanistically follow the rearrangements of the solvent around the inorganic brick. After about 11 ps we observe a series of states which are pictorially represented in **Figure 6a-d**, bottom panel and can be visualized in Movie MTD1 of the Supporting Information. First, a water molecule coming from the pore inserts between the Zr-H<sub>2</sub>O and the Zr-OH groups (**Figure 6a**) and pushes the physisorbed molecule towards the side of the pore. This third water molecule is now very close to the Zr-OH group (**Figure 6b**) and forms a strong hydrogen bond with it, leading to a proton shift. The zirconium atom is now coordinated to a hydroxyl group and to a water molecule. The Zr-OH bond on the 9-fold coordinated zirconium is thus stronger and pushes the water molecule even more strongly to the side (**Figure 6c**). At the same time, the water molecule that was pushed away forms a hydrogen bond with the linker, which is in turn decoordinated from the zirconium atom, bringing the zirconium atom back to the more stable 8-fold coordination. This results in configuration (+1,-1) with a partially decoordinated linker (**Figure 6d**), which is stabilized by hydrogen bonds with the solvent. The free energy barrier for this overcoordination events amounts to about 60 kJ/mol and is of the same order of magnitude of the undercoordinated event. After this event, the linker sometimes temporarily recoordinates to the zirconium but decoordinates shortly again hereafter. From now on the system remains in a regime with CVs fluctuating between 0 and 2 and the zirconium atom coordination ranging from 7 to 9. The states encountered here, with partially decoordinated linkers might be important configurations for PSLE. Previous simulations clearly show the crucial role of solvent water, inducing the coordination changes of zirconium and helping to stabilize the partially disconnected linkers. During this biased simulation we observed a dynamic evolution of the system, and a creation of a plethora of active sites that are generated through different mechanisms.

Similarly as in the first study case we also performed a MTD simulation starting from an initial structure with focus on the coordination of the water molecules with a zirconium atom on the other side of the defective brick. The processes encountered during this simulation are similar compared to previous case, with solvent exchange by undercoordination and overcoordination of the zirconium atoms, as well as linker decoordination. To account for possible proton transfers, a similar MTD simulation was performed involving both adjacent zirconium atoms instead of a single zirconium site. The encountered processes are similar, but we see that also the Zr-OH group can be decoordinated, stabilized by the solvent, and eventually be protonated by the solvent to allow the creation of two adjacent Lewis acid sites. More detailed results are reported in the Supporting Information (**Figure S9-S18**).

In the **second case study** we investigate the decoordination of one linker by performing a MTD simulation along the linker coordination number CN<sub>L</sub> as collective variable, as visualized in the initial structure of **Figure 7**. In this case, we are directly enhancing the sampling along states where the coordination of two zirconium atoms with the organic linker may vary. The evolution of the collective variable is displayed in **Figure 7**.



**Figure 6:** top: free energy profile for the first MTD simulation along the CV representing the coordination between two zirconium atoms and a linker, middle: evolution of the collective variable, bottom: snapshots of the linker decoordination

The simulation starts in the equilibrium structure where each zirconium atom is 8-fold coordinated, as shown in **Figure 7a** (configuration  $(0,0)$ ). At the same time, we are monitoring the coordination of the two active zirconium atoms (Zr1 and Zr2, highlighted in yellow) with all water molecules. This coordination is indicated as  $CN_W$  in the figure, and is considered with respect to its equilibrium value  $CN_{W,eq} = 2$  ( $CN_{W,eq} = 1$  for each zirconium atom, as shown in **Figure 5**). After some ps, the system explores regions where one bond of the linker is broken due to a rotation of the linker (**Figure 7b**, configuration  $(0,-1)$ ). The free energy associated to this decoordination is of the order of 50 kJ/mol. Translation of the linker is also observed, which results in a metastable chelated structure displayed in **Figure 7c**, where both oxygens are coordinated to the same zirconium atom. After about 28 ps of simulation, states are explored where the second bond is also broken leading to a dangling linker state (**Figure 7d**, configuration  $(0,-2)$ ). This state is associated to a higher energy barrier compared to the first Zr-O bond cleavage. However, this barrier is overestimated due to the short simulation time compared to the longer time scale of the event, which should involve diffusion and adsorption of solvent. As reported by Paesani *et al.*, the diffusion constant of water in the pores is decreased by one order of magnitude for MIL-53 compared to the bulk<sup>40</sup>. This type of simulation demonstrates a pathway for the breakage of the zirconium-oxygen bond with the linker, without overcoordination of the zirconium atom by solvent. The role of the solvent, however, is expected to be important, as it plays a role in stabilizing the dangling linker via hydrogen bonding with the carboxylic oxygen. The simulation does not display minima on the free energy profile, at  $CV = -1$  and  $CV = -2$  because in these states the zirconium atom remains undercoordinated. One can imagine that if a water molecule diffuses from the pore and coordinates to the undercoordinated zirconium atom, this would restore the 8-fold coordination, lowering the energy. However, during the simulation time, this event is not observed. The interactions around the linkers are dominated by hydrophobic effects, and the solvent molecules are hindered by the dynamic motions of the linker.

Summarizing, based on different biased simulations, we come to the conclusion that some features like the solvent exchange and linker decoordination may result from either an undercoordinated or overcoordinated configuration of the zirconium atom. Solvent exchange (**Figure 5a**) can proceed via a stepwise mechanism, characterized by a temporary undercoordination of the zirconium atoms, or a concerted mechanism, in which the zirconium atom is temporarily overcoordinated. A similar pattern is observed for the linker decoordination (**Figure 5b**). The metal-linker bond can be broken directly, without influence of the solvent, leading to an undercoordination of the zirconium atom, but can also be broken as a result of an overcoordination of an additional solvent molecule. Moreover, solvent can stabilize the intermediate configurations along the process and assist in stabilizing the charged species via hydrogen bonding. In earlier work we had already observed mobility of the linkers in the brick at activation conditions<sup>21</sup>, but this is the first time that such process has been computationally modelled at catalytic conditions in the presence of a solvent and this mobility does not involve any rearrangement of the brick. These findings are in line with the possible hydrolysis of the metal-ligand bond in MOFs in the presence of water that was proposed in a previous theoretical work<sup>53</sup>. This linker exchange has been documented experimentally in methanol as well, and there is reason to believe that the same mechanism may occur as in water, given the similar acidity of the molecule. Despite being very stable in the presence of water<sup>54, 55</sup>, UiO-66 can be structurally modified, which was shown here at operating conditions using first principle MD simulations

### Conclusions

This work examines the structural integrity of defective UiO-66 material and the role of a protic solvent as water and methanol in sustaining structural rearrangements in the material at operating conditions. Earlier work gave evidence for the exceptional stability of the empty UiO-66 even during processes where linkers become mobile. Such events were observed during simulations of the dehydration process of the material. On the one hand we observed that the structure of the solvent is impacted by both its hydrophobic and hydrophylic interactions with the framework. However, the structure of the material remains intact in the presence of protic solvents. On the other hand, we simulated some activated processes which may lead to coordination changes of the zirconium atom. The strong tendency of the solvent molecules to adsorb on the zirconium atom and the possible hydrogen bond stabilization with linkers, allow a dynamic behaviour of the linkers. These findings shed light on the exceptional dynamic stability of the defective UiO-66 material and its dynamic interactions with protic solvents during post synthetic treatment. These interactions may indicate a dynamic response of the material during catalytic processes in some protic solvents, in which linkers may be temporarily decoordinate creating Lewis acid sites. The observed fluctuating coordination number of the zirconium atoms at the defect site gives a variable Lewis acidity to the metal, offering ideal opportunities to induce Lewis catalysed reactions. Finally, we have observed for the first time how overcoordination of the zirconium atom with solvent water can tune the structural properties of the material. This can be the first step in activation processes such as PSLE, but also in other processes in which active sites are generated. The exceptionally high connectivity of the material allows for a whole plethora of dynamic events where linkers, bricks and solvent can exchange without altering the stability of the structure.

### **Computational Methodology**

The investigated structures were constructed from an optimized 2-brick unit cell where one linker has been removed, selected among the possible structures proposed in the work of Rogge et al. and De Vos et al<sup>56, 57</sup>. Starting structures where solvent is introduced in the pores are generated with Monte Carlo simulations (MC). Regular MD calculations on the empty and solvated unit cells and bulk solvent were performed to gain insight at equilibrium conditions, followed by MTD simulations.

### **Starting structures calculations**

The static calculations on the UiO-66 unit cell were performed with a periodic density functional theory (DFT) approach. The methodology and level of theory used were the same as in previous works of the presenting authors<sup>22</sup>. The periodic VASP code<sup>32-36</sup> was used applying the projector augmented wave approximation (PAW)<sup>58</sup> with gamma point approximation. We optimized the empty UiO-66 unit cell at the PBE-D3 level of theory<sup>59-62</sup>. The energy cutoff was set to 700 eV, with a 10E-5 eV convergence threshold for the electronic SCF calculations, and a gaussian smearing of 0.025 eV was included. Total Hessian frequency calculations were performed for this structure using finite displacements. To generate starting structures, MC calculations have been performed using the RASPA software<sup>63</sup>. Two solvated structures were generated with 80 and 75 water molecules adsorbed in the unit cell. The value of 80 water molecules corresponds to what is reported by Ghosh et al.<sup>24</sup> in the same defective UiO-66 unit cell at 1 bar and 298 K, obtained by Grand Canonical MC simulations performed with RASPA. MC simulations were also used to generate the bulk solvent unit cells, where the number of molecules was chosen to replicate the experimental density.

### **MD simulations**

The DFT MD simulations were performed using the CP2K simulation software<sup>37</sup> with the PLUMED code<sup>64</sup>. The electronic structure was determined with the PBE-D3 functional<sup>59-62</sup>, employing a DZVP-MOLOPT-GTH basis set and GTH pseudopotentials<sup>65</sup>. A hybrid Gaussian – plane wave basis set approach<sup>66, 67</sup> was used, with a cutoff of 400 Ry. The level of theory was chosen for better comparison with previous static and dynamic results. The time step was set to 0.5 fs and a Nose-Hoover thermostat with five beads and 0.3 ps time constant was used to set the temperature to 298 K for water and 330 K for methanol<sup>68</sup>. An equilibration run was performed in the NPT ensemble at the simulation temperature and 1 bar using a MTK barostat with 0.1 ps time constant<sup>69</sup>, followed by 50 ps of NVT simulation.

### **MTD simulations**

In order to sample the activated states, MTD simulations have been performed<sup>46, 47</sup> starting from the equilibrated NVT simulations. Gaussian hills are added every 25 fs along a chosen CV, which represents the coordination between zirconium and water molecules, or zirconium and carboxylate oxygens of a linker. A 1D free energy diagram can be reconstructed from this bias potential. More details are reported in the Supporting Information (**Figure S9-S18**).

### Conflicts of interest

The authors declare no conflicts of interest.

### Acknowledgements

This project has received funding from the European Union's Horizon 2020 research and innovation program under the Marie Skłodowska-Curie (grant agreement No 641887, acronym: DEFNET). The authors further acknowledge financial support from the European Research Council (consolidator ERC Grant Agreement No 647755 – DYNPOR (2015-2020)) and the Research Board of Ghent University (BOF). The computational resources and services used in this work were provided by the VSC (Flemish Supercomputer Center), funded by the Hercules foundation and the Flemish Government – department EWI.

### References

1. S. J. Garibay and S. M. Cohen, *Chemical Communications*, 2010, **46**, 7700-7702.
2. M. Kandiah, M. H. Nilsen, S. Usseglio, S. Jakobsen, U. Olsbye, M. Tilset, C. Larabi, E. A. Quadrelli, F. Bonino and K. P. Lillerud, *Chemistry of Materials*, 2010, **22**, 6632-6640.
3. M. Kim, J. F. Cahill, H. Fei, K. A. Prather and S. M. Cohen, *Journal of the American Chemical Society*, 2012, **134**, 18082-18088.
4. F. Vermoortele, R. Ameloot, A. Vimont, C. Serre and D. De Vos, *Chemical Communications*, 2011, **47**, 1521-1523.
5. F. Vermoortele, M. Vandichel, B. Van de Voorde, R. Ameloot, M. Waroquier, V. Van Speybroeck and D. E. De Vos, *Angewandte Chemie International Edition*, 2012, **51**, 4887-4890.
6. H. Furukawa, K. E. Cordova, M. O'Keeffe and O. M. Yaghi, *Science*, 2013, **341**, 1230444.
7. J. Liu, L. Chen, H. Cui, J. Zhang, L. Zhang and C.-Y. Su, *Chemical Society Reviews*, 2014, **43**, 6011-6061.
8. J.-R. Li, R. J. Kuppler and H.-C. Zhou, *Chemical Society Reviews*, 2009, **38**, 1477-1504.
9. J. E. Mondloch, M. J. Katz, W. C. Isley Iii, P. Ghosh, P. Liao, W. Bury, G. W. Wagner, M. G. Hall, J. B. DeCoste, G. W. Peterson, R. Q. Snurr, C. J. Cramer, J. T. Hupp and O. K. Farha, *Nat Mater*, 2015, **14**, 512-516.
10. A. M. Plonka, Q. Wang, W. O. Gordon, A. Balboa, D. Troya, W. Guo, C. H. Sharp, S. D. Senanayake, J. R. Morris, C. L. Hill and A. I. Frenkel, *Journal of the American Chemical Society*, 2017, **139**, 599-602.
11. Y. Bai, Y. Dou, L.-H. Xie, W. Rutledge, J.-R. Li and H.-C. Zhou, *Chemical Society Reviews*, 2016, **45**, 2327-2367.
12. J. H. Cavka, S. Jakobsen, U. Olsbye, N. Guillou, C. Lamberti, S. Bordiga and K. P. Lillerud, *Journal of the American Chemical Society*, 2008, **130**, 13850-13851.
13. K. Leus, T. Bogaerts, J. De Decker, H. Depauw, K. Hendrickx, H. Vrielinck, V. Van Speybroeck and P. Van Der Voort, *Microporous and Mesoporous Materials*, 2016, **226**, 110-116.
14. L. Valenzano, B. Civalleri, S. Chavan, S. Bordiga, M. H. Nilsen, S. Jakobsen, K. P. Lillerud and C. Lamberti, *Chemistry of Materials*, 2011, **23**, 1700-1718.
15. O. V. Gutov, M. G. Hevia, E. C. Escudero-Adán and A. Shafir, *Inorganic Chemistry*, 2015, **54**, 8396-8400.
16. G. C. Shearer, S. Chavan, J. Ethiraj, J. G. Vitillo, S. Svelle, U. Olsbye, C. Lamberti, S. Bordiga and K. P. Lillerud, *Chemistry of Materials*, 2014, **26**, 4068-4071.
17. G. C. Shearer, S. Chavan, S. Bordiga, S. Svelle, U. Olsbye and K. P. Lillerud, *Chemistry of Materials*, 2016, **28**, 3749-3761.
18. M. J. Cliffe, W. Wan, X. Zou, P. A. Chater, A. K. Kleppe, M. G. Tucker, H. Wilhelm, N. P. Funnell, F.-X. Coudert and A. L. Goodwin, *Nature Communications*, 2014, **5**.

19. F. Vermoortele, B. Bueken, G. I. Le Bars, B. Van de Voorde, M. Vandichel, K. Houthoofd, A. Vimont, M. Daturi, M. Waroquier and V. Van Speybroeck, *Journal of the American Chemical Society*, 2013, **135**, 11465-11468.
20. G. C. Shearer, S. Forslev, S. Chavan, S. Bordiga, K. Mathisen, M. Bjorgen, S. Svelle and K. P. Lillerud, *Top Catal*, 2013, **56**, 770-782.
21. J. Hajek, C. Caratelli, R. Demuynck, K. De Wispelaere, L. Vanduyfhuys, M. Waroquier and V. Van Speybroeck, *Chemical Science*, 2018, **9**, 2723-2732.
22. C. Caratelli, J. Hajek, S. M. J. Rogge, S. Vandenbrande, E. J. Meijer, M. Waroquier and V. Van Speybroeck, *Chemphyschem*, 2018, **19**, 420-429.
23. J. Marreiros, C. Caratelli, J. Hajek, A. Krajnc, G. Fleury, B. Bueken, D. E. De Vos, G. Mali, M. B. J. Roeffaers, V. Van Speybroeck and R. Ameloot, *Chemistry of Materials*, 2019, **31**, 1359-1369.
24. P. Ghosh, Y. J. Colon and R. Q. Snurr, *Chem Commun (Camb)*, 2014, **50**, 11329-11331.
25. D. Yang, V. Bernales, T. Islamoglu, O. K. Farha, J. T. Hupp, C. J. Cramer, L. Gagliardi and B. C. Gates, *Journal of the American Chemical Society*, 2016, **138**, 15189-15196.
26. L. Grajciar, C. J. Heard, A. A. Bondarenko, M. V. Polynski, J. Meeprasert, E. A. Pidko and P. Nachtigall, *Chemical Society Reviews*, 2018, **47**, 8307-8348.
27. S. M. J. Rogge, A. Bavykina, J. Hajek, H. Garcia, A. I. Olivos-Suarez, A. Sepulveda-Escribano, A. Vimont, G. Clet, P. Bazin, F. Kapteijn, M. Daturi, E. V. Ramos-Fernandez, F. X. Llabres i Xamena, V. Van Speybroeck and J. Gascon, *Chemical Society Reviews*, 2017, **46**, 3134-3184.
28. P. Valvakens, F. Vermoortele and D. De Vos, *Catalysis Science & Technology*, 2013, **3**, 1435-1445.
29. J. Canivet, M. Vandichel and D. Farrusseng, *Dalton Transactions*, 2016, **45**, 4090-4099.
30. C. Caratelli, J. Hajek, F. G. Cirujano, M. Waroquier, F. X. L. I. Xamena and V. Van Speybroeck, *Catal*, 2017, **352**, 401-414.
31. F.-X. Coudert, R. Vuilleumier and A. Boutin, *ChemPhysChem*, 2006, **7**, 2464-2467.
32. G. Kresse and J. Furthmuller, *Phys. Rev. B*, 1996, **54**, 11169-11186.
33. G. Kresse and J. Furthmuller, *Comp Mater Sci*, 1996, **6**, 15-50.
34. G. Kresse and J. Hafner, *Phys Rev B Condens Matter*, 1993, **47**, 558-561.
35. G. Kresse and J. Hafner, *Phys Rev B Condens Matter*, 1994, **49**, 14251-14269.
36. G. Kresse and D. Joubert, *Phys. Rev. B*, 1999, **59**, 1758-1775.
37. J. VandeVondele, M. Krack, F. Mohamed, M. Parrinello, T. Chassaing and J. Hutter, *Comput Phys Commun*, 2005, **167**, 103-128.
38. I. V. Alabugin, M. Manoharan, S. Peabody and F. Weinhold, *Journal of the American Chemical Society*, 2003, **125**, 5973-5987.
39. A. C. Fogarty, F.-X. Coudert, A. Boutin and D. Laage, *ChemPhysChem*, 2014, **15**, 521-529.
40. G. R. Medders and F. Paesani, *The Journal of Physical Chemistry Letters*, 2014, **5**, 2897-2902.
41. S. Dalla Bernardino, E. Paineau, J.-B. Brubach, P. Judeinstein, S. Rouzière, P. Launois and P. Roy, *Journal of the American Chemical Society*, 2016, **138**, 10437-10443.
42. G. Cicero, J. C. Grossman, E. Schwegler, F. Gygi and G. Galli, *Journal of the American Chemical Society*, 2008, **130**, 1871-1878.
43. R. H. Tunuguntla, R. Y. Henley, Y.-C. Yao, T. A. Pham, M. Wanunu and A. Noy, *Science*, 2017, **357**, 792-796.
44. J. Hajek, B. Bueken, M. Waroquier, D. De Vos and V. Van Speybroeck, *ChemCatChem*, 2017, **9**, 2203-2210.
45. J. Hajek, M. Vandichel, B. Van de Voorde, B. Bueken, D. De Vos, M. Waroquier and V. Van Speybroeck, *J Catal*, 2015, **331**, 1-12.
46. A. Laio and F. L. Gervasio, *Rep Prog Phys*, 2008, **71**.
47. A. Laio and M. Parrinello, *P Natl Acad Sci USA*, 2002, **99**, 12562-12566.
48. L. Maragliano and E. Vanden-Eijnden, *Chemical Physics Letters*, 2006, **426**, 168-175.
49. Y. Sugita and Y. Okamoto, *Chemical Physics Letters*, 1999, **314**, 141-151.

50. R. W. Zwanzig, *The Journal of Chemical Physics*, 1954, **22**, 1420-1426.
51. V. Haigis, F.-X. Coudert, R. Vuilleumier, A. Boutin and A. H. Fuchs, *The Journal of Physical Chemistry Letters*, 2015, **6**, 4365-4370.
52. J. K.-C. Lau and B. Ensing, *Physical Chemistry Chemical Physics*, 2010, **12**, 10348-10355.
53. J. J. Low, A. I. Benin, P. Jakubczak, J. F. Abrahamian, S. A. Faheem and R. R. Willis, *Journal of the American Chemical Society*, 2009, **131**, 15834-15842.
54. J. Canivet, A. Fateeva, Y. M. Guo, B. Coasne and D. Farrusseng, *Chemical Society Reviews*, 2014, **43**, 5594-5617.
55. C. Wang, X. Liu, N. Keser Demir, J. P. Chen and K. Li, *Chemical Society Reviews*, 2016, **45**, 5107-5134.
56. A. De Vos, K. Hendrickx, P. Van Der Voort, V. Van Speybroeck and K. Lejaeghere, *Chem Mater*, 2017, **29**, 3006-3019.
57. S. M. J. Rogge, J. Wieme, L. Vanduyfhuys, S. Vandenbrande, G. Maurin, T. Verstraelen, M. Waroquier and V. Van Speybroeck, *Chemistry of Materials*, 2016, **28**, 5721-5732.
58. P. E. Blochl, *Phys. Rev. B*, 1994, **50**, 17953-17979.
59. J. P. Perdew, K. Burke and M. Ernzerhof, *Physical Review Letters*, 1996, **77**, 3865-3868.
60. J. P. Perdew, K. Burke and M. Ernzerhof, *Physical Review Letters*, 1997, **78**, 1396.
61. S. Grimme, *J Comput Chem*, 2004, **25**, 1463-1473.
62. S. Grimme, J. Antony, S. Ehrlich and H. Krieg, *J Chem Phys*, 2010, **132**, 154104.
63. D. Dubbeldam, S. Calero, D. E. Ellis and R. Q. Snurr, *Mol Simulat*, 2016, **42**, 81-101.
64. G. A. Tribello, M. Bonomi, D. Branduardi, C. Camilloni and G. Bussi, *Comput Phys Commun*, 2014, **185**, 604-613.
65. S. Goedecker, M. Teter and J. Hutter, *Phys Rev B Condens Matter*, 1996, **54**, 1703-1710.
66. G. Lippert, J. Hutter and M. Parrinello, *Mol Phys*, 1997, **92**, 477-487.
67. G. Lippert, J. Hutter and M. Parrinello, *Theor Chem Acc*, 1999, **103**, 124-140.
68. D. Frenkel and B. Smit, *Journal*, 2001.
69. G. J. Martyna, D. J. Tobias and M. L. Klein, *Journal of Chemical Physics*, 1994, **101**, 4177-4189.

Electronic supplementary material for:

## Dynamic interplay between defective UiO-66 and protic solvents in activated processes

Chiara Caratelli<sup>1</sup>, Julianna Hajek<sup>1</sup>, Evert Jan Meijer<sup>2</sup>, Michel Waroquier<sup>1</sup>, Veronique Van Speybroeck<sup>1</sup>

<sup>1</sup>Center for Molecular Modeling, Ghent University, Technologiepark 46, 9052 Zwijnaarde, Belgium

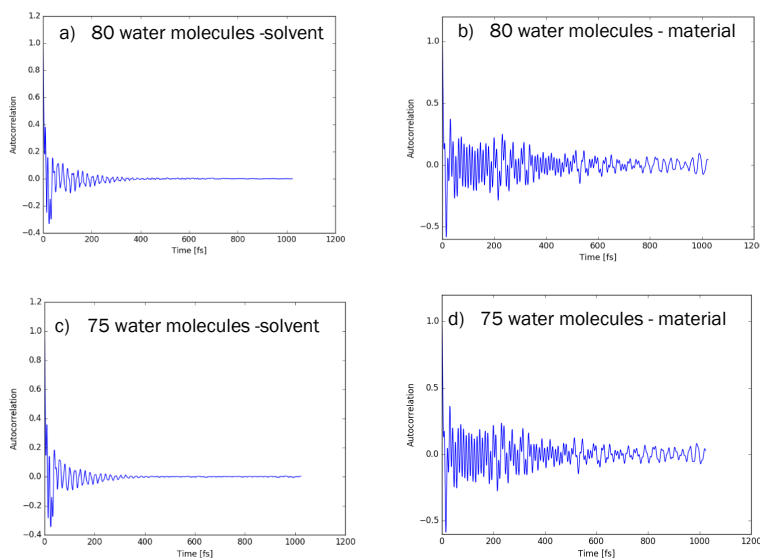
<sup>2</sup>Van 't Hoff Institute for Molecular Sciences, University of Amsterdam, Science Park 904, 1098 XH Amsterdam, The Netherlands

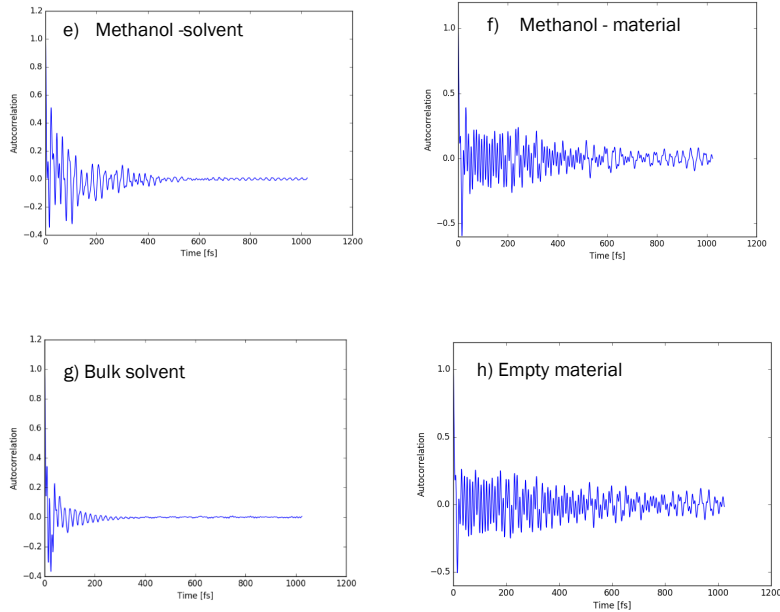
### Vibrational analysis

Vibrational density of states for the systems under consideration were obtained from the power spectrum of the autocorrelation function of the velocities of the atoms in the unit cell after DFT-MD simulations in an NVT ensemble.

### Velocity autocorrelation functions

In Figure S1 we report the velocity autocorrelation functions obtained for the two major components of the system under study: solvent and material.

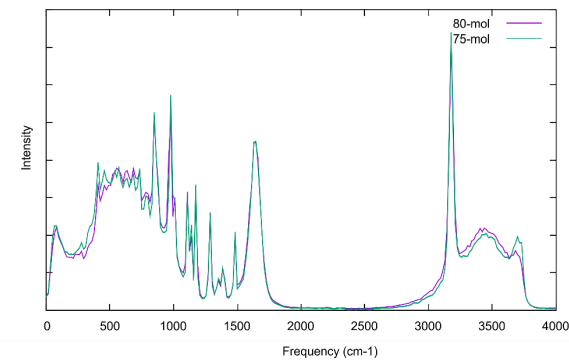




**Figure S1** velocity autocorrelation functions for the reported spectra obtained from the MD calculations.

**Vibrational spectrum obtained for the whole material**

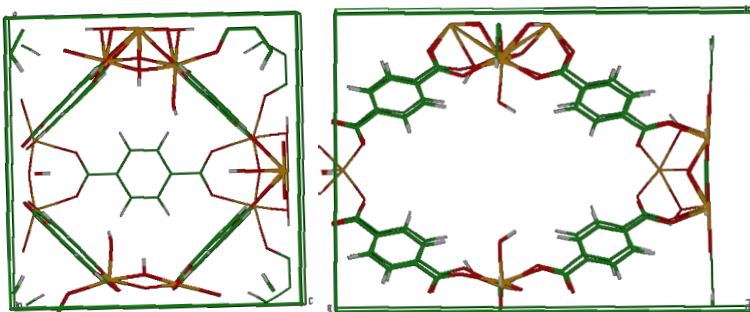
**Figure S2** shows the vibrational DOS calculated for all the atoms of the simulation (material + solvent) with water solvent.



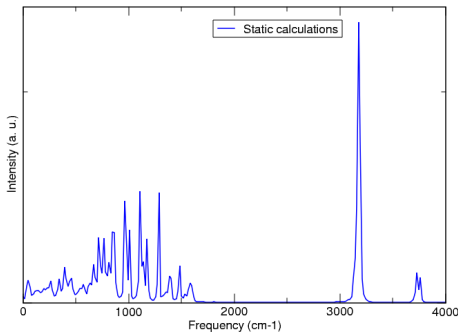
**Figure S2** Total vibrational density of states calculated for the solvated material at two different loadings of solvent water.

### Static calculations

Static calculations have been performed with the VASP code<sup>1-5</sup> using the finite displacement method on an empty UiO-66 unit cell (**Figure S3**) where on each defect site a hydroxyl group is chemisorbed on a zirconium atom, while the other metal site is open. The spectrum in **Figure S4** is obtained by summing Lorentzian functions of width  $\Gamma=10 \text{ cm}^{-1}$  to each vibrational frequency. This allows to identify the vibrational modes corresponding to each frequency. Given the high number of modes (654) it would be inconvenient to report all of them in this document. For this reason, a log file in Gaussian<sup>6</sup> format is provided, where all the frequency modes can be visualized (the file can be opened with different programs such as Molden<sup>7,8</sup>, Avogadro<sup>9</sup>, or Openbabel<sup>10</sup>).



**Figure S3** 2-brick defective unit cell used in the static calculations



**Figure S4** vibrational density of states obtained from static calculations with VASP.

### Radial distribution functions (RDFs)

RDFs have been calculated by analyzing the distances between certain atom pairs during the whole simulations, and are reported with a resolution of 0.05 Å.

#### Solvent-Solvent

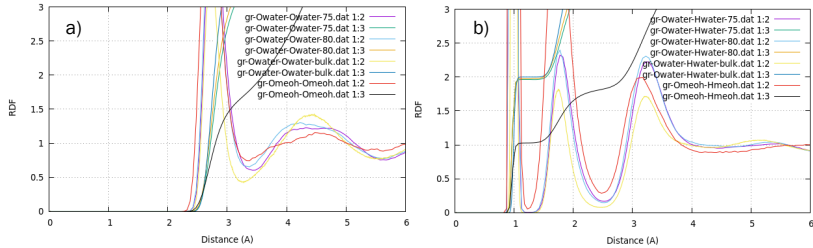
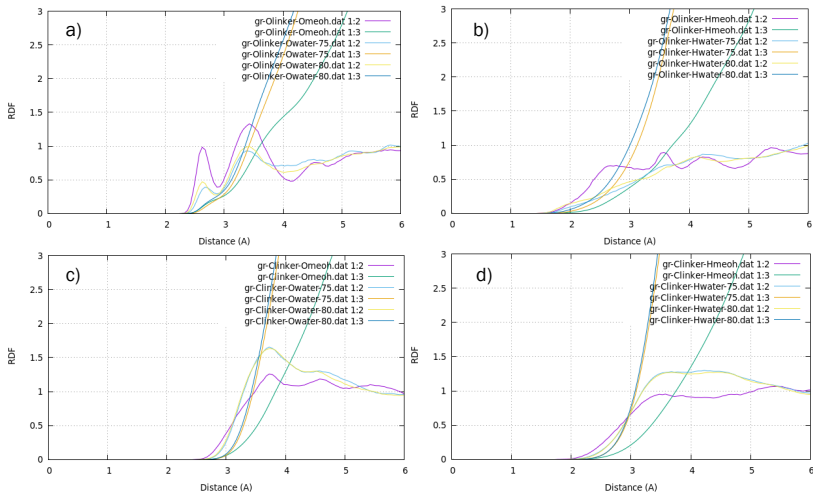
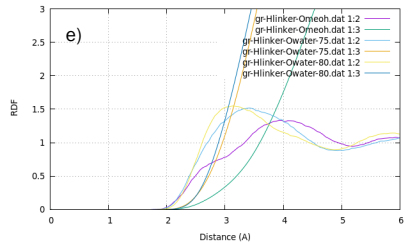


Figure S5 RDFs between solvent atoms: a) Osolv – Osolv, b) Osolv– Hsolv (for MeOH, Hsolv is the one bonded to O)

#### Linkers-solvent

The integrated RDF between linker and solvent atoms does not show particular plateaus due to the hydrophobic interactions.

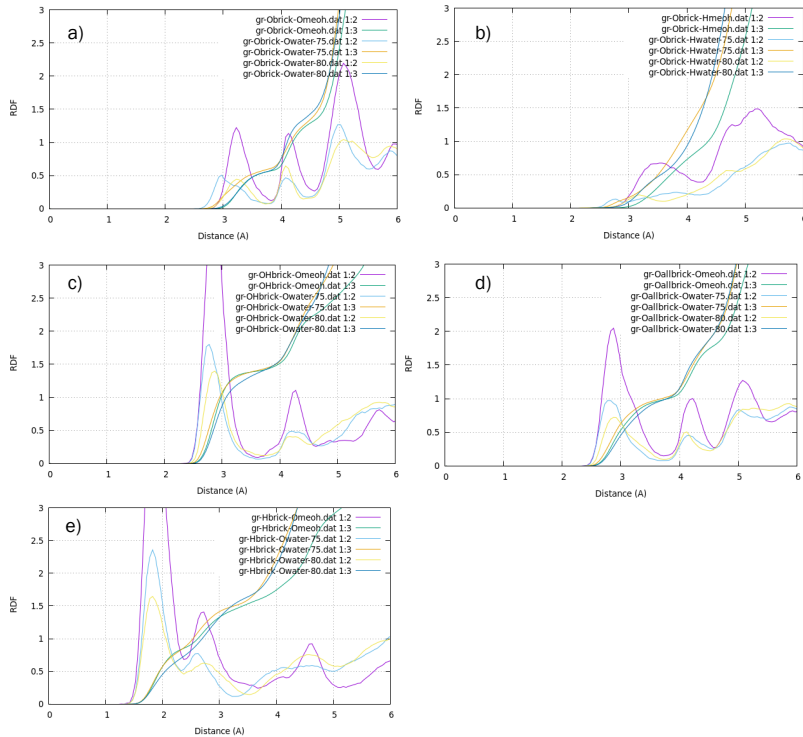




**Figure S6** RDFs between linker atoms and solvent a) Olinker – Osolv; b) Olinker Hsolv; c) Clinker – Osolv; d) Clinker -Hsolv; e) Hlinker – Osolv (for MeOH, Hsolv is the one bonded to O)

### Brick-solvent

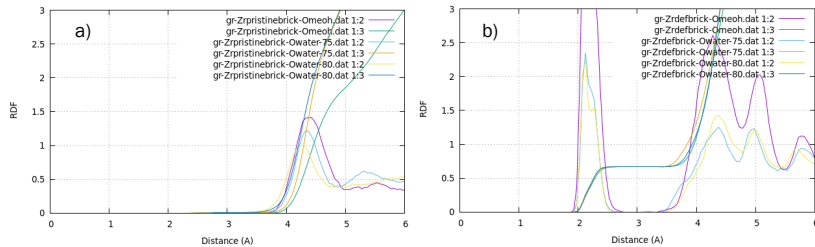
The integrated RDF in **Figure S7c** and **S7e** reaches some plateau of 1.5 water molecules after 3.5 Å. This non-integer number is due to the presence of the defective sites where there is a strong interaction with solvent molecules. Two of the eight  $\mu_3\text{-OH}$  oxygen atoms in the 2 bricks unit cell have therefore two additional water species adsorbed on these sites



**Figure S7** RDFs between brick atoms and solvent a)  $\mu_3\text{-O} - \text{Osolv}$ ; b)  $\mu_3\text{-O} - \text{Hsolv}$ ; c)  $\mu_3\text{-OH} - \text{Osolv}$ ; d)  $\mu_3\text{-O(H)} - \text{Osolv}$ ; e)  $\mu_3\text{-OH} - \text{Osolv}$  (for MeOH, Hsolv is only the one bonded to O)

### Zirconium-solvent

The first peak in **Figure S8** is very sharp and the integrated RDF reaches a plateau of 0.66, reflecting that only 4 of the 6 zirconium atoms in the brick are directly connected to a water species.



**Figure S8** RDFs between Zr atoms and solvent a) Zr(pristine brick) – Osolv; b ) Zr(defective brick) – Osolv

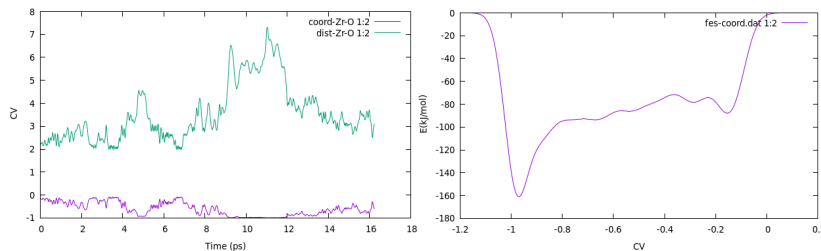
### Metadynamics

#### Alternative choice of collective variable

The choice of the collective variable (CV) is far from trivial, especially in such complex system. For this reason, we report some of the trials that we performed which were not successful in activating the processes in the material. In the following two MTDs, the CV is referred to a single solvent molecule. In these cases, when the water molecule leaves the active site, it is highly improbable that exactly the same molecule coordinates back, in such environment where other solvent molecules are present. What we observe is that when the water molecule leaves, another molecule takes its place on the active site, leading to a chemically equivalent configuration. We report two attempts in the choice of collective variable, which did not lead to reasonable results.

#### Coordination between Zr and O of one specific water molecule

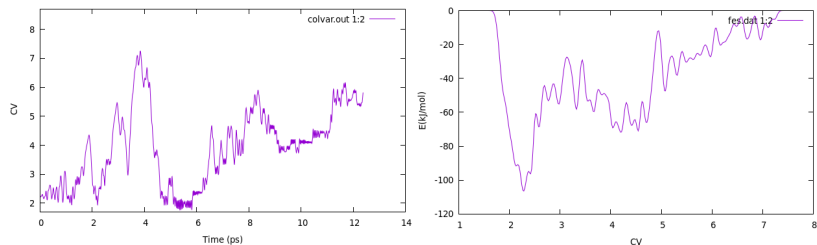
In this simulation, the CV is defined as coordination between Zr and the O atom of a fixed water molecule. The time evolution and the free energy profile are displayed in **Figure S9**.



**Figure S9** left: evolution of the Zr-O CN as collective variable during the simulation (purple curve). The Zr-O distance is also monitored (green curve); right: free energy profile in kJ/mol associated to the CN collective variable.

### Distance between Zr and O one specific water molecule

In this simulation, the CV is defined as distance between Zr and the O atom of a fixed water molecule. The time evolution and the free energy profile are displayed in **Figure S10**.



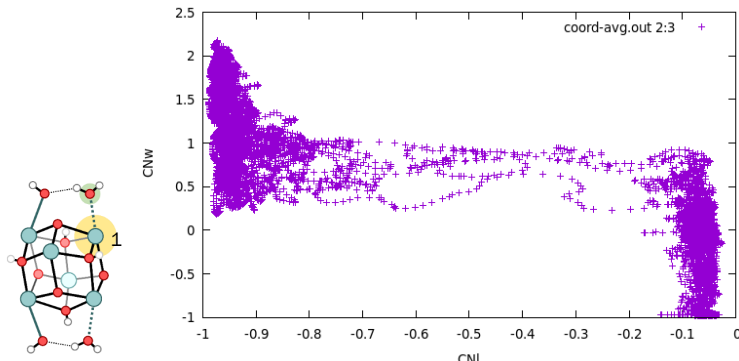
**Figure S10** left: evolution of the distance Zr-O as collective variable during the simulation; right: free energy profile in kJ/mol associated to the collective variable.

### Evolution of CV and relevant CN during simulations

In this section, we report the time evolution of relevant coordination numbers during the simulations.

#### Simulation 1: Coordination between Zr1 and water

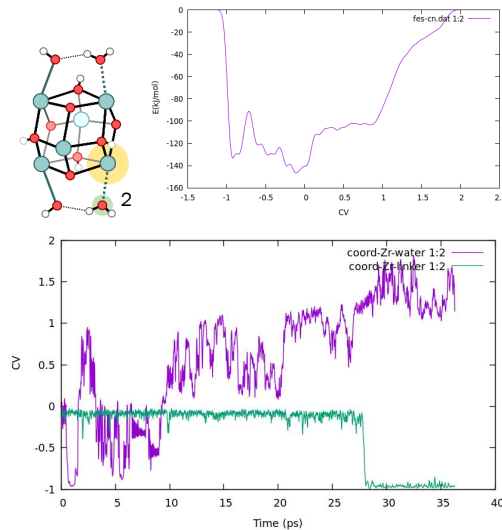
We report the time evolution of the two CNs of zirconium with water and linker during the first simulation where the  $CN_W$  is biased (**Figure S11**). At the beginning, the linker is bonded to the zirconium atom ( $CNI = 0$ ) and  $CN_W$  can go from values of +1 to -1. When the linker is decoordinated ( $CNI = -1$ ),  $CN_W$  goes from 0 to +2



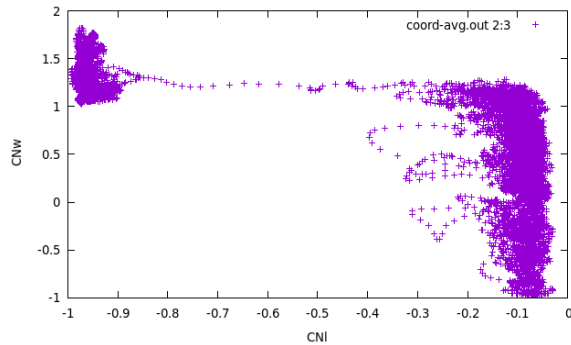
**Figure S11** Time evolution of the system along the two coordination numbers  $CN_W$  and  $CNI$  during the simulation where  $CN_W$  is biased.

### Simulation 1': Coordination between Zr2 and water

This simulation is performed on the zirconium atom on the opposite side of the brick. We observe similar configurations which are reported below (**Figure S12-13**).



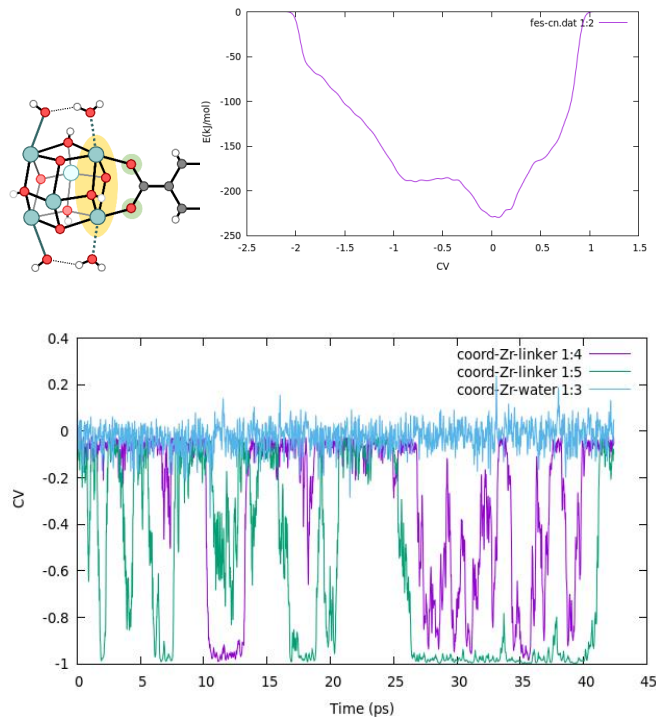
**Figure S12** above: free energy profile in kJ/mol associated to the collective variable  $CN_w$ . below: time evolution of  $CN_w$  and  $CN_L$  during the simulation



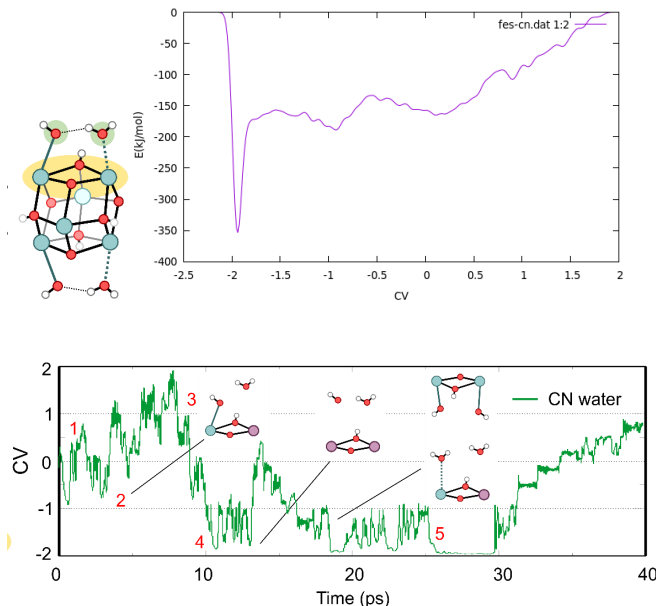
**Figure S13** Time evolution of the system along the two coordination numbers  $CN_w$  and  $CNI$  during the simulation.

### Simulation 2: Coordination between Zr and linker

In simulation 2 the  $CN_L$  between two zirconium atoms and the defect bridging linker is biased (**Figure S14**). The evolution of the  $CN_L$  of the two Zr-O bonds with the linker is monitored separately.



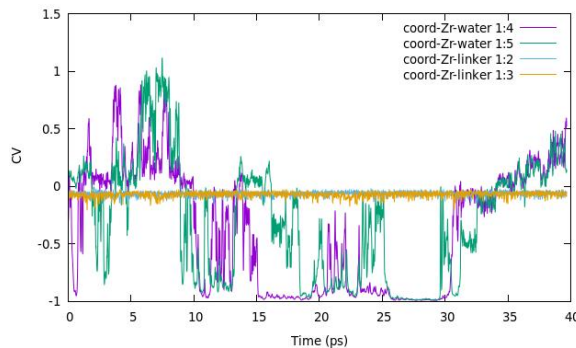
**Figure S14** above: free energy profile in kJ/mol associated to the collective variable of the simulation; below: time evolution of the  $CN_L$  of the two Zr-linker bonds separately (green, purple) and  $CN_w$  (cyan) during the simulation. The CV used in the simulation is the sum of the two  $CN_L$  of the two zirconium atoms, which here are reported separately.

**Simulation 3: Coordination between adjacent Zr atoms and two water molecules**


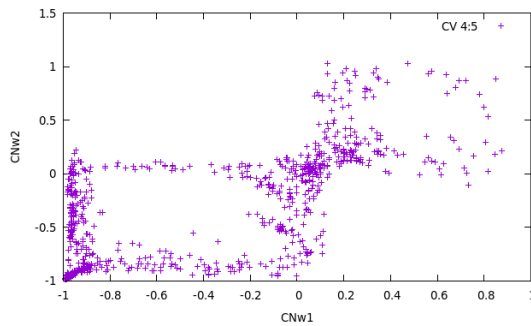
**Figure S15** above: free energy profile in  $\text{kJ/mol}$  associated to the collective variable of the simulation; below: time evolution of the CN of the two Zr-linker bonds

In this case study (**Figure S15**) we examine the evolution of the system when considering the global coordination number of the solvent water molecules with the two zirconium atoms of the defective site as collective variable. Again, we consider the collective variable as relative with respect to the equilibrium coordination number which is equal to 2 as visualized in figure. One of the zirconium atoms is coordinated with a hydroxyl group in the hydrated brick and the other with a water molecule. We start the MTD simulation from configuration 1. The system falls almost immediately after adding hills to the undercoordinated configuration 2. The next part of the simulation, after about 4 ps, is characterized by an overcoordination of the zirconium atom, which is now 9-fold coordinated, and by several concerted exchanges of water molecules on the active sites. The system can be biased even further to induce a decoordination of both  $\text{Zr-OH}_2$  and the adjacent  $\text{Zr-OH}$  creating two adjacent zirconium Lewis acid sites (configuration 4 ;  $\text{CV}=-2$ ). Both decoordination events are activated processes with a higher barrier for the second. This is in line with the stronger adsorption of the OH group to the zirconium atom which has also been shown by static calculations<sup>11-13</sup>. After about 18 ps, a proton is exchanged to the active site to the  $\text{Zr-OH}$  group, leading to a configuration with two physisorbed water molecules that are now more loosely coordinated to the active site, and can desorb more easily (configuration 5). After this exchange, the system resides at the undercoordinated regime for the remaining part of the simulation. Proton

exchanges occur at regular basis but we don't see a removal of the proton of the  $\mu_3\text{OH}$  group, as was observed in refs. <sup>11, 12</sup>. The separate evolution of the Zr-O coordination for the two zirconium atoms is reported in **Figure S16-S17**.



**Figure S16** Time evolution of the  $\text{CN}_{\text{w}}$  for the two zirconium atoms considered (green, purple) and the  $\text{CN}_{\text{L}}$  for the two Zr-linker bonds (yellow, cyan) during the simulation. The CV used in the simulation is the sum of the two  $\text{CN}_{\text{w}}$  of the two zirconium atoms, which here are reported separately.



**Figure S17** Evolution of the system along the coordination numbers  $\text{CN}_{\text{w}}$  for the two Zr atoms during the simulation.

## References

1. G. Kresse and J. Furthmuller, *Phys. Rev. B*, 1996, **54**, 11169-11186.
2. G. Kresse and J. Furthmuller, *Comp Mater Sci*, 1996, **6**, 15-50.
3. G. Kresse and J. Hafner, *Phys Rev B Condens Matter*, 1993, **47**, 558-561.
4. G. Kresse and J. Hafner, *Phys Rev B Condens Matter*, 1994, **49**, 14251-14269.
5. G. Kresse and D. Joubert, *Phys. Rev. B*, 1999, **59**, 1758-1775.
6. M. J. Frisch, G. W. Trucks, H. B. Schlegel, G. E. Scuseria, M. A. Robb, J. R. Cheeseman, G. Scalmani, V. Barone, G. A. Petersson, H. Nakatsuji, X. Li, M. Caricato, A. V. Marenich, J. Bloino, B. G. Janesko, R. Gomperts, B. Mennucci, H. P. Hratchian, J. V. Ortiz, A. F. Izmaylov, J. L. Sonnenberg, Williams, F. Ding, F. Lipparini, F. Egidi, J. Goings, B. Peng, A. Petrone, T. Henderson, D. Ranasinghe, V. G. Zakrzewski, J. Gao, N. Rega, G. Zheng, W. Liang, M. Hada, M. Ehara, K. Toyota, R. Fukuda, J. Hasegawa, M. Ishida, T. Nakajima, Y. Honda, O. Kitao, H. Nakai, T. Vreven, K. Throssell, J. A. Montgomery Jr., J. E. Peralta, F. Ogliaro, M. J. Bearpark, J. J. Heyd, E. N. Brothers, K. N. Kudin, V. N. Staroverov, T. A. Keith, R. Kobayashi, J. Normand, K. Raghavachari, A. P. Rendell, J. C. Burant, S. S. Iyengar, J. Tomasi, M. Cossi, J. M. Millam, M. Klene, C. Adamo, R. Cammi, J. W. Ochterski, R. L. Martin, K. Morokuma, O. Farkas, J. B. Foresman and D. J. Fox, *Journal*, 2016.
7. G. Schaftenaar and J. H. Noordik, *J Comput Aided Mol Des*, 2000, **14**, 123-134.
8. G. Schaftenaar, E. Vlieg and G. Vriend, *J Comput Aided Mol Des*, 2017, **31**, 789-800.
9. M. D. Hanwell, D. E. Curtis, D. C. Lonie, T. Vandermeersch, E. Zurek and G. R. Hutchison, *Journal of cheminformatics*, 2012, **4**, 17-17.
10. N. M. O'Boyle, M. Banck, C. A. James, C. Morley, T. Vandermeersch and G. R. Hutchison, *Journal of Cheminformatics*, 2011, **3**, 33.
11. S. L. Ling and B. Slater, *Chemical Science*, 2016, **7**, 4706-4712.
12. M. Vandichel, J. Hajek, A. Ghysels, A. De Vos, M. Waroquier and V. Van Speybroeck, *CrystEngComm*, 2016, **18**, 7056 - 7069.
13. C. Caratelli, J. Hajek, S. M. J. Rogge, S. Vandenbrande, E. J. Meijer, M. Waroquier and V. Van Speybroeck, *Chemphyschem*, 2018, **19**, 420-429.



## Publication List

Updated May 2019

### Publications in international peer-reviewed journals

1. M. Filez, C. Caratelli, M. Rivera-Torrente, F. Muniz-Miranda, M. Hoek, M. F.M. Altelaar, A. J.R. Heck, A.K Dutta Chowdhury, V. Van Speybroeck, B. M. Weckhuysen, *Molecular Nucleation Mechanism of Zeolitic Imidazolate Frameworks*, in preparation
2. J. Hajek, C. Caratelli, ... M. Waroquier, V. Van Speybroeck, *Investigating zirconium coordination changes in MOF-808 upon activation processes*, in preparation
3. C. Caratelli, J. Hajek, E.J. Meijer, M. Waroquier, V. Van Speybroeck, *Dynamic interplay between defective UiO-66 and protic solvents in activated processes*, Submitted
4. J. Marreiros, C. Caratelli, J. Hajek, A. Krajnc, G. Fleury, B. Bueken, D. De Vos, G. Mali, M. Roeffaers, V. Van Speybroeck, R. Ameloot, *Active*

*Role of Methanol in Post-Synthetic Linker Exchange in the Metal-Organic Framework UiO-66*, Chemistry of Materials, **31** (4), 1359–1369 (2019)  
 IF: 9.890

5. J. Hajek, C. Caratelli, R. Demuynck, K. De Wispelaere, L. Vanduyfhuys, M. Waroquier, V. Van Speybroeck, *On the intrinsic dynamic nature of the rigid UiO-66 metal-organic framework*, Chemical Science, **8**, 2723–2732 (2018)  
 IF: 8.688
6. C. Caratelli, J. Hajek, S.M.J. Rogge, S. Vandenbrande, E.J. Meijer, M. Waroquier, V. Van Speybroeck, *Influence of a confined methanol solvent on the reactivity of active sites in UiO-66*, ChemPhysChem, **19**, 420–4290 (2018)  
 IF: 3.075
7. C. Caratelli, J. Hajek, F. G. Cirujano, M. Waroquier, F. X. Llabrés i Xamena, V. Van Speybroeck, *Nature of active sites on UiO-66 and beneficial influence of water in the catalysis of Fischer esterification*, Journal of Catalysis, **352**, 401–414 (2017)  
 IF: 6.844

## Conference contributions

### Oral presentations

1. Dynamic interplay between solvent and material in UiO-66 at catalytic conditions  
C. Caratelli, J. Hajek, S. M.J. Rogge, M. Waroquier, V. Van Speybroeck  
 Europacat 2019, Aachen, Germany, 18-23 August 2019
2. Dynamic interplay between defective UiO-66 and confined solvent: insights into a reaction environment at operating conditions  
C. Caratelli, J. Hajek, S. M.J. Rogge, A. Lamaire, M. Waroquier, V. Van Speybroeck  
 XXth Netherlands' Catalysis and Chemistry Conference (NCCC XX), Noordwijkerhout, The Netherlands, Mar 4–6 2019
3. Modeling nanoporous materials at the nanoscale: the role of high performance computing in materials science  
C. Caratelli  
 HPC-UGent User Meeting, Ghent, Belgium, Jan 28 2019
4. Post synthetic linker exchange of UiO-66: understanding the role of solvent and defects by time resolved characterization  
J. Marreiros, C. Caratelli, J. Hajek, A. Krajnc, G. Fleury, B. Bueken, D. De Vos, V. Van Speybroeck, G. Mali, M. Roeffaers, R. Ameloot

IVth International Conference on Metal-Organic Frameworks and Open Framework Compounds (MOF 2018), Auckland, New Zealand, 9–13 December 2018

5. Investigating solvent effect in the acidity of UiO-66 metal organic framework for catalysis  
C. Caratelli, J. Hajek, A. Tiwari, S. M.J. Rogge, B. Ensing, M. Waroquier, E.J. Meijer, V. Van Speybroeck  
IVth International Conference on Metal-Organic Frameworks and Open Framework Compounds (MOF 2018), Auckland, New Zealand, 9–13 December 2018
6. Towards a molecular level understanding of chemical and physical phenomena in metal-organic frameworks  
J. Wieme, C. Caratelli, R. Demuynck, A. De Vos, J. Hajek, A. E. J. Hoffman, A. Lamaire, K. Lejaeghere, S. M.J. Rogge, S. Vandenbrande, L. Vanduyfhuys, M. Waroquier, V. Van Speybroeck  
Congrès français des MOFs, Paris, France, 16–18 May 2018
7. Influence of structural topology on the catalytic properties of Zr based MOFs: the case of UiO-66 and MOF-808  
J. Hajek, C. Caratelli, M. Waroquier, V. Van Speybroeck  
XIXth Netherlands' Catalysis and Chemistry Conference (NCCC XIX), Noordwijkerhout, The Netherlands, 5–7 March 2018
8. Influence of a confined methanol solvent on the reactivity of active sites on UiO-66  
C. Caratelli, J. Hajek, M. Waroquier, E.J. Meijer, V. Van Speybroeck  
2nd DEFNET School, Bochum, Germany, 18–21 September 2017
9. First principle study of active sites on UiO-66 for Fischer esterification  
C. Caratelli, J. Hajek, F. G. Cirujano, M. Waroquier, F.X. Llabrés i Xamena, V. Van Speybroeck  
Europacat 2017, Florence, Italy, 27–31 August 2017
10. First principle characterization of active sites on UiO-66 and their role in the catalysis of Fischer esterification  
C. Caratelli, J. Hajek, F. G. Cirujano, M. Waroquier, F. X. Llabrés i Xamena, V. Van Speybroeck  
XVIIIth Netherlands' Catalysis and Chemistry Conference (NCCC XVIII), Noordwijkerhout, The Netherlands, 6–8 March 2017
11. Nature of active sites on UiO-66 and UiO-66-NH<sub>2</sub> in the catalysis of Fischer esterification  
C. Caratelli, J. Hajek, G. Cirujano, A. Corma, M. Waroquier, F.X. Llabrés i Xamena, V. Van Speybroeck

Chemical Research in Flanders Symposium (CRF-1), Blankenberge, Belgium,  
24–26 October 2016

12. Mechanistic study of Fischer esterification on UiO-66 and UiO-66-NH<sub>2</sub>  
C. Caratelli, J. Hajek, F.G. Cirujano, A. Corma, M. Waroquier, F.X. Llabrés i Xamena, V. Van Speybroeck  
1st DEFNET School, Valencia, Spain, 21–24 June 2016

## Poster presentations

1. How the connectivity of stable Zr-based MOFs affects the metal coordination and the nature of the active sites  
J. Hajek, C. Caratelli, M. Waroquier, V. Van Speybroeck  
MOFSIM 2019, Ghent, Belgium, Apr 10–12 2019
2. Dynamic creation of active sites on UiO-66 by interaction with protic solvents  
C. Caratelli, J. Hajek, S. M.J. Rogge, M. Waroquier, B. Ensing, E.J. Meijer, V. Van Speybroeck  
MOFSIM 2019, Ghent, Belgium, Apr 10–12 2019
3. Dynamic creation of active sites on UiO-66 by interaction with protic solvents  
C. Caratelli, J. Hajek, S. M.J. Rogge, M. Waroquier, B. Ensing, E.J. Meijer, V. Van Speybroeck  
1st KNCV-CTC symposium, Amsterdam, The Netherlands, Mar 26 2019
4. How the connectivity of stable Zr-based MOFs affects the metal coordination and the nature of the active sites  
J. Hajek, C. Caratelli, M. Waroquier, V. Van Speybroeck  
XXth Netherlands' Catalysis and Chemistry Conference (NCCC XX), Noordwijkerhout, The Netherlands, Mar 4–6 2019
5. Exploring the intrinsic dynamics of rigid Zr-based MOFs  
J. Hajek, C. Caratelli, R. Demuynck, K. De Wispelaere, L. Vanduyfhuys, M. Waroquier, V. Van Speybroeck  
IVth International Conference on Metal-Organic Frameworks and Open Framework Compounds (MOF 2018), Auckland, New Zealand, 9–13 December 2018
6. Modeling reactive processes in nanoporous materials: a look into the complexity  
C. Caratelli, K. De Wispelaere, J. Hajek, P. Cnudde, S. M.J. Rogge, S. Vandenbrande, R. Demuynck, L. Vanduyfhuys, M. Waroquier, V. Van Speybroeck  
Ghent, Belgium, Jun 1 2018
7. Investigating the outstanding dynamic behavior of protons on UiO-66 defective sites

C. Caratelli, J. Hajek, A. Tiwari, M. Waroquier, B. Ensing, E. Jan Meijer, V. Van Speybroeck

EuroMOF 2017, Delft, The Netherlands, Oct 29 -- Nov 1 2017

8. Post synthetic linker exchange of UiO-66: understanding the role of solvent and defects by time resolved characterization

J. Marreiros, C. Caratelli, J. Hajek, A. Krajnc, G. Fleury, V. Van Speybroeck, G. Mali, M. Roeffaers, R. Ameloot

EuroMOF 2017, Delft, The Netherlands, Oct 29 -- Nov 1 2017

9. Influence of a confined methanol solvent on the reactivity of active sites in UiO-66

C. Caratelli, J. Hajek, S. M.J. Rogge, S. Vandenbrande, E.J. Meijer, M. Waroquier, V. Van Speybroeck

XIXth Netherlands' Catalysis and Chemistry Conference (NCCC XIX), Nordanwijkerhout, The Netherlands, Mar 5–7 2018

10. Catalytic sites on UiO-66 for Fischer esterification

C. Caratelli, J. Hajek, G. Cirujano, A. Corma, M. Waroquier, F.X. Llabrés i Xamena, V. Van Speybroeck

MOLSIM 2017: Understanding Molecular Simulations, Amsterdam, The Netherlands, Jan 9–20 2017

11. Catalytic sites on UiO-66 for Fischer esterification

C. Caratelli, J. Hajek, G. Cirujano, A. Corma, M. Waroquier, F.X. Llabrés i Xamena, V. Van Speybroeck

Annual IAP Meeting IAP-PAI P7/05, Liège, Belgium, 12 October 2016

12. Catalytic role of UiO-66 and UiO-66-NH<sub>2</sub> in Fischer esterification: a mechanistic study

C. Caratelli, J. Hajek, G. Cirujano, A. Corma, M. Waroquier, F.X. Llabrés i Xamena, V. Van Speybroeck

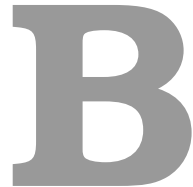
3rd DEFNET workshop, Ghent, Belgium, 22–24 March 2016

13. Catalytic role of UiO-66 and UiO-66-NH<sub>2</sub> in Fischer esterification: a mechanistic study

C. Caratelli, J. Hajek, G. Cirujano, A. Corma, M. Waroquier, F.X. Llabrés i Xamena, V. Van Speybroeck

XVIIth Netherlands' Catalysis and Chemistry Conference (NCCC XVII), Nordanwijkerhout, The Netherlands, 7–9 March 2016





## Granted computational Projects

### **Granted computational projects under the Vlaams Super Computing Centrum infrastructure**

1. Operando study of post synthetic structural modifications in UiO-66  
Mar 2019 - Nov 2019  
4176 node days (Breniac)
2. Active sites on MOF-808 for industrially relevant MPV reduction  
Nov 2018 - Jul 2019  
4236 node days (Breniac)
3. Intrinsic dynamics of rigid Zr-based metal organic frameworks  
Jul 2018 - Mar 2019  
2766 node days (Breniac)
4. Investigating solvent effect in the acidity of UiO-66 metal organic framework for catalysis  
Jul 2018 - Mar 2019  
4764 node days (Breniac)
5. Probing the strength of basic sites on UiO-66 using pKa calculations  
Jul 2017 - Jan 2017  
4450 node days (Breniac)

6. *Ab initio* umbrella sampling simulations of dehydration of UiO-66  
Nov 2016 - Apr 2017  
3972 node days (Breniac)
7. Pilot Tier 1 project  
Jul 2016  
1000 node days (Breniac)
8. Investigating active sites in hydroxylated and dehydroxylated UiO-66 for  
catalysis of Oppenauer-type oxidation  
Feb 2016 - Oct 2016  
2110 node days (Muk)

A large, bold, gray letter 'C' with a thick, rounded font style.

## Acknowledgement

This project has received funding from the European Union's Horizon 2020 research and innovation program under the Marie Skłodowska-Curie (grant agreement No 641887, acronym: DEFNET). The authors further acknowledge financial support from the European Research Council (consolidator ERC Grant Agreement No 647755 – DYNPOR (2015–2020)) and the Research Board of Ghent University (BOF).

The computational resources and services used in this work were provided by the VSC (Flemish Supercomputer Center), funded by the Hercules foundation and the Flemish Government – department EWI.



**European Research Council**

Established by the European Commission



# Bibliography

- [1] I. Atadashi, M. Aroua, and A. A. Aziz, "Biodiesel separation and purification: a review," *Renewable Energy*, vol. 36, no. 2, pp. 437–443, 2011.
- [2] A. S. Chouhan and A. Sarma, "Modern heterogeneous catalysts for biodiesel production: A comprehensive review," *Renewable and Sustainable Energy Reviews*, vol. 15, no. 9, pp. 4378–4399, 2011.
- [3] A. D. McNaught and A. D. McNaught, *Compendium of chemical terminology*, vol. 1669. Blackwell Science Oxford, 1997.
- [4] O. K. Farha, I. Eryazici, N. C. Jeong, B. G. Hauser, C. E. Wilmer, A. A. Sarjeant, R. Q. Snurr, S. T. Nguyen, A. z. Yazaydin, and J. T. Hupp, "Metal–organic framework materials with ultrahigh surface areas: Is the sky the limit?," *Journal of the American Chemical Society*, vol. 134, no. 36, pp. 15016–15021, 2012. PMID: 22906112.
- [5] I. M. Hönicke, I. Senkovska, V. Bon, I. A. Baburin, N. Bönisch, S. Raschke, J. D. Evans, and S. Kaskel, "Balancing mechanical stability and ultrahigh porosity in crystalline framework materials," *Angewandte Chemie International Edition*, vol. 57, no. 42, pp. 13780–13783, 2018.
- [6] J. Liang, Z. Liang, R. Zou, and Y. Zhao, "Heterogeneous catalysis in zeolites, mesoporous silica, and metal–organic frameworks," *Advanced Materials*, vol. 29, no. 30, p. 1701139, 2017.
- [7] V. Van Speybroeck, K. Hemelsoet, L. Joos, M. Waroquier, R. G. Bell, and C. R. A. Catlow, "Advances in theory and their application within the field of zeolite chemistry," *Chemical Society Reviews*, vol. 44, no. 20, pp. 7044–7111, 2015.
- [8] S. R. Batten, B. F. Hoskins, and R. Robson, "Two interpenetrating 3d networks which generate spacious sealed-off compartments enclosing of the order of 20 solvent molecules in the structures of  $\text{zn}(\text{cn})(\text{no}_3)(\text{tpt})\frac{2}{3}\cdot\text{cntdot}\cdot\text{solv}$  ( $\text{tpt}=2, 4, 6$ -tri (4-pyridyl)-1, 3, 5-triazine,  $\text{solv}=$  apprx.  $3/4\text{c}2\text{h}2\text{cl}4$ .  $\text{cntdot}$ .  $3/4\text{ch}3\text{oh}$  or. apprx.  $3/2\text{chcl}3$ .  $\text{cntdot}$ .  $1/3\text{ch}3\text{oh}$ ) $,$ " *Journal of the American Chemical Society*, vol. 117, no. 19, pp. 5385–5386, 1995.

- [9] B. Hoskins and R. Robson, "Design and construction of a new class of scaffolding-like materials comprising infinite polymeric frameworks of 3d-linked molecular rods. a reappraisal of the zinc cyanide and cadmium cyanide structures and the synthesis and structure of the diamond-related frameworks [n (ch3) 4][cuiznii (cn) 4] and cui [4, 4', 4'', 4'''-tetracyanotetraphenylmethane] bf4. xc6h5no2," *Journal of the American Chemical Society*, vol. 112, no. 4, pp. 1546–1554, 1990.
- [10] S. Kitagawa, S. Matsuyama, M. Munakata, and T. Emori, "Synthesis and crystal structures of novel one-dimensional polymers,[{M (bpen) X} $\infty$ ][[m= cu i, x= pf 6–; m= ag i, x= clo 4–; bpen= trans-1, 2-bis (2-pyridyl) ethylene] and [{Cu (bpen)(CO)(CH 3 CN)(PF 6)} $\infty$ ]," *Journal of the Chemical Society, Dalton Transactions*, no. 11, pp. 2869–2874, 1991.
- [11] S. Kitagawa, S. Kawata, Y. Nozaka, and M. Munakata, "Synthesis and crystal structures of novel copper (i) co-ordination polymers and a hexacopper (i) cluster of quinoline-2-thione," *Journal of the Chemical Society, Dalton Transactions*, no. 9, pp. 1399–1404, 1993.
- [12] O. Yaghi and H. Li, "Hydrothermal synthesis of a metal-organic framework containing large rectangular channels," *Journal of the American Chemical Society*, vol. 117, no. 41, pp. 10401–10402, 1995.
- [13] D. Riou and G. Férey, "Hybrid open frameworks (mil-n). part 3 crystal structures of the ht and lt forms of mil-7: a new vanadium propylenediphosphonate with an open-framework. influence of the synthesis temperature on the oxidation state of vanadium within the same structural type," *Journal of Materials Chemistry*, vol. 8, no. 12, pp. 2733–2735, 1998.
- [14] H. Furukawa, K. E. Cordova, M. O'Keeffe, and O. M. Yaghi, "The chemistry and applications of metal-organic frameworks," *Science*, vol. 341, no. 6149, p. 1230444, 2013.
- [15] N. Stock and S. Biswas, "Synthesis of metal-organic frameworks (mofs): routes to various mof topologies, morphologies, and composites," *Chemical reviews*, vol. 112, no. 2, pp. 933–969, 2011.
- [16] H.-C. Zhou and S. Kitagawa, "Metal-organic frameworks (mofs).," 2014.
- [17] H.-C. Zhou, J. R. Long, and O. M. Yaghi, "Introduction to metal-organic frameworks," 2012.
- [18] M. Eddaoudi, J. Kim, N. Rosi, D. Vodak, J. Wachter, M. O'keeffe, and O. M. Yaghi, "Systematic design of pore size and functionality in isoreticular mofs and their application in methane storage," *Science*, vol. 295, no. 5554, pp. 469–472, 2002.

- [19] S. Kitagawa and M. Kondo, "Functional micropore chemistry of crystalline metal complex-assembled compounds," *Bulletin of the Chemical Society of Japan*, vol. 71, no. 8, pp. 1739–1753, 1998.
- [20] R. Matsuda, R. Kitaura, S. Kitagawa, Y. Kubota, T. C. Kobayashi, S. Horike, and M. Takata, "Guest shape-responsive fitting of porous coordination polymer with shrinkable framework," *Journal of the American Chemical Society*, vol. 126, no. 43, pp. 14063–14070, 2004.
- [21] F.-X. Coudert, "Responsive metal–organic frameworks and framework materials: under pressure, taking the heat, in the spotlight, with friends," *Chemistry of Materials*, vol. 27, no. 6, pp. 1905–1916, 2015.
- [22] D. S. Sholl and R. P. Lively, "Defects in metal–organic frameworks: Challenge or opportunity?," *The Journal of Physical Chemistry Letters*, vol. 6, no. 17, pp. 3437–3444, 2015. PMID: 26268796.
- [23] Z. Fang, B. Bueken, D. E. De Vos, and R. A. Fischer, "Defect-engineered metal–organic frameworks," *Angewandte Chemie International Edition*, vol. 54, no. 25, pp. 7234–7254, 2015.
- [24] M. J. Cliffe, W. Wan, X. Zou, P. A. Chater, A. K. Kleppe, M. G. Tucker, H. Wilhelm, N. P. Funnell, F.-X. Coudert, and A. L. Goodwin, "Correlated defect nanoregions in a metal–organic framework," *Nature communications*, vol. 5, p. 4176, 2014.
- [25] D. Yang and B. C. Gates, "Catalysis by metal organic frameworks: Perspective and suggestions for future research," *ACS Catalysis*, vol. 9, no. 3, pp. 1779–1798, 2019.
- [26] S. M. Rogge, A. Bavykina, J. Hajek, H. Garcia, A. I. Olivos-Suarez, A. Sepúlveda-Escribano, A. Vimont, G. Clet, P. Bazin, F. Kapteijn, *et al.*, "Metal–organic and covalent organic frameworks as single-site catalysts," *Chemical Society Reviews*, vol. 46, no. 11, pp. 3134–3184, 2017.
- [27] S. S.-Y. Chui, S. M.-F. Lo, J. P. Charmant, A. G. Orpen, and I. D. Williams, "A chemically functionalizable nanoporous material [cu3 (tma) 2 (h2o) 3] n," *Science*, vol. 283, no. 5405, pp. 1148–1150, 1999.
- [28] M. Vandichel, J. Hajek, F. Vermoortele, M. Waroquier, D. E. De Vos, and V. Van Speybroeck, "Active site engineering in uiO-66 type metal–organic frameworks by intentional creation of defects: a theoretical rationalization," *CrystEngComm*, vol. 17, no. 2, pp. 395–406, 2015.
- [29] Z. Wang and S. M. Cohen, "Postsynthetic modification of metal–organic frameworks," *Chem. Soc. Rev.*, vol. 38, pp. 1315–1329, 2009.
- [30] S. M. Cohen, "Postsynthetic methods for the functionalization of metal–organic frameworks," *Chemical reviews*, vol. 112, no. 2, pp. 970–1000, 2011.

- [31] Y. Z. Baiyan Li, Matthew Chrzanowski and S. Ma, "Applications of metal-organic frameworks featuring multi-functional sites," *Coordination Chemistry Reviews*, vol. 307, pp. 106 – 129, 2016. Chemistry and Applications of Metal Organic Frameworks.
- [32] S. J. Garibay and S. M. Cohen, "Isoreticular synthesis and modification of frameworks with the uio-66 topology," *Chemical communications*, vol. 46, no. 41, pp. 7700–7702, 2010.
- [33] A. J. Howarth, Y. Liu, P. Li, Z. Li, T. C. Wang, J. T. Hupp, and O. K. Farha, "Chemical, thermal and mechanical stabilities of metal–organic frameworks," *Nature Reviews Materials*, vol. 1, no. 3, p. 15018, 2016.
- [34] K. W. Chapman, G. J. Halder, and P. J. Chupas, "Pressure-induced amorphization and porosity modification in a metal- organic framework," *Journal of the American Chemical Society*, vol. 131, no. 48, pp. 17546–17547, 2009.
- [35] P. Horcajada, T. Chalati, C. Serre, B. Gillet, C. Sebrie, T. Baati, J. F. Eubank, D. Heurtaux, P. Clayette, C. Kreuz, *et al.*, "Porous metal–organic-framework nanoscale carriers as a potential platform for drug delivery and imaging," *Nature materials*, vol. 9, no. 2, p. 172, 2010.
- [36] S. Keskin, T. M. van Heest, and D. S. Sholl, "Can metal–organic framework materials play a useful role in large-scale carbon dioxide separations?," *ChemSusChem*, vol. 3, no. 8, pp. 879–891, 2010.
- [37] J. Canivet, A. Fateeva, Y. Guo, B. Coasne, and D. Farrusseng, "Water adsorption in mofs: fundamentals and applications," *Chemical Society Reviews*, vol. 43, no. 16, pp. 5594–5617, 2014.
- [38] A. C. Kizzie, A. G. Wong-Foy, and A. J. Matzger, "Effect of humidity on the performance of microporous coordination polymers as adsorbents for co<sub>2</sub> capture," *Langmuir*, vol. 27, no. 10, pp. 6368–6373, 2011.
- [39] J. A. Greathouse and M. D. Allendorf, "The interaction of water with mof-5 simulated by molecular dynamics," *Journal of the American Chemical Society*, vol. 128, no. 33, pp. 10678–10679, 2006.
- [40] J. J. Low, A. I. Benin, P. Jakubczak, J. F. Abrahamian, S. A. Faheem, and R. R. Willis, "Virtual high throughput screening confirmed experimentally: porous coordination polymer hydration," *Journal of the American Chemical Society*, vol. 131, no. 43, pp. 15834–15842, 2009.
- [41] S. S. Kaye, A. Dailly, O. M. Yaghi, and J. R. Long, "Impact of preparation and handling on the hydrogen storage properties of zn4o (1, 4-benzenedicarboxylate) 3 (mof-5)," *Journal of the American Chemical Society*, vol. 129, no. 46, pp. 14176–14177, 2007.

- [42] J. B. DeCoste, G. W. Peterson, B. J. Schindler, K. L. Killops, M. A. Browe, and J. J. Mahle, "The effect of water adsorption on the structure of the carboxylate containing metal–organic frameworks cu-btc, mg-mof-74, and uio-66," *Journal of Materials Chemistry A*, vol. 1, no. 38, pp. 11922–11932, 2013.
- [43] K. Leus, T. Bogaerts, J. De Decker, H. Depauw, K. Hendrickx, H. Vrielinck, V. Van Speybroeck, and P. Van Der Voort, "Systematic study of the chemical and hydrothermal stability of selected “stable” metal organic frameworks," *Microporous and Mesoporous Materials*, vol. 226, pp. 110–116, 2016.
- [44] H. Furukawa, F. Gándara, Y.-B. Zhang, J. Jiang, W. L. Queen, M. R. Hudson, and O. M. Yaghi, "Water adsorption in porous metal–organic frameworks and related materials," *Journal of the American Chemical Society*, vol. 136, no. 11, pp. 4369–4381, 2014.
- [45] Y. Bai, Y. Dou, L.-H. Xie, W. Rutledge, J.-R. Li, and H.-C. Zhou, "Zr-based metal–organic frameworks: design, synthesis, structure, and applications," *Chemical Society Reviews*, vol. 45, no. 8, pp. 2327–2367, 2016.
- [46] J. H. Cavka, S. Jakobsen, U. Olsbye, N. Guillou, C. Lamberti, S. Bordiga, and K. P. Lillerud, "A new zirconium inorganic building brick forming metal organic frameworks with exceptional stability," *Journal of the American Chemical Society*, vol. 130, no. 42, pp. 13850–13851, 2008.
- [47] J. E. Mondloch, W. Bury, D. Fairén-Jimenez, S. Kwon, E. J. DeMarco, M. H. Weston, A. A. Sarjeant, S. T. Nguyen, P. C. Stair, R. Q. Snurr, *et al.*, "Vapor-phase metalation by atomic layer deposition in a metal–organic framework," *Journal of the American Chemical Society*, vol. 135, no. 28, pp. 10294–10297, 2013.
- [48] L. Valenzano, B. Civalleri, S. Chavan, S. Bordiga, M. H. Nilsen, S. Jakobsen, K. P. Lillerud, and C. Lamberti, "Disclosing the complex structure of uio-66 metal organic framework: a synergic combination of experiment and theory," *Chemistry of Materials*, vol. 23, no. 7, pp. 1700–1718, 2011.
- [49] G. Wißmann, A. Schaate, S. Lilienthal, I. Bremer, A. M. Schneider, and P. Behrens, "Modulated synthesis of zr-fumarate mof," *Microporous and Mesoporous Materials*, vol. 152, pp. 64–70, 2012.
- [50] A. Schaate, P. Roy, A. Godt, J. Lippke, F. Waltz, M. Wiebcke, and P. Behrens, "Modulated synthesis of zr-based metal–organic frameworks: from nano to single crystals," *Chemistry—A European Journal*, vol. 17, no. 24, pp. 6643–6651, 2011.
- [51] A. Schaate, P. Roy, T. Preuß, S. J. Lohmeier, A. Godt, and P. Behrens, "Porous interpenetrated zirconium–organic frameworks (pizofs): A chemi-

- cally versatile family of metal–organic frameworks,” *Chemistry—A European Journal*, vol. 17, no. 34, pp. 9320–9325, 2011.
- [52] M. Kim, J. F. Cahill, H. Fei, K. A. Prather, and S. M. Cohen, “Postsynthetic ligand and cation exchange in robust metal–organic frameworks,” *Journal of the American Chemical Society*, vol. 134, no. 43, pp. 18082–18088, 2012.
- [53] G. C. Shearer, S. Chavan, J. Ethiraj, J. G. Vitillo, S. Svelle, U. Olsbye, C. Lamberti, S. Bordiga, and K. P. Lillerud, “Tuned to perfection: Ironing out the defects in metal–organic framework uio-66,” *Chemistry of Materials*, vol. 26, no. 14, pp. 4068–4071, 2014.
- [54] H. Wu, Y. S. Chua, V. Krungleviciute, M. Tyagi, P. Chen, T. Yildirim, and W. Zhou, “Unusual and highly tunable missing-linker defects in zirconium metal–organic framework uio-66 and their important effects on gas adsorption,” *Journal of the American Chemical Society*, vol. 135, no. 28, pp. 10525–10532, 2013.
- [55] G. C. Shearer, S. Chavan, S. Bordiga, S. Svelle, U. Olsbye, and K. P. Lillerud, “Defect engineering: tuning the porosity and composition of the metal–organic framework uio-66 via modulated synthesis,” *Chemistry of Materials*, vol. 28, no. 11, pp. 3749–3761, 2016.
- [56] J. Ren, H. W. Langmi, B. C. North, M. Mathe, and D. Bessarabov, “Modulated synthesis of zirconium-metal organic framework (zr-mof) for hydrogen storage applications,” *international journal of hydrogen energy*, vol. 39, no. 2, pp. 890–895, 2014.
- [57] I. Stassen, B. Bueken, H. Reinsch, J. Oudenhoven, D. Wouters, J. Hajek, V. Van Speybroeck, N. Stock, P. Vereecken, R. Van Schaijk, et al., “Towards metal–organic framework based field effect chemical sensors: Uio-66-nh 2 for nerve agent detection,” *Chemical science*, vol. 7, no. 9, pp. 5827–5832, 2016.
- [58] D. Cunha, M. Ben Yahia, S. Hall, S. R. Miller, H. Chevreau, E. Elkaïm, G. Maurin, P. Horcajada, and C. Serre, “Rationale of drug encapsulation and release from biocompatible porous metal–organic frameworks,” *Chemistry of Materials*, vol. 25, no. 14, pp. 2767–2776, 2013.
- [59] F. Vermoortele, B. Bueken, G. Le Bars, B. Van de Voorde, M. Vandichel, K. Houthoofd, A. Vimont, M. Daturi, M. Waroquier, V. Van Speybroeck, et al., “Synthesis modulation as a tool to increase the catalytic activity of metal–organic frameworks: the unique case of uio-66 (zr),” *Journal of the American Chemical Society*, vol. 135, no. 31, pp. 11465–11468, 2013.
- [60] S. M. J. Rogge, J. Wieme, L. Vanduyfhuys, S. Vandenbrande, G. Maurin, T. Verstraelen, M. Waroquier, and V. Van Speybroeck, “Thermodynamic insight in the high-pressure behavior of uio-66: Effect of linker defects and

- linker expansion," *Chemistry of Materials*, vol. 28, no. 16, pp. 5721–5732, 2016. PMID: 27594765.
- [61] A. De Vos, K. Hendrickx, P. Van Der Voort, V. Van Speybroeck, and K. Lejaeghere, "Missing linkers: an alternative pathway to uio-66 electronic structure engineering," *Chemistry of Materials*, vol. 29, no. 7, pp. 3006–3019, 2017.
- [62] D. D. Borges, S. Devautour-Vinot, H. Jobic, J. Ollivier, F. Nouar, R. Semino, T. Devic, C. Serre, F. Paesani, and G. Maurin, "Proton transport in a highly conductive porous zirconium-based metal–organic framework: Molecular insight," *Angewandte Chemie International Edition*, vol. 55, no. 12, pp. 3919–3924, 2016.
- [63] K. L. Svane, J. K. Bristow, J. D. Gale, and A. Walsh, "Vacancy defect configurations in the metal–organic framework uio-66: energetics and electronic structure," *Journal of Materials Chemistry A*, vol. 6, no. 18, pp. 8507–8513, 2018.
- [64] Y. Liu, R. C. Klet, J. T. Hupp, and O. Farha, "Probing the correlations between the defects in metal–organic frameworks and their catalytic activity by an epoxide ring-opening reaction," *Chemical Communications*, vol. 52, no. 50, pp. 7806–7809, 2016.
- [65] F. Vermoortele, M. Vandichel, B. Van de Voorde, R. Ameloot, M. Waroquier, V. Van Speybroeck, and D. E. De Vos, "Electronic effects of linker substitution on lewis acid catalysis with metal–organic frameworks," *Angewandte Chemie International Edition*, vol. 51, no. 20, pp. 4887–4890, 2012.
- [66] S. Øien, D. Wragg, H. Reinsch, S. Svelle, S. Bordiga, C. Lamberti, and K. P. Lillerud, "Detailed structure analysis of atomic positions and defects in zirconium metal–organic frameworks," *Crystal Growth & Design*, vol. 14, no. 11, pp. 5370–5372, 2014.
- [67] C. A. Trickett, K. J. Gagnon, S. Lee, F. Gándara, H.-B. Bürgi, and O. M. Yaghi, "Definitive molecular level characterization of defects in uio-66 crystals," *Angewandte Chemie International Edition*, vol. 54, no. 38, pp. 11162–11167, 2015.
- [68] S. Ling and B. Slater, "Dynamic acidity in defective uio-66," *Chemical science*, vol. 7, no. 7, pp. 4706–4712, 2016.
- [69] M. Vandichel, J. Hajek, A. Ghysels, A. De Vos, M. Waroquier, and V. Van Speybroeck, "Water coordination and dehydration processes in defective uio-66 type metal organic frameworks," *CrystEngComm*, vol. 18, no. 37, pp. 7056–7069, 2016.

- [70] J. M. Taylor, S. Dekura, R. Ikeda, and H. Kitagawa, "Defect control to enhance proton conductivity in a metal–organic framework," *Chemistry of Materials*, vol. 27, no. 7, pp. 2286–2289, 2015.
- [71] R. C. Klet, Y. Liu, T. C. Wang, J. T. Hupp, and O. K. Farha, "Evaluation of brønsted acidity and proton topology in zr-and hf-based metal–organic frameworks using potentiometric acid–base titration," *Journal of Materials Chemistry A*, vol. 4, no. 4, pp. 1479–1485, 2016.
- [72] D. Yang, V. Bernales, T. Islamoglu, O. K. Farha, J. T. Hupp, C. J. Cramer, L. Gagliardi, and B. C. Gates, "Tuning the surface chemistry of metal organic framework nodes: proton topology of the metal-oxide-like zr<sub>6</sub> nodes of uio-66 and nu-1000," *Journal of the American Chemical Society*, vol. 138, no. 46, pp. 15189–15196, 2016.
- [73] J. B. DeCoste, G. W. Peterson, H. Jasuja, T. G. Glover, Y.-g. Huang, and K. S. Walton, "Stability and degradation mechanisms of metal–organic frameworks containing the zr 6 o 4 (oh) 4 secondary building unit," *Journal of Materials Chemistry A*, vol. 1, no. 18, pp. 5642–5650, 2013.
- [74] M. Kandiah, M. H. Nilsen, S. Usseglio, S. Jakobsen, U. Olsbye, M. Tilset, C. Larabi, E. A. Quadrelli, F. Bonino, and K. P. Lillerud, "Synthesis and stability of tagged uio-66 zr-mofs," *Chemistry of Materials*, vol. 22, no. 24, pp. 6632–6640, 2010.
- [75] M. Kandiah, S. Usseglio, S. Svelle, U. Olsbye, K. P. Lillerud, and M. Tilset, "Post-synthetic modification of the metal–organic framework compound uio-66," *Journal of Materials Chemistry*, vol. 20, no. 44, pp. 9848–9851, 2010.
- [76] M. Kim and S. M. Cohen, "Discovery, development, and functionalization of zr (iv)-based metal–organic frameworks," *CrystEngComm*, vol. 14, no. 12, pp. 4096–4104, 2012.
- [77] F. Vermoortele, R. Ameloot, A. Vimont, C. Serre, and D. De Vos, "An amino-modified zr-terephthalate metal–organic framework as an acid–base catalyst for cross-alcohol condensation," *Chemical communications*, vol. 47, no. 5, pp. 1521–1523, 2011.
- [78] M. N. Timofeeva, V. N. Panchenko, J. W. Jun, Z. Hasan, M. M. Matrosova, and S. H. Jhung, "Effects of linker substitution on catalytic properties of porous zirconium terephthalate uio-66 in acetalization of benzaldehyde with methanol," *Applied Catalysis A: General*, vol. 471, pp. 91–97, 2014.
- [79] F. Cirujano, A. Corma, and F. L. i Xamena, "Zirconium-containing metal organic frameworks as solid acid catalysts for the esterification of free fatty acids: Synthesis of biodiesel and other compounds of interest," *Catalysis Today*, vol. 257, pp. 213–220, 2015.

- [80] F. Cirujano, A. Corma, and F. L. i Xamena, "Conversion of levulinic acid into chemicals: Synthesis of biomass derived levulinate esters over zr-containing mofs," *Chemical Engineering Science*, vol. 124, pp. 52–60, 2015.
- [81] J. Hajek, M. Vandichel, B. Van de Voorde, B. Bueken, D. De Vos, M. Waroquier, and V. Van Speybroeck, "Mechanistic studies of aldol condensations in uiO-66 and uiO-66-nh2 metal organic frameworks," *Journal of catalysis*, vol. 331, pp. 1–12, 2015.
- [82] E. Plessers, G. Fu, C. Tan, D. De Vos, and M. Roeffaers, "Zr-based mof-808 as meerwein–ponndorf–verley reduction catalyst for challenging carbonyl compounds," *Catalysts*, vol. 6, no. 7, p. 104, 2016.
- [83] H.-H. Mautschke, F. Drache, I. Senkovska, S. Kaskel, and F. L. i Xamena, "Catalytic properties of pristine and defect-engineered zr-mof-808 metal organic frameworks," *Catalysis Science & Technology*, vol. 8, no. 14, pp. 3610–3616, 2018.
- [84] J. Jiang, F. Gándara, Y.-B. Zhang, K. Na, O. M. Yaghi, and W. G. Klemperer, "Superacidity in sulfated metal–organic framework-808," *Journal of the American Chemical Society*, vol. 136, no. 37, pp. 12844–12847, 2014.
- [85] M. Frisch, G. Trucks, H. Schlegel, G. Scuseria, M. Robb, J. Cheeseman, G. Scalmani, V. Barone, B. Mennucci, G. Petersson, *et al.*, "Gaussian 09, revision a. 02; gaussian, inc: Wallingford, ct, 2009," *There is no corresponding record for this reference*, 2015.
- [86] C. Caratelli, J. Hajek, F. G. Cirujano, M. Waroquier, F. X. L. i Xamena, and V. Van Speybroeck, "Nature of active sites on uiO-66 and beneficial influence of water in the catalysis of fischer esterification," *Journal of catalysis*, vol. 352, pp. 401–414, 2017.
- [87] K. D. Wispelaere, L. Vanduyfhuys, and V. V. Speybroeck, "Chapter 6 - entropy contributions to transition state modeling," in *Modelling and Simulation in the Science of Micro- and Meso-Porous Materials* (C. R. A. Catlow, V. V. Speybroeck, and R. A. van Santen, eds.), pp. 189 – 228, Elsevier, 2018.
- [88] P. P. Ewald, "Die berechnung optischer und elektrostatischer gitterpotentiale," *Annalen der Physik*, vol. 369, no. 3, pp. 253–287, 1921.
- [89] J. Marreiros, C. Caratelli, J. Hajek, A. Krajnc, G. Fleury, B. Bueken, D. E. De Vos, G. Mali, M. B. Roeffaers, V. Van Speybroeck, *et al.*, "The active role of methanol in post-synthetic linker exchange in the metal-organic framework uiO-66," *Chemistry of Materials*, 2019.
- [90] M. Born and R. Oppenheimer, "Zur quantentheorie der moleküle," *Annalen der Physik*, vol. 389, no. 20, pp. 457–484, 1927.

- [91] M. Ceriotti, W. Fang, P. G. Kusalik, R. H. McKenzie, A. Michaelides, M. A. Morales, and T. E. Markland, "Nuclear quantum effects in water and aqueous systems: Experiment, theory, and current challenges," *Chemical Reviews*, vol. 116, no. 13, pp. 7529–7550, 2016. PMID: 27049513.
- [92] L. Vanduyfhuys, S. Vandenbrande, T. Verstraelen, R. Schmid, M. Waroquier, and V. Van Speybroeck, "Quickff: A program for a quick and easy derivation of force fields for metal-organic frameworks from ab initio input," *Journal of computational chemistry*, vol. 36, no. 13, pp. 1015–1027, 2015.
- [93] A. C. T. van Duin, S. Dasgupta, F. Lorant, and W. A. Goddard, "Reaxff: A reactive force field for hydrocarbons," *The Journal of Physical Chemistry A*, vol. 105, no. 41, pp. 9396–9409, 2001.
- [94] L. H. Thomas, "The calculation of atomic fields," *Mathematical Proceedings of the Cambridge Philosophical Society*, vol. 23, no. 5, p. 542–548, 1927.
- [95] E. Fermi, "Eine statistische methode zur bestimmung einiger eigenschaften des atoms und ihre anwendung auf die theorie des periodischen systems der elemente," *Zeitschrift für Physik*, vol. 48, pp. 73–79, Jan 1928.
- [96] P. Hohenberg and W. Kohn, "Inhomogeneous electron gas," *Phys. Rev.*, vol. 136, pp. B864–B871, Nov 1964.
- [97] W. Kohn and L. J. Sham, "Self-consistent equations including exchange and correlation effects," *Phys. Rev.*, vol. 140, pp. A1133–A1138, Nov 1965.
- [98] S. H. Vosko, L. Wilk, and M. Nusair, "Accurate spin-dependent electron liquid correlation energies for local spin density calculations: a critical analysis," *Canadian Journal of Physics*, vol. 58, no. 8, pp. 1200–1211, 1980.
- [99] A. D. Becke, "Density-functional exchange-energy approximation with correct asymptotic behavior," *Phys. Rev. A*, vol. 38, pp. 3098–3100, Sep 1988.
- [100] C. Lee, W. Yang, and R. G. Parr, "Development of the colle-salvetti correlation-energy formula into a functional of the electron density," *Phys. Rev. B*, vol. 37, pp. 785–789, Jan 1988.
- [101] J. P. Perdew, K. Burke, and M. Ernzerhof, "Generalized gradient approximation made simple," *Phys. Rev. Lett.*, vol. 77, pp. 3865–3868, Oct 1996.
- [102] J. P. Perdew, K. Burke, and M. Ernzerhof, "Generalized gradient approximation made simple [phys. rev. lett. 77, 3865 (1996)]," *Phys. Rev. Lett.*, vol. 78, pp. 1396–1396, Feb 1997.
- [103] A. D. Becke, "Density-functional thermochemistry. iii. the role of exact exchange," *The Journal of Chemical Physics*, vol. 98, no. 7, pp. 5648–5652, 1993.

- [104] C. Adamo and V. Barone, "Toward reliable density functional methods without adjustable parameters: The pbe0 model," *The Journal of Chemical Physics*, vol. 110, no. 13, pp. 6158–6170, 1999.
- [105] S. Grimme, J. Antony, S. Ehrlich, and H. Krieg, "A consistent and accurate ab initio parametrization of density functional dispersion correction (dft-d) for the 94 elements h-pu," *The Journal of Chemical Physics*, vol. 132, no. 15, p. 154104, 2010.
- [106] T. Bučko, S. Lebègue, T. Gould, and J. G. Ángyán, "Many-body dispersion corrections for periodic systems: an efficient reciprocal space implementation," *Journal of Physics: Condensed Matter*, vol. 28, p. 045201, jan 2016.
- [107] A. Ambrosetti, A. M. Reilly, R. A. DiStasio, and A. Tkatchenko, "Long-range correlation energy calculated from coupled atomic response functions," *The Journal of Chemical Physics*, vol. 140, no. 18, p. 18A508, 2014.
- [108] J. Wieme, K. Lejaeghere, G. Kresse, and V. Van Speybroeck, "Tuning the balance between dispersion and entropy to design temperature-responsive flexible metal-organic frameworks," *Nature communications*, vol. 9, no. 1, p. 4899, 2018.
- [109] J. Hajek, J. Van der Mynsbrugge, K. De Wispelaere, P. Cnudde, L. Vanduyfhuyse, M. Waroquier, and V. Van Speybroeck, "On the stability and nature of adsorbed pentene in brønsted acid zeolite h-zsm-5 at 323 k," *Journal of catalysis*, vol. 340, pp. 227–235, 2016.
- [110] T. Verstraelen, V. Van Speybroeck, and M. Waroquier, "Zeobuilder: A gui toolkit for the construction of complex molecular structures on the nanoscale with building blocks," *Journal of Chemical Information and Modeling*, vol. 48, no. 7, pp. 1530–1541, 2008. PMID: 18543904.
- [111] A. Heyden, A. T. Bell, and F. J. Keil, "Efficient methods for finding transition states in chemical reactions: Comparison of improved dimer method and partitioned rational function optimization method," *The Journal of Chemical Physics*, vol. 123, no. 22, p. 224101, 2005.
- [112] W. H. Press, W. H. Press, B. P. Flannery, B. P. Flannery, S. A. Teukolsky, W. T. Vetterling, and W. T. Vetterling, *Numerical recipes in Pascal: the art of scientific computing*, vol. 1. Cambridge University Press, 1989.
- [113] D. E. Vanpoucke, K. Lejaeghere, V. Van Speybroeck, M. Waroquier, and A. Ghysels, "Mechanical properties from periodic plane wave quantum mechanical codes: The challenge of the flexible nanoporous mil-47 (v) framework," *The Journal of Physical Chemistry C*, vol. 119, no. 41, pp. 23752–23766, 2015.

- [114] F. Birch, "Finite elastic strain of cubic crystals," *Physical review*, vol. 71, no. 11, p. 809, 1947.
- [115] F. Murnaghan, "The compressibility of media under extreme pressures," *Proceedings of the national academy of sciences of the United States of America*, vol. 30, no. 9, p. 244, 1944.
- [116] A. Ghysels, T. Verstraelen, K. Hemelsoet, M. Waroquier, and V. Van Speybroeck, "Tamkin: a versatile package for vibrational analysis and chemical kinetics," 2010.
- [117] A. Ghysels, D. Van Neck, and M. Waroquier, "Cartesian formulation of the mobile block hessian approach to vibrational analysis in partially optimized systems," *The Journal of chemical physics*, vol. 127, no. 16, p. 164108, 2007.
- [118] V. Van Speybroeck, K. De Wispelaere, J. Van der Mynsbrugge, M. Vandichel, K. Hemelsoet, and M. Waroquier, "First principle chemical kinetics in zeolites: the methanol-to-olefin process as a case study," *Chemical Society Reviews*, vol. 43, no. 21, pp. 7326–7357, 2014.
- [119] R. Car and M. Parrinello, "Unified approach for molecular dynamics and density-functional theory," *Physical review letters*, vol. 55, no. 22, p. 2471, 1985.
- [120] P. Ehrenfest, "Bemerkung über die angenäherte gültigkeit der klassischen mechanik innerhalb der quantenmechanik," *Zeitschrift für Physik A Hadrons and Nuclei*, vol. 45, no. 7, pp. 455–457, 1927.
- [121] D. Marx and J. Hutter, *Ab initio molecular dynamics: basic theory and advanced methods*. Cambridge University Press, 2009.
- [122] S. Rogge, L. Vanduyfhuys, A. Ghysels, M. Waroquier, T. Verstraelen, G. Maurin, and V. Van Speybroeck, "A comparison of barostats for the mechanical characterization of metal–organic frameworks," *Journal of chemical theory and computation*, vol. 11, no. 12, pp. 5583–5597, 2015.
- [123] G. J. Martyna, D. J. Tobias, and M. L. Klein, "Constant pressure molecular dynamics algorithms," *The Journal of Chemical Physics*, vol. 101, no. 5, pp. 4177–4189, 1994.
- [124] R. Kubo, "Statistical-mechanical theory of irreversible processes. i. general theory and simple applications to magnetic and conduction problems," *Journal of the Physical Society of Japan*, vol. 12, no. 6, pp. 570–586, 1957.
- [125] L. Grajciar, C. J. Heard, A. A. Bondarenko, M. V. Polynski, J. Meeprasert, E. A. Pidko, and P. Nachtigall, "Towards operando computational modeling in heterogeneous catalysis," *Chemical Society Reviews*, vol. 47, no. 22, pp. 8307–8348, 2018.

- [126] E. Cances, B. Mennucci, and J. Tomasi, "A new integral equation formalism for the polarizable continuum model: Theoretical background and applications to isotropic and anisotropic dielectrics," *The Journal of chemical physics*, vol. 107, no. 8, pp. 3032–3041, 1997.
- [127] D. Dubbeldam, A. Torres-Knoop, and K. S. Walton, "On the inner workings of monte carlo codes," *Molecular Simulation*, vol. 39, no. 14–15, pp. 1253–1292, 2013.
- [128] S. Vandenbrande, T. Verstraelen, J. J. Gutiérrez-Sevillano, M. Waroquier, and V. Van Speybroeck, "Methane adsorption in zr-based mofs: comparison and critical evaluation of force fields," *The Journal of Physical Chemistry C*, vol. 121, no. 45, pp. 25309–25322, 2017.
- [129] R. Demuynck, S. M. Rogge, L. Vanduyfhuys, J. Wieme, M. Waroquier, and V. Van Speybroeck, "Efficient construction of free energy profiles of breathing metal–organic frameworks using advanced molecular dynamics simulations," *Journal of chemical theory and computation*, vol. 13, no. 12, pp. 5861–5873, 2017.
- [130] O. Valsson, P. Tiwary, and M. Parrinello, "Enhancing important fluctuations: Rare events and metadynamics from a conceptual viewpoint," *Annual review of physical chemistry*, vol. 67, pp. 159–184, 2016.
- [131] A. Laio and M. Parrinello, "Escaping free-energy minima," *Proceedings of the National Academy of Sciences*, vol. 99, no. 20, pp. 12562–12566, 2002.
- [132] L. Sutto, S. Marsili, and F. L. Gervasio, "New advances in metadynamics," *Wiley Interdisciplinary Reviews: Computational Molecular Science*, vol. 2, no. 5, pp. 771–779, 2012.
- [133] E. Carter, G. Ciccotti, J. T. Hynes, and R. Kapral, "Constrained reaction coordinate dynamics for the simulation of rare events," *Chemical Physics Letters*, vol. 156, no. 5, pp. 472–477, 1989.
- [134] E. Darve and A. Pohorille, "Calculating free energies using average force," *The Journal of Chemical Physics*, vol. 115, no. 20, pp. 9169–9183, 2001.
- [135] C. Jarzynski, "Nonequilibrium equality for free energy differences," *Physical Review Letters*, vol. 78, no. 14, p. 2690, 1997.
- [136] L. Rosso, P. Mináry, Z. Zhu, and M. E. Tuckerman, "On the use of the adiabatic molecular dynamics technique in the calculation of free energy profiles," *The Journal of chemical physics*, vol. 116, no. 11, pp. 4389–4402, 2002.
- [137] J. R. Gullingsrud, R. Braun, and K. Schulten, "Reconstructing potentials of mean force through time series analysis of steered molecular dynamics

- simulations," *Journal of Computational Physics*, vol. 151, no. 1, pp. 190–211, 1999.
- [138] K. De Wispelaere, C. S. Wondergem, B. Ensing, K. Hemelsoet, E. J. Meijer, B. M. Weckhuysen, V. Van Speybroeck, and J. Ruiz-Martínez, "Insight into the effect of water on the methanol-to-olefins conversion in h-sapo-34 from molecular simulations and in situ microspectroscopy," *ACS Catalysis*, vol. 6, no. 3, pp. 1991–2002, 2016.
- [139] K. De Wispelaere, B. Ensing, A. Ghysels, E. J. Meijer, and V. Van Speybroeck, "Complex reaction environments and competing reaction mechanisms in zeolite catalysis: insights from advanced molecular dynamics," *Chemistry—A European Journal*, vol. 21, no. 26, pp. 9385–9396, 2015.
- [140] P. Cnudde, K. De Wispelaere, J. Van der Mynsbrugge, M. Waroquier, and V. Van Speybroeck, "Effect of temperature and branching on the nature and stability of alkene cracking intermediates in h-zsm-5," *Journal of catalysis*, vol. 345, pp. 53–69, 2017.
- [141] V. Haigis, F.-X. Coudert, R. Vuilleumier, A. Boutin, and A. H. Fuchs, "Hydrothermal breakdown of flexible metal–organic frameworks: a study by first-principles molecular dynamics," *The journal of physical chemistry letters*, vol. 6, no. 21, pp. 4365–4370, 2015.
- [142] T. Bučko, L. Benco, J. Hafner, and J. G. Ángyán, "Monomolecular cracking of propane over acidic chabazite: An ab initio molecular dynamics and transition path sampling study," *Journal of catalysis*, vol. 279, no. 1, pp. 220–228, 2011.
- [143] G. Fraux and F.-X. Coudert, "Recent advances in the computational chemistry of soft porous crystals," *Chemical Communications*, vol. 53, no. 53, pp. 7211–7221, 2017.
- [144] C. Dellago, P. G. Bolhuis, and P. L. Geissler, "Transition path sampling," *Advances in chemical physics*, vol. 123, pp. 1–78, 2002.
- [145] Y. Sugita and Y. Okamoto, "Replica-exchange molecular dynamics method for protein folding," *Chemical physics letters*, vol. 314, no. 1-2, pp. 141–151, 1999.
- [146] G. M. Torrie and J. P. Valleau, "Nonphysical sampling distributions in monte carlo free-energy estimation: Umbrella sampling," *Journal of Computational Physics*, vol. 23, no. 2, pp. 187–199, 1977.
- [147] G. Patey and J. Valleau, "A monte carlo method for obtaining the interionic potential of mean force in ionic solution," *The Journal of Chemical Physics*, vol. 63, no. 6, pp. 2334–2339, 1975.

- [148] M. A. Rohrdanz, W. Zheng, and C. Clementi, "Discovering mountain passes via torchlight: Methods for the definition of reaction coordinates and pathways in complex macromolecular reactions," *Annual review of physical chemistry*, vol. 64, pp. 295–316, 2013.
- [149] A. Barducci, M. Bonomi, and M. Parrinello, "Metadynamics," *Wiley Interdisciplinary Reviews: Computational Molecular Science*, vol. 1, no. 5, pp. 826–843, 2011.
- [150] S. Kumar, J. M. Rosenberg, D. Bouzida, R. H. Swendsen, and P. A. Kollman, "The weighted histogram analysis method for free-energy calculations on biomolecules. i. the method," *Journal of computational chemistry*, vol. 13, no. 8, pp. 1011–1021, 1992.
- [151] G. Kresse and J. Furthmüller, "Efficient iterative schemes for ab initio total-energy calculations using a plane-wave basis set," *Physical review B*, vol. 54, no. 16, p. 11169, 1996.
- [152] G. Kresse and J. Hafner, "Ab initio molecular dynamics for liquid metals," *Physical Review B*, vol. 47, no. 1, p. 558, 1993.
- [153] G. Kresse and J. Hafner, "Ab initio molecular-dynamics simulation of the liquid-metal–amorphous-semiconductor transition in germanium," *Physical Review B*, vol. 49, no. 20, p. 14251, 1994.
- [154] G. Kresse and J. Furthmüller, "Efficiency of ab-initio total energy calculations for metals and semiconductors using a plane-wave basis set," *Computational materials science*, vol. 6, no. 1, pp. 15–50, 1996.
- [155] G. Kresse and D. Joubert, "From ultrasoft pseudopotentials to the projector augmented-wave method," *Physical Review B*, vol. 59, no. 3, p. 1758, 1999.
- [156] J. VandeVondele, M. Krack, F. Mohamed, M. Parrinello, T. Chassaing, and J. Hutter, "Quickstep: Fast and accurate density functional calculations using a mixed gaussian and plane waves approach," *Computer Physics Communications*, vol. 167, no. 2, pp. 103–128, 2005.
- [157] D. Dubbeldam, S. Calero, D. E. Ellis, and R. Q. Snurr, "Raspa: molecular simulation software for adsorption and diffusion in flexible nanoporous materials," *Molecular Simulation*, vol. 42, no. 2, pp. 81–101, 2016.
- [158] G. A. Tribello, M. Bonomi, D. Branduardi, C. Camilloni, and G. Bussi, "Plumed 2: New feathers for an old bird," *Computer Physics Communications*, vol. 185, no. 2, pp. 604–613, 2014.
- [159] J. Hajek, C. Caratelli, R. Demuynck, K. De Wispelaere, L. Vanduyfhuys, M. Waroquier, and V. Van Speybroeck, "On the intrinsic dynamic nature of the rigid uio-66 metal–organic framework," *Chemical science*, vol. 9, no. 10, pp. 2723–2732, 2018.

- [160] J. Canivet, M. Vandichel, and D. Farrusseng, "Origin of highly active metal–organic framework catalysts: defects? defects!," *Dalton Transactions*, vol. 45, no. 10, pp. 4090–4099, 2016.
- [161] P. Ghosh, Y. J. Colón, and R. Q. Snurr, "Water adsorption in uiO-66: the importance of defects," *Chemical Communications*, vol. 50, no. 77, pp. 11329–11331, 2014.
- [162] G. C. Shearer, S. Forselv, S. Chavan, S. Bordiga, K. Mathisen, M. Bjørgen, S. Svelle, and K. P. Lillerud, "In situ infrared spectroscopic and gravimetric characterisation of the solvent removal and dehydroxylation of the metal organic frameworks uiO-66 and uiO-67," *Topics in Catalysis*, vol. 56, no. 9–10, pp. 770–782, 2013.
- [163] J. Nishida, A. Tamimi, H. Fei, S. Pullen, S. Ott, S. M. Cohen, and M. D. Fayer, "Structural dynamics inside a functionalized metal–organic framework probed by ultrafast 2d ir spectroscopy," *Proceedings of the National Academy of Sciences*, vol. 111, no. 52, pp. 18442–18447, 2014.
- [164] C. Caratelli, J. Hajek, S. M. Rogge, S. Vandenbrande, E. J. Meijer, M. Waroquier, and V. Van Speybroeck, "Influence of a confined methanol solvent on the reactivity of active sites in uiO-66," *ChemPhysChem*, vol. 19, no. 4, pp. 420–429, 2018.
- [165] F.-X. Coudert, R. Vuilleumier, and A. Boutin, "Dipole moment, hydrogen bonding and ir spectrum of confined water," *ChemPhysChem*, vol. 7, no. 12, pp. 2464–2467, 2006.
- [166] S. Dalla Bernardina, E. Paineau, J.-B. Brubach, P. Judeinstein, S. Rouziére, P. Launois, and P. Roy, "Water in carbon nanotubes: the peculiar hydrogen bond network revealed by infrared spectroscopy," *Journal of the American Chemical Society*, vol. 138, no. 33, pp. 10437–10443, 2016.
- [167] G. Cicero, J. C. Grossman, E. Schwegler, F. Gygi, and G. Galli, "Water confined in nanotubes and between graphene sheets: A first principle study," *Journal of the American Chemical Society*, vol. 130, no. 6, pp. 1871–1878, 2008.
- [168] S. Kashtanov, A. Augustson, J.-E. Rubensson, J. Nordgren, H. Ågren, J.-H. Guo, and Y. Luo, "Chemical and electronic structures of liquid methanol from x-ray emission spectroscopy and density functional theory," *Physical Review B*, vol. 71, no. 10, p. 104205, 2005.
- [169] M. Pagliai, G. Cardini, R. Righini, and V. Schettino, "Hydrogen bond dynamics in liquid methanol," *The Journal of chemical physics*, vol. 119, no. 13, pp. 6655–6662, 2003.

- [170] J. A. Morrone and M. E. Tuckerman, "Ab initio molecular dynamics study of proton mobility in liquid methanol," *The Journal of chemical physics*, vol. 117, no. 9, pp. 4403–4413, 2002.

